Non-ideal magnetohydrodynamics in low-mass star formation

Jacques Masson

ÉCOLE NORMALE SUPÉRIEURE DE LYON

Centre de Recherches Astrophysiques de Lyon

THÈSE

en vue de l'obtention du grade de

Docteur de l'Université de Lyon, délivré par l'École Normale Supérieure de Lyon

Discipline : physique

Spécialité : astrophysique

ÉCOLE DOCTORALE : Physique et Astrophysique de Lyon

Présentée et soutenue publiquement le 13/11/2013

par

Jacques MASSON

Étude des effets de magnétohydrodynamique non idéale sur la formation des étoiles de faible masse

Non-ideal magnetohydrodynamics in low-mass star formation

sous la direction de :

Gilles Chabrier et Patrick Hennebelle

Après avis de :

M. Philippe André
M. Sébastien Fromang

Devant la commission d'examen formée de :

M. Philippe André	Rapporteur
M. Gilles Chabrier	Directeur
M. Jonathan Ferreira	Membre
M. Sébastien Fromang	Rapporteur
M. Patrick Hennebelle	Directeur
M. Guillaume Pineau des Forêts	President

À mes parents.

Remerciements

C'est l'aboutissement de trois ans de travail, de voyages, d'échanges et d'entraides. Le chemin n'est que rarement dégagé, les embûches et embranchements nombreux.

Mon équipe c'est tout d'abord Gilles et Patrick. Qu'on se croise par hasard à Paris ou que le plan de bataille soit discuté en avance, ils ont balisé le chemin au début et indiqué les directions prometteuses, parfois divergentes tout en me laissant libre d'explorer mes propres idées. Les bureaux et autres salles cafés résonnent des discussions montagne, naines brunes, guerre préhistorique, fragmentation et rapports sur les appareils volants non identifiés. De grands mystères encore à résoudre ! Merci à vous, de m'avoir suivi pendant ces trois ans.

Merci également à tous les autres membres de mon jury : Philippe André, Jonathan Ferreira, Sébatien Fromang et Guillaume Pineau des Forêts, de s'être déplacé à Lyon pour écouter la soutenance de ma thèse. Merci également pour la lecture, relecture et les conseils concernant le manuscrit, toujours donnés dans un but constructif. Et bien sûr, je vous suis très reconnaissant pour les commentaires élogieux et les encouragements pour la suite, qui m'ont fait très plaisir.

Avant la thèse, le match avait déjà commencé : je remercie tous ces professeurs qui m'ont donné envie de continuer dans les sciences et en particulier quand ça commençait à devenir intense, en prépa avec M. Archambault. Je n'oublie pas non plus Franck le Petit et Jacques le Bourlot, avec qui j'ai eu de longues discussions concernant la thèse ou la science, et sans qui je n'en serais pas là aujourd'hui.

Il y a bien sûr la faune et la flore du labo à qui je dois beaucoup ! GG, toujours là pour un conseil, de l'aide ou partager des souvenirs de chinoiseries d'une autre époque. François, allié de Stéphanie pour la chevalerie des tâches administratives pour nous autres pauvres thésards virtuels (Jeremy, c'est à toi !), qui a toujours pu être là quand il fallait et continue à laisser trainer une oreille concernée outre-atlantique. Quelques bureaux plus loin, Neil (il fait beau ?) et la toute nouvelle plante du labo, Benoit, que je vais importuner en buvant mon café. Stephanie, notre ange multitâches. Christophe, indéfectible pilier, compagnon d'aventures parfois, et de cafés plus que matinaux presque aussi souvent ! Mickael, grimpeur et magnetohydrodynamicien, avec qui on a chassé le soleil à Aussois. Sasha, dont le sourire et la motivation sont à toute épreuve. Alex, Fosca et Thomas, la team cosmo, qui régulièrement nous remplit le tableau de signes cabalistiques (Hodge star, je te vois !). Adrien, la nouvelle recrue de Gilles, notre nouveau DISCO. Dans les contrées dangereuses et reculées du bout du couloir on trouve également Rofl, Doris, France, Bernd. Les alliés de l'observatoire, JF, Bruno, qui ont dû en voir passer, des signatures. Une note suisse en revenant à Lyon, Cyril, et les raclettes mémorables. Enfin, la flore du labo : on la cultive activement dans le frigo, où de nouvelles espèces sont en train de naître !

L'équipe, c'est aussi les amis. De près, de loin, vus souvent ou vieux amis. Lyon, Paris ou ailleurs. Sans eux, je n'y serais pas arrivé. Vivien, Coline, Adrien, Vincent, Sylvain, Laurent, Antoine, Vincent, Boris, Chloé, Benjamain, Benoit, Laurie, Meriem, Elsa, Valerian, Camille, Pascal, Kevin, et tous les autres cachanais, amis d'enfance perdus de vus et amis en approche, merci ! Je remercie également Marie, pour tout son soutien et son amour, qui m'a convaincu que j'avais le potentiel de commencer, et finir une thèse. Et qui avait raison.

Je ne remercierai jamais assez ma famille, et en particulier mes parents, qui ont toujours été là

pour moi. Mes remerciements vont également à mes grands-parents (cannes à pêches et télescopes !), oncles, tantes et cousins cousines (et des mots de courage pour Chloé, la prochaine sur la liste !). Ils n'ont jamais douté et leur regard n'est que bienveillance, c'est un baume magnifique.

Enfin, je remercie tout l'encadrement de l'ENS de Lyon et de l'école doctorale de physique et d'astrophysique, que ce soit pour l'enseignement ou la vie dans le laboratoire.

Contents

Introduction

Stars are for astrophysicists as they appear when looking at the night sky: they seem to be everywhere. They recycle the very elements of the universe through their cycle of life and have a major impact on many other astrophysical objects through feedback (heating, ionisation rate). They have been used to probe the universe in terms of distance or mass and they now enable us to detect earth-like planets dozens of lightyears away. It is still however not clear how stars form and ever more detailed models are of paramount importance for a better understanding of the universe's most fundamental building blocks.

Stars form in giant gas clouds in the interstellar medium. This medium is not at rest: magnetic fields, ionisation from nearby stars, turbulence and chemical reactions are all at play, and none perfectly understood. Studying star formation therefore implies resolving non-linear multi-scale problems. Numerical simulations are a privileged tool, which still needs to be linked with observations to formulate the correct assumptions and gain insight into these processes.

The following work focuses primarily on the impact of magnetic fields on star formation with particular emphasis on the case of non-ideal magnetohydrodynamics. The angular momentum transport, as well as the formation of disks and their fragmentation will be discussed.

The manuscript is structured as follow:

Chapter 1 opens with an introductory chapter in which I present the history of star formation, namely the succession of discoveries that occurred since the first attempts at explaining star formation. The breakthroughs that strongly affected the theory of stars formation are highlighted, and the physics at stake described. This chapter ends by depicting a contemporary picture of low-mass star formation.

Chapter 2 focuses on the numerical methods used and developed during this thesis work and their contribution to the field of star formation. I shortly describe `RAMSES`, the numerical code used to conduct numerical experiments of star formation. The implementation of non-ideal magnetohydrodynamics in this code is then described.

Chapter 3 presents a chemical network developed to output more accurate resistivities for non-ideal magnetohydrodynamics simulations. A non-ideal gas equation of state essential to model the second phase of collapsing cores is also described, refining further the physics of our numerical predictions.

Finally, Chapter 4 reports the simulations carried out and their various results. The chapter closes with some preliminary second-core collapse simulations that have been performed using all the physics previously described.

Version française

Les étoiles sont pour les astrophysiciens comme dans le ciel nocturne : partout présentes où qu'on regarde. Les étoiles recyclent les éléments constitutifs de l'univers au cours de leur cycle de vie. Leur présence et leur rayonnement influence la formation et le développement d'autres objets astrophysiques. Elles ont également été utilisées pour mesurer et cartographier l'univers en termes de distance ou de masse et elles permettent la détection de planètes de type terrestre à des dizaines d'années lumières. Cependant, la compréhension des étapes de leur formation est toujours incomplète et l'étude de modèles de plus en plus détaillés est primordiale pour améliorer notre connaissance d'un des constituants les plus fondamental de l'univers.

Les étoiles naissent dans des nuages moléculaires géants dans le milieu interstellaire. Ce milieu est complexe, traversé par des champs magnétiques, subissant le rayonnement des étoiles proches, agité par des mouvements turbulents et est le terrain de réactions chimiques. Ainsi, l'étude de la formation des étoiles est un problème non-linéaire, multi-échelle et multi-physique. Les simulations numériques sont un outil privilégié qui permet de telles études, tout en devant être relié aux observations pour faire les bonnes approximations et mieux appréhender tous ces problèmes.

Le travail présenté dans cette thèse se focalise principalement sur l'impact des champs magnétiques sur la formation des étoiles, et en particulier sur l'influence de la magnétohydrodynamique non idéale. Le transport du moment angulaire ainsi que la formation des disques protoplanétaires seront au cœur de la problématique étudiée.

Le manuscrit est composé comme suit :

Le chapitre 1 commence avec une introduction dans laquelle est présentée l'histoire de l'étude de la formation des étoiles, en suivant et en détaillant la physique des grandes étapes qui ont menées à notre compréhension actuelle du sujet. Le chapitre est conclu par une description des défis contemporains dans le domaine la formation des étoiles.

Le chapitre 2 se focalise sur les méthodes numériques utilisées et développées pendant cette thèse et sur leur contribution au domaine de la formation des étoiles. Je décris le code `RAMSES`, utilisé pour simuler les effondrements de cœurs denses en protoétoiles. S'ensuit la description précise de l'implémentation de la magnétohydrodynamique non idéale dans ce code.

Le chapitre 3 présente le réseau chimique utilisé pour une description plus précise des différents effets de magnétohydrodynamique non idéale dans les simulations. Une equation d'état réaliste, essentielle pour décrire les stades ultimes de formation des étoiles, est également présentée.

Finalement, le chapitre 4 fait état des simulations conduites durant la thèse et de leurs résultats. Le chapitre termine sur des résultats préliminaires de simulations du second cœur de Larson parmi les plus complètes à ce jour.

Chapter 1

History and theory of star formation

"*Bright points in the sky or a blow on the head will equally cause one to see stars.*"
Percival Lowell, Mars, 1895.

Contents

Introduction

In this first chapter I try and give an insight on how the modern theory of stars formation was built over the years. I proceed historically, focusing on the physics at work at each new step and the reasons for the constant questioning of the up-to-date theory.

I emphasize that this chapter's objective is to describe the general train of thoughts that led to today's theory of stars formation, which also inevitably includes theories that were subsequently disproved. Nonetheless, equations later deemed inaccurate in the context of star formation have led, either directly or indirectly, to a better understanding of the physical processes involved by exploring every possible alternative.

1.1 First ages: the broad picture

1.1.1 Baby steps

The history of the study of star formation really began almost a century ago, with the progress summarized in a review written by L. Spitzer (see Spitzer (1949)). At the time, the assumption was that stars would form all the same and then slowly radiate their mass as light, following a common evolutionary sequence. Already, several observations challenged the theory: the stars couldn't be as old as theorized.

- The universe didn't appear to be old enough for stars to radiate away a significant fraction of their mass. The idea that *something* had happened several billion years ago was already there.
- Nuclear physicists could tell that the only process of importance permitting to convert mass into light in stellar interiors would be the fusion of four hydrogen atoms into an helium atom, which did not allow for significant mass loss.
- Supergiant stars radiating tremendous amounts of energy (some ten thousand times more than that of our sun) would consume all their hydrogen in a few hundred million years, and must therefore have been formed only recently.

These considerations along with recent discoveries in the composition of the interstellar medium (mostly hydrogen atoms, with other elements scarcely found) led astronomers to a general theory in which the interstellar medium slowly aggregates due to an effective force due to the radiation of nearby stars, resulting in dark clouds called "globules" (see also Bok and Reilly (1947)). At the point when gravitation can overcome the effect of thermal pressure in overdense regions called *dense cores*, the cloud would contract and give birth to a star.

Virial theorem. This picture is supported by a fundamental theorem first expressed by Rudolf Clausius in 1870. It links the potential gravitational energy with the pressure exerted by every particle moving and colliding with others. It can therefore be used to assess the stability of any self-gravitating structure when both thermodynamics and gravity are operating. Let's assume a particle of mass m, position $\mathbf{r}$, with the (gravitational in this case) force exerted on the particle $\mathbf{F}$. The fundamental principle of Newtonian dynamics reads $m\frac{\mathrm{d}^2\mathbf{r}}{\mathrm{d}t^2} = \mathbf{F}$. Introducing the quantity, known as the *virial*, $\mathbf{F}\cdot\mathbf{r}$ yields

$$m\frac{\mathrm{d}}{\mathrm{d}t}(\mathbf{r}\cdot\frac{\mathrm{d}\mathbf{r}}{\mathrm{d}\mathbf{r}}) = m(\frac{\mathrm{d}\mathbf{r}}{\mathrm{d}t})^2 + \mathbf{F}\cdot\mathbf{r}. \tag{1.1}$$

For a system of N particles of respective mass m_i (i representing a given particle) and position $\mathbf{r_i}$, of inertial moment $I = \sum_i m_i {\mathbf{r_i}}^2$ and of total kinetic energy $\mathcal{T} = \frac{1}{2}\sum_i m_i \left(\frac{\mathrm{d}\mathbf{r_i}}{\mathrm{d}t}\right)^2$, equation (1.1) becomes

$$\frac{1}{2}\ddot{I} = 2\mathcal{T} + \Omega \tag{1.2}$$

where $\Omega = \sum_i \mathbf{F_i} \cdot \mathbf{r_i}$, with $\mathbf{F_i}$ being the force exerted on the particle i. This quantity has to be evaluated in each case, depending on the forces at play. For the pure gravitational case,

$$\Omega = -\sum_i \sum_{j \neq i} G m_i m_j \frac{(\mathbf{r_j} - \mathbf{r_i})}{|\mathbf{r_j} - \mathbf{r_i}|^3} \mathbf{r_i} \tag{1.3}$$

$$= -\frac{1}{2}\sum_{i \neq j} G \frac{m_i m_j}{|\mathbf{r_j} - \mathbf{r_i}|} \tag{1.4}$$

where we recognize Ω the gravitational potential energy.

The application to the formation of stars is straightforward, since we wish to compare the effect of gravity against thermal pressure. We assume a star-to-be with a constant density ρ, a radius R and total mass M. The potential energy is the sum of the potential energy of each shell $dm(r)$, $dm(r) = 4\pi r^2 dr$ being the mass comprised between a radius r and $r + dr$. If $m(r) = \frac{4}{3}\pi r^3 \rho$ is the mass of the sphere of radius r, the potential energy becomes

$$\Omega = -\int_0^R G \frac{m(r)\mathrm{d}m}{r} \tag{1.5}$$

$$= -\frac{16}{15}\pi^2 \rho^2 G R^5 \tag{1.6}$$

$$= -\frac{3}{5}\frac{GM^2}{R}. \tag{1.7}$$

For the same sphere, we can calculate the inertial momentum under the assumption of a ideal monomolecular isothermal gas

$$I = \frac{3}{2} N k_B T \tag{1.8}$$

$$= \frac{3}{2}\frac{M k_B T}{\mu m_H} \tag{1.9}$$

with μm_H the mean atomic mass. Equation (1.2) in its equilibrium form reads

$$0 = 2\mathcal{T} + \Omega \tag{1.10}$$

which is satisfied only for $R = R_{\mathrm{crit}}$ and $M = M_{\mathrm{crit}}$, given by

$$R_{\mathrm{crit}} = \sqrt{\frac{15 k_B T}{4\pi \rho G \mu m_H}}, \tag{1.11}$$

$$M_{\mathrm{crit}} = \frac{4}{3}\pi R_{\mathrm{crit}}^3 \rho. \tag{1.12}$$

The critical radius and mass can be interpreted as the size and mass of an isothermal, spherical cloud of gas with a uniform density for which thermal pressure and gravity are in equilibrium. For bigger (respectively smaller) masses than the critical value the gravity (resp. the pressure) will be dominant and the cloud will collapse (resp. expand).

We described the stability of a uniform spherical cloud regarding energetics. A different question can be tackled using a linear stability analysis: can a local density enhancement grow into an unstable bulk of gas ?

Jeans length. Another fundamental length (or mass) is known as the *Jeans length* (or mass). It describes the gravitational stability of a uniform, isothermal and infinite medium, using a linear perturbation analysis. In order to derive this criteria, we use the Euler set of equations, including gravity

$$\Delta\Phi = 4\pi\rho G \quad \text{(Poisson equation for the gravitational potential)} \tag{1.13}$$

$$\frac{\partial\rho}{\partial t} + \boldsymbol{\nabla}\cdot(\rho\mathbf{u}) = 0 \quad \text{(Mass conservation)} \tag{1.14}$$

$$\frac{\partial\rho\mathbf{u}}{\partial t} + \boldsymbol{\nabla}\cdot(\rho\mathbf{u}\otimes\mathbf{u} + P\mathbb{1}) = -\rho\boldsymbol{\nabla}\Phi \quad \text{(Momentum conservation)} \tag{1.15}$$

$$\frac{\partial E}{\partial t} + \boldsymbol{\nabla}\cdot[\mathbf{u}(E + P + \rho\Phi)] = -\rho\mathbf{u}\boldsymbol{\nabla}\Phi \quad \text{(Energy conservation)} \tag{1.16}$$

with $E = \epsilon + \rho\frac{u^2}{2}$, ϵ being the internal energy density. ρ stands for the density and $\mathbf{u}$ the velocity of the fluid. P is the pressure and Φ the gravitational potential.

We now consider a perturbation, using subscript 0 for equilibrium quantities and 1 for perturbed ones. Initially, the medium is at rest (i.e. $\mathbf{u_0} = \mathbf{0}$) and we have

$$\mathbf{u} = \mathbf{u_1} \tag{1.17}$$

$$\rho = \rho_0 + \rho_1 \tag{1.18}$$

$$\Phi = \Phi_0 + \Phi_1. \tag{1.19}$$

Linearizing and combining the previous set of equations, using the isothermal sound speed $c_s^2 = \frac{P}{\rho} = \frac{k_B T}{\mu m_H}$ gives

$$\frac{\partial^2\rho_1}{\partial t^2} = \rho_0\boldsymbol{\nabla}^2\Phi_1 + c_s^2\boldsymbol{\nabla}^2\rho_1. \tag{1.20}$$

Assuming a density wave $\rho_1(t) = \rho_{1,0}e^{i(\mathbf{k}\cdot\mathbf{r}+\omega t)}$ results in the dispersion relation $\omega^2 = k^2c_s^2 - 4\pi G\rho_0$. For $\omega^2 < 0$, we have $\rho_1(t) = \rho_{1,0}e^{i(\mathbf{k}\cdot\mathbf{r})}e^{\pm\tilde{\omega}}$ with $\omega = i\tilde{\omega}$. The unstable modes have a wave number k which satisfies

$$k < k_{\text{Jeans}} = \left(\frac{4\pi G\rho_0}{c_s^2}\right). \tag{1.21}$$

This condition leads to the definition of the Jeans length ($\lambda_{\text{Jeans}} = \frac{2\pi}{k_{\text{Jeans}}}$) and the Jeans mass that characterize a critically stable bulk of gas

$$\lambda_{\text{Jeans}} = c_s\sqrt{\frac{\pi}{G\rho_0}}, \tag{1.22}$$

$$M_{\text{Jeans}} = \frac{4\pi}{3}\lambda_{\text{Jeans}}^3\rho_0. \tag{1.23}$$

We note that the expression for the Jeans length (equation (1.22)) is similar to the expression found using the virial theorem, except for the numerical prefactor. An interesting property is that since $M_{\text{Jeans}} \propto \rho^{-\frac{1}{2}}$ when the density increases the Jeans mass decreases, leading to a never-ending collapse.

In addition, letting go of the isothermal assumption and replacing it with a polytropic gas equation of state defined by $P \propto \rho^n$ (see Appendix 1.A) leads to a Jeans mass which depends on the polytropic index n

$$M_{\text{Jeans}} \propto \rho^{\frac{3}{2}n-2}. \tag{1.24}$$

The value $n = \frac{4}{3}$ separates the stable cases ($n > \frac{4}{3}$, for which the Jeans mass increases with density) from the unstable cases ($n < \frac{4}{3}$, in which case the Jeans mass decreases with increasing density).

These order of magnitude calculations furnish a simple, yet solid basis for the study of collapsing clouds. There is however more to the formation of stars than simple polytropic evolutions or isothermal uniform spheres.

Typical time for the collapse A very early analytical work addressed the problem of trying to estimate the typical time required for a cloud to collapse. The easiest derivation makes abstraction of the thermal and rotational support. It is then possible to derive a simple time evolution for the density. We begin with the equation of motion for a particle (or a shell, since spherical symmetry holds) at a distance r, embedded in a homogeneous cloud of density ρ_0

$$\frac{\mathrm{d}^2 r}{\mathrm{d}t^2} = -\frac{GM_{\text{inside}}}{r^2} \tag{1.25}$$

where $M_{\text{inside}} = \frac{4}{3}\pi\rho_0 r_0^3$ is the initial mass inside the shell of initial radius r_0. Newton's third law of motion gives the time for a body of mass m to complete an orbit around a massive body of mass M: $t_{\text{orbit}} = \sqrt{\frac{4\pi R^3}{GM}}$, independently of the eccentricity of the trajectory. A degenerate ellipse (eccentricity 1 and semi-major axis $\frac{R}{2}$) can describe a linear trajectory of length R corresponding to the free-fall on a central object or equivalent in uniform density. In this last case, the free-fall time is half the orbital time for a circular orbit at a radius $\frac{R}{2}$ (the semi-major axis), and is the same for every particle at every radius: $t_{\text{ff}} = \frac{t_{\text{orbit}}}{2} = \sqrt{\frac{3\pi}{32\rho G}}$. When starting at rest the collapse occurs at every point of the sphere simultaneously with the same free-fall time t_{ff}, meaning that every shell will reach the center at the same time and that the mass contained inside a given shell will always remain the same. This allows for an easy solving of equation (1.25) to express density as function of time. Using the self-similar variable $\cos^2(\beta) = \frac{r}{r_0}$ and multiplying 1.25 by $\frac{\mathrm{d}r}{\mathrm{d}t}$, we obtain

$$\beta + \frac{1}{2}\sin(2\beta) = t\left(\frac{8\pi G\rho_0}{3}\right)^{\frac{1}{2}} \tag{1.26}$$

which gives the evolution of the radius with time. For $r = 0$ ($\beta = \frac{\pi}{2}$) we retrieve the free-fall time

$$t_{\text{ff}} = \sqrt{\frac{3\pi}{32G\rho_0}}. \tag{1.27}$$

Density profile at equilibrium A few years after, Bonnor (1956) and Ebert (1955) were interested in the density profile of such clouds of gas in thermal-gravitational balance. It is indeed possible to derive the (again, self-similar) density profile of a sphere taking into account thermal pressure. We present here the calculation for an isothermal ideal gas with a polytropic index $n = 1$ (see appendix 1.A for further details) and no rotation.

The governing equations involved read

$$\Delta\Phi = 4\pi G\rho \tag{1.28}$$

$$\frac{\mathrm{d}\mathbf{v}}{\mathrm{d}t} = -\frac{1}{\rho}\boldsymbol{\nabla} P - \boldsymbol{\nabla\Phi} \tag{1.29}$$

$$p = \kappa\rho^n, \tag{1.30}$$

yielding for the equilibrium of an ideal isothermal gas

$$\Delta\Phi = 4\pi G\rho \tag{1.31}$$

$$\mathbf{0} = -\frac{1}{\rho}\boldsymbol{\nabla} P - \boldsymbol{\nabla}\boldsymbol{\Phi} \tag{1.32}$$

$$p = \rho c_s^2 \tag{1.33}$$

where c_s is the sound speed. Using the following dimensionless quantities

$$D = \frac{\rho}{\rho_c} \tag{1.34}$$

$$x = r\frac{\sqrt{4\pi g\rho_c}}{c_s} \tag{1.35}$$

where ρ_c is the central density, we get

$$\frac{1}{x^2}\frac{d}{dx}\left(x^2\frac{1}{D}\frac{dD}{dx}\right) = -D. \tag{1.36}$$

Using the Poisson equation we obtain $\Delta(\ln(D) + \frac{\Phi}{4\pi G\rho_c}) = -D + \frac{\rho}{\rho_c} = 0$, which allows us to write $D \propto \exp(-\Phi)$. We can finally write the well-known Lane-Emden equation

$$\frac{d^2\Phi}{dx^2} + \frac{2}{x}\frac{d\Phi}{dx} = \exp(-\Phi) \tag{1.37}$$

with the following initial conditions

$$\rho(0) = \rho_c \Rightarrow \Phi(0) = 0 \tag{1.38}$$

$$\lim_{r\to 0}\nabla\Phi = \lim_{r\to 0} -\frac{GM(r)}{r^2} \propto \lim_{r\to 0} r = 0. \tag{1.39}$$

Unfortunately in the particular case of the isothermal ideal gas, there is no analytical solution. Using a numerical integration, one finds a flat inner density profile followed by a decreasing density $\rho(r) \propto r^{-2}$. The solutions are governed by the external radius of the cloud, $x_{\max}$. In addition, the stability of the cloud against small perturbations can be assessed by studying the sign of the derivative $\frac{\partial P}{\partial V}$: if it's positive the cloud is stable against gravitational collapse because a slight increase in pressure will result in an increase of the volume followed by a decrease in pressure. On the other hand, if $\frac{\partial P}{\partial V} < 0$ the cloud is unstable. Bonnor (1956) and Ebert (1955) used this criterion to derive a critical radius $x_{\text{crit}} = 6.451$ and a set of self-similar solutions with a flat inner density profile and an outer density profile $\rho(r) \propto r^{-2}$. They were subsequently named Bonnor-Ebert solutions (hereafter BE). When $x_{\max} \Rightarrow \infty$ the sphere is highly unstable, a setup known as the singular isothermal sphere (see Shu (1977)). A graphical review of this discussion is shown in Fig. 1.1.

One can refine the previous equations using a polytropic law $P \propto \rho^{n}$[1]. In this case the Lane-Emden equation reads

$$\frac{1}{x^2}\frac{d}{dx}\left(x^2\frac{d\theta}{dx}\right) = \frac{d^2\theta}{d\xi^2} + \frac{2}{\xi}\frac{d\theta}{dx} = -\theta^{\tilde{n}} \tag{1.40}$$

where $\theta^{\tilde{n}} = \frac{\rho}{\rho_c}$ and $\xi = r\left(\frac{\kappa(n+1)}{4\pi G b}\rho_c^{\frac{1-\tilde{n}}{\tilde{n}}}\right)^{-0.5}$. In terms of density profiles, these spheres still feature the flat central part and the r^{-2} tail.

[1] We use here a shorter expression for the polytropic law. The classical polytropic index is usually defined as follow (we use the letter $\tilde{n}$): $P = \kappa\rho^{1+\frac{1}{\tilde{n}}}$ with $1 + \frac{1}{\tilde{n}} = n$.

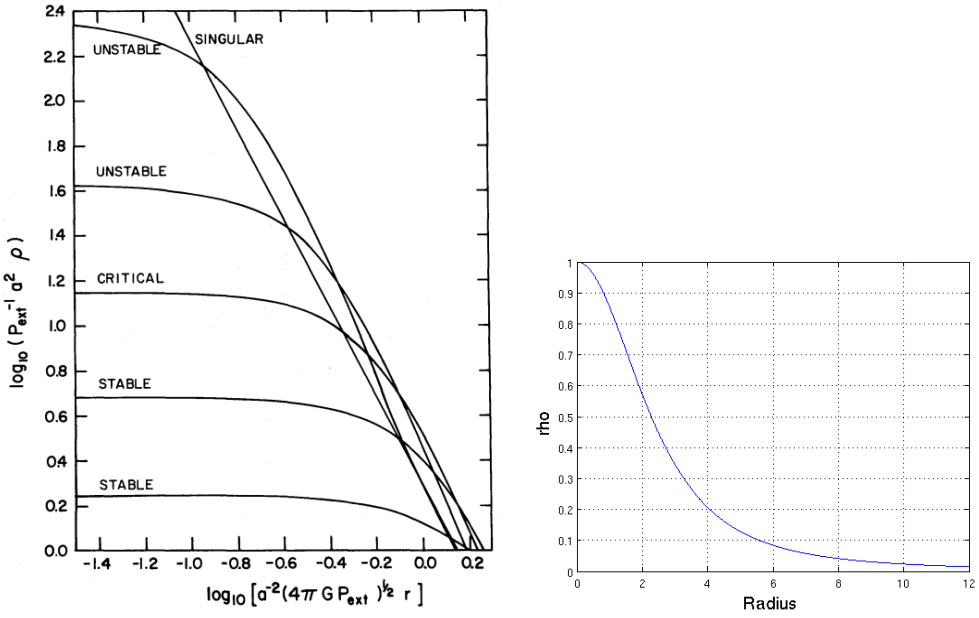

Figure 1.1: Density profile versus radius for an isothermal ideal gas spherical cloud at the equilibrium. Left: taken from Shu (1977), the various curves correspond to different values for $x_{\rm crit}$ (intersection between the abscissa axis and the curve). Right: same density profile for a stable BE sphere, calculated via a personal numerical integration (arbitrary units).

Spinning stars and the angular momentum problem The main concern in star formation studies in mid-way through the twentieth century lied with the conservation of angular momentum and its transport. As an isolated system, the cloud's angular momentum is conserved during the contraction. In the simple case of a uniform density sphere of initial radius R_0 in solid body rotation (with an angular velocity ω_0), the initial angular momentum is $J_0 = \omega_0 R_0^2$. Since it is conserved through the collapse, at all time $J = \omega(t)R(t)^2 = J_0$, yielding

$$\omega(t) = \omega_0 \left(\frac{R_0}{R(t)}\right)^2. \tag{1.41}$$

Thus, transferring the momentum of a gigantic dark cloud of about a light-year in diameter to a small stellar object would cause the latter to be torn to pieces due to colossal rotation speeds ($\frac{R_0}{R_{\rm star}} \simeq 2 \times 10^{14}$). This was the first angular momentum problem: stars can only form if angular momentum is transported away efficiently. Turbulent motions and/or galactic magnetic fields have been called in as possible mechanisms to prevent this dramatic increase in momentum. This will be discussed in this chapter.

Further refinements and studies by Hoyle (1953); Mestel and Spitzer (1956) eventually led to a precise picture involving an initial free-fall phase while the optical thickness remained low enough for all the compressional energy to be radiated away. When (and if) the optical thickness becomes high enough, the thermal energy is trapped and equilibrium is attained between thermal pressure and gravity, thus halting the collapse. Slow accretion and Helmoltz contraction[2] then follows until the temperature becomes high enough for the dissociation of molecular hydrogen (H_2) to occur, acting as a new energy sink and allowing the collapse to resume.

[2]The conversion of gravitational energy from the contraction produces heat, or in the other way around the contraction of the core due to cooling of its surface.

Since turbulence was, and still is, a tricky business, magnetic fields were the first focus of researchers attempting to solve the momentum problem.

Polytropic spinning stars The exact same stability analysis as in § 1.1.1 can be applied to rotating stars. One can notice that it will only add a pressure term in the Navier-Stokes equation that can be written $\boldsymbol{\nabla}\Phi_{\rm rot}$ giving

$$\mathbf{0} = -\frac{1}{\rho}\boldsymbol{\nabla}P - \boldsymbol{\nabla}\boldsymbol{\Phi} - \boldsymbol{\nabla}\Phi_{\rm rot}. \tag{1.42}$$

.

Using the Poisson equation we now obtain for an ideal isothermal sphere of gas $\Delta(\ln(\frac{\rho}{\rho_c}) + \frac{\Phi+\Phi_{\rm rot}}{4\pi G\rho_c}) = 0$ from which we can write $\frac{\rho}{\rho_c} \propto \exp(-\Phi - \Phi_{\rm rot})$. Again, we can do the same with another polytrope (and solve numerically if no exact solution is available).

1.1.2 Galactic magnetic fields

One of the first attempt to take into account the effect of large-scale magnetic fields in the formation of stars was made by Mestel and Spitzer (1956). At the time, several observations and physical mechanisms suggested that such magnetic fields indeed existed. The polarization of starlight involving magnetically oriented grains was a central part of the proof for the presence of magnetic fields in molecular clouds. Theoretical mechanisms explaining the means to accelerate cosmic rays[3] or explaining the lateral equilibrium of galactic spiral arms also made use of a large-scale field. As hard evidence was gathering through observations (see Field (1970) for an early review on this issue), theoretical developments on the influence of magnetic fields on gravitational collapse emerged. After the *angular momentum problem*^{number1} came the *angular momentum problem*^{number2}: magnetic fields act as an additional support against gravitational collapse and can slow down the rotation of the protostar and its surroundings to the point of removing all the angular momentum. This is problematic because rotationally supported disks are known to exist around evolved protostars. Finally, Gillis et al. (1974) or Mouschovias and Spitzer (1976) took a different pathway to proving the existence of magnetic fields by searching for a consistent theory of star formation including magnetic fields as an essential ingredient...

Magnetized virial theorem The virial theorem is based upon the fundamental principle of dynamics and can thus be easily extended including magnetic forces. The problem at hand is to study the equilibrium of a uniform sphere permeated by a uniform magnetic field. We consider the more general framework of a fluid particle, using the Navier-Stokes equation to describe a magnetized fluid (a valid framework for the formation of stars using molecular clouds)

$$\rho\frac{\mathrm{d}\mathbf{u}}{\mathrm{d}t} = -\boldsymbol{\nabla}P + \mathbf{F}_{\rm gravitationnal} + \mathbf{F}_{\rm magnetic} + F_{\rm others}. \tag{1.43}$$

As in the hydrodynamical case, we begin by multiplying equation (1.43) by $\cdot\mathbf{r}$. We then integrate over the whole volume V ($M_{\rm total} = \int_V \rho\,\mathrm{d}V$) to derive a global criterion:

$$\int_V \rho\mathbf{r}\cdot\frac{\mathrm{d}\mathbf{u}}{\mathrm{d}t}\,\mathrm{d}V = \frac{1}{2}\frac{\mathrm{d}^2 I}{\mathrm{d}t^2} - 2\mathcal{T} \tag{1.44}$$

[3]Cosmic rays are very high-energy particles that were created in astrophysical objects that we can receive and detect on earth, using for example the sea as a detector.

with $I = \int_V r^2 \rho \, \mathrm{d}V$ the inertia momentum and $\mathcal{T} = \int_V \frac{\rho u^2}{2} \, \mathrm{d}V$ the kinetic energy (same terms as in 1.2). The pressure term yields

$$\int_V \mathbf{r} \cdot \boldsymbol{\nabla} P \, \mathrm{d}V = \int_V \boldsymbol{\nabla} \cdot P\mathbf{r} \, \mathrm{d}V - \int_V P \boldsymbol{\nabla} \cdot \mathbf{r} \, \mathrm{d}V \tag{1.45}$$

$$= \int_\Sigma P\mathbf{r} \cdot \mathbf{dS} - 3 \int_V P \, \mathrm{d}V \tag{1.46}$$

$$= \int_\Sigma P\mathbf{r} \cdot \mathbf{dS} - 3(\gamma - 1)U \tag{1.47}$$

where we have assumed (locally) the ideal gas equation of state, $P = (\gamma - 1)e$. The total internal energy U is defined as $\int_V \epsilon \, \mathrm{d}V = U$. Σ, where Σ is the closed surface derived from the volume V. Equation (1.47) was obtained by integrating over the whole volume and γ must be volume averaged for the relation to hold.

The magnetic term gives (see § 2.2 for more details)

$$\int_V \mathbf{r} \cdot \mathbf{F}_{\text{magnetic}} = \int_V \frac{B^2}{2\mu_0} \, \mathrm{d}V + \int_\Sigma \left[(\mathbf{B} \cdot \mathbf{r}) \frac{\mathbf{B}}{\mu_0} - \frac{B^2}{2\mu_0} \mathbf{r} \right] \cdot \mathbf{dS}. \tag{1.48}$$

The quantity $\mathcal{M} = \int_V \frac{B^2}{2\mu_0} \, \mathrm{d}V$ is the total magnetic energy. Finally, the gravitational term can be treated in the same as previously described in equation (1.40) with difference that the sums now become volume integrals, yielding

$$\int_V \mathbf{r} \cdot \mathbf{F}_{\text{gravitationnal}} \, \mathrm{d}V = -\frac{G}{2} \int_V \int_{V'} \rho(\mathbf{r}) \rho(\mathbf{r}') \frac{\mathrm{d}V \, \mathrm{d}V'}{|\mathbf{r} - \mathbf{r}'|} \tag{1.49}$$

$$= \Omega. \tag{1.50}$$

If no other forces are present, the general expression of the virial theorem (for an ideal gas) is:

$$2\mathcal{T} + 3(\gamma - 1)U + \Omega + \mathcal{M} = \frac{1}{2} \ddot{I} - \int_\Sigma \mathbf{dS} \cdot \left[(\mathbf{B} \cdot \mathbf{r}) \frac{\mathbf{B}}{\mu_0} - (P + \frac{B^2}{2\mu_0}) \mathbf{r} \right] \tag{1.51}$$

We can now examine this complete expression which describes the energetics of a magnetized object. In a simplified case of a spherical magnetic cloud, with no rotation, turbulence, external pressure nor external magnetic field, the virial equilibrium theorem reads

$$3(\gamma - 1)U + \mathcal{M} + \Omega = 0. \tag{1.52}$$

In the framework of ideal MHD, the freezing of field lines into the matter leads to an increase of the magnetic field as of the rotation: $B_0 R_0^2 = B(t) R(t)^2$. If B remains uniform as the collapse progresses, the total magnetic energy increases as $\mathcal{M} = \frac{4\pi}{3} R(t)^3 \frac{B^2}{2\mu_0} \propto \frac{1}{R(t)}$, a growth rate identical to that of the negative gravitational energy. The conclusion is that the magnetic field acts against gravity in a way that is independent of the density. This implies that a cloud with an initial mass large enough for gravity to overcome magnetic pressure will start to collapse, a contraction that magnetic fields alone won't be able to stop. The minimum mass is therefore given for $U = 0$ since any thermal energy (or rotation or turbulence) will only add to the support against gravitational collapse. We get

$$M_{\text{minimum}} = \frac{B^3}{(6\mu_0 G)^{\frac{3}{2}}} \left(\frac{5^3}{\frac{4\pi}{3}} \right)^{\frac{1}{2}} \frac{1}{\rho^2}. \tag{1.53}$$

For typical values of $B \simeq 10^{-6}$ gauss for $\rho = 1.66 \times 10^{-23}$ g.cm^{-3} (see estimates from Mestel and Spitzer (1956)) we obtain $M_{\text{minimum}} \simeq 5 \times 10^2 \, M_\odot$. In other words, in the flux freezing approximation,

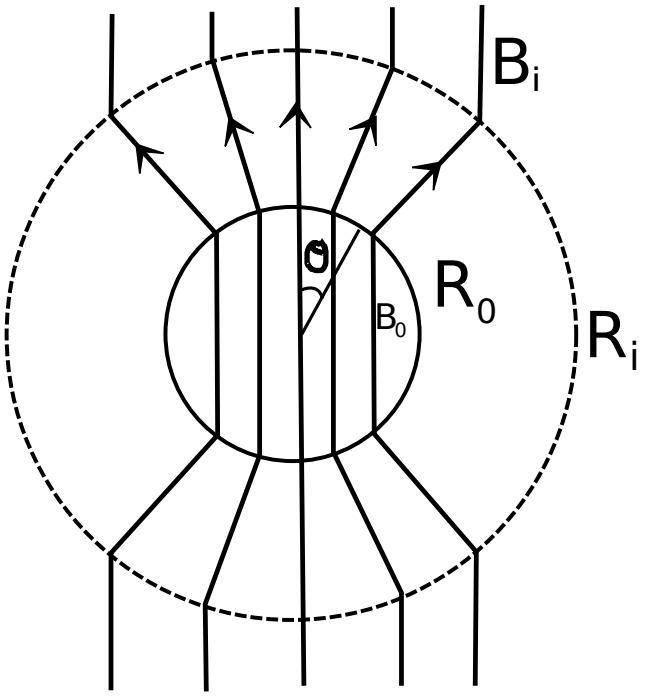

Figure 1.2: Simplified setup studied in Gillis et al. (1974).

the smallest fragment a cloud could break into has the mass of several hundred suns, which is a lot. This explains the preliminary conclusion that magnetic fields prevent star formation, or at least the idea of stars forming from dense cores of about the same mass as the final star.

One may raise the issue of a cylinder permeated by field lines along its height: it would allow for contraction along the field lines without any hindrance from the build-up of magnetic pressure. Nevertheless, this is unlikely to occur. The height of a cylinder of matter needed to allow contraction to a radius R along the field lines is several hundred times this final size R. In other words the matter would more likely fragment in smaller pieces instead of collapsing as a whole along the field lines, forming a central oblate object. The length of such a cylinder would be orders of magnitude larger than the Jeans length, which can still be used as an indicator for cloud fragmentation as long as the collapse occurs along the field lines.

As a conclusion, a moderate large-scale magnetic field seems to prevent star formation in the ideal MHD framework . The idea that the magnetic fields must then be decoupled from the neutral matter naturally arose. Over the few last pages, we have shown that the angular momentum and magnetic pileup in the proto-star are both major issues, since they can prevent the formation of star-like objects.

Torsional Alfvén waves So far, we have shown that magnetic fields tend to be a hindrance to star formation. Nonetheless, the magnetic fields analysis yielded the first clue for solving the angular momentum problem. This is by removing, or more accurately moving somewhere else the angular momentum of a collapsing cloud. As pointed out by Mestel and Spitzer (1956) on their conclusion, angular momentum can be transported through Alfvén waves and then allow the star not to be teared apart by incredible rotational velocity. This idea was followed up by von Hoerner et al. (1959) and detailed calculations in a simple case study were made by Gillis et al. (1974). It is the latter that we will summarize in the next paragraph, to try and understand how magnetic fields can enable angular momentum transport.

The setup is an initial spherical cloud of radius R_i permeated by a uniform magnetic field $\mathbf{B_i}$ ($\mathbf{B_i} = B_i \cos(\theta)\mathbf{e_r} - B_i \sin(\theta)\mathbf{e}_\theta$ in spherical coordinates). The cloud is supposed to collapse to another spherical cloud of uniform density and radius R_0 with a uniform magnetic field $\mathbf{B_0} = \frac{1}{\eta^2}\mathbf{B_i}$ (with $\eta = \frac{R_0}{R_i}$ measuring the contraction of the cloud). In the region between R_0 and R_i they assume a very simple radial field of varying intensity depending on the angle θ as $\mathbf{B}(R_0 < r < R_i) = \frac{B_0 R_0^2}{r^2}\cos(\theta)\mathbf{e_r}$. A graphical representation of the setup is represented Fig 1.2. They argue that even though the setup is idealized (uniform density, spherical clouds, simple structure of the magnetic field) it is likely to underestimate the magnetic braking. As only a raw understanding of how magnetic fields can't transport angular momentum is required for the purpose of this section, the full details will not be made explicit here. One of the key aspects of their work is however worth understanding, as it deals with finding a method to study the collapse using time-dependent boundaries.

- First, suppose that the centrifugal forces are small (no centrifugal balance). The cloud therefore collapses approximately at a rate given by the magnetically-diluted gravitational forces (see the previous paragraph). The ratio η should then be independent of the magnetic braking (in that case η is given by a free-fall time). Finally, one should ask whether or not the braking is able to keep the centrifugal forces low enough throughout the collapse.

- Then, suppose that the cloud is initially in centrifugal balance. η is directly dependent on the angular momentum removal which enables the cloud to contract. The question is: do gravitational forces ever overtake centrifugal forces and allow the cloud to gravitationally collapse.

These questions might seem unimportant, but in order to study analytically a time-dependent problem they need to be answered. This can be done following a *suppose...* then *verify...* reasoning.

Suppose that the cloud is kept in centrifugal balance (until contraction to a radius R_0). Then at a radius $R_0 = \eta R_i$, the angular velocity is

$$\Omega_0^2 = \frac{\Omega_i^2}{\eta^3} = \frac{GM}{R_0^3} \tag{1.54}$$

and the loss of angular momentum is

$$\frac{2}{5}M\Omega_i R_i^2 - \frac{2}{5}M\Omega_0 R_0^2 = \frac{2}{5}M\Omega_i R_i^2(1 - \sqrt{\eta}). \tag{1.55}$$

Verify that the magnetic braking time is longer than the time for the cloud to collapse under magnetically-diluted self-gravitation with no centrifugal forces. Otherwise, the cloud could not be at centrifugal balance at that time because a substantial removal of angular momentum will have occurred in the meantime.

They summarize this method as following: *we replace the real problem with the time-dependent boundary R_0 by a pseudo-problem with a fixed boundary, but with the understanding that the solution is valid only for a limited period, after which a new, smaller value of η is appropriate.*

Using a purely rotatory velocity field $\mathbf{v} = \Omega r \sin(\theta)\mathbf{e}_\phi$ for $R_0 < r < R_i$, we get for the induction equation ($\frac{\partial \mathbf{B}}{\partial t} = \boldsymbol{\nabla} \times (\mathbf{v} \times \mathbf{B})$ in the ideal case) and the torque equation ($\frac{\mathrm{d}\mathbf{L_0}}{\mathrm{d}t} = \sum_f \sigma_\mathbf{f}$ with $\mathbf{L_0}$ the angular momentum and $\sigma_\mathbf{f}$ the torque of the force f, here the Lorentz force $(\boldsymbol{\nabla} \times \mathbf{B}) \times \mathbf{B}$):

$$\frac{\partial B_\phi}{\partial t} = B_r r \sin(\theta)\frac{\partial \Omega}{\partial r} \tag{1.56}$$

$$\rho_i r^2 \sin^2(\theta)\frac{\partial \Omega}{\partial t} = \frac{B_r}{4\pi}\sin(\theta)\frac{\partial r B_\phi}{\partial r} \tag{1.57}$$

Combining them yields:

$$\frac{\partial^2\Omega}{\partial t^2} = (B_i R_i^2)^2 \frac{\cos^2(\theta)}{4\pi\rho_i r^4} \frac{\partial^2\Omega}{\partial r^2} \tag{1.58}$$

$$= v_A^2 \frac{\partial^2\Omega}{\partial r^2} \tag{1.59}$$

which is a wave equation with a local Alfvén speed $v_A(r) = \frac{V_i R_i^2 \cos(\theta)}{r^2}$, where $V_i = \frac{B_i}{\sqrt{4\pi\rho_i}}$. For $r > R_i$, the same equations lead to the usual wave equation with the Alfén speed V_i:

$$\frac{\partial^2\Omega}{\partial t^2} = V_i^2 \frac{\partial^2\Omega}{\partial z^2} \tag{1.60}$$

From these equations, we understand that angular momentum is transported by the magnetic field, along the field lines. The complete solution (mostly consisting of solving the time dependent angular momentum loss for a given contraction factor η) for these equations is fully detailed in Gillis et al. (1974) and they find that both assumptions can be correct. Indeed, for any contraction factor η, they can find a value of an initial magnetic field $\mathbf{B_i}$ less than the critical value for which collapse occurs given by the virial theorem ($B_{\rm virial}$), which enables the cloud to remain in a state of centrifugal balance while collapsing. They also find that they can always find $B_i < B_{\rm virial}$ for which the braking is efficient enough to keep the rotation below centrifugal balance (even though they note that they can never reach co-rotation with the outside parent cloud). This was unsatisfactory as they couldn't conclude but only assess that their setup was too simplified. Subsequent refined work of the same problem by the same authors (see Gillis et al. (1979); Mestel and Paris (1979)) and others, focusing in particular on the time-scales and the influence of the angle between the magnetic field and the axis of rotation (see Mouschovias (1978, 1979); Mouschovias and Paleologou (1978, 1979, 1980a,b)) tend to show that collapsing clouds would actually tend to co-rotate with their parent cloud.

1.1.3 Dissipating the flux

The very first reference to a possible drift between charged particles and the neutral background (mostly molecular hydrogen H_2) in the case of star formation is due to Mestel and Spitzer (1956). They wrote the basic equations (see also § 1.3 for another formulation of the equations) and tried to calculate some orders of magnitude, yet because of a lack of data (either the magnitude of the field or the rough ionisation fraction) they remained inconclusive regarding the possibility and consequences of such a drift. Years later Shu et al. (1987) reformulated the problem and named it ambipolar diffusion. In media such as molecular clouds, where the ionization fraction is low, the neutral matter interacts with the magnetic field only via collisions with charged particles. This is ambipolar diffusion: magnetic forces acting on neutral particles through collisions with scarce charged particles. The result is an effective drift of the fluid of neutrals through the magnetic field lines (see appendix 1.B for some details on the term *diffusion*). This formulation allows the use of only one fluid (the neutrals) because of the very low ionization fraction. Other approaches (for example the *three-fluid* approach, by Pinto and Galli (2008, 2009)) also exist for other astrophysical objects with different properties. A common approximation for the ionization fraction is (from Elmegreen (1979)):

$$\rho_i = C\sqrt{\rho_n} \tag{1.61}$$

where $C \simeq 3.0 \times 10^{-16}$ cm$^{\frac{3}{2}}$.g$^{\frac{1}{2}}$, which gives an ionization fraction of 10^{-7} at hydrogen densities of 10^4 cm^{-3}. More detailed studies using simplified chemical networks were carried out (e.g. Umebayashi and Nakano (1990) amongst others) and more or less confirmed the qualitative trend of equation (1.61).

This *one fluid approximation* lead to the following induction equation (again, see § 1.3.2 for details of the steps of the calculations[4]):

$$\frac{\partial \mathbf{B}}{\partial t} + \boldsymbol{\nabla} \times (\mathbf{B} \times \mathbf{v_n}) = \boldsymbol{\nabla} \times \Big\{ \frac{\mathbf{B}}{\gamma_{\rm AD} \rho_i \rho} \times \big[\mathbf{B} \times (\boldsymbol{\nabla} \times \mathbf{B}) \big] \Big\} \tag{1.62}$$

where $\gamma_{\rm AD}$ accounts for the drag between ions and neutral due to momentum exchange. A classical value is $\gamma_{\rm AD} \simeq 3.5 \times 10^{13}$ cm^3.g^{-1}.s^{-1} provided the Langevin approximation holds, meaning that the relative velocities are not too different, $\lesssim 10$ km.s^{-1}. Several approximations (some not easily justified[5] allows to write equation (1.62) as a diffusion equation with a diffusion coefficient $D_{\rm AD}$ equal to

$$D_{\rm AD} = \frac{B^2}{\gamma_{\rm AD} \rho_i \rho} \tag{1.63}$$

$$= v_A^2 t_{\rm ni} \tag{1.64}$$

where $v_A = \big(\frac{B^2}{\rho}\big)^{\frac{1}{2}}$ is the Alfvén speed using the neutral density, and $t_{\rm ni} = \frac{1}{\gamma_{\rm AD} \rho_i}$ is the mean collision time between a neutral particle with an ion. We have then

$$\frac{\partial \mathbf{B}}{\partial t} + \boldsymbol{\nabla} \times (\mathbf{B} \times \mathbf{v_n}) = D_{\rm AD} \Delta \mathbf{B}. \tag{1.65}$$

Writing $\tau_{\rm AD} \simeq \frac{L^2_{\rm cloud}}{D_{\rm AD}}$ for the ambipolar diffusion timescale and $\tau_{\rm dyn} \simeq \frac{L}{v_A}$ for the dynamical timescale (time for an Alfvén wave to cross a cloud of characteristic length L), we get for the ratio:

$$\frac{\tau_{\rm AD}}{\tau_{\rm dyn}} \simeq \frac{\gamma_{\rm AD} C}{\sqrt{G}} \tag{1.66}$$

using the fact that for a magnetically critical cloud the Alfén speed matches naturally the speed required by the virial equilibrium ($v_A^2 = \frac{B^2}{\rho} \simeq v^2_{\rm virial} = \frac{G M_{\rm cloud}}{L}$) and that $M_{\rm cloud} \propto L^3 \rho$.

Two points are worth highlighting:

- First, the ratio does not depend on the cloud's mass, size or density. This means that for a given cloud and magnetic field geometry, the ratio of the ambipolar to the dynamical timescale remains constant.

- Second, Lizano and Shu (1987) calculated the numerical value of this ratio for a slab geometry and found $\frac{\tau_{\rm AD}}{\tau_{\rm dyn}} \simeq 8$. As they concluded, ambipolar diffusion can thus be expected to be a slow process compared to the dynamical timescale (provided the ionization fraction does not skyrocket).

The intensity of the magnetic field is as important as its geometry. For a given geometry, it is possible to derive analytically useful quantities which give an estimate of the field's impact on the collapse.

[4] We basically wrote down the induction equation for the ions and replaced the ions speed $\mathbf{v_i}$ with the neutrals speed using $\mathbf{v_i} - \mathbf{v_n} = \frac{1}{\gamma_{\rm AD} \rho_i \rho_n} (\boldsymbol{\nabla} \times \mathbf{B}) \times \mathbf{B}$

[5] see Appendix 1.B for a discussion of this issue or § 4.4 for an example of the difference it can make on a precise case-study of the ABC dynamo

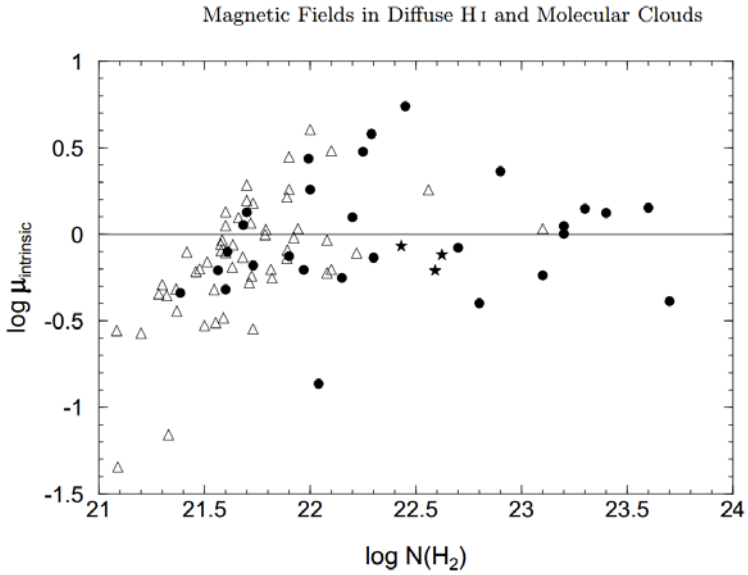

Figure 1.3: Taken from Heiles and Crutcher (2005). $\mu_{intrinsic}$ are the observed mass to magnetic flux rations with projection bias taken into account, in units of the critical value. $\mu_{intrinsic} > 1$ is supercritical, while $\mu_{intrinsic} < 1$ is subcritical. Various points type account for various ways to measure the magnetic field magnitude.

The mass-to-flux ratio In the ideal framework of magnetohydrodynamics, the matter is frozen in magnetic flux tubes; there is a perfect coupling between matter and magnetic fields and matter can only move along the field lines. Mouschovias and Spitzer (1976) demonstrated that the quantity controlling the collapse (or the stability against collapse) for a spherical cloud of homogeneous density permeated by a homogeneous magnetic field is the ratio of the mass of the cloud (M) to the magnetic flux permeating this cloud (ϕ_B). They derived the critical value in the above-mentioned case $(\frac{M}{\phi_B})_{\text{critical}} = \frac{0.53}{3\pi}\sqrt{(\frac{5}{G})}$, and called the measure of the stability $\mu = \frac{\frac{M}{\phi_B}}{(\frac{M}{\phi_B})_{\text{critical}}}$. Clouds with $\mu > 1$ will collapse; they are called super-critical. On the other hand, clouds with $\mu < 1$ are called sub-critical; they do not collapse, the magnetic support ensures their stability. In the context of molecular clouds, observations tend to show (for example see Crutcher et al. (1999) and Fig.1.3) that the clouds are usually slightly super-critical. This supports the idea of strong initial magnetic fields being dissipated slowly by turbulence and/or ambipolar diffusion until reaching the super-critical state, then allowing collapse to proceed. Some differences in the mass-to-flux ratio between the molecular cloud, the envelope and the dense part of the core can emerge, both when ambipolar diffusion or turbulent density enhancement are operating. Due to the observational issues in measuring magnetic field orientation and strength, it is currently not possible to determine which is the dominant mechanism. The most advanced work on the subject has be done by Crutcher et al. (2009) who could still not differentiate between the two scenarios.

A more detailed discussion on the mass-to-flux ratio for different initial configuration (inhomogeneous field and density profile) can be found section 4.1.2.

Turbulence Turbulence was, is and will ever be a tricky business. Analytical understanding of turbulence is by nature limited to statistics, because of its intrinsic chaotic behavior. Famous work on turbulence was carried out by Kolmogorov (1941) who determined some of its statistical properties. Many studies extended the theory to compressible or magnetized turbulence. Its influence was

foreseen to be of major importance to the process of star formation (e.g. von Hoerner (1951) or the recent studies by Joos et al. (2013); Lazarian (2013); Seifried et al. (2013)) and its tracers are observed everywhere (see for example the analysis of two molecular clouds by Hily-Blant et al. (2008)). In the context of core collapse, turbulence can be considered as an initial input, a perturbation of the smooth initial conditions. Its main role lies in its dissipative properties and the ways in which it enhances or interferes with other dissipative processes such as ambipolar diffusion.

It is neither the aim of this paragraph nor of the thesis to develop the latest breakthrough in theoretical turbulence. We will simply present some turbulent simulations and the consequences on star formations processes.

1.1.4 Conclusions

The objective of this first section was to give the reader the necessary tools to understand star formation in the context of angular momentum transport and magnetohydrodynamics. The major theoretical milestones were reported, from the very early years to modern day problems. Of course, there are many developments that were not mentioned here, such as radiative transfer, detailed chemistry or the study of the initial mass function. These very refined physics are a necessary part of star formation but are beyond the scope of this introduction. The obvious counterpart to theory is the information supplied by observational studies. These will be discussed in the next section, with an emphasis on dense cores.

1.2 Experiments

Experiments in astrophysics are rare and difficult to carry out. Some dense, cold plasmas can under particular conditions be studied in laboratories. High energy physics (LASERS, electromagnetic confinements, particle physics) are more easily studied on earth's surface. But astrophysics are usually synonymous of cataclysmic events, with timescales of the order of a planet's lifetime or more, length-scales larger than the size of the earth's orbit around the sun. Thus inevitably making laboratory experiments difficult to perform.

One way to experiment in astrophysics is simply to look up. Stars have been forming and dying for billions of years. Instead of waiting for a single star to form in a particular molecular cloud, the universe is large enough to provide many snapshots in many different molecular clouds. The full picture is harder to grasp, because every snapshot comes with a slightly or sometimes completely different story. Nevertheless, experiments exist, and it's a matter of how well we can see inside structures to extract the relevant information to broaden our understanding of star formation.

Second, the vast development of computational power and efficient algorithms has enabled the solving of virtually any kind of equation, spawning an new field of physics. This field is by far not limited to astrophysics, but enables the testing of theories in a slightly different manner than observers. One can turn in or out some of the physics, study precise phenomena or imagine a relevant filter to produce synthesic observations for direct comparison with real ones.

Both these points of view share some common features, and we will present them in parallel in this section. Of course, they differ in many ways and have different goals, but they both rely on interpreting more or less complete data. Moreover, both approaches require constant interaction with the theories: deriving new ones as well as refuting others to improve our understanding of the universe.

1.2.1 The basics

Dark clouds had been known for many years but the lack of quantitative observations was a hindrance to the development of the theory (see Myers et al. (1983) for the first reference, and the many

following papers for details). The research and development of new instruments in the early 21st century allowed for a better characterization of these structures and the upcoming of refinements to the theory (see Andre et al. (2000)).

1.2.1.1 Larson cores

The already well developed theory of the formation of stars (as presented § 1.1) remained untested until the first numerical simulations of Larson (1969), in the late 60s. Although he used simple initial conditions and idealized hypothesis, he successfully drew the first coherent picture of the star formation process. His simulations started from a slightly unstable isothermal, uniform sphere of molecular hydrogen initially at rest. The picture is as follows:

- First, there is an isothermal ($T = 10$K) phase of free-fall, during which the density profile closely approaches the theoretical profile $\rho(r) \propto r^{-2}$. It should be noted that the same conclusion, namely that a cloud collapse leading to star formation can be well approximated by a similarity solution, was found independently the same year by Penston (1969).

- Then, when the central object becomes dense enough ($\rho \simeq 10^{-13}$ g.cm^{-3}) to be optically thick, the temperature rises because the heat generated by the collapse is trapped inside. The compression becomes adiabatic and a core in almost hydrostatic equilibrium forms. This core, called the first Larson core, continues to accrete and grows in mass while its size remains approximately constant.

- Accretion goes on and the temperature rises along with the increase of density, reaching about 2000K. This is still orders of magnitude below the temperature at which nuclear reactions begin. However at this temperature the dihydrogen molecules undergo dissociation, a highly endothermic chemical reaction. Consequently, the energy sink[6] created allows for contraction to restart. Another way to picture this phenomena is that the polytropic index changes from a value $\gamma \simeq \frac{7}{5}$ or $\frac{5}{3} \gtrsim \frac{4}{3}$ to a value $\gamma \simeq 1.1 < \frac{4}{3}$. As highlighted in the previous section, this value of $\frac{4}{3}$ describes a critical state that separates stable from unstable regions against collapse.

- Finally when all molecular hydrogen has been dissociated, the energy gap is filled and heat is once again trapped in the central part of the collapsing cloud. Thus, another quasi-equilibrium hydrostatic core forms: the second Larson core.

After this already tremendous amount of work, he tried to follow the evolution of the newborn star along the Hertzsprung-Russell (HR) diagram and studied the main accretion phase. His pioneering work included also some variations of the initial hypothesis and conditions, to tackle the robustness of the results. Apart from small differences, the resulting star was in all cases similar to a *conventional Hayashi pre-main sequence model*[7].

Since this work, the main picture, from a theoretical point of view, remained basically unchanged. Another groundbreaking numerical and analytical work was presented by Shu (1977). The study begins with the analytically derived singular isothermal sphere (see chapter 1.1) to obtain a different dynamical conclusion: in this case the collapse happens *inside-out*. It starts from the central part, for example the newly formed star, and proceeds outwards as gas falls into the central object. This led to numerous arguments about which model and the initial conditions were the most realistic. It was later revealed that the picture described by Larson (1969) matches more precisely observations and infalling motions than the Shu (1977) model. What we can retain from it is that it is the only analytical (semi-analytical) model for star formation, and that it still allows for more refinements to probe for specific aspects of the problem.

[6] The energy necessary to dissociate dihydrogen molecules.

[7] The Hayashi track is a common behavior on the HR diagram followed by low mass stars.

However, these models (and others, as derived by Hunter (1977) later) share some common important features. For example, only a small fraction of the initial dense core ends up forming a star. Most of the material remains in the infalling envelope, and can then be accreted or used to form another star (leading to a possible pathway to forming binary stars) or massive disks (which have not yet been observed with significant statistics in early stages of star formation).

1.2.1.2 Observing cores

We have now reached a time when dense cores have been observed for the first time ! Thanks to new telescopes, such as the Institut de Radio Astronomie Millimétrique (IRAM) telescope or the James Clerk Maxwell Telescope (JCMT), young stellar objects inside dark clouds can be studied. In this section we will summarize the picture painted by this novel observational point of view.

Observations usually come with entangled and noisy data. Complex statistics and data reduction are necessary to extract as much as possible from the raw data, but it is beyond the scope of this thesis to describe this process thoroughly. We only wish to point out breakthroughs and some of the issues in observing dense cores. The reader is referred to the references given therein for any further details.

SED Standing for spectral energy distribution, SEDs are one of the most useful tools to probe star forming regions. Fitting a black-body model to the far-infrared region of the SED can provide insights into the structures of the cores. Under the assumption that dust grains are the main emitting particles in this frequency range, the infrared emission is primarily of thermal nature, and the SED will look very similar to a black-body spectrum. It can yield information on the dust and gas temperature (if coupling is strong), and provide approximate values for the dust and gas mass. Moreover, abnormalities in the SEDs are the subsequent proof of the existence of a radiating central body or of serious anisotropies both in density and chemical composition (for example, the presence of a thin hot disk or outflow cavities will have consequences on the shape of the SED).

This fact, along with the observed SED for various dark clouds, led to the development of the evolutionary history and classification of young stellar objects by André (2002), which had eversince been widely used to refer to a particular step in the formation of stars. This classification can be seen Fig. 1.4. Note that this thesis will be focused on the fragment to late class 0 stages.

In the early phases, the SED looks exactly like a cold black-body emission at a given temperature (rising from the dense core where $T \gtrsim 10$K). Even if the central part of the core is denser and hotter, the surrounding cold material shades it and only the outer layers take part in the emission. As collapse proceeds, this remains true until the formation of the two Larson cores, with a slight increase in bolometric temperature ($\lesssim 70$K). The transition between late class 0 to early class I objects remains unclear from a theoretical point of view since the precise picture of disk formation is still a matter of debate. From an observational point of view, however, the difference is obvious: when the SED changes from a black-body to a black-body with additional emission in the infrared (accounting for the central object emission and the disk), class I is reached. Quantitatively, the most precise way to distinguish from class 0 to class I is arbitrary and consists of comparing the mass of the envelope (M_{envelope}) and of the central object ($M_{\odot}$). Class 0 have $M_{\text{envelope}} > M_{\odot}$ while class I have $M_{\text{envelope}} < M_{\odot}$. The later stages are mainly the consequences of the disk evolution, accretion onto the star and the formation of planets. The SED thus changes until it looks like a usual stellar black body, when the disk finally is gone.

Disks There is not much room for doubts as to the existence of massive Kelperian disks during the late stages presented above. Amazing pictures are available since the release of the Hubble space telescope, showing flat structures around young stars (see Watson et al. (2007a)) identified as disks.

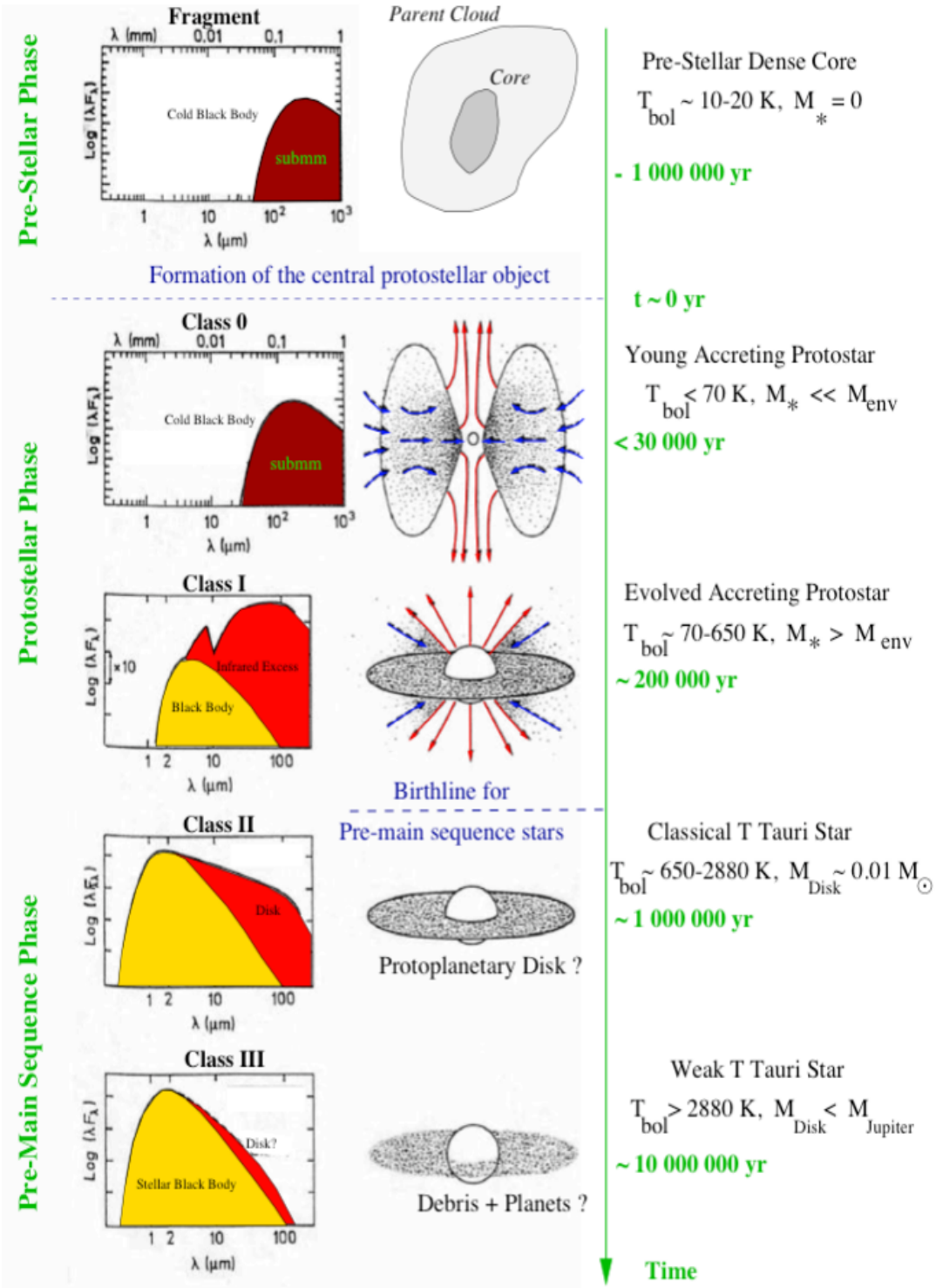

Figure 1.4: Taken from André (2002). A schematic view of the SED for some keystones of the evolution of a dense core to a proto-star.

Further study of these disks led to the conclusion that they are abundant around class II and III (a recent survey is described in Spezzi et al. (2013)) but there are very few solid proofs of their existence around younger objects, namely class 0 proto-stars. Numerical simulations have trouble forming these disks around young objectis (see amongst others Dapp and Basu (2010); Hennebelle and Ciardi (2009); Krumholz et al. (2013); Machida and Matsumoto (2011)) and observers struggle with inconclusive data (or more accurately: observers accumulate proofs of their non-existence, as can be seen in Maury et al. (2010); Watson et al. (2007b)). Hopefully, thanks to the Herschel program, details of the structures around class 0 objects should improve our knowledge of low-mass star formation.

Disks are a whole subject of study by themselves, as can be seen by the many unanswered issues they raise:

- Their formation: when ? what size ?
- Their composition: debris disks, gas disks, dust disks
- Their interactions with the star and the embedded magnetic structure: disk-winds, episodic accretion/ejection
- Their ability to explain either close (for disks around class 0ish proto-stars) or wide (for massive disks around evolved objects) binaries via fragmentation
- The many instabilities that can occur within their complex structure with major consequences on planet formation (magneto-rotational instability (see Balbus and Hawley (1991)), streaming instability or Kelvin-Helmoltz instability for which details can be found in a side-work, in appendix C)

Magnetic fields To address the issue of the role of magnetic fields, the importance of measurements and their reliability is of major interest. In numerical simulations, magnetic fields can be simulated in detail. On the other hand, when it comes to observations, it is very difficult to accurately map the direction and magnitude of the magnetic field. There are a few means to measure some components of the field separately, then statistics come into action and maps of the magnetic vector field can be created. A very complete review on these many techniques can be found in Heiles and Crutcher (2005), which we will very quickly summarize here.

- Oldest but still used, the starlight polarization by the dust. There is a degree of freedom of 90 degrees: the spinning dust grains can be aligned either perpendicular or parallel to the component of the field projected onto the plane of the sky $B_\perp$. The resulting starlight polarization is also in principle subject to this 90 degrees of uncertainty. The right answer (polarization parallel to the field) is found empirically by looking at the polarization in dense gas close to the galactic plane, where the field structure is known on the large scales. It gives a measure of the direction of the component projected onto the plane of the sky $B_\perp$. Some knowledge of the intensity of this component can be accessed, depending on the extinction: a farther star can yield more extinction, as the line of sight increases.
- Similar to the starlight polarization by the dust, the polarization by thermal grains can provide the same kind of information. Interestingly, it does not need closeby stars to illuminate the dust. Even very weak magnetic fields can align grains, rendering this technique as difficult as the previous one to accurately describe the magnitude of the field. It has been suggested by Chandrasekhar and Fermi (1953) that a detailed study of the small-scale polarization randomness could yield some more quantitative knowledge. Numerical experiments confirmed this insight on a statistical point of view (meaning that it can work or not depending on the particular cloud of interest).

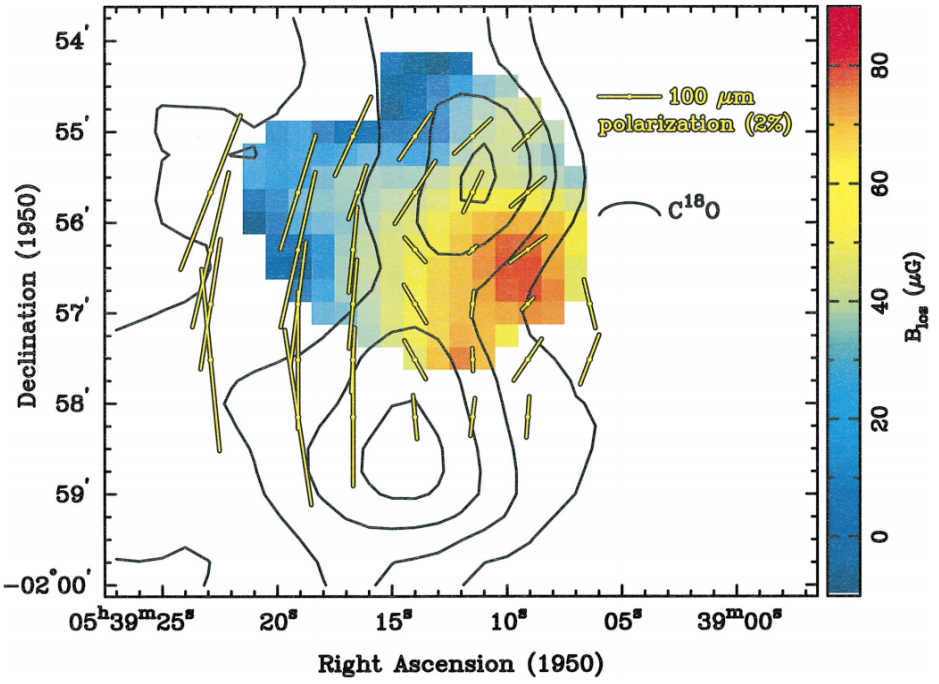

Figure 1.5: Taken from Crutcher et al. (1999). The black contours represent iso-density traced by $C^{18}O$ emission. The intensity of the line of sight component is coded in the colormap. The projected $B_\perp$ is represented by the segments.

- Zeeman splitting is the last of the three main techniques to measure magnetic fields. Depending on the molecule, Zeeman splitting can be measured accurately to give a value for $B_\parallel$.

With this array of solutions and through a great many statistics, observers can produce accurate maps of the direction and intensity of the magnetic field. Ultimately, maps look like the one in Fig. 1.5.

Coherence and turbulence The last point I want to mention concerns turbulence in dense cores and the related phenomena named coherence. Measurements of some particular line width[8] versus the radius of the dense core (or structure) of interest has been known since Larson's work (see Larson's laws: Larson (1981)). A broaden line width compared to the thermal line width is observational evidence for supra-thermal random motions. First pointed out by Goodman et al. (1998) and refined recently by Pineda et al. (2010), a transition from the turbulent signature at larger scales to coherence at the core's scale occurs when looking at the line width-size relation inside dense cores. The radius at which the transition occurs is found observationally to be $R_{\text{coherence}} \sim 0.1$ pc. The line width remains significantly larger than if fully thermal but the motion inside the cores decreases to subsonic velocities (while supersonic in the molecular cloud). Another interesting observation is that the line width-size relation remains constant at smaller radii, justifying the chosen name of *coherent* cores. The reason for this transition can be multiple, since many physics involved can explain (to order of magnitude) the transition radius from scalable turbulence to coherence. Details on this particular subject can be found in the above-mentioned papers. This work is still in early progress, but it should be kept closely in mind while setting up initial conditions for turbulent core collapse

[8] OH and $C^{18}O$ emission for example, in Goodman et al. (1998).

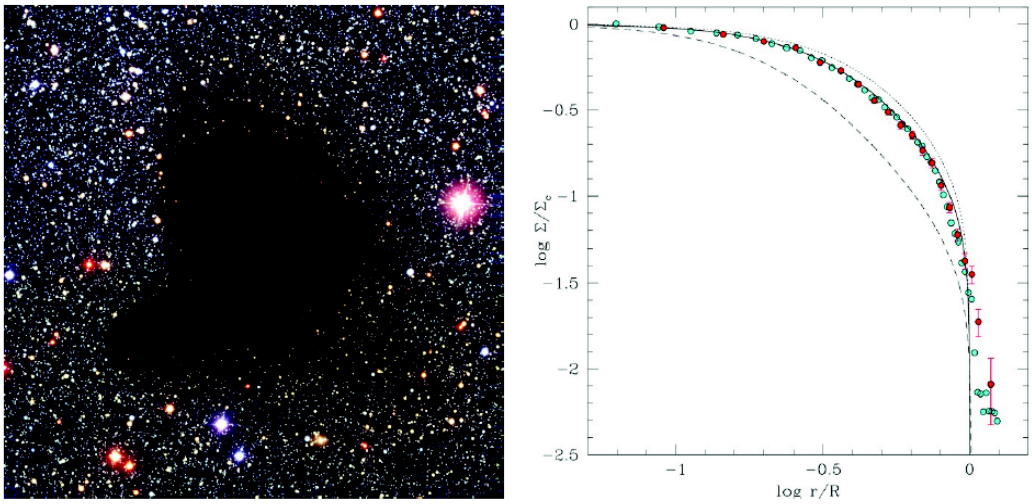

Figure 1.6: Taken from Burkert and Alves (2009). *Left*: Barnard 68 dense core. *Right*: Surface density profile from simulations (blue dots), observations (red dots) from Burkert and Alves (2009) and various analytical Bonnor-Ebert models (with a maximum radius $x_{\max} = 6, 7, 10$).

simulations. It might also be a possible field of investigation in large-scale turbulent simulations, since numerical simulations offer the satisfying possibility to get rid of projection effects.

1.2.2 From clouds to cores

The formation of the dense cores themselves remains an unknown mechanism. Many physical mechanisms might play a role, and whether one is dominant over the others may even depend on the parent molecular cloud. The classical ideas involve density enhancement through magnetosonic waves (coupling between the Lorentz force and thermal pressure, van Loo et al. (2008)), shocks due to colliding or supersonic (or super-Alfvènic) waves, or turbulence. Each of the mentioned mechanism raises new issues such as the way to drive turbulence at large scales, the scale of the dissipation or the properties of the resulting dense cores. Some observations tend to support the hypothesis of a local collapse along magnetic field lines initiated by any kind of density enhancement (turbulence, instability, shock, etc.), ending in a more gravitationally unstable core which thus continues to collapse. Note that observational evidence suggests that the Larson-Penston (LP) solution is very close to the reality, as can be seen Fig. 1.6. In this figure, one can see the theoretical model of a Bonnor-Ebert sphere with tuned conditions to fit the density profile of the dark cloud. The observational data are in very good agreement with a BE profile. Moreover, another key aspect of the LP solution is infall motions from all the cloud, which also tends to be supported by observational evidence (see Lee et al. (2004); Zhou et al. (1993)).

Some large scale simulations have been carried out, mostly to try to recover an initial mass fonction for both cores and stars (see mostly Bate and Bonnell (2005), with a smoothed particle hydrodynamics code and no magnetic field, or Krumholz et al. (2012) for a grid-based simulation taking into account magnetic fields). We also carried out a global simulation (200 $M_\odot$) with non-ideal MHD, radiative transfer and sink particles to follow the gas up to the first core (see § 4.3 for more details). The simulation takes, as expected, many hours to advance for each time-step and results are to be coming later.

Closely related to the title of this paragraph, the initial core function and the initial mass function

remain a huge challenge for the near future. Understanding the physical processes converting the core mass function to the star mass function is a major unsolved problem, with issues as diverse as the amount of binaries, the effect of turbulence, magnetic fields or radiative feedback. It is very peculiar a subject as it gathers the three branches of fundamental astrophysics: pen-and-paper theory (for example Kroupa et al. (2013) or Hennebelle and Chabrier (2011a,b) for a cosmology-inspired theory of turbulent star formation), observations (amongst many others, Holman et al. (2013); Schmalzl et al. (2010)) and numerical simulations (see for example Krumholz et al. (2012) or Bonnell et al. (2006)).

1.3 Non-ideal magnetohydrodynamics

In this more technical chapter, we present the ideal magnetohydrodynamics (hereafter, we will refer to magnetohydrodynamics as MHD) equations and the non-ideal refinements added in the one-fluid approximation. We wish this chapter to be more of a reminder of the various equations at stake than a detailed course, explaining the overabundance of equations compared to detailed explanations. In the following, equations are written in rational units : $\mathbf{B_{rat}} = \frac{B_{cgs}}{4\pi}$.

1.3.1 Fundamental equations of ideal MHD

First, we describe a fluid of charged particles all the same, moving at velocity $\mathbf{v}$ and with a density ρ. The equations describing the motion and evolution of a fluid particle are the following.

Mass conservation equation

$$\frac{\partial \rho}{\partial t} + \nabla \cdot (\rho \mathbf{v}) = 0 \tag{1.67}$$

Momentum equation

$$\rho \frac{D\mathbf{v}}{Dt} = -\nabla P + \mathbf{F}_L \tag{1.68}$$

where $\frac{D}{Dt} = \frac{\partial}{\partial t} + (\mathbf{v} \cdot \nabla)\mathbf{v}$ is the total (Lagrangian) derivative, and $\mathbf{F}_L = (\nabla \wedge \mathbf{B}) \wedge \mathbf{B}$ the Lorentz force.

Induction equation

$$\frac{\partial \mathbf{B}}{\partial t} = \nabla \wedge (\mathbf{v} \wedge \mathbf{B}) \tag{1.69}$$

Internal energy equation Writing e the internal specific energy and s the specific entropy we get:

$$\begin{aligned} \rho \frac{De}{Dt} =& \rho T \frac{Ds}{Dt} + P \frac{D \ln \rho}{Dt} = \rho T \frac{Ds}{Dt} + \frac{P}{\rho}\left(\frac{\partial \rho}{\partial t} + \nabla \cdot (\rho \mathbf{v})\right) - P \nabla \cdot \mathbf{v} \\ =& \rho T \frac{Ds}{Dt} - P \nabla \cdot \mathbf{v} \end{aligned} \tag{1.70}$$

The energy We are going to derive the energy of the system $E_{hydro} = \rho\epsilon + \rho v^2/2$ where ϵ is the internal specific energy. First: $(1.68) \cdot \mathbf{v}$ gives

$$\rho \frac{D\frac{\mathbf{v}^2}{2}}{Dt} = -\nabla \cdot (P\mathbf{v}) + P \nabla \cdot \mathbf{v} + \mathbf{F}_L \cdot \mathbf{v} \tag{1.71}$$

Then (1.68) + (1.70) yields:

$$\rho \frac{D}{Dt}\left(\frac{\mathbf{v}^2}{2}+e\right) = -\nabla\cdot(P\mathbf{v}) + \mathbf{F}_L\cdot\mathbf{v} + \rho T\frac{Ds}{Dt} \tag{1.72}$$

Interestingly[9], introducing the mass conservation equation in (1.72) and noticing that the electric field $\mathbf{E}$ verifies $\mathbf{E} = -\mathbf{v}\wedge\mathbf{B}$ brings:

$$\frac{\partial}{\partial t}\left(\rho(\frac{v^2}{2}+e)\right) + \nabla\cdot\left(\rho\mathbf{v}(\frac{v^2}{2}+e) + P\mathbf{v}\right) - \rho T\frac{Ds}{Dt} = \mathbf{v}\cdot[\mathbf{J}\wedge\mathbf{B}] = \mathbf{J}\cdot(\mathbf{B}\wedge\mathbf{v}) = \mathbf{J}\cdot\mathbf{E} \tag{1.73}$$

The next step is to derive $\mathbf{J}\cdot\mathbf{E}$:

$$\mathbf{J}\cdot\mathbf{E} = (\nabla\wedge\mathbf{E})\cdot\mathbf{B} - \nabla\cdot(\mathbf{E}\wedge\mathbf{B}) = -\frac{\partial B^2/2}{\partial t} - \nabla\cdot(\mathbf{E}\wedge\mathbf{B}) \tag{1.74}$$

Last, we have to develop:

$$\nabla\cdot(\mathbf{E}\wedge\mathbf{B}) = \nabla\cdot[(\mathbf{B}\cdot\mathbf{B})\mathbf{v} - (\mathbf{v}\cdot\mathbf{B})\mathbf{B}] \tag{1.75}$$

Finally, we can write the equation for the evolution of the energy (with $\frac{Ds}{Dt}=0$ because there is no entropy created in ideal MHD):

$$\frac{\partial E_{tot}}{\partial t} = -\nabla\cdot\Big[(E_{tot}+P_{tot})\mathbf{v} - (\mathbf{v}\cdot\mathbf{B})\mathbf{B}\Big] \tag{1.76}$$

with $E_{tot} = \rho\epsilon + \rho v^2/2 + B^2/2$ and $P_{tot} = P + B^2/2$.

1.3.2 Non ideal MHD

A simple way to approach non-ideal MHD is to imagine three moving fluids with neutral, positively and negatively charged particles colliding with each other. Every fluid is described by the previous set of equations, with an additional term accounting for collisions. Depending on the situation, one can neglect the inertia of the electrons, of the ions, the collisions between charged particles, between neutral and charged particles, etc. Ambipolar diffusion is the common name to describe a neutral fluid with some charged particles.

Note that the two-fluid approximation (see Toth (1994)), three-fluid approximation (see Pinto and Galli (2008, 2009); Pinto et al. (2008)) or the multi-fluid framework (for example in Falle (2003) or Kunz and Mouschovias (2009)) use the same equations. In these frameworks, one can neglect the collisions between specific particles (for example the charged grains collisions in Falle (2003)) again depending on the physical situation. The difference lies in the fact that the momentum equation for charged species are solved instead of inputing them in the neutral momentum equation. For example, in multi-fluid calculations there is one momentum equation per chemical species considered.

We present here the one-fluid approximation, in the context of low ionization fractions. The *non-ideal terms* kept in this setup are the collisions between neutral and charged particles. It enables the neutral field to respond to the magnetic forces, via collisions to charged particles (ions).

Ambipolar diffusion, the one-fluid approximation With ambipolar diffusion in a weakly ionized medium, the momentum equation has to be written for the neutrals, whose velocity is $\mathbf{u}_n$ (the contribution by the ions is neglected):

$$\rho \frac{D}{Dt}\left(\frac{\mathbf{u}_n^2}{2}+e\right) = -\nabla\cdot(P\mathbf{u}_n) + \mathbf{F}_L\cdot\mathbf{u}_n + \rho T\frac{Ds}{Dt} \tag{1.77}$$

[9]Let A be a scalar, then : $\rho\frac{DA}{Dt} = \rho\left[\frac{\partial A}{\partial t} + (\mathbf{v}\cdot\nabla)A\right] + A\left[\frac{\partial\rho}{\partial t} + \nabla\cdot(\rho\mathbf{v})\right] = \frac{\partial}{\partial t}(\rho A) + \nabla\cdot(\rho A\mathbf{v})$

With the description of the plasma by a single fluid as in Shu et al. (1987) (see also § 1.3.3 for more details), the velocity drift is related to the magnetic force:

$$\frac{1}{\gamma_{\rm AD}\rho_i\rho}\mathbf{F}_L = \mathbf{v}_i - \mathbf{v}_n \tag{1.78}$$

Replacing in the induction equation for the ions, it leads to:

$$\frac{\partial \mathbf{B}}{\partial t} = \nabla \wedge (\mathbf{u}_n \wedge \mathbf{B} + \mathbf{F}_L \wedge \mathbf{B}) \tag{1.79}$$

The first term will lead to the energy equation as in equation (1.76) with $\mathbf{u}_n$ instead of $\mathbf{v}$ for the velocity (focusing on the ions). The second term can be written as a divergence and an additional term:

$$\mathbf{J}\cdot\mathbf{E} = -\nabla\cdot(\mathbf{E}\wedge\mathbf{B}) - \frac{\partial \frac{\mathbf{B}^2}{2}}{\partial t} - \mathbf{B}\cdot(\nabla\wedge(\mathbf{F}_L\wedge\mathbf{B})) \tag{1.80}$$

with $\mathbf{B}\cdot(\nabla\wedge(\mathbf{F}_L\wedge\mathbf{B})) = \nabla\cdot[(\mathbf{F}_L\wedge\mathbf{B})\wedge\mathbf{B}] + (\mathbf{F}_L\wedge\mathbf{B})\cdot(\nabla\wedge\mathbf{B}) = \nabla\cdot[(\mathbf{F}_L\wedge\mathbf{B})\wedge\mathbf{B}] - \|\mathbf{J}\wedge\mathbf{B}\|^2$
Now, the equation with ambipolar diffusion reads:

$$\frac{\partial E_{tot}}{\partial t} = -\nabla\cdot\Big[(E_{tot}+P_{tot})\mathbf{u}_n - (\mathbf{u}_n\cdot\mathbf{B})\mathbf{B} - (\mathbf{F}_L\wedge\mathbf{B})\wedge\mathbf{B}\Big] - \|\mathbf{J}\wedge\mathbf{B}\|^2 + \rho T\frac{Ds}{Dt} \tag{1.81}$$

with $E_{tot} = \rho\epsilon + \rho v^2/2 + B^2/2$ and $P_{tot} = P + B^2/2$. There is still conservation of total energy ($\frac{\partial E_{tot}}{\partial t} + \nabla\cdot\mathbf{F}_{\rm energy} = 0$), and that leads to the two equations:

$$\frac{\partial E_{tot}}{\partial t} = -\nabla\cdot\Big[(E_{tot}+P_{tot})\mathbf{u}_n - (\mathbf{u}_n\cdot\mathbf{B})\mathbf{B} - (\mathbf{F}_L\wedge\mathbf{B})\wedge\mathbf{B}\Big] \tag{1.82}$$

$$\rho T\frac{Ds}{Dt} = \|\mathbf{J}\wedge\mathbf{B}\|^2 \tag{1.83}$$

where equation (1.83) means that the dissipation at the microscopic scale by the ambipolar diffusion leads to the creation of entropy.

1.3.3 Complete calculation for non ideal terms in the one-fluid approximation

In order to get a more general view of non-ideal terms in MHD, we describe here a calculation taking into account collisions between charged particles and or neutrals, neglecting only the inertia of ions and electrons.

The Lorentz force Because of the small fractional ionization in molecular clouds, quasi-equilibrium holds between the plasma-neutral friction force and the Lorentz force ($\omega << \gamma_{in}\rho_i$). Therefore we can drop the pressure and gravitational forces for ions (of atomic number Z) and electrons. The two equations which represent momentum balance are:

$$\begin{aligned} Zen_i(\mathbf{E}+\mathbf{v_i}\times\mathbf{B}) - \rho_i\sum_{j=e,n}\nu_{ij}(\mathbf{v_i}-\mathbf{v_j}) = 0 \\ -en_e(\mathbf{E}+\mathbf{v_e}\times\mathbf{B}) - \rho_e\sum_{j=i,n}\nu_{ej}(\mathbf{v_e}-\mathbf{v_j}) = 0 \end{aligned} \tag{1.84}$$

where $\rho_i\nu_{ij}(\mathbf{v_i}-\mathbf{v_j})$ is the force on ions (or electrons) due to collisions with the species j. The collisions rates read:

$$\nu_{\mathbf{kj}} = \rho_j\gamma_{kj} = \rho_j < \sigma v >_{kj} (m_j+m_k)^{-1} \tag{1.85}$$

where $< \sigma v >_{kj}$ is the average collisional rate between species k and j.. Adding the two equations (1.84) and with the current vector $\mathbf{J} = en_e(\mathbf{v_i} - \mathbf{v_e})$ we get:

$$\mathbf{J} \times \mathbf{B} + \gamma_{in}\rho_i\rho_n(\mathbf{v_n} - \mathbf{v_i}) + \rho_e\rho_n\frac{< \sigma v >_{en}}{m_e + m_n}(\mathbf{v_n} - \mathbf{v_e}) = 0 \tag{1.86}$$

We can neglect the last term in equation (1.86) because it is small compared to the others. Finally we get the expression for the Lorentz force:

$$\mathbf{J} \times \mathbf{B} = \gamma_{in}\rho_i\rho_n(\mathbf{v_i} - \mathbf{v_n}) \tag{1.87}$$

The induction equation Including the drift between ions and electrons and neutrals and electrons in the force balance equation for electrons, equation (1.84), we obtain:

$$\mathbf{E} + \Big[\mathbf{v} + (\mathbf{v_e} - \mathbf{v_i}) + (\mathbf{v_i} - \mathbf{v})\Big] \times \mathbf{B} + \frac{n_n m_e < \sigma_{en} v_e >}{e}\Big[(\mathbf{v_e} - \mathbf{v_i}) + (\mathbf{v_i} - \mathbf{v})\Big] = 0. \tag{1.88}$$

Providing the two drifts $(\mathbf{v_i} - \mathbf{v})$ and $(\mathbf{v_e} - \mathbf{v})$ are not too different (which does not mean that $\|\mathbf{v_i} - \mathbf{v_e}\| << 1$) we can drop the last term of equation (1.88): $\frac{n_n m_e <\sigma_{en} v_e>}{e}\Big[(\mathbf{v_i} - \mathbf{v})\Big]$. Finally, with $\gamma_{\rm AD} = \frac{<\sigma_{in} v_i>}{(m_i + m_n)}$ and $\sigma = \frac{n_e e^2}{n_n m_e <\sigma_{en} v_e>}$, and by computing the curl of equation (1.88) we have:

$$\partial_t \mathbf{B} = \nabla \times \Big[\mathbf{v_n} \times \mathbf{B} - \frac{\mathbf{J} \times \mathbf{B}}{en_e} + \frac{\big[(\nabla \times \mathbf{B}) \times \mathbf{B}\big] \times \mathbf{B}}{\gamma_{\rm AD}\rho\rho_i} - \frac{\mathbf{J}}{\sigma}\Big] \tag{1.89}$$

In (1.89) the second term on the right hand side represents the Hall effect, and the last stands for Ohmic resistivity. If we are only interested in ambipolar diffusion, we may drop them and write the corresponding induction equation:

$$\partial_t \mathbf{B} = \nabla \times \Big[\mathbf{v_n} \times \mathbf{B} + \frac{\big[(\nabla \times \mathbf{B}) \times \mathbf{B}\big] \times \mathbf{B}}{\gamma_{\rm AD}\rho\rho_i}\Big] = \nabla \times \Big[\mathbf{v_i} \times \mathbf{B}\Big] \tag{1.90}$$

These statements remain correct provided the ions-neutrals collision time remains larger than the inverse of the cyclotron frequency (which yield to the two equations (1.84)). Additionally, the drift between ions and neutrals and electrons and neutrals must not be too large in order to neglect the last term in equation (1.88)[10]. A more detailed study of the relative importance of these terms (but without taking into account the fact that there is a possibly large difference between ions-neutrals drift velocity and electrons-neutrals drift velocity) has been performed by Balbus and Terquem (2001).

$\|\mathbf{v_e} - \mathbf{v_n}\|$ ... We have to compare the two terms $\frac{<\sigma v>_{in}}{m_n + m_i}\rho_i\|\mathbf{v_i} - \mathbf{v_n}\|$ and $\frac{<\sigma v>_{en}}{m_n + m_e}\rho_e\|\mathbf{v_e} - \mathbf{v_n}\|$. Taking the most extreme case in Pinto et al. (2008) we have:

$$\begin{cases} \gamma_{in}^{min} \simeq & 10^{13} \quad (HCO^+/H_2) \\ \gamma_{en}^{max} \simeq & 10^{15} \quad (e/H_2) \end{cases} \tag{1.91}$$

with $\gamma_{ij} = \frac{<\sigma v>_{ij}}{m_i + m_j}$. Then, $\frac{\rho_i}{\rho_e} = \frac{m_i}{Zm_e} \gtrsim \frac{Zm_p \times 10}{Zm_e} \gtrsim 20000$. Finally there is about two orders of magnitude between the two terms.

[10] This is the case, at least while the Hall effect is negligible

Comparing with Pandey and Wardle (2008) Pandey and Wardle (2008) derived the exact same equations with the same approximations, but backwards. They began from the same equations but took into account the inertia of ions, without any assumptions on the timescale and equilibrium between the Lorentz force and the drag force, only neglecting the inertia of electrons. Then, they needed to neglect $\mathbf{v_d v_d}$ (this notation standing for a tensor product), $\mathbf{v_d} = \mathbf{v_i} - \mathbf{v_n}$, which finally led to a condition on the cyclotron frequency $\omega < \gamma_{in}\rho_i$. Additionally, when writing the momentum equations for ions and neutrals they drop the term in $\|\mathbf{v_e} - \mathbf{v_n}\|$, as in our study. The one equation more general is the following:

$$\frac{\partial \rho \mathbf{v}}{\partial t} + \nabla \cdot (\rho_i \mathbf{v_i} \mathbf{v_i} + \rho_n \mathbf{v_n} \mathbf{v_n}) = \frac{\partial \rho \mathbf{v}}{\partial t} + \nabla \cdot (\rho \mathbf{v}\mathbf{v} + \frac{\rho_i \rho_n}{\rho} \mathbf{v_d} \mathbf{v_d}) = \mathbf{J} \times \mathbf{B} \tag{1.92}$$

with $\rho = \rho_i + \rho_n + \rho_e \simeq \rho_i + \rho_n$ and $\mathbf{v} = \frac{\rho_n \mathbf{v_n} + \rho_i \mathbf{v_i}}{\rho}$. But it is not (to our current understanding) possible to use it in numerical simulations.

1.4 Contemporary issues in low-mass stars formation

The study of star formation involves many different physical processes, over a very wide range of scales. Much has been done since the pioneers and much remains to be understood. The observers ask for better and better telescopes, and turn to theorists to size their needs depending on what they want to observe. Theorists turn into numericists to stress out their ideas and ask observers to give them constraints to probe the parameter space more effectively. Everyone needs interaction from all the possible fields. This is the study of star formation today: an incredibly large play-field for every kind of physicist or chemist to try and find part of the answer. In this paragraph we detail the work that has been carried out in this thesis and the related issues that we tackled.

The impact of magnetic fields on various objects in astrophysics is now well established. They play a major role on a wide range of scales, from the study of the early universe, the stellar and intergalactic medium to the formation and interiors of stars or the accretion flows around stellar objects. They are difficult to study both from an observational and a theoretical (and numerical) point of view. Several implementations of ideal MHD have been performed since the last decade (Fromang et al. (2006), Stone and Norman (1992), Machida et al. (2005) among others), and numerical issues concerning the divergence free condition have now been resolved. However, ideal magnetohydrodynamics (MHD) is in many circumstances a poor approximation and non-ideal MHD effects need to be thoroughly considered.

The angular momentum problem lies in the amount of angular momentum transfered to the central object. In an hydrodynamical framework, as emphasized in the beginning of the chapter, the angular momentum is conserved throughout the collapse. A small amount of rotational energy at the molecular cloud scale results in unrealistic rotation velocity for the proto-star that can even destroy it. The *issue* is that there is a need for a physical process that can break down the rotation of the central regions in order to form stars. Similarly to the angular momentum, the magnetic flux is conserved throughout the collapse in the ideal magnetohydrodynamics framework, leading to unrealistic magnetic fields magnitude in the central object. Again, the *issue* associated is not a physical puzzle, it is the knowledge that the answer to star formation is not complete yet and the need for more detailed physics. The presence of magnetic field also allows for efficient braking of the inner regions. Angular momentum is transferred from inner regions to the outer part of the cloud via Alfvén waves. In the case of a moderately strong magnetic field, it can remove most of the rotational energy and inhibits disk formation (see Hennebelle and Teyssier (2008)). Regulating the loss of angular momentum is correlated to regulating the amount of magnetic energy accumulated in the central object. Non-ideal magnetohydrodynamics allow for a drift between particles, redistributing the magnetic flux and acting on both the angular momentum and magnetic flux conservation *issues*.

Ambipolar diffusion is expected to play a major role in star formation (Mestel and Spitzer (1956)), at the scale of molecular clouds by enabling the collapse of otherwise magnetically supported clouds (Basu and Ciolek (2004)) and at the scale of the first Larson's core with the formation of a centrifugally supported disk and the well-known *fragmentation crisis* (Hennebelle and Teyssier (2008)). Ambipolar diffusion is also important in protoplanetary disks as they are in general only partially ionised. The microscopic and entropic heating resulting from the drift and collision between neutral and charged species is another very important and relatively unknown aspect which is crucial as soon as cooling or heating of the gas (thus radiative transfert) is taken into account (in contrast it is not relevant when using a barotropic equation of state). Magnetic resistivity effects range from prohibiting long-term MHD turbulence in molecular clouds (Basu and Dapp (2010)) to preventing the *magnetic braking catastrophe* on small scales (Dapp and Basu (2010)). Its importance is also crucial in order to study disk formation around protostellar objects (Krasnopolsky et al. (2010)) and the physics of binary formation and brown dwarfs. Developing and using non-ideal magnetohydrodynamics was the keystone of this thesis.

Allowing fluid particles to tresspass magnetic field lines seems a win-win. It is nevertheless not as simple as the resistivity controls the results and depends on the microphysics of dense core collapse. The first step is to account for a detailed chemical network, as explained § 3.1. There are many unsolved issues regarding chemical evolution of particules during core collapse simulations:

- the ionization rate is a key parameter in computing the chemical equilibrium (or non-equilibrium) abundances of the many different particles in dense clouds. It is quite poorly known, and studies currently carried out could completely change the relative abundances and therefore the diffusion of the magnetic field at densities corresponding to the first Larson core. A similar work on the scale of molecular clouds and the interstellar medium has been performed by Padovani and Galli (2013), and will be continued in the case of dense core collapse. We were able to assess the validity of our results concerning resistivities by using an upper and lower limit for the ionization rate.

- chemical networks and their coupling to hydrodynamical simulations may cause unforeseen changes. Particles in outflows, in circumstellar disks or in the densest part of the cores have a very different history[11]. Again, we were able to probe this issue by using a time-dependent integration for the chemical network. We concluded that a simple time integration does not lead to significant differences, but this issue remains as we expect history-related effects to be non-negligible (see Hincelin (2012)).

Last, most simulations used to treat heating and cooling using a barotropic equation of states. In order to precisely account for radiative transfer, the energy equation has to be solved. This assessment is also true for ideal MHD simulations but has important implications in the case of ambipolar heating, in particular in first core outflows (see Panoglou et al. (2012)). Detailed radiative transfer accounts for shadows and secondary emission, while more evolved multi-frequency models release the simple *grey* hypothesis and have yet to be studied in three dimensions. Extensive work has been done by Vaytet et al. (2012, 2013a,b) which we extended to three dimensions (see § 2.3), opening a new ground for experiments on 3D-shocks and core collapse simulations. We could not extensively study its consequences on core collapse but were able to present encouraging early results.

Non-ideal MHD have been studied by several authors in the recent history of star formation. Duffin and Pudritz (2008) included ambipolar diffusion in a fashion similar to ours, and we followed them to test our implementation using a C-shock. They however did not extensively study the effects of ambipolar diffusion on core collapse in a fully 3D case and only conducted a preliminary study of an initially subcritical Bonnor-Ebert sphere (i.e. supported against gravitational collapse through magnetic fields).

[11] We call history the time dependent variables (ρ, T) for a given particle.

Other authors (see Machida et al. (2006, 2007a); Machida and Matsumoto (2011)) included resistive effects using a single Laplace operator, which is valid for Ohmic dissipation but incorrect when studying ambipolar diffusion. Indeed, the exact expression for the ambipolar diffusion yields important differences that can be highlighted for example in the study of the fundamental problem of the kinetic ABC dynamo (see § 4.4 for more details). They conducted a parameter study focused on the second core formation and Ohmic dissipation with a given prescription for the resistivity coefficient. Their results showed significant differences on the shape and properties of the second Larson core compared to the ideal MHD case with possible consequences on wide binary-stars formation.

More consistently, Kunz and Mouschovias (2009) and Kunz and Mouschovias (2010) used a detailed chemical network to implement in the public code Zeus-MD non-ideal MHD. They found in one and two dimensional simulations an efficient decoupling between magnetic fields and the evolution of the neutrals due to ambipolar diffusion rather than Ohmic dissipation, with the magnetic field magnitude reaching a plateau at about 0.1 G along with a wall of magnetic energy (a shock) outside the first core. Li et al. (2011) used the same network to study first core formation with all three resistive effects. Their results were controversial and not in neat agreement with previous studies (Machida et al. (2010) for example found that even with only the fiducial Ohmic dissipation resistivity a disk is created while Li et al. (2011) didn't). We explain these differences through an unsolved issue concerning their resistivities that results in erroneous values and therefore conclusions (see § 3.1 for more details on this issue). However, their study is very insightful and in particular motivated the development of the chemical network presented § 3.1: resistivities deeply affect the dynamics of core collapse and we wanted to be able to easily control some parameters such as the grain size distribution and draw conclusions on the limits of our results.

As a conclusion, non-ideal MHD are of the essence in contemporary star formation and little is know on their precise effects on magnetic field dissipation and the related fragmentation crisis or disk formation and evolution. To continue this study is the subject of this thesis.

1.A Polytropic or adiabatic index ?

There are many confusions between the polytropic index and the adiabatic index since both of them are usually noted with γ. This short section will clarify this point. The polytropic index will be noted n hereafter, while we will keep γ for the adiabatic index.

The adiabatic index is the ratio of the heat capacity at constant pressure (C_P) to heat capacity at constant volume (C_V). It describes the state of the gas (or fluid) considered. For ideal gases, it can be linked to the degrees of freedom of the molecules: $\gamma = 1 + \frac{2}{f}$ where f is the number of degrees of freedom. For a monoatomic gas ($f = 3$ degrees of freedom: translation in any direction) $\gamma = \frac{5}{3}$ while for a diatomic gas ($f = 5$, three translational and two rotational degrees of freedom) $\gamma = \frac{7}{5}$. A real gas can obviously have more complex behaviors, and thus the adiabatic index can vary in time and be different from these two particular values.

The polytropic index is defined for a given process. It links the evolution of the volume V and the pressure P, and can be applied to either gases, liquids or solids. The key point is to accurately describe the *process*. In terms of density, this yields:

$$P \propto \rho^n. \tag{1.93}$$

Some particular values for n are worth highlighting:

- $n = 0$ (or $P =$ constant) describes an isobaric process
- $n = 1$ describes an isothermal process since $P \propto \rho$ and $P = \rho k_B T$ (for a perfect gas)
- $n = \gamma$ describes an adiabatic process (for a perfect gas with $PV = nRT$). To demonstrate this, start with $P \propto V^{-n}$, then use the definition of an adiabatic process $\delta Q = 0$ and express the internal energy U as $dU = C_V dT = \frac{C_{V,\mathrm{mol}}}{R}(PdV + VdP)$. Finally, we find that $n = \gamma$.
- $n = \infty$ describes an isochoric process

The case $n = \gamma$ is the reason of the existing confusion. We want to emphasize here that it is not usually the case: it is for adiabatic processes. In the case of star formation, this happens twice: when the opacity becomes high enough in the first time and then in the second Larson core. In that case, the process is actually an adiabatic contraction, therefore the adiabatic and polytropic indices are equal.

In addition, a polytrope is the solution to the Lame-Emden equation for a Newtonian self-gravitating, spherically symmetric polytropic fluid.

As a conclusion, a fluid or a gas is not polytropic *per se* but instead can follow a polytropic law. A polytrope is not a type of fluid but the solution to the Poisson equation in a precise framework (known as the Lame-Emden equation). And finally, the adiabatic and polytropic index describe completely different things but happen to be the same for adiabatic processes.

Finally, the polytropic index $\tilde{n}$ is sometimes defined as $P \propto \rho^{1+\frac{1}{\tilde{n}}}$. It is obviously not equal to the previously defined n. The physical description remains the same, with other corresponding values than highlighted for $\tilde{n}$.

1.B Is ambipolar diffusion a diffusion ?

In this appendix we briefly discuss the difference between the expression for the ambipolar diffusion and a diffusion equation. We therefore focus on the term:

$$\frac{\partial \mathbf{B}}{\partial t} + \boldsymbol{\nabla} \times (\mathbf{B} \times \mathbf{v_n}) = \boldsymbol{\nabla} \times \Big(\frac{1}{\gamma \rho_i \rho} [(\boldsymbol{\nabla} \times \mathbf{B}) \times \mathbf{B}] \times \mathbf{B} \Big) \tag{1.94}$$

$$= \boldsymbol{\nabla} \times \Big(\frac{1}{\gamma \rho_i \rho} [\mathbf{B} \cdot (\boldsymbol{\nabla} \times \mathbf{B})] \mathbf{B} - (\mathbf{B} \cdot \mathbf{B}) \boldsymbol{\nabla} \times \mathbf{B} \Big) \tag{1.95}$$

$$= -\boldsymbol{\nabla} \times \Big(\frac{\mathbf{B} \cdot \mathbf{B}}{\gamma \rho_i \rho} (\boldsymbol{\nabla} \times \mathbf{B}) \Big) \tag{1.96}$$

Equation (4.15) is not easily simplified into a Laplace operator with a diffusion coefficient, since:

$$\boldsymbol{\nabla} \times \Big(\frac{\mathbf{B} \cdot \mathbf{B}}{\gamma \rho_i \rho} (\boldsymbol{\nabla} \times \mathbf{B}) \Big) = -\frac{B^2}{\gamma \rho_i \rho} \Delta \mathbf{B} + \boldsymbol{\nabla} (\frac{\mathbf{B} \cdot \mathbf{B}}{\gamma \rho_i \rho}) \times (\boldsymbol{\nabla} \times \mathbf{B}) \tag{1.97}$$

The difficulty is that the diffusion coefficient is an explicit function of the magnetic field, therefore there is no easy way to neglect the second term on the right hand-side. This is very different from the Ohmic diffusion case where the diffusion coefficient can be considered constant under reasonable hypothesis and then written as a real diffusion with a Laplace operator.

It may or may not be relevant given the case studied, but it should never be taken for granted that ambipolar diffusion is a *simple* diffusion. This is particularly true when studying dynamos, as will be highlighted in § 4.4.

Flux freezing and magnetic reconnection It is not the aim of this appendix to derive a full theory of non-ideal magnetohydrodynamics, yet a few words on reconnection and whether or not it is relevant for non ideal effects, will be useful for the general understanding of these effects. Flux-freezing is derived from the fact that we better apprehend the magnetic field using field lines, while in reality the magnetic field is a vector field. What we call field line is a curve that is in any point tangent to the direction of the magnetic field. It is a very useful mathematical object, but does not *always* account for the very physics at stake. What *should* be considered instead is either the vector field, or the charged particles at the origin of this magnetic field (this has been pointed out very early by Alfven (1976), but somehow got forgotten along the way). Using the previous derivation of non-ideal terms (equation (1.89) or just equation (1.90) for ambipolar diffusion), we can see that what is called flux-freezing[12] is just the plasma carrying what we call the field-lines at the speed $\mathbf{v}$. In ideal MHD $\mathbf{v} = \mathbf{v}_{\text{neutrals}}$, and with ambipolar diffusion it seems as if $\mathbf{v} = \mathbf{v}_{\text{ions}}$. This is the reason why it is admitted that there is no reconnection with ambipolar diffusion, as reconnection is simply the fact that the magnetic flux is not conserved through a given contour. On the other hand, Ohmic diffusion cannot be accounted for just by defining a new relevant speed $\mathbf{v}$ and therefore the not-so-well-called *flux-freezing* is violated and reconnection can (will) occur.

Last but not least, one must remember that in § 1.3.3 we dropped a term, namely $\rho_e \rho_n \frac{<\sigma v>_{en}}{m_e + m_n} (\mathbf{v_n} - \mathbf{v_e})$. This term is actually interesting, since when retaining it through the calculation you end up with a different form for the induction equation (see Tsap et al. (2012) for a recent study of this issue in a different framework) which cannot be written entirely as $\boldsymbol{\nabla} \times (\mathbf{v}_{\text{arbitrary}} \times \mathbf{B})$. Therefore, the commonly admitted assumption that there is no reconnection with ambipolar diffusion is not exactly true (it is true under the assumption that this term is negligible, which should be the case in star forming clouds).

[12] The fact that the derivative of the flux reads $\frac{\mathrm{d}\phi}{\mathrm{d}t} = -\int_{S(t)} \boldsymbol{\nabla} \times (\mathbf{E} + \mathbf{v} \times \mathbf{B})$, with $\mathbf{E} + \mathbf{v} \times \mathbf{B} = \mathbf{0}$, means that the flux remains constant in time.

1.C Timescale for magnetic braking

The magnetic braking timescale has been extensively studied by Mouschovias (1978, 1979); Mouschovias and Paleologou (1979, 1980b). Recently, Joos et al. (2012) presented refinements of these orders of magnitude calculation for aligned and perpendicular rotators. They found that taking into account the fanning-out and entanglement of the field lines yields a different conclusion than the one Mouschovias and Paleologou (1980b) found. The timescale for magnetic braking in the aligned case with fanning-out ($\tau_{\parallel,f-o}$) is smaller than the perpendicular case ($\tau_{\perp}$). Accordingly, the efficiency of the braking is greater in the aligned case than in the perpendicular one. Their analysis was based on equating the angular momentum in the core and in its surroundings. We confirm here his calculation for the aligned case and precise the topology in which it is derived.

1.C.1 Aligned rotator with fanning-out

In this case we do not take into account the entanglement of the field lines but only the fanning-out due to the collapse and the flux-freezing. We begin with the assumptions of co-rotation between a volume V_A and its surroundings, and the conservation of angular momentum in the cloud (of momentum of inertia $I = \frac{2MR_{cloud}^2}{G}$):

$$I\frac{\partial\Omega}{\partial t} + \iiint_{V_a} r^2\Omega \mathrm{d}m = 0 \tag{1.98}$$

where Ω the rotation speed and V_a the volume defined by the propagation of Alfvén waves along the field lines. The braking timescale is then simply:

$$\tau_{\mathrm{braking}} = \frac{\Omega}{\partial\Omega/\partial t} \tag{1.99}$$

For a spherical cloud of initial radius R_0, actual radius R_c and with radial field lines, we find $\tau_{\mathrm{braking}} \propto \frac{R_c^5}{R_0^4 v_{\mathrm{a,ext}}\rho_{\mathrm{ext}a}}$. In the case of an (not too) oblate cloud of height Z with radial field lines we get:

$$\tau_{\mathrm{braking}} \propto \frac{R_c^4 Z}{R_0^4 v_{\mathrm{a,ext}}\rho_{\mathrm{ext}a}} \tag{1.100}$$

which is the result found by Joos et al. (2012).

In this derivation, we forgot to take into account the entanglement of the field lines. This effect will supposedly give a larger braking time since the volume of gas susceptible to corotate is smaller. Without the constant Alfvén speed assumption, the braking time would increase even more.

1.C.2 Perpendicular rotator

For the perpendicular rotator we can't calculate simply the braking time without using global criteria as in Joos et al. (2012). It is not even clear that angular momentum propagates along field lines with the Alfvén speed, since the topology of the field is highly twisted compared to Gillis et al. (1979). For these reasons, we can't add informations to the order of magnitude study by Joos et al. (2012) for this case.

Chapter 2

Numerical star formation

"*Astronomers, like burglars and jazz musicians, operate best at night.*"
Miles Kington, Welcome to Kington, 1989.

Contents

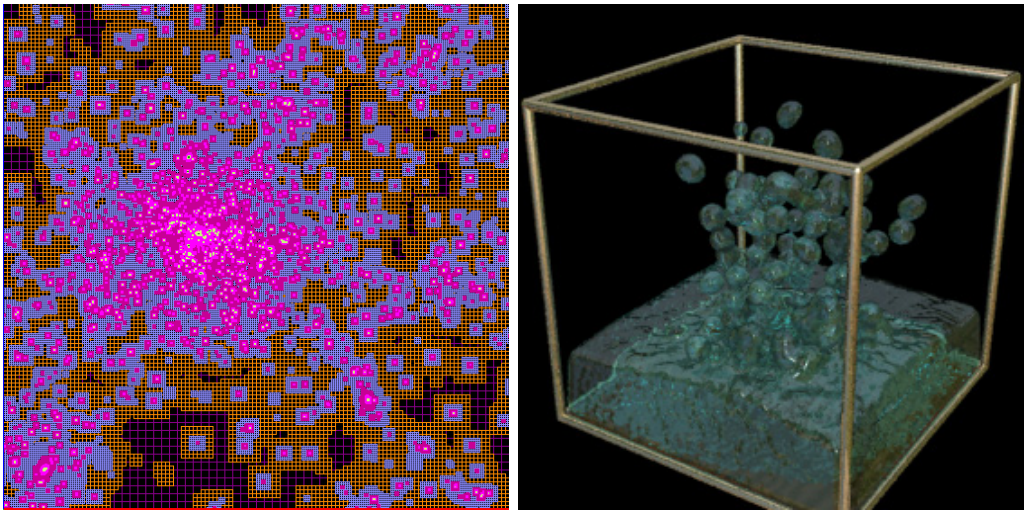

Figure 2.1: Comparison between an AMR code (RAMSES) on the left and a SPH code (SPLASH) on the right.

Introduction

Numerical star formation changed in the past half-century. First, astrophysicists divided the problems they wanted to study in smaller bits and used numerical methods to solve complex sets of equations. Nowadays, thanks to the tremendous advances in computational power and numerical methods, we can begin to solve only the fundamental equations[1] and approach star formation on a more consistent way. In this chapter, we shortly present the code we used to simulate low-mass star formation and the refinements we added.

2.1 The AMR code RAMSES

2.1.1 RAMSES

RAMSES, standing for Raffinement à Maille Adaptative Sans Effort Surhumain, is an adaptive mesh refinement grid code. AMR was first introduced by Berger and Oliger (1984). It consists in a dynamical nested grid, where cells can have different sizes depending on the resolution needed. The refinement criteria is usually user-defined, in order to match the relevant physics. The structure of the grid in RAMSES is *tree-based*, meaning that the refinement is made cell-by-cell, creating children or unrefining a group of 8 cells (an oct) when needed. The AMR structure has then to be coupled with a grid-based hydrodynamical solver to describe fluid motions. Nowadays, Godunov schemes are widely used for their efficiency to capture discontinuities (e.g. shocks) within a few cells (see for example Teyssier (2002)). Moreover, Godunov schemes can be adapted to the magnetohydrodynamics framework, where they still accurately capture discontinuities but also allow for an exact conservation of $\boldsymbol{\nabla} \cdot \mathbf{B}$, mandatory to describe charged fluids motions (a precise description of the method is in Fromang et al. (2006)).

[1] The laws of conservation, Navier-Stokes equation, induction equation, radiation, etc.

2.1.1.1 Eulerian hydrodynamics

The Eulerian frame is appropriate for grid based codes. It means that the grid is fixed, and the primitive variables are the density ρ, the velocity of the fluid $\mathbf{v}$ and the internal energy $\rho\epsilon$ (or the pressure P). Conservative variables are a combination of the previous three to write the whole set of equation in a conservative form. The set of equation for an inviscid compressible flow reads in conservative form:

$$\frac{\partial U}{\partial t} + \nabla \cdot F(U) = 0 \quad \text{with} \quad U = \begin{cases} \rho \\ \rho\mathbf{v} \\ E \end{cases} \quad \text{and} \quad F = \begin{cases} \rho\mathbf{v} \\ \rho\mathbf{v} \otimes \mathbf{v} + p \\ \mathbf{v}(E+p) \end{cases} \tag{2.1}$$

with $E = \frac{1}{2}\rho\mathbf{v}^2 + \rho\epsilon$. The set of equations is closed with the perfect gas equation of state $\frac{P}{\rho} = \frac{k_B T}{\mu m_H} = (\gamma - 1)\epsilon$, with P the gas pressure, μ the mean molecular weight of the particles constituting the fluid, m_H the hydrogen mass, γ the ratio of specific heats, T the temperature of the gas and k_B the Boltzmann constant.

There are two means to solve the set of equations: the finite difference method (e.g. the ZEUS code, Hayes et al. (2006); Stone and Norman (1992)) and the finite volume method (e.g. the `RAMSES` code, Teyssier (2002)). In finite difference methods variables are sampled on a discrete grid in space and time. Partial derivatives are also sampled on a grid (the same or a half-grid) and all variables are updated using Euler set of equations. In finite volume methods, flow variables are averaged over a given volume (the cell) and obey the conservation laws in the integral form. It means that even if defined at the center of the cell, any flow variable is exactly the integral of the values over the cell, disregarding the position. It also means that the scheme is conservative and that the evolution of the variables is completely defined through the many fluxes at each cell interface.

We can rewrite equation (2.1) with the Jacobian matrix of F, diagonalizable (explanations in Toro (2009) page 199: we describe an hyberbolic system of equations),

$$\frac{\partial U}{\partial t} + \nabla_U F(U) \nabla_x U = 0. \tag{2.2}$$

It can be useful to remark that in primitive form, equation (2.1) yield

$$\frac{\partial V}{\partial t} + B(V)\nabla_x U = 0 \quad \text{with} \quad V = \begin{cases} \rho \\ \mathbf{v} \\ P \end{cases} \tag{2.3}$$

with unchanged spectral properties for $B(V)$. Note that this form can lead to inaccurate wave propagation speed and therefore should be used only when absolutely needed. In `RAMSES` the conservative form is always used, except when it gives negative temperature. In this specific case, the primitive form is used to get the correct temperature and pressure fields.

Once integrated in space and time, equation (2.1) yields

$$\int_{x_1}^{x_2} (U(t_2) - U(t_1))\, dx + \int_{t_1}^{t_2} (F(x_1) - F(x_2))\, dt = 0. \tag{2.4}$$

In order to evolve the various flow variables, as is obvious in equation (2.4), one must know the fluxes at the interfaces of the cell (at x_1 and x_2 in one dimension). Finite difference methods suppose a piecewise constant value for each variable in the cell. There is therefore a discontinuity at each cell interface where fluxes need to be computed (this is the Godunov method, Godunov (1959)). This is called a *Riemann problem*. Solving a Riemann problem can involve exact or approached

methods, usually depending on the problem. The formulation of the first order Godunov method is the following:

$$\frac{U_i^{n+1} - U_i^n}{\Delta t} + \frac{F_{i+1/2}^{n+1/2} - F_{i-1/2}^{n+1/2}}{\Delta x} = 0 \tag{2.5}$$

where the Godunov fluxes $F_{i+1/2}^{n+1/2}$ and $F_{i-1/2}^{n+1/2}$ are given by solving the Riemann problem at the cell interfaces. To the first order $F_{i+1/2}^{n+1/2} = F^\star(U_i^n, U_i^{n+1})$.

A detailed resolution of a one dimensional Riemann problem in a Godunov scheme is described in the appendix B, using first an exact solver and then presenting approximates solvers such as the ones used in RAMSES. A major drawback of first order Riemann solvers is a high diffusivity, smoothing inhomogeneities. To increase the accuracy and reduce the diffusivity, second order Godunov methods (and associated Riemann solvers) have been developed (see van Leer (1979)). In RAMSES, the predictor-corrector second order in time and space scheme MUSCL is used.

2.1.1.2 The MUSCL predictor-corrector scheme

MUSCL stands for **M**onotone **U**pstream-centered **S**cheme for **C**onservative **L**aws. Contrary to the first order, the flow variables in the cell are not supposed constant aymore but rather follow a given piecewise linear extrapolation. Note that this introduces a length to define a slope and the Riemann solver is not self-similar anymore. The piecewise approximation is of the form:

$$U_i(x) = U_i^n + \frac{x - x_i}{\Delta x}\Delta i \quad x \in [0; \Delta x] \tag{2.6}$$

where Δi controls the slope. For monoticity reasons, the slope in each cell has to be limited instead of using a simple central finite difference. We will come back to this later. At the cells interfaces, we have:

$$U_i^L = U_i^n - \frac{1}{2}\Delta i \quad ; \quad U_i^R = U_i^n + \frac{1}{2}\Delta i. \tag{2.7}$$

Solving a Riemann problem using U_i^L and U_i^R at the half time-step $\frac{\Delta t}{2}$ yields the predicted states:

$$\begin{array}{l} \bar{U}_i^L = U_i^L + \frac{1}{2}\frac{\Delta t}{\Delta x}[F(U_i^L) - F(U_{i-1}^R)], \\ \bar{U}_i^R = U_i^R + \frac{1}{2}\frac{\Delta t}{\Delta x}[F(U_i^L) - F(U_{i+1}^R)]. \end{array} \tag{2.8}$$

The fluxes for the global problem can now be estimated:

$$F_{i+1/2}^{n+1/2} = \frac{1}{\Delta t}\int_{t^n}^{t^{n+1}} F_{i+1/2}\,\mathrm{d}t \simeq F(\bar{U}_i(\frac{\Delta t}{2})) \tag{2.9}$$

which is simply solving the Riemann problem at the interface $i + \frac{1}{2}$ using $(U_L = \bar{U}_i^L; U_R = \bar{U}_{i+1}^R)$. We used predicted approximate steps and corrected them solving a second Riemann problem. This scheme grants second order precision in both time and space. The only remaining decision to make is the slope limiter.

The slope limiter Δi must assure the monotonicity. There is a solution called TVD: **T**otal **V**ariation **D**iminishing, introduced by Harten (1983). Monotonicity is preserved provided $\sum_i^N |U_{i+1}^{n+1} - U_i^{n+1}| \leq \sum_i^N |U_{i+1}^n - U_i^n|$. In RAMSES there are several choices for the slope limiter, and the most common is called *minmod* (see Fig. 2.2).

To deal with multi-dimensional grids, one has to use directional splitting. It means that a MUSCL step is carried out in every direction independently and a conservative update is performed using unidimensional fluxes.

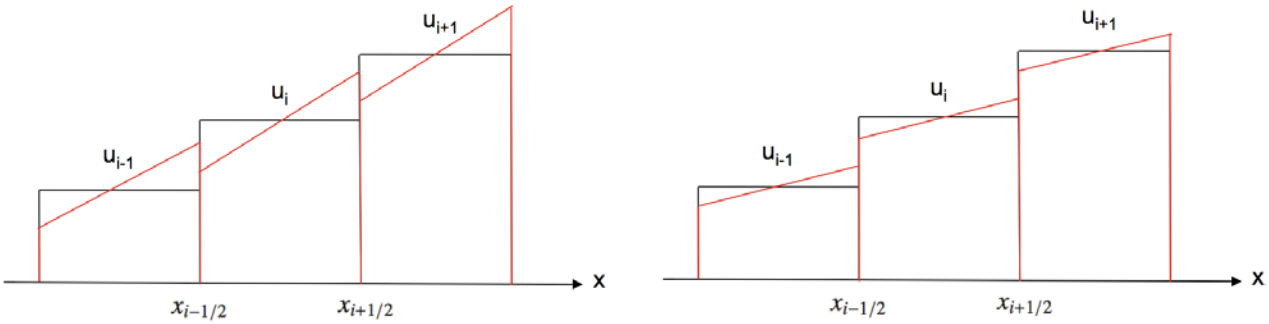

Figure 2.2: Left: *moncen*, assuring $U_{i-1} \leq U_{i+\frac{1}{2},L} \leq U_{i+1}$. Right: *minmod*, assuring $U_{i+\frac{1}{2},L} \leq U_{i+\frac{1}{2},R}$. From Romain Teyssier Lecture.

Last, the stability criteria is the usual Courant condition because of the explicit discretization of the Euler set of equations:

$$\Delta t \leq C_{CFL} \frac{\Delta x}{c_s + u} \text{ avec } C_{CFL} < 1. \tag{2.10}$$

2.1.1.3 Mesh refinement

AMR is the possibility to have high resolution in user-defined dynamical regions. It means that it is extremely efficient in structure formation, where resolution can be linked to a given criteria. Shocks can be studied using a refinement criteria based on gradients. Fragmentation or collapse simulations will use mass-based criteria such as the Jeans mass or length. On the other hand, the refinement criteria has to be chosen with care: the filling factor of refined cells shouldn't exceed 30% because then a uniform grid is found to be more efficient.

The structure is a tree-based one, called **F**ully **T**hreaded **T**ree (TFF, Khokhlov (1998)). The grid is organized in *octs* that comprise (2^{dim}) cells for a *dim*-dimensional problem. Given a refinement criteria, cells can be flagged for refinement or not. When a cell is flagged for refinement, it creates an oct on a finer level. If a cell has no children, it is called a *leaf* cell. Otherwise, the cell is called a *split* cell and no hydrodynamics calculations will be performed on it. The structure is represented in a 2-dimensional example Fig. 2.3. Each level of refinement can be evolved with a different time-step, abiding by the Courant condition with different Δx in each level.

As stated previously, an adapted refinement criteria for core collapse studies is the Jeans length. In `RAMSES` we define a number of cells per Jeans length N_j as a refinement criteria. For a level l_i, the mesh is refined if the following inequality is verified:

$$\frac{L_{\text{box}}}{2^{l_i}} < \frac{\lambda_J}{N_j} \tag{2.11}$$

where $\frac{L_{\text{box}}}{2^{l_i}}$ is the size of a cell at the level l_i.

2.1.2 Solving magnetohydrodynamics equations

Solving MHD equations is a difficult task. The divergence free constraint along with vectorial equations complexifies the Godunov method. `RAMSES` makes use of a magnetohydrodynamics solver developed by Fromang et al. (2006); Teyssier et al. (2006). In addition to modifying the Euler set

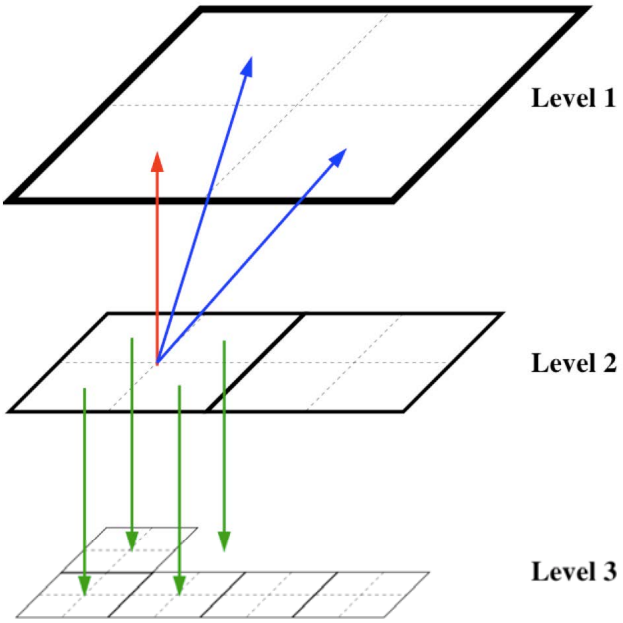

Figure 2.3: Octal structure in two dimensions: each oct at level l points to its parent cell at coarser level $l-1$, to the $2\times dim$ neighbours of the parent cell and to the 2^{dim} child octs at level $l+1$. From Romain Teyssier Lecture.

of equations, magnetohydrodynamics introduces the induction equation. This equation couples the field to the motion of the fluid particles:

$$\frac{\partial \mathbf{B}}{\partial t} = \nabla \times (\mathbf{u} \times \mathbf{B}). \tag{2.12}$$

The Euler set of equation is modified accordingly, using the Lorentz force:

$$\mathbf{j} \times \mathbf{B} = (\mathbf{B} \cdot \nabla)\mathbf{B} - \nabla(\frac{\mathbf{B} \cdot \mathbf{B}}{2}) \tag{2.13}$$

with the magnetic tension (first term on the right) and pressure (second term in the right). The complete magnetohydrodynamics set now reads:

$$\begin{cases} \frac{\partial U}{\partial t} + \nabla \cdot F(U) = 0 \quad \text{with} \quad U_t = \begin{cases} \rho \\ \rho\mathbf{u} \\ E \end{cases} \quad \text{and} \quad F = \begin{cases} \rho\mathbf{u} \\ \rho\mathbf{u} \otimes \mathbf{u} - \mathbf{B} \otimes \mathbf{B} + P_{tot} \\ \mathbf{u}(E + P_{tot}) - \mathbf{B}(\mathbf{B} \cdot \mathbf{u}) \end{cases} \\ \frac{\partial \mathbf{B}}{\partial t} = \nabla \times (\mathbf{u} \times \mathbf{B}) \end{cases} \tag{2.14}$$

with P_{tot} the total pressure (magnetic and thermal):

$$P_{tot} = P + \frac{\mathbf{B} \cdot \mathbf{B}}{2} \tag{2.15}$$

and E the total energy per unit volume:

$$E = \rho(\epsilon + \frac{\mathbf{u} \cdot \mathbf{u}}{2}) + \frac{\mathbf{B} \cdot \mathbf{B}}{2}. \tag{2.16}$$

As previously the system of equations is closed using the perfect gas equation of state $\frac{P}{\rho} = (\gamma - 1)\epsilon$. In order to abide by the new divergence free constraint $\nabla \cdot \mathbf{B} = 0$ while solving the induction equation, RAMSES uses the constraint transport method.

2.1.2.1 The constraint transport

The constraint transport (see Fromang et al. (2006)) consists in a finite volume method with an exact conservation of $\nabla \cdot \mathbf{B} = 0$. In its integral form, the induction equation yields:

$$\frac{\partial \Phi}{\partial t} = \iint \frac{\partial \mathbf{B}}{\partial t} \cdot d\mathbf{S} = \iint \nabla \times (\mathbf{u} \times \mathbf{B}) \cdot d\mathbf{S} = \oint \mathbf{E} \cdot d\mathbf{l}. \tag{2.17}$$

The magnetic field components are face centered:

$$\mathbf{B}_{x,i-1/2,j,k} = \frac{1}{\Delta y \Delta z} \int_{y_j-1/2}^{y_j+1/2} \int_{z_k-1/2}^{z_k+1/2} \mathbf{B}_x(x_i - 1/2, y', z')\, dy'\, dz'. \tag{2.18}$$

Using these notations, we can rewrite the discretized induction equation:

$$\frac{\mathbf{B}^{n+1}_{x,i-1/2,j,k} - \mathbf{B}^{n}_{x,i-1/2,j,k}}{\Delta t} - \frac{\mathbf{E}^{n+1/2}_{z,i-1/2,j+1/2,k} - \mathbf{E}^{n+1/2}_{z,i-1/2,j-1/2,k}}{\Delta y} + \frac{\mathbf{E}^{n+1/2}_{y,i-1/2,j,k+1/2} - \mathbf{E}^{n+1/2}_{y,i-1/2,j,k-1/2}}{\Delta z} = 0. \tag{2.19}$$

Again, as described in the Godunov scheme, the induction equation will make use of a predictor/corrector scheme to achieve second order precision. The electromotive forces ($E^{n+1/2}_{y,i-1/2,j,k+1/2}$ etc.) must be evaluated at a time $t + 1/2$ solving 2D Riemann problems at the edges of the cell. Details can be found in either Teyssier et al. (2006) or Fromang et al. (2006).

As for the Euler set of equations including the Lorentz force, the resolution is the same, with more eigenvalues to consider. There are exactly 7 waves: 2 Alfén waves, 2 slow magneto-acoustic waves, 2 fast magneto-acoustic waves and 1 entropy wave. Approximate solvers such as HLLD used in `RAMSES` take into account 5 waves, dropping the slow magneto-sonic waves. The Lax-Friedrich (respectively Roe) solver uses less (respectively more) waves, resulting in a more (respectively less) diffusive solver. Depending on the situation and the computational cost, one can change from one solver to another.

2.2 Non-ideal magnetohydrodynamics, implementation in `RAMSES`

Following § 1.4, it appears necessary to introduce the ambipolar and Ohmic diffusion in a 3D MHD code. Before exploring the astrophysical impact of such a study, however, the accuracy of the treatment of the complete MHD set of equations must be unambiguously assessed. This is the very aim of the present chapter, in which we describe a prescription to incorporate ambipolar and Ohmic diffusion in the multi-dimensional MHD AMR code `RAMSES` (Teyssier (2002)), extending the ideal MHD version presented in Teyssier et al. (2006) and Fromang et al. (2006).

Several numerical treatments have been derived from ideal MHD models, following different aims and thus using different methods. The first attempt to implement ambipolar diffusion in a code was made by Black and Scott (1982) using an iterative approximation in an implicit first-order code. Toth (1994) used a semi-explicit method in a two-dimensional code to investigate instabilities in C-schocks. Mac Low et al. (1995) presented a widely used explicit method (Choi et al. (2009), Mellon and Li (2009), Li et al. (2011)) to implement single-fluid ambipolar diffusion in the strong coupling limit, and then developed a two-fluid model in order to capture shock instabilities. Tilley and Balsara (2008) and more recently Tilley and Balsara (2011) presented a semi-implicit scheme for solving two-fluid ambipolar diffusion, arguing that the single fluid approximation does not carry the full set of MHD waves that can propagate in a poorly ionized system. Multi-fluid approaches including ambipolar diffusion and Ohmic diffusion have been suggested by Falle (2003), or O'Sullivan and Downes (2006) and then investigated by e.g. Kunz and Mouschovias (2009). Recently, Li et al. (2011) used the single-fluid approach including more realistic resistivities based on a multi-fluid approach for

ambipolar diffusion, Ohmic diffusion and Hall effect in two-dimensional (axi-symmetric) calculations. Another approach has been used by Machida et al. (2006) was to describe both ambipolar diffusion and Ohmic diffusion in one single Laplace operator $\eta\Delta B$, with η taking into account every diffusive process at stake. These numerous studies have also given rise to several numerical tests, a number of which we will either perform directly or slightly modify to assess the accuracy of our treatment.

Our current study focusses on the one-fluid approximation (Shu et al. (1987)) described § 1.3.2, as in previous calculations by Mac Low et al. (1995) and Duffin and Pudritz (2008). We used a direct explicit method to implement non-ideal MHD terms in both the induction and energy equations (Mac Low et al. (1995)) in an AMR framework. We did not choose to account for non-ideal effects by adding ambipolar diffusion and Ohmic dissipation in a single Laplace operator as Machida et al. (2006). Instead we kept the full expressions and proceeded separately for each non-ideal effect.

The chapter is organized as follows. In § 2.2.1, we first derive the equations for ambipolar diffusion in the single fluid approximation. We then describe the various tests we have performed, first without the hydrodynamics and then in a complete MHD situation, exploring in particular the propagation of Alfvén waves. Comparisons with existing analytical or benchmark solutions are presented in details, demonstrating the validity and the accuracy of our scheme. § 2.2.2 addresses the case of Ohmic diffusion, following the same procedure as for ambipolar diffusion, while § 2.2.3 is devoted to the conclusion.

2.2.1 Ambipolar diffusion

2.2.1.1 Equations

When the ions pressure and momentum are negligible compared to those of neutral species (as is the case for example in molecular clouds), the Lorentz force exerted on the ions is in equilibrium with the drag force exerted by the neutrals, which corresponds to a situation of strong coupling between the neutral fluid and the field lines. In such a situation, the plasma can be adequately described by a single fluid (Shu et al. (1987) and Choi et al. (2009)) of mass density ρ, and neutrals and ions mass densities $\rho_n \approx \rho$ and $\rho_i \ll \rho_n$ respectively. Interestingly, in the case of the one-fluid approximation the results can be directly compared with the ones obtained with ideal MHD giving clear insights about MHD wave propagation properties in the non-ideal case (Balsara (1996)).The present study is devoted to the technical resolution of the resistive MHD equations and we will also ignore gravity (and thus the Poisson equation). The MHD equations are given by the usual continuity, momentum, energy and induction equations, completed by the magnetic field divergence-free condition (in rational units, $\mathbf{B}_{rat} = \mathbf{B}_{cgs}/\sqrt{4\pi}$):

$$\frac{\partial \rho}{\partial t} + \nabla.(\rho \mathbf{v}) = 0 \tag{2.20}$$

$$\rho \frac{\partial \mathbf{v}}{\partial t} + \rho\,(\mathbf{v}.\nabla)\mathbf{v} + \nabla P - \mathbf{F}_L = 0 \tag{2.21}$$

$$\frac{\partial E_{tot}}{\partial t} + \nabla.\big((E_{tot} + P_{tot})\mathbf{v} - (\mathbf{v}.\mathbf{B})\mathbf{B} - \mathbf{E}_{AD} \times \mathbf{B}\big) = 0 \tag{2.22}$$

$$\frac{\partial \mathbf{B}}{\partial t} - \nabla \times (\mathbf{v} \times \mathbf{B}) - \nabla \times \mathbf{E}_{AD} = 0 \tag{2.23}$$

$$\nabla \cdot \mathbf{B} = 0. \tag{2.24}$$

E_{tot} denotes the total energy

$$E_{tot} = \rho\epsilon + \frac{1}{2}\rho v^2 + \frac{1}{2}B^2, \tag{2.25}$$

where ϵ is the specific internal energy.

P_{tot} is the total pressure

$$P_{tot} = (\gamma - 1)\rho\epsilon + \frac{1}{2}B^2, \tag{2.26}$$

where γ is the adiabatic index.

$\mathbf{F}_L$ denotes the Lorentz force

$$\mathbf{F}_L = (\nabla \times \mathbf{B}) \times \mathbf{B}, \tag{2.27}$$

with

$$\mathbf{v_i} - \mathbf{v_n} = \frac{1}{\gamma_{AD}\rho_i\rho}\mathbf{F_L}. \tag{2.28}$$

The ambipolar electromagnetic force (EMF) is given by

$$\mathbf{E}_{AD} = (\mathbf{v}_i - \mathbf{v}_n) \times \mathbf{B} = \frac{1}{\gamma_{AD}\rho_i\rho}\mathbf{F}_L \times \mathbf{B}, \tag{2.29}$$

where $\mathbf{v}_i$ and $\mathbf{v}_n$ denote respectively the ions and neutrals velocities, and γ_{AD} is the drift coefficient between ions and neutrals due to ambipolar diffusion. The last equality in Equation (2.29) illustrates the balance between magnetic and drag forces in the ion fluid, while Equation (2.22) is accounting for ambipolar heating of neutrals by ions (Shu (1992)). In order to write both Equation (2.22) and Equation (2.29) we need to assume that the velocity drift between ions and neutrals and the one between electrons and neutrals are not too different (by a factor $\simeq \frac{m_i}{m_e}$). Therefore, as long as the Hall effect is negligible, these equations remain valid (see Pinto et al. (2008) for a more detailed study).

Equation (2.22) (the conservation of energy: $\frac{\partial E}{\partial t} + \nabla \cdot \mathcal{F}_{\text{energy}} = 0$) is equivalent to

$$\rho T \frac{ds}{dt} = \frac{\|(\nabla \times \mathbf{B}) \times \mathbf{B}\|^2}{\gamma_{AD}\rho\rho_i}, \tag{2.30}$$

where we can see that the neutrals-ions friction term heats up the gas and increases the entropy.

2.2.1.2 Computing the ambipolar diffusion terms

In this subsection, we describe the numerical implementation of the previous equations, focusing on the ambipolar diffusion terms in the energy and induction equations.

The ambipolar EMF The ambipolar term in the induction equation can be considered as an additional electromotive force (EMF). To update the magnetic field the values of the EMF have to be defined as time and space averages along cell edges (Teyssier et al. (2006)). For instance, the EMF in the z direction is defined at $x_{i-\frac{1}{2}}, y_{j-\frac{1}{2}}, z_k$ (and the same for the other directions with circular permutations) where i,j and k are the cell indices in the x, y, z directions respectively.

We focus now on the EMF in the z direction, defined at $x_{i-\frac{1}{2}}, y_{j-\frac{1}{2}}, z_k$ and explain in details how it is computed. $\mathbf{E}_{AD}$ writes

$$\mathbf{E}_{AD} = \frac{1}{\gamma_{AD}\rho_i\rho}\left[(\nabla \times \mathbf{B}) \times \mathbf{B}\right] \times \mathbf{B} = \mathbf{v_d} \times \mathbf{B} \tag{2.31}$$

with the drift velocity $\mathbf{v_d} = \mathbf{v_i} - \mathbf{v_n} = \frac{1}{\gamma_{AD}\rho_i\rho}\mathbf{F_L}$. We therefore have to evaluate $\frac{1}{\gamma_{AD}\rho_i\rho}$, $\mathbf{F_L}$ and $\mathbf{B}$ at $x_{i-\frac{1}{2}}, y_{j-\frac{1}{2}}, z_k$, and then calculate

$$E^{AD}_{z;i-\frac{1}{2},j-\frac{1}{2},k} = (v_d)_{x;i-\frac{1}{2},j-\frac{1}{2},k} B_{y;i-\frac{1}{2},j-\frac{1}{2},k} - (v_d)_{y;i-\frac{1}{2},j-\frac{1}{2},k} B_{x;i-\frac{1}{2},j-\frac{1}{2},k}. \tag{2.32}$$

The `RAMSES` code is based on the Constrained Transport scheme for the magnetic field evolution (Teyssier et al. (2006)), for which the components of the magnetic field are defined at the center of

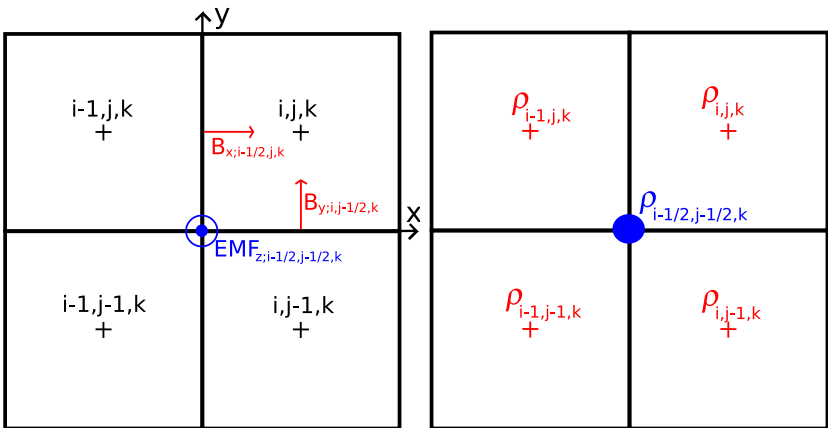

Figure 2.4: Left: coordinates of the center of neighbouring cells, with the natural places where the magnetic field and the EMF are defined. Right: computation of the density at $x_{i-\frac{1}{2}}, y_{j-\frac{1}{2}}, z_k$ by averaging over neighbouring cells.

cell faces: if x_i, y_j, z_k are the coordinates of a cell center, B_x is defined at position $x_{i-\frac{1}{2}}, y_j, z_k$, B_y at $x_i, y_{j-\frac{1}{2}}, z_k$ and B_z at $x_i, y_j, z_{k-\frac{1}{2}}$ (see Figure 2.4). Each magnetic field component is computed using the finite-surface approximation, which reads for the x component:

$$\left\langle B_{x;i-\frac{1}{2},j,k} \right\rangle = \frac{1}{\Delta y}\frac{1}{\Delta z}\int_{y_{i-\frac{1}{2}}}^{y_{i+\frac{1}{2}}}\int_{z_{i-\frac{1}{2}}}^{z_{i+\frac{1}{2}}} B_x(x_{i-\frac{1}{2}}, y, z)dydz, \tag{2.33}$$

while other components are defined by circular permutations.

We also need to define the drift velocity $\mathbf{v_d}$ at $x_{i-\frac{1}{2}}, y_{j-\frac{1}{2}}, z_k$ using the Lorentz force $\mathbf{F_L}$, the density ρ and the ions density ρ_i. The two latter quantities are cell-centered quantities (in contrast to the magnetic field):

$$\langle \rho_{i,j,k} \rangle = \frac{1}{\Delta x}\frac{1}{\Delta y}\frac{1}{\Delta z}\int_{x_{i-\frac{1}{2}}}^{x_{i+\frac{1}{2}}}\int_{y_{i-\frac{1}{2}}}^{y_{i+\frac{1}{2}}}\int_{z_{i-\frac{1}{2}}}^{z_{i+\frac{1}{2}}} \rho(x,y,z)dxdydz, \tag{2.34}$$

and

$$\langle \rho_{\mathrm{ions};i,j,k} \rangle = \frac{1}{\Delta x}\frac{1}{\Delta y}\frac{1}{\Delta z}\int_{x_{i-\frac{1}{2}}}^{x_{i+\frac{1}{2}}}\int_{y_{i-\frac{1}{2}}}^{y_{i+\frac{1}{2}}}\int_{z_{i-\frac{1}{2}}}^{z_{i+\frac{1}{2}}} \rho_i(x,y,z)dxdydz, \tag{2.35}$$

We then define the edge-centered density (and the ions edge-centered density) as an arithmetic average of surrounding cells (see Figure 2.4, right panel):

$$\rho_{i-\frac{1}{2},j-\frac{1}{2},k} = \frac{1}{4}[\rho_{i,j,k} + \rho_{i,j-1,k} + \rho_{i-1,j,k} + \rho_{i-1,j-1,k}]. \tag{2.36}$$

This definition is adapted for the components of the magnetic field to compute them at $x_{i-\frac{1}{2}}, y_{j-\frac{1}{2}}, z_k$ (see Figure 2.5):

$$B_{x;i-\frac{1}{2},j-\frac{1}{2},k} = \frac{1}{2}\left[B_{x;i-\frac{1}{2},j,k} + B_{x;i-\frac{1}{2},j-1,k}\right] \tag{2.37}$$

$$B_{y;i-\frac{1}{2},j-\frac{1}{2},k} = \frac{1}{2}\left[B_{y;i,j-\frac{1}{2},k} + B_{y;i-1,j-\frac{1}{2},k}\right]. \tag{2.38}$$

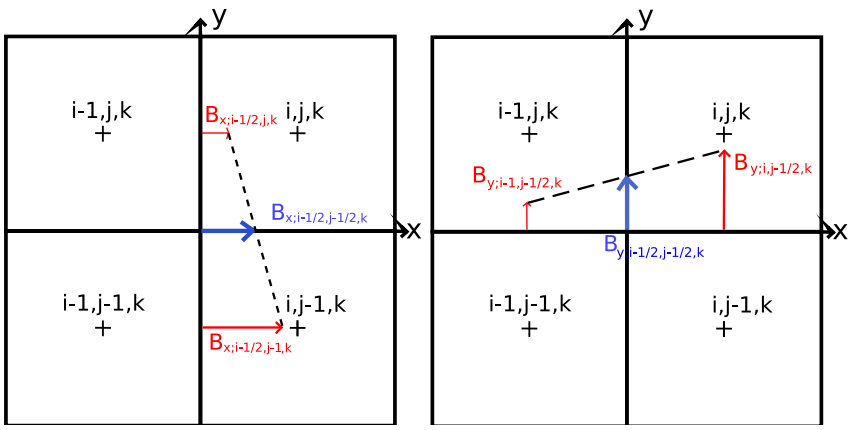

Figure 2.5: Computation of the magnetic field B_x and B_y at $x_{i-\frac{1}{2}}, y_{j-\frac{1}{2}}, z_k$.

Given the Lorentz force at $x_{i-\frac{1}{2}}, y_{j-\frac{1}{2}}, z_k$ (see subsections 2.2.1.2 and 2.2.1.2), it is possible to compute the first component (z direction, with unit vector $\mathbf{e_Z}$) of the ambipolar EMF: $\mathbf{E_{AD}} \cdot \mathbf{e_z} = E^{AD}_{z;i-\frac{1}{2},j-\frac{1}{2},k}$, while the two other components are obtained through circular permutations.

These ambipolar EMFs are then added to the ideal MHD EMFs calculated with a 2D Riemann solver, as described in Teyssier et al. (2006) and Fromang et al. (2006).

The Lorentz force as the product of the current and the magnetic field We now focus on the computation of the Lorentz force $\mathbf{F_L}$ at $x_{i-\frac{1}{2}}, y_{j-\frac{1}{2}}, z_k$. The first way to calculate this term is to explicitly compute the magnetic field components and the current $\mathbf{J} = \nabla \times \mathbf{B}$ at $x_{i-\frac{1}{2}}, y_{j-\frac{1}{2}}, z_k$, as:

$$\mathbf{F_L} = \mathbf{J} \times \mathbf{B}. \tag{2.39}$$

$\mathbf{J_z} = \frac{\partial B_y}{\partial x} - \frac{\partial B_x}{\partial y}$ is naturally defined at $x_{i-\frac{1}{2}}, y_{j-\frac{1}{2}}, z_k$ and $\mathbf{J_x}$ and $\mathbf{J_y}$ are naturally defined respectively at $x_i, y_{j-\frac{1}{2}}, z_{k-\frac{1}{2}}$ and $x_{i-\frac{1}{2}}, y_j, z_{k-\frac{1}{2}}$. In order to have all three components of $\mathbf{J}$ at the location of the EMF $(x_{i-\frac{1}{2}}, y_{j-\frac{1}{2}}, z_k)$ we need to use the magnetic field components at specific positions, as follows:

$$J_x = \Delta y^{-1}(B_{z;i-\frac{1}{2},j,k} - B_{z;i-\frac{1}{2},j-1,k}) - \Delta z^{-1}(B_{y;i-\frac{1}{2},j-\frac{1}{2},k+\frac{1}{2}} - B_{y;i-\frac{1}{2},j-\frac{1}{2},k-\frac{1}{2}}) \tag{2.40}$$

$$J_y = \Delta z^{-1}(B_{x;i-\frac{1}{2},j-\frac{1}{2},k+\frac{1}{2}} - B_{x;i-\frac{1}{2},j-\frac{1}{2},k-\frac{1}{2}}) - \Delta x^{-1}(B_{z;i,j-\frac{1}{2},k} - B_{z;i-1,j-\frac{1}{2},k}) \tag{2.41}$$

$$J_z = \Delta x^{-1}(B_{y;i,j-\frac{1}{2},k} - B_{y;i-1,j-\frac{1}{2},k})) - \Delta y^{-1}(B_{x;i-\frac{1}{2},j,k} - B_{x;i-\frac{1}{2},j-1,k}). \tag{2.42}$$

As above, we have to express each of these terms through arithmetic averages of the naturally defined components of the magnetic field:

$$B_{x;i-\frac{1}{2},j,k} \quad \text{and} \quad B_{y;i,j-\frac{1}{2},k} \tag{2.43}$$

$$B_{z;i,j-\frac{1}{2},k} \quad \text{and} \quad B_{z;i-\frac{1}{2},j,k} \tag{2.44}$$

$$B_{y,i-\frac{1}{2},j-\frac{1}{2},k-\frac{1}{2}} \quad \text{and} \quad B_{x,i-\frac{1}{2},j-\frac{1}{2},k-\frac{1}{2}}. \tag{2.45}$$

B_x and B_y are naturally defined at $x_{i-\frac{1}{2}}, y_j, z_k$ and $x_i, y_{j-\frac{1}{2}}, z_k$ respectively, and thus the two terms in Equation (2.43) need not to be computed again.

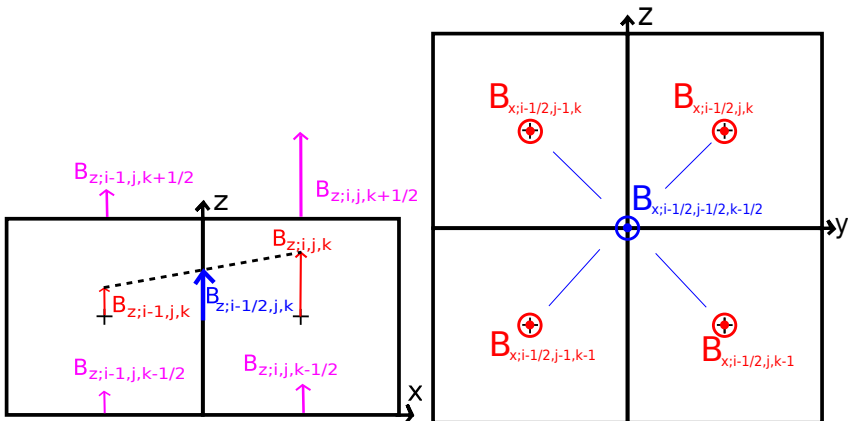

Figure 2.6: Left: $B_{z;i-\frac{1}{2},j,k}$ as an average over surrounding cells. Right: $B_{x,i-\frac{1}{2},j-\frac{1}{2},k-\frac{1}{2}}$.

The terms in Equation (2.44) and Equation (2.45) are obtained thanks to averages on four components (see Figure 2.6):

$$\begin{aligned} B_{z;i-\frac{1}{2},j,k} &= \frac{1}{4}\left[B_{z;i,j,k+\frac{1}{2}} + B_{z;i,j,k-\frac{1}{2}} + B_{z;i-1,j,k+\frac{1}{2}} + B_{z;i-1,j,k-\frac{1}{2}}\right] \\ &= \frac{1}{2}\left[B_{z;i,j,k} + B_{z;i-1,j,k}\right] \qquad (2.46) \\ B_{z;i,j-\frac{1}{2},k} &= \frac{1}{2}\left[B_{z;i,j,k} + B_{z;i,j-1,k}\right] \qquad (2.47) \\ B_{x,i-\frac{1}{2},j-\frac{1}{2},k-\frac{1}{2}} &= \frac{1}{4}\left[B_{x;i-\frac{1}{2},j,k} + B_{x;i-\frac{1}{2},j-1,k} + B_{x;i-\frac{1}{2},j,k-1} + B_{x;i-\frac{1}{2},j-1,k-1}\right] \qquad (2.48) \\ B_{y,i-\frac{1}{2},j-\frac{1}{2},k-\frac{1}{2}} &= \frac{1}{4}\left[B_{y;i,j-\frac{1}{2},k} + B_{y;i-1,j-\frac{1}{2},k} + B_{y;i,j-\frac{1}{2},k-1} + B_{y;i-1,j-\frac{1}{2},k-1}\right]. \qquad (2.49) \end{aligned}$$

The Lorentz force for the other components of the EMF (x and y directions) are obtained through circular permutations.

The Lorentz force as the divergence of a flux Another way to compute the Lorentz force is to express it as the divergence of a well chosen flux:

$$\mathbf{F_L} = (\nabla \cdot \mathcal{F}_\mathbf{i})\mathbf{e_i}, \qquad (2.50)$$

and

$$\mathcal{F}_\mathbf{i} = B_i B_j \mathbf{e_j} - \delta_{ij} e_{\text{mag}} \mathbf{e_j}, \qquad (2.51)$$

with $i, j \in [x, y, z]$ and $e_{\text{mag}} = \frac{1}{2}(B_x^2 + B_y^2 + B_z^2)$.

Let us focus on the x component of the Lorentz force for the EMF in the z direction. It reads:

$$\mathbf{F_L} \cdot \mathbf{e_x} = \partial_x(B_x^2 - e_{\text{mag}}) + \partial_y(B_x B_y) + \partial_z(B_x B_z). \qquad (2.52)$$

In order to compute the Lorentz force at $x_{i-\frac{1}{2}}, y_{j-\frac{1}{2}}, z_k$, we compute each term at specific posi-

tions:

$$\begin{aligned}\partial_x(B_x^2 - e_{\rm mag}) = \frac{1}{2\Delta x}\big[&(B^2_{x;i,j-\frac{1}{2},k} - B^2_{x;i-1,j-\frac{1}{2},k})\\ &-(B^2_{y;i,j-\frac{1}{2},k} - B^2_{y;i-1,j-\frac{1}{2},k})\\ &-(B^2_{z;i,j-\frac{1}{2},k} - B^2_{z;i-1,j-\frac{1}{2},k})\big]\end{aligned} \tag{2.53}$$

$$\partial_y(B_xB_y) = \frac{1}{\Delta y}\big[B_{x,i-\frac{1}{2},j,k}B_{y,i-\frac{1}{2},j,k} - B_{x,i-\frac{1}{2},j-1,k}B_{y,i-\frac{1}{2},j-1,k}\big] \tag{2.54}$$

$$\partial_z(B_xB_z) = \frac{1}{\Delta z}\big[B_{x,i-\frac{1}{2},j-\frac{1}{2},k+\frac{1}{2}}B_{z,i-\frac{1}{2},j-\frac{1}{2},k+\frac{1}{2}} - B_{x,i-\frac{1}{2},j-\frac{1}{2},k-\frac{1}{2}}B_{z,i-\frac{1}{2},j-\frac{1}{2},k-\frac{1}{2}}\big]. \tag{2.55}$$

We then only need to compute each component of the magnetic field at $x_{i-\frac{1}{2}}, y_{j-\frac{1}{2}}, z_k$ in order to get the EMF in the z direction.

As explained in the previous paragraph, an average over well chosen (where the magnetic field is naturally defined) surrounding cells is used (see Figures 2.5 and 2.7):

$$B_{x;i,j-\frac{1}{2},k} = \frac{1}{2}\big[B_{x;i,j,k} + B_{x;i,j-1,k}\big] \tag{2.56}$$

$$B_{z;i,j-\frac{1}{2},k} = \frac{1}{2}\big[B_{z;i,j,k} + B_{z;i,j-1,k}\big] \tag{2.57}$$

$$B_{y;i-\frac{1}{2},j,k} = \frac{1}{2}\big[B_{y;i,j,k} + B_{y;i-1,j,k}\big] \tag{2.58}$$

$$\begin{aligned}B_{x,i-\frac{1}{2},j-\frac{1}{2},k-\frac{1}{2}} = \frac{1}{4}[&B_{x;i-\frac{1}{2},j,k} + B_{x;i-\frac{1}{2},j-1,k}\\ &+ B_{x;i-\frac{1}{2},j,k-1} + B_{x;i-\frac{1}{2},j-1,k-1}]\end{aligned} \tag{2.59}$$

$$\begin{aligned}B_{z,i-\frac{1}{2},j-\frac{1}{2},k-\frac{1}{2}} = \frac{1}{4}[&B_{z;i,j,k-\frac{1}{2}} + B_{z;i,j-1,k-\frac{1}{2}}\\ &+ B_{z;i-1,j,k-\frac{1}{2}} + B_{z;i-1,j-1,k-\frac{1}{2}}],\end{aligned} \tag{2.60}$$

and

$$B_{x;i-\frac{1}{2},j-\frac{1}{2},k} = \frac{1}{2}\big[B_{x;i-\frac{1}{2},j,k} + B_{x;i-\frac{1}{2},j-1,k}\big] \tag{2.61}$$

$$B_{y;i-\frac{1}{2},j-\frac{1}{2},k} = \frac{1}{2}\big[B_{y;i,j-\frac{1}{2},k} + B_{y;i-1,j-\frac{1}{2},k}\big] \tag{2.62}$$

$$\begin{aligned}B_{z;i-\frac{1}{2},j-\frac{1}{2},k} = \frac{1}{4}\Big[&\frac{1}{2}(B_{z;i,j,k-\frac{1}{2}} + B_{z;i,j-1,k-\frac{1}{2}})\\ &+ \frac{1}{2}(B_{z;i-1,j,k-\frac{1}{2}} + B_{z;i-1,j-1,k-\frac{1}{2}})\\ &+ \frac{1}{2}(B_{z;i,j,k+\frac{1}{2}} + B_{z;i,j-1,k+\frac{1}{2}})\\ &+ \frac{1}{2}(B_{z;i-1,j,k+\frac{1}{2}} + B_{z;i-1,j-1,k+\frac{1}{2}})\Big]\\ = \frac{1}{4}[&B_{z;i,j,k} + B_{z;i,j-1,k}\\ &+ B_{z;i-1,j,k} + B_{z;i-1,j-1,k}].\end{aligned} \tag{2.63}$$

Again and as highlighted previously, in order to get the two other components of the EMF one only needs to perform circular permutations.

These two methods (described in subsections 2.2.1.2 and 2.2.1.2) to compute the Lorentz force are implemented in `RAMSES` and show similar performances. This method might work better under

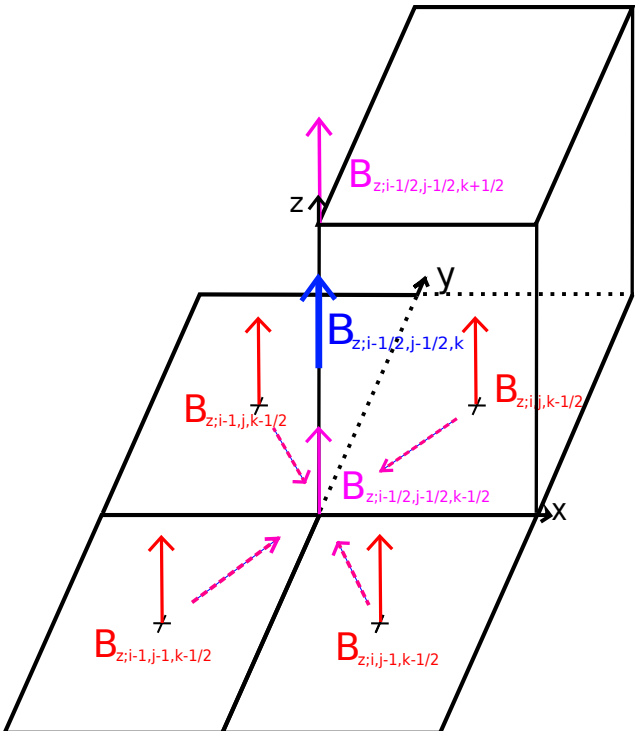

Figure 2.7: Computation of $B_{z;i-\frac{1}{2},j-\frac{1}{2},k}$ as an average over eight naturally defined magnetic components.

certain conditions, for a particular setup of the magnetic field lines. Nonetheless, when counting the number of floating point operations, the computer performs using this method 4911 more additions and 8047 more multiplications for a given cell than with the previously described method.

Contribution of ambipolar diffusion to the energy flux The ambipolar energy flux (see Equation 2.64) has to be evaluated on each face of the cell, that is to say at locations $(x_{i\pm\frac{1}{2}}, y_j, z_k)$, $(x_i, y_{j\pm\frac{1}{2}}, z_k)$ and $(x_i, y_j, z_{k\pm\frac{1}{2}})$. Again, as in § 2.2.1.2, the needed components are obtained thanks to averages over neighbouring cells (averages which are not detailed here).

$$\mathcal{F}_{\mathbf{AD}} = -\mathbf{E_{AD}} \times \mathbf{B} = -\frac{1}{\gamma_{AD}\rho_i\rho} ((\mathbf{J} \times \mathbf{B}) \times \mathbf{B}) \times \mathbf{B}. \tag{2.64}$$

Computation of the time step in presence of ambipolar diffusion The ambipolar diffusion timescale can be estimated through the drift velocity of ions. Recalling Equation (2.29) we get:

$$\begin{aligned} \|\mathbf{v}_{\text{drift}}\| &\propto \frac{1}{\gamma_{AD}\rho\rho_i}\|\mathbf{F_L}\| \\ &\propto \frac{v_A^2}{\gamma_{AD}\rho_i L_{AD}}, \end{aligned} \tag{2.65}$$

where L_{AD} is a characteristic length for ambipolar diffusion, which can be estimated as $L_{AD}^{-1} = \frac{\nabla(\|B\|)}{\|B\|}$. We then have the timescale:

$$\tau_{AD} = \frac{L_{AD}}{\|\mathbf{v}_{\text{drift}}\|} = \frac{\gamma_{AD}\rho_i L_{AD}^2}{v_A^2}. \tag{2.66}$$

Written as a diffusion, $\tau_{AD} = \frac{L_{AD}^2}{D}$ with the ambipolar diffusion coefficient $D = \frac{v_A^2}{\gamma_{AD}\rho_i}$, where $\mathbf{v_A} = \frac{\mathbf{B}}{\sqrt{\rho}}$ is the Alfvén speed and $(\gamma_{AD}\rho_i)^{-1}$ is the characteristic collision time between ions and neutrals. A Von Neumann analysis for the diffusion part of the equation can be performed for the scheme used:

$$\frac{\partial \mathbf{B}}{\partial t} - \nabla \times \mathbf{E}_{AD} = 0. \tag{2.67}$$

It can be differenced (in one dimension):

$$\frac{B^{n+1}_{x;i-\frac{1}{2},j,k} - B^{n}_{x;i-\frac{1}{2},j;k}}{\Delta t} = D\frac{\Delta t}{\Delta x^2}(B^n_{x;i-\frac{1}{2},j+1,k} - 2B^n_{x;i-\frac{1}{2},j,k} + B^n_{x;i-\frac{1}{2},j-1,k}). \tag{2.68}$$

Using $B^n_j = \epsilon^n e^{ikjh}$,

$$\epsilon = 1 + 2\frac{D\Delta t}{\Delta x^2}(\cos(kh) - 1). \tag{2.69}$$

Equation (2.69) shows that the scheme is stable according to Von Neumann stability analysis provided the coefficient is lower than 0.5:

$$|\epsilon| < 1 \Leftrightarrow \Delta t < \frac{1}{2}\frac{\Delta x^2}{D} = \frac{1}{2}\frac{\Delta x^2 \gamma_{AD}\rho_i \rho}{B^2}. \tag{2.70}$$

For the three dimensional case, this time-step constraint is more stringent than for the one dimensional case presented above.

Therefore, the time step used to update the solution is computed by taking the minimum of the usual MHD Courant condition (Fromang et al. (2006)) and the ambipolar timestep defined by

$$t_{AD} = 0.1 \times \min(\frac{\gamma_{AD}\,\rho_i}{v_A^2}\,\Delta x^2), \tag{2.71}$$

where the minimum is taken over all the cells of the computational grid. The coefficient $0.1 < \frac{1}{2}$ is taken to achieve better convergence. This choice is based on the various tests performed, and might not be suited to all other problems. As can be noted in equation (2.71), the time-step scales as Δx^2. Even though this is very demanding in terms of numerical resources as the grid becomes more and more refined, there are means to speed-up the calculations, as explained in the following paragraph.

The ambipolar time step is proportional to ρ_i (see Equation (2.71)), which is assumed to be proportional to ρ^k: $\rho_i = C\sqrt{\rho}$ (see Elmegreen (1979)). Both the factor (C) and the power law ($\rho^{\frac{1}{2}}$) are very dependent on the microphysics and the geometry of the grains. This assumption is thus made for the sake of simplicity, but might not always be valid. In some cases, for example in star formation simulations, the time-step can become unphysically small in very diffuse regions where the ionisation approximated as above (Equation (2.71)) is very small. Following Nakamura and Li (2008), we use a threshold in order to limit the time-step when needed. On the other hand, in very dense parts where the grid is fairly refined (where Δx is small), the dependence of ρ_i and γ_{AD} with the density prevent the time-step from becoming too small.

2.2.1.3 The AMR scheme

The AMR algorithm used in `RAMSES` is described in Teyssier (2002), and its extension to MHD is first described in Teyssier et al. (2006) and then in Fromang et al. (2006). We briefly recall the main features here. It is a tree-based AMR code whose data structure is a 'Fully Threaded Tree" (Khokhlov (1998)). The grid is divided into "octs" which are groups of 8 cells with the same parent cell. The first

level of refinement ($l = 1$) corresponds to the unit cube, which defines the computational domain. The grid is recursively refined from the $l = 1$ to the minimum level of refinement l_{min}, in order to build the base Cartesian grid. Adaptive refinement then proceeds from this coarse grid up to the user-defined maximum level of refinement l_{max}. When $l_{max} = l_{min}$ the computational grid is a traditional Cartesian grid. Issues arise when refined cells are created, in the case where $l_{max} > l_{min}$. Concerning the non-ideal MHD, the EMF and energy fluxes are simply added to the existing ideal MHD EMF and fluxes. As a consequence, there are no more complications in refining and derefining cells than in the ideal MHD case.

Divergence-free prolongation operator: refining cells The "prolongation operator" is the creation of a new "oct" of 8 cells when a cell is newly refined. Cell-centered variables and magnetic field components are needed for each refined cell. This is usually done using a conservative interpolation of the variables, yet in the case of magnetic fields, the divergence-free constraint has to be fulfilled by each of the new cells which makes things more complicated in details. A critical step has been solved by Balsara (2001) and Toth and Roe (2002) in the constrained transport framework. The idea developed in those articles is to use slope limiters to interpolate the magnetic field components in each parent face conserving the flux, and then to perform a three dimensional (which is divergence-free inside the cell volume) reconstruction in order to compute the new magnetic field components for each children faces. The same slope limiters as the ones used in the Godunov scheme for the hydrodynamics are used in this step.

Magnetic flux corrections: derefining cells The "Restriction Operator" is, in the multigrid terminology, the operation of derefining a split cell. The divergence-free constraint still needs to be satisfied, so that the magnetic field components in the coarse faces are simply the arithmetic averages of the four fine faces values. This is the parallel in MHD of the "flux correction step" for the Euler system.

EMF corrections This is specific to the induction equation: for a coarse face adjacent to a refined face, the coarse EMF in the conservative update of the solution needs to be replaced by the arithmetic average of the two fine EMF vectors. This is mandatory to guarantee that the magnetic field remains divergence-free even at coarse/fine boundaries.

2.2.1.4 Tests for the ambipolar diffusion

The Barenblatt diffusion test In this subsection, we first test the accuracy of the calculation of the ambipolar term alone. For sake of simplicity, we assume that the magnetic field has the form $B_y(x, z)$, with $B_x = 0$ and $B_z = 0$, that all the velocities remain equal to zero and that density and thermal pressure are constant. The induction equation takes the form of a diffusion equation:

$$\frac{\partial B_y}{\partial t} = \frac{\partial}{\partial x}\Big(\frac{B_y^2}{\gamma_{AD}\rho_i\rho}\frac{\partial}{\partial x}(B_y)\Big) + \frac{\partial}{\partial z}\Big(\frac{B_y^2}{\gamma_{AD}\rho_i\rho}\frac{\partial}{\partial z}(B_y)\Big), \tag{2.72}$$

which can also be written in compact form:

$$\frac{\partial B_y}{\partial t} = \nabla.\Big(\frac{v_A^2}{\gamma_{AD}\rho_i}\nabla B_y\Big). \tag{2.73}$$

This is a non-linear diffusion equation, since the diffusion coefficient, $\eta_{AD} = \frac{v_A^2}{\gamma_{AD}\rho_i}$, depends non-linearly on the magnetic field. Here, $v_A = B_y/\sqrt{\rho}$ denotes the y-component of the Alfvén velocity. The solution of this problem with a Dirac pulse as initial condition (known as the Barenblatt-Pattle

Variable	ρ	v_x	v_y	B_x	B_y	P
Pre-shock value	0.5	5	0	$\sqrt{2}$	$\sqrt{2}$	0.125
Post-shock value (isothermal)	1.0727	2.3305	1.3953	$\sqrt{2}$	3.8809	0.2681
Post-shock value (non-isothermal)	0.9880	2.5303	1.1415	$\sqrt{2}$	3.4327	1.4075

Table 2.1: Initial conditions used for the oblique C-shock test, as described in subsection 2.2.1.4.

solutions) has been derived by Grundy and McLaughlin (1982) (See Appendix 2.A for more details about the analytical solution).

The initial states in one and two dimensions are respectively:

$$B_{y0} = \begin{cases} 1 & \text{if } \|x - x_{center}\| \leq 0.9\,\Delta x_{level=3} \\ 0 & \text{elsewhere} \end{cases} \tag{2.74}$$

$$B_{y0} = \begin{cases} 1 & \text{if } \sqrt{(x - x_{center})^2 + (z - z_{center})^2} \leq 0.9\,\Delta x_{level=3} \\ 0 & \text{elsewhere.} \end{cases} \tag{2.75}$$

with $\Delta x_{level=3}$ being the cell size at the lowest level of refinement used (in this case: 3). This ensures that the initial perturbation is the same for the case of an AMR grid and a fully refined grid.

We performed the test both with a uniform grid and using the AMR with the same maximum level. The level of refinement refers to the number of cells used: 2^{ND} cells are used for the level of refinement N in a D-dimensional calculation. As seen in the figures, the agreement between the numerical and the analytical curves is excellent, a few tenths of a percent on average. The results obtained on an AMR grid (with levels varying from 3 to 7, corresponding to a mesh size $\Delta x = 0.5^3$ and $\Delta x = 0.5^7$) are almost as good as the ones obtained on a regular grid corresponding to the highest level of refinement (level 7, with a cell size $\Delta x = 0.5^7$ and 128 cells): the maximum relative error is less than one percent except where the magnetic field equals zero. The difference between AMR and uniform grid is less than 2.10^{-4} for values of magnetic field of about 0.01.

The results for $B_y(x)$ are shown on Figure 2.8, where we have taken $\gamma_{AD} = 1$, $\rho_i = 1$ and $\rho = 1$ and on Figure 2.9 for $B_y(x, z)$.

The grid is refined if the gradient of magnetic field is greater than 0.1 (this insures for this test that the error on the AMR grid and on the regular grid are about the same). We also checked that the same accuracy is obtained for any orientation of the magnetic field (using Bx or Bz instead of By). Figure 2.10 represents the evolution of the error calculated as $\epsilon = \sqrt{\sum_{i=1}^{N} \frac{(By_{\text{numerical}} - By_{\text{analytical}})^2}{N}}$ as function of the mesh size (N being the number of cells for each level).

In terms of computational time for this particular test using the refinement strategy described above, the time is about the same for a regular grid at level 7 as for a grid going from levels 5 to 7, but there is a gain of about 40% in the number of cells. One level further (regular grid at level 8 or AMR grid going from levels 5 to 8) the computation is 30% faster in the AMR case and needs 55% less cells. For a regular grid at level 9 or an AMR grid going from levels 5 to 9 the calculation is 60% faster with 70% less cells needed.

The C-shock test Following Duffin and Pudritz (2008) and Mac Low et al. (1995), we have tested our new scheme for the case of both isothermal and non-isothermal oblique C-shock including ambipolar heating as given by Equation (2.22). We start from a steep function as initial state for the different variables, whose values are the ones taken at infinity ahead of and behind the shock. Our calculation takes place in the frame of the shock. The post- and pre-shock values are displayed in Table 2.1. The angle between the shock normal and the magnetic field is set to 45°.

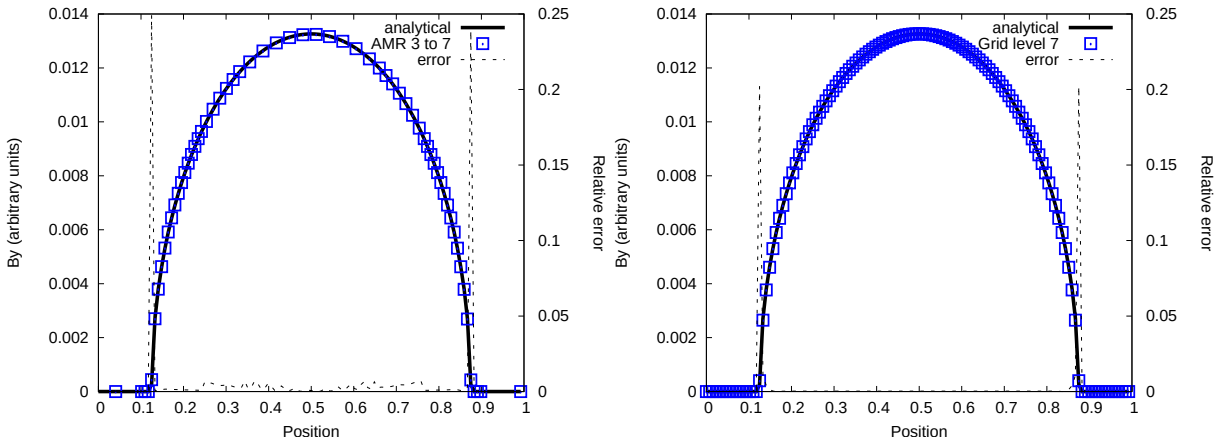

Figure 2.8: Barenblatt diffusion test for ambipolar diffusion at $t = 200$ with B_y being a function of x only. The left panel is a snapshot of the AMR run with levels from 3 to 7. The right panel corresponds to a fully refined Cartesian grid up to level 7.

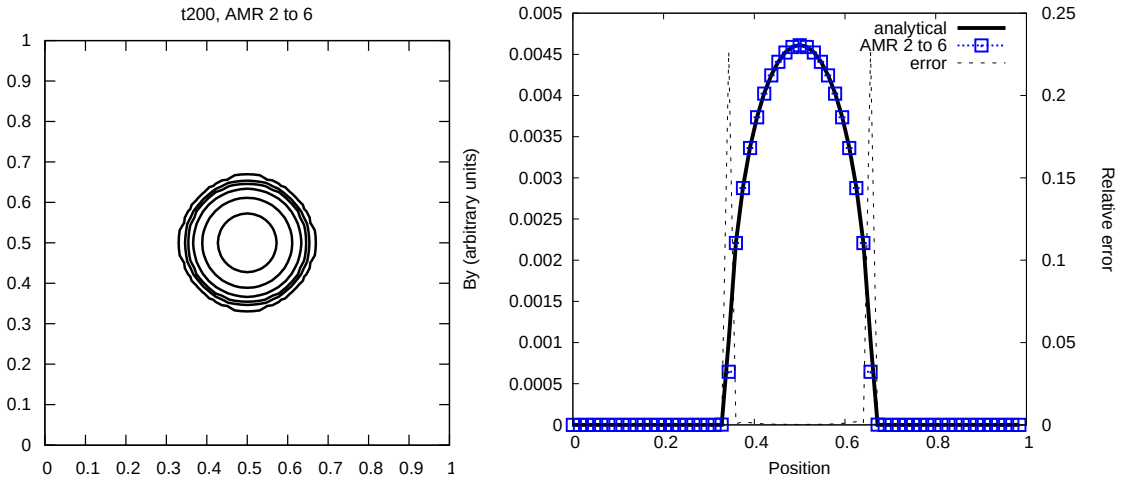

Figure 2.9: Barenblatt diffusion test in 2D with B_y depending on x and z. Here, the calculation was performed on an AMR grid from level 2 to 6. The left snapshot is a 2D contour plot at $t = 200$: the symmetry of the solution is preserved. The right snapshot (same legend as in Figure 2.8) is a 1D cut across the maximum at $t = 200$.

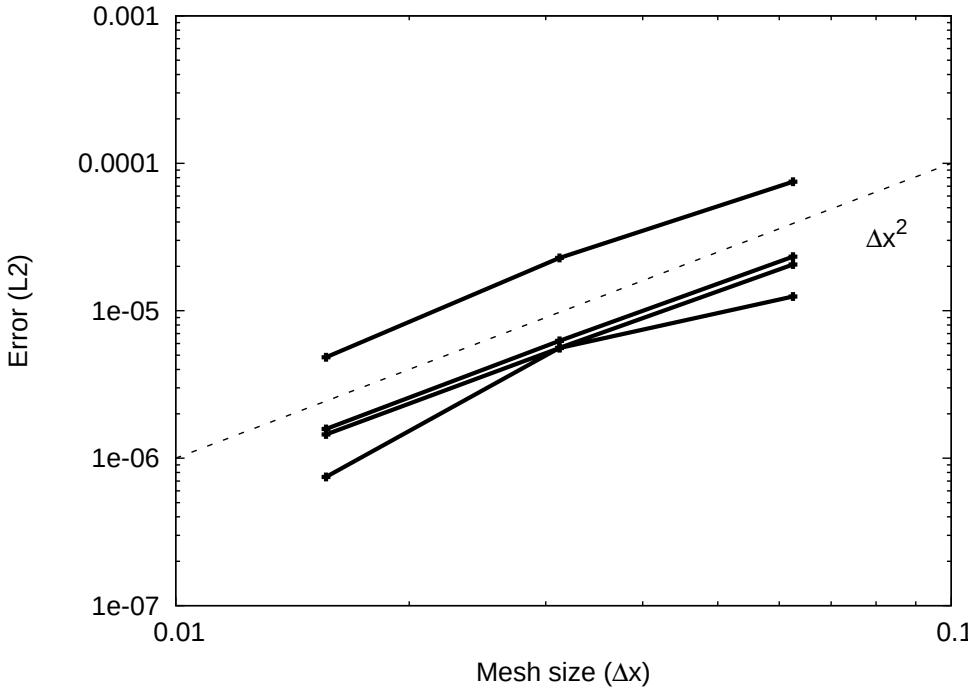

Figure 2.10: Evolution of the error for the Barenblatt test for several times, taking the error as $\epsilon = \sqrt{\sum_{i=1}^{N} \frac{(By_{\text{numerical}} - By_{\text{analytical}})^2}{N}}$, with N the number of cells. The dashed line corresponds to $\epsilon \propto \Delta x^2$.

For this test, we set $\gamma_{AD} = 75$, $\rho_i = 1$. The sonic Mach number is $\mathcal{M} = 10$ and the Alfvén Mach number is $\mathcal{M}_A = 1.8$. Outflow boundary conditions are used in the simulation. After a short transient phase, the shock becomes stationary.

The isothermal shock is modeled through $P_n = \rho_n c_s^2$ with $c_s = 0.5$ the sound speed, and without solving the energy Equation (2.22). Results are shown in Figure 2.11 and compared to the semi-analytical solution described in Mac Low et al. (1995) (see Appendix 2.B for more details).

For the non-isothermal case the energy Equation (2.22) is solved assuming a perfect gas with an adiabatic index $\gamma = \frac{5}{3}$ and without any additional cooling. The semi-analytical set of equations to be solved is derived from Duffin and Pudritz (2008), where we assume a constant ion density (see Appendix 2.C for more details). The steady-state is not very different from the isothermal case, except for the pressure. The results for the non-isothermal case are shown Figure 2.12. Our results are significantly different from Duffin and Pudritz (2008) in the pressure across the shock. This is explained by the additional heating term (and an artificial cooling term necessary for the equations to converge) in their set of equations. Therefore the equations tested are not exactly the same and thus neither are the semi-analytical solution nor the results.

In astrophysical simulations solving *non-isothermal* ambipolar diffusion only makes sense if cooling or heating of the gas is properly taken into account, i.e. if radiative transfer is solved. Otherwise, the set of MHD Equations ((2.20), (2.21), (2.23) and (2.24)) is closed by an equation of state (a barotropic one in most cases).

We also checked that the results are similar for any orientation of the initial magnetic field and velocity field. Using AMR gives results almost as good as with a regular grid corresponding to the highest level of refinement (not displayed here for conciseness).

The grid is refined if the gradient of magnetic field, pressure, density or velocity is greater than 0.1 (this insures for this test that the error on the AMR grid and on the regular grid are about the

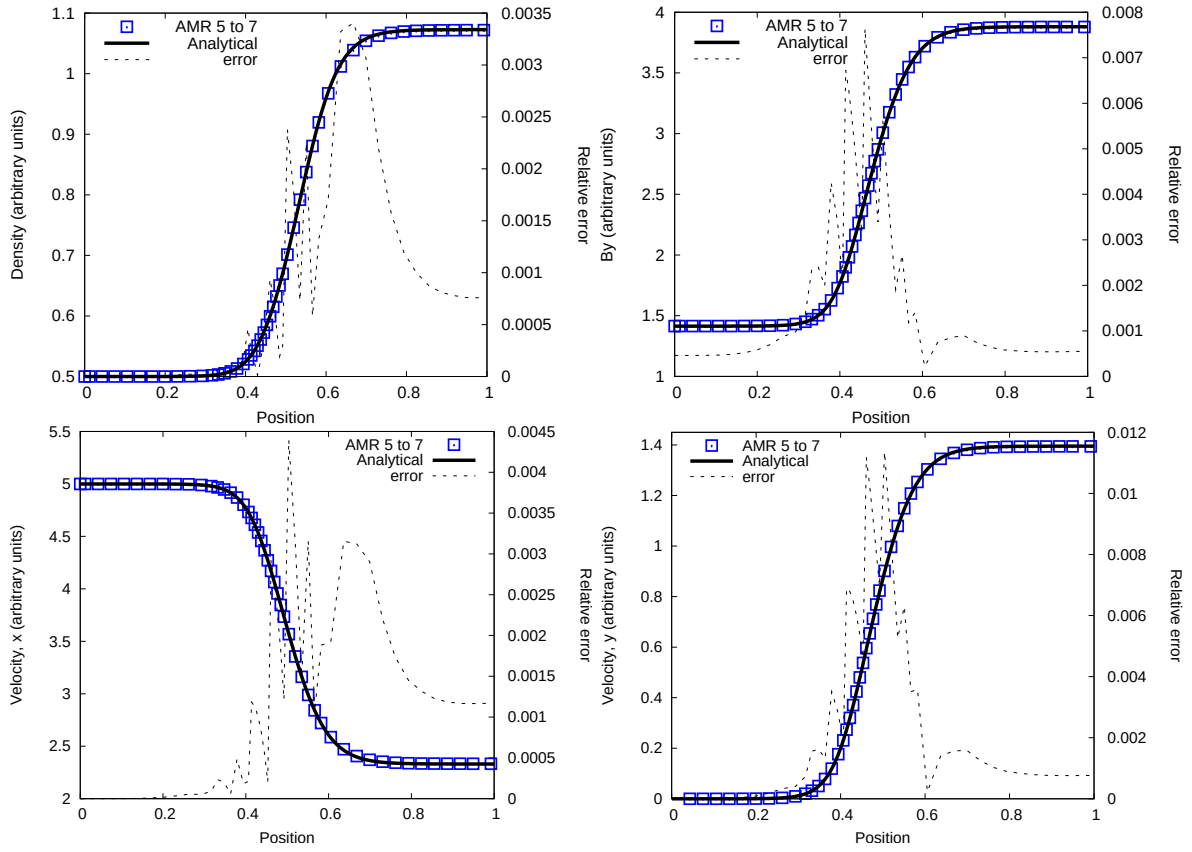

Figure 2.11: Isothermal oblique shock with ambipolar diffusion. Lines and symbols are the same as in Figure 2.8. The levels of refinement vary from 5 to 7.

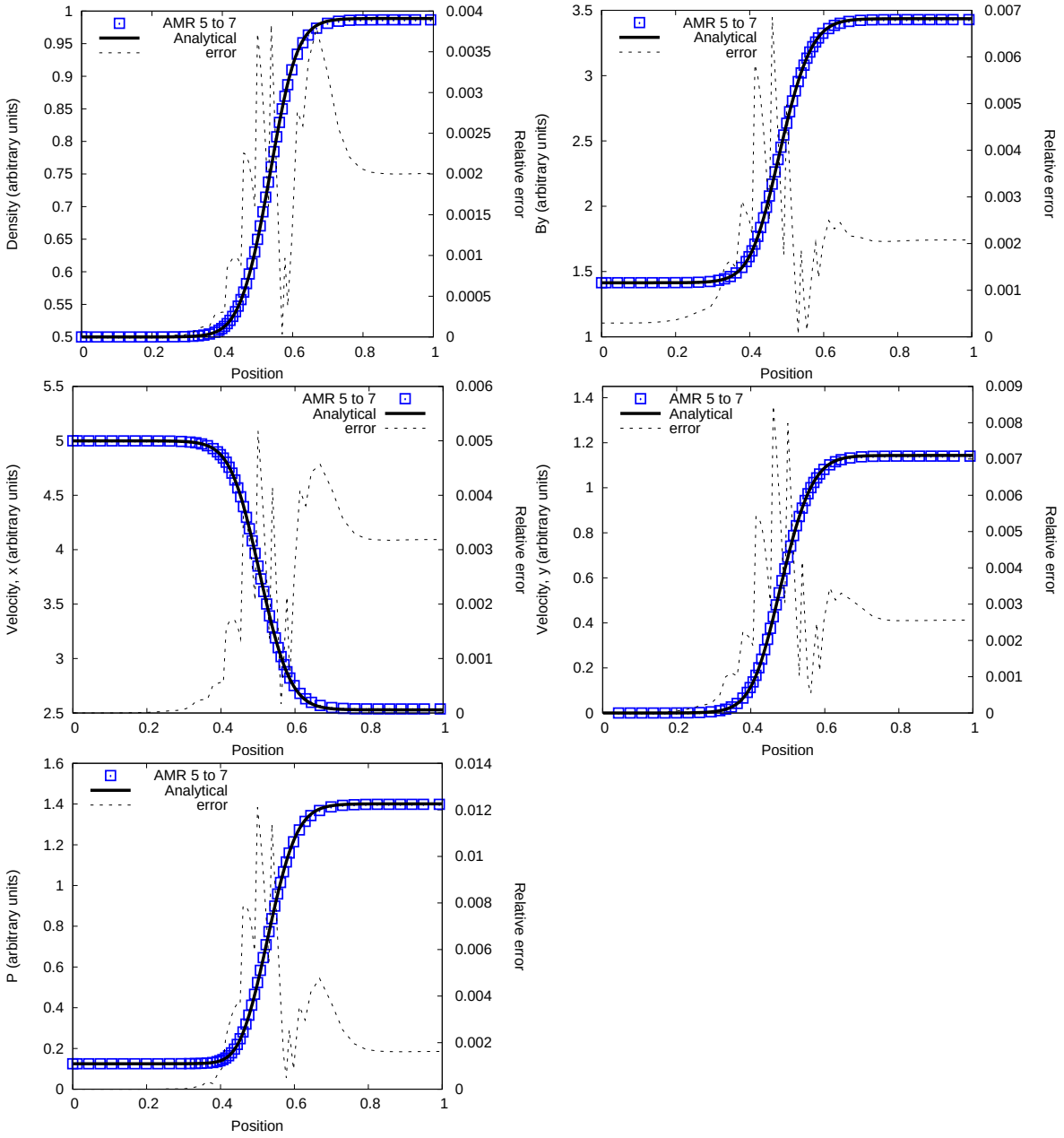

Figure 2.12: Non-isothermal oblique shock with ambipolar diffusion. Lines and symbols are the same as in Figure 2.8. The levels of refinement vary from 5 to 7.

same).

The Alfvén wave test Studying the decay of Alfvén waves in an ionized plasma provides a stringent test of the coupling between the flow and the magnetic field due to ambipolar diffusion. Following Choi et al. (2009), we have examined the behaviour of propagating and standing Alfvén waves in such a plasma. We closely follow the prescription and the notations defined by Lesaffre and Balbus (2007) for the study of Alfvén waves in a plasma with Ohmic diffusion, and adapt them to the ambipolar diffusion case. Here we derive exact solutions for torsional Alfvén waves in a non-isothermal plasma with ambipolar diffusion.

The unperturbed state without Alfvén waves is defined as:

$$\begin{aligned} \rho_0 = 1, \rho_{0n} &= 1, \rho_{0i} = 1 \\ V_{0x} = 0, V_{0y} &= 0, V_{0z} = 0 \\ B_{0x} = 0, B_{0y} &= 0, B_{0z} = 1. \end{aligned} \tag{2.76}$$

We seek for perturbed solutions of the form

$$\mathbf{u} = \delta\mathbf{u} \exp(st + ikz) \tag{2.77}$$

$$\text{and} \quad \mathbf{B} = B_0\hat{\mathbf{z}} + \mathbf{b} = B_0\hat{\mathbf{z}} + \delta\mathbf{b} \exp(st + ikz), \tag{2.78}$$

where $\delta\mathbf{b} = \delta b_x\,\hat{\mathbf{x}} + \delta b_y\,\hat{\mathbf{y}}$ and $\delta\mathbf{u} = \delta u_x\,\hat{\mathbf{x}} + \delta u_y\,\hat{\mathbf{y}}$. s is the wave angular frequency and k the wave number. For a perturbation wavelength λ along the z direction, the wave vector k is set to $k = 2\pi/\lambda$. For such solutions, the mass density remains constant along the wave trajectory ($\rho \equiv \rho_0$).

Following Lesaffre and Balbus (2007), we restrict ourselves to MHD flows satisfying $\nabla(P+\frac{1}{2}B^2) \equiv \mathbf{0}$, so that the momentum equation reads:

$$\partial_t\mathbf{u} = \frac{B_0}{\rho_0}\partial_z\mathbf{b} \tag{2.79}$$

and the induction equation simplifies to:

$$\partial_t\mathbf{b} = B_0\partial_z\mathbf{u} + \frac{B_0^2}{\gamma_{AD}\rho_{i0}\rho_0}\partial_z^2\mathbf{b}. \tag{2.80}$$

Combining Equation (2.79) and Equation (2.80) gives a quadratic dispersion relation:

$$s^2 + k^2\eta_{AD}s + k^2v_A^2 = 0, \tag{2.81}$$

where the ambipolar diffusion coefficient is defined by $\eta_{AD} = v_A^2/\gamma_{AD}\rho_{i0}$ and the Alfvén velocity by $v_A = B_0/\sqrt{\rho_0}$. This equation is similar to the dispersion relation obtained by Balsara (1996), but we have derived it for the more general adiabatic, non-isothermal case, and also for any amplitude in $|\delta\mathbf{b}|$, provided that $\nabla(P + \frac{1}{2}B^2) \equiv \mathbf{0}$. If we restrict ourselves to circularly polarized waves with e.g., $\delta b_y = i\delta b_x$ then $\nabla(\frac{1}{2}B^2) \equiv \mathbf{0}$ will also ensure $\nabla(P) \equiv \mathbf{0}$ as we now demonstrate.

It is clear from Equation (2.81) that Alfvén waves propagate ($s_i \neq 0$, with s_i the imaginary part of s) only for $v_A > k\eta_{AD}/2$. The solutions of Equation (2.81) are given by:

$$s = -\frac{k^2\eta_{AD}}{2} \pm i\sqrt{k^2v_A^2 - \left(\frac{k^2\eta_{AD}}{2}\right)^2}. \tag{2.82}$$

In the numerical tests that follow, we restrict ourselves to $\lambda = 1$ and equal to the box size, so that $k = 2\pi$. We will explore first a value $\gamma_{AD} = 80$, yielding a diffusion coefficient $\eta_{AD} = 1.25 \times 10^{-2}$, and resulting in a moderate damping with imaginary part $s_i = \pm 6.2783387$ and real part $s_r = -0.2467401$. We then consider the case $\gamma_{AD} = 30$ ($\eta_{AD} = 0.0333$), resulting in a stronger damping with $s_i = \pm 6.2486389$ and $s_r = -0.6579736$.

Estimating numerical diffusion In order to estimate the quality of our numerical solution we need to compute the leading order error term in the ideal MHD scheme. This is done usually using the Modified Equation approach where a Taylor expansion of the numerical solution is performed. We restrict our analysis to the propagation of Alfvén waves since the Modified Equation is much simpler to handle in this case. We use the characteristic variable $\alpha^{\pm} = \mathbf{u} \mp \mathbf{b}/\sqrt{\rho_0}$, so that the system describing the propagation of Alfvén waves becomes

$$\partial_t \alpha^{\pm} \pm v_A \partial_z \alpha^{\pm} = 0. \tag{2.83}$$

We consider here only the right-propagating wave, dropping the superscript $+$. The conservative update writes

$$\frac{\alpha_i^{n+1} - \alpha_i^n}{\Delta t} + v_A \frac{\alpha_{i+\frac{1}{2}}^{n+\frac{1}{2}} - \alpha_{i-\frac{1}{2}}^{n+\frac{1}{2}}}{\Delta z} = 0. \tag{2.84}$$

Since the Riemann solver accounts for Alfvén waves, the interface flux is given by the upwind value, solution of the predictor step.

$$\alpha_{i+\frac{1}{2}}^{n+\frac{1}{2}} = \alpha_i^n + (\partial_z \alpha)_i^n \frac{\Delta z}{2}. \tag{2.85}$$

This entirely defines our second-order accurate numerical solution. We assumed here that the time-step is much smaller than the Courant time step, so that $v_A \Delta t/\Delta z \ll 1$. Taylor expanding the solution and its spatial derivative to the first non vanishing order in respect to α_i^n leads to the following Modified Equation with a second-order leading error term

$$\partial_t \alpha + v_A \partial_z \alpha \simeq \frac{v_A \Delta z^2}{12} \partial_z^3 \alpha \simeq \eta_{num} \partial_z^2 \alpha. \tag{2.86}$$

The right-hand-side represents a third-order derivative of the solution, usually interpreted as a dispersive term. We nevertheless restrict ourselves to the test case studied in this paper, namely a sinusoidal wave of period equal to the box size L, and approximate the leading-order term as a diffusive term with numerical diffusion coefficient, namely:

$$\eta_{num} = \frac{2\pi v_A \Delta z^2}{12L}. \tag{2.87}$$

From this analysis, we can estimate the amplitude of the diffusion due to the hyperbolic solver that needs to be added to the physical (whether ambipolar or Ohmic) diffusion to interpret the numerical solution. We also conclude that the leading order term coming from the ideal MHD solver scales as Δx^2. This sets the physical range of ambipolar and Ohmic diffusion one can expect to explore for a given mesh resolution. For a mesh of 16^3 cells the numerical diffusivity is six times smaller than the ambipolar diffusion with $\gamma_{AD} = 80$: $\eta_{num} = 0.002$ and $\eta_{AD} = 0.0125$. This is a good test case in order to assess the accuracy of the correction: the dominant term is still coming from the physics, but the numerical contribution is not negligible.

For Alfvén standing waves, the same study can be done. Considering two waves: α^+ and α^-, one propagating to the right and the other to the left. The system describing the standing Alfvén waves is

$$\partial_t \alpha^+ + v_A \partial_z \alpha^+ + \partial_t \alpha^- - v_A \partial_z \alpha^- = 0. \tag{2.88}$$

The interface flux are given by the upwind value for α^+

$$\alpha_{i+\frac{1}{2}}^{n+\frac{1}{2}} = \alpha_i^n + (\partial_z \alpha)_i^n \frac{\Delta z}{2} \tag{2.89}$$

$$\alpha_{i-\frac{1}{2}}^{n+\frac{1}{2}} = \alpha_{i-1}^n + (\partial_z \alpha)_{i-1}^n \frac{\Delta z}{2}, \tag{2.90}$$

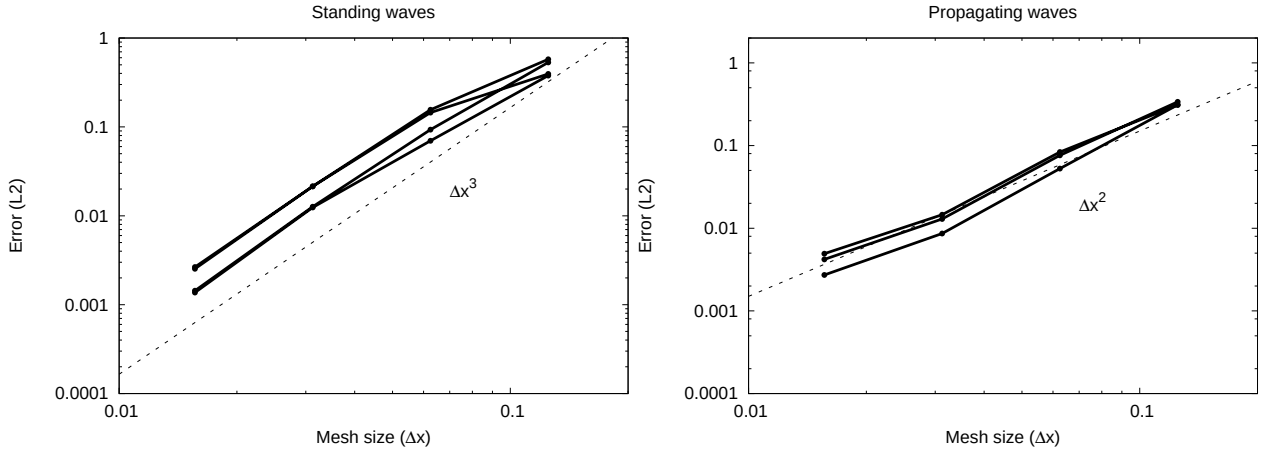

Figure 2.13: Evolution of the error $\epsilon = \sqrt{\sum_{i=1}^{N} \frac{(By_{\text{numerical}} - By_{\text{analytical}})^2}{N}}$ with the mesh size Δx for Alfvén standing waves (left plot) and Alfvén propagating waves (right plot) at different times. The dashed lines correspond to two slopes: $\epsilon \propto \Delta x^3$ for the standing waves and $\epsilon \propto \Delta x^2$ for the propagating waves.

and the downwind value for α^-

$$\alpha_{i+\frac{1}{2}}^{n+\frac{1}{2}} = \alpha_{i+1}^{n} - (\partial_z \alpha)_{i+1}^{n} \frac{\Delta z}{2} \tag{2.91}$$

$$\alpha_{i-\frac{1}{2}}^{n+\frac{1}{2}} = \alpha_{i}^{n} - (\partial_z \alpha)_{i}^{n} \frac{\Delta z}{2}, \tag{2.92}$$

where we then express each term (values and spatial derivatives) in terms of α_i^n, using a third order Taylor expansion in Δz.

We then obtain for the two propagating waves:

$$\partial_t \alpha^+ + v_A \partial_z \alpha^+ \simeq + \frac{v_A \Delta z^2}{12} \partial_z^3 \alpha^+ - \frac{v_A \Delta z^3}{48} \partial_z^4 \alpha^+ \tag{2.93}$$

$$\partial_t \alpha^- - v_A \partial_z \alpha^- \simeq - \frac{v_A \Delta z^2}{12} \partial_z^3 \alpha^- - \frac{v_A \Delta z^3}{48} \partial_z^4 \alpha^-. \tag{2.94}$$

Combining those two equations in order to obtain Equation (2.88) leads to the solution:

$$\partial_t \alpha^+ + v_A \partial_z \alpha^+ + \partial_t \alpha^- - v_A \partial_z \alpha^- \simeq - \frac{v_A \Delta z^3}{24} \partial_z^4 \alpha^-. \tag{2.95}$$

Again, we interpret this fourth order term as a diffusive term with numerical diffusion coefficient:

$$\eta_{num} = \frac{2\pi v_A \Delta z^3}{24 L^2}. \tag{2.96}$$

These two expressions for numerical diffusion ($\propto \Delta z^2$ for propagating waves, and $\propto \Delta z^3$ for standing waves) are representative of the real diffusion, as confirmed by the study of the evolution of the error (Figure 2.13).

To take into account this numerical diffusivity, we solve again the equations of induction (Equation 2.80) and momentum (Equation 2.79) for a dispersion equation with an additional (numerical)

diffusion:

$$\partial_t \mathbf{u} = \frac{B_0}{\rho_0}\partial_z \mathbf{b} + \eta_{num}\partial_z^2 \mathbf{u} \tag{2.97}$$

$$\partial_t \mathbf{b} = B_0 \partial_z \mathbf{u} + \frac{B_0^2}{\gamma_{AD}\rho_{i0}\rho_0}\partial_z^2 \mathbf{b} + \eta_{num}\partial_z^2 \mathbf{b} \tag{2.98}$$

yield

$$s = -\frac{k^2(\eta_{AD} + 2\eta_{num})}{2} \pm i\sqrt{k^2 v_A^2 - \left(\frac{k^2\eta_{AD}}{2}\right)^2}. \tag{2.99}$$

As we have restricted the numerical effect to a diffusion, there is no contribution to the imaginary part of the pulsation, as can be seen in Equation (2.99).

The propagating Alfvén waves test We start the simulation with an initial perturbed state with $B_{1x} = \mathcal{R}e(\delta b_x e^{ikx})$, $\delta b_x = 1$, $B_{1y} = \mathcal{R}e(i\delta b_x e^{ikx})$, and $v_{1nx} = \mathcal{R}e(\frac{ikB_0}{\rho s}B_{1x})$ and $v_{1ny} = \mathcal{R}e(\frac{ikB_0}{\rho s}B_{1y})$, where $\mathcal{R}e$ denotes the real part of a complex number. For the propagating wave test, we have chosen our initial conditions so that $s_i \geq 0$.

The internal energy equation (see Shu (1992)) can be written as:

$$\frac{\partial \rho\epsilon}{\partial t} + \nabla.(\rho\epsilon\mathbf{v}) = -P\nabla.\mathbf{v} + \frac{((\nabla \times \mathbf{B}) \times \mathbf{B})^2}{\gamma_{AD}\rho_i\rho}. \tag{2.100}$$

In the case of perfect gases, we have $P = (\gamma - 1)\rho\epsilon$. Since Alfvén waves are transverse waves, $\nabla.\mathbf{v} = 0$ and $\nabla.(\rho e\mathbf{v}) = 0$. The energy equation thus reduces to

$$\frac{\partial P}{\partial t} = \frac{\gamma - 1}{\gamma_{AD}\rho_i\rho}((\nabla \times \mathbf{B}) \times \mathbf{B})^2 \tag{2.101}$$

. This last equation, combined with our choice $\delta b_y = i\delta b_x$, gives $\nabla(P) \equiv \mathbf{0}$.

Using Equation (2.101), the time evolution of the pressure writes

$$P = P_{init} + (\gamma - 1)\frac{k^2\,\eta_{AD}}{2s_r}(e^{2s_r t} - 1). \tag{2.102}$$

Figure 2.14 shows profiles of B_{1x}, v_{1nx}, B_{1y}, v_{1ny}, ρ and P along the z direction after three wave periods (*i.e*, $t = 3 \times \frac{2\pi}{s_i}$), for $\gamma_{AD} = 80$, with a fully refined grid using 32 cells. The solid line represents the analytical solution. The agreement between the numerical and the analytical solution is excellent (see the amplitude of the error on the figure), even after the wave amplitude has decreased by a factor of about 2.

In order to check for the numerical diffusion as explained in Equation (2.99) we need to perform the same simulation using less cells for the numerical diffusivity (η_{num}) to be not negligible compared to the physical diffusivity (η_{AD}). The profiles of B_{1x}, v_{1nx}, B_{1y} and v_{1ny} along the z direction after five wave periods (*i.e*, $t = 5 \times \frac{2\pi}{s_i}$) for $\gamma_{AD} = 80$ with a grid of 16 cells is represented Figure 2.15. The solid lines represent the analytical solutions either without taking into account the numerical diffusivity (the *not corrected curves*), or correcting the damping factor according to Equation (2.99) (the *corrected* curves). The agreement between the numerical and the analytical solution taking into account numerical diffusivity is excellent (see the amplitude of the error on the figure).

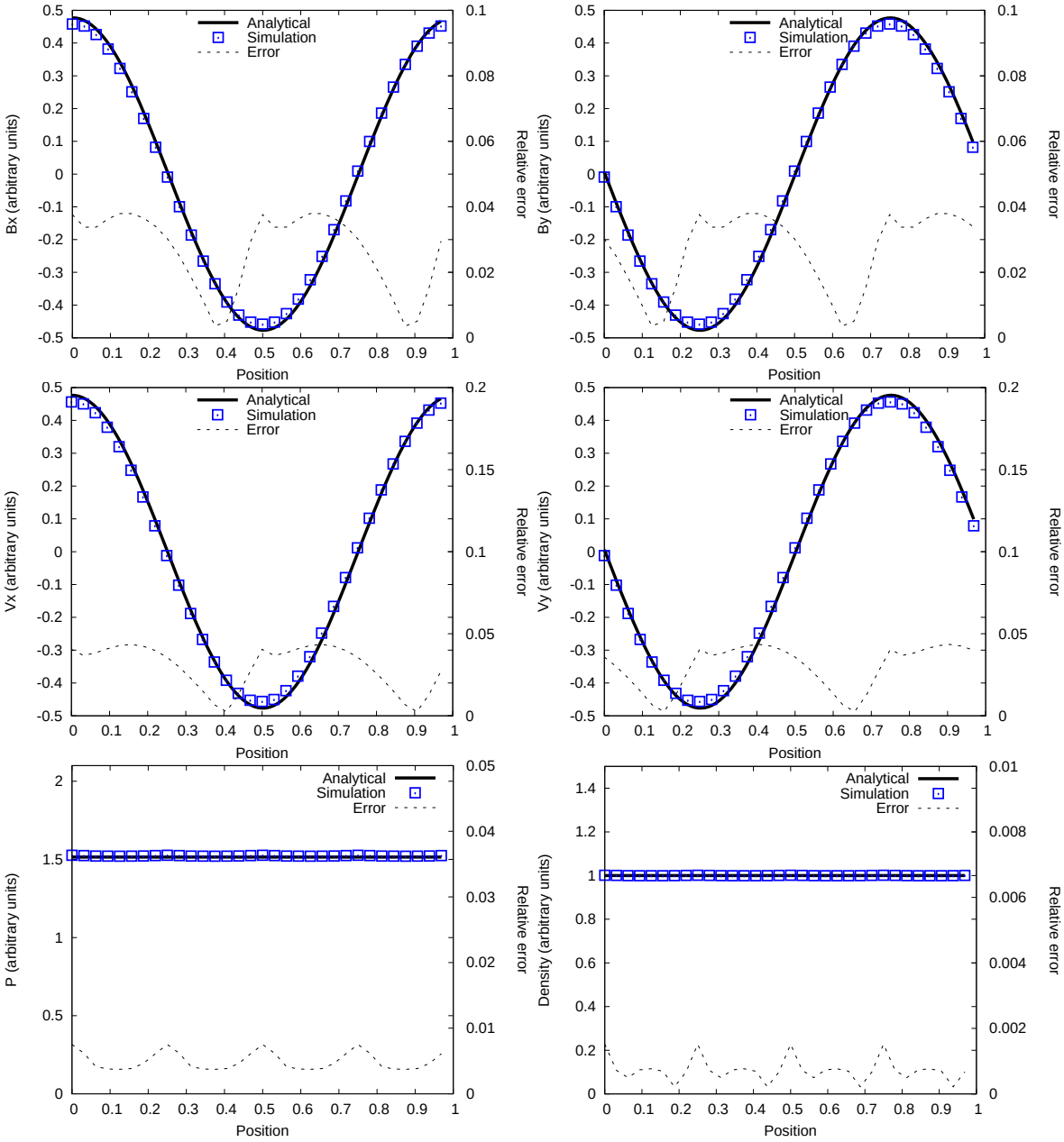

Figure 2.14: The propagating Alfvén waves test with ambipolar diffusion ($\gamma_{AD} = 80$) after about five periods. The simulation is represented by squares, while the solid-line is the analytical solution. The dotted line is the relative error. We use for this test a fully refined Cartesian grid with 32 cells.

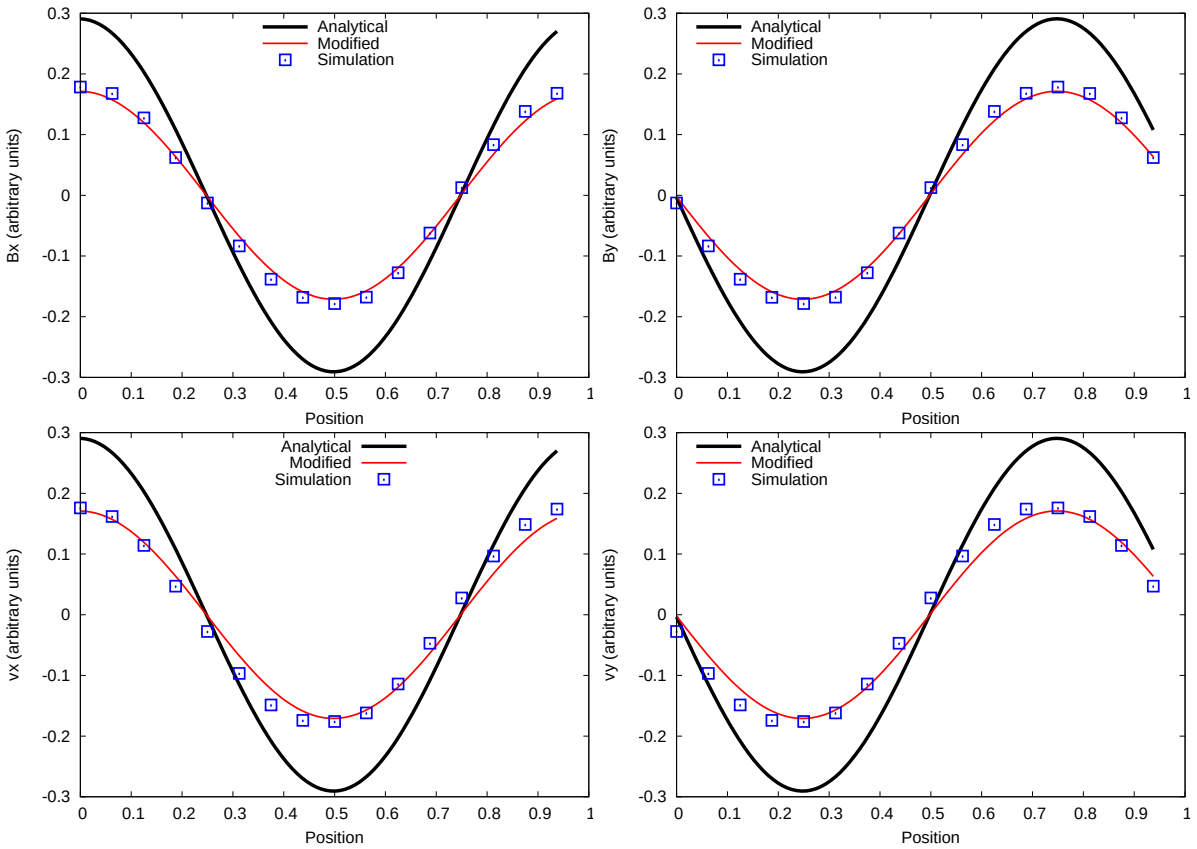

Figure 2.15: The propagating Alfvén waves test with ambipolar diffusion ($\gamma_{AD} = 80$) after about five periods. The simulation is represented by squares, while the solid-lines are the two exact solutions (taking into account or not the effect of numerical diffusion according to Equation (2.99)). We use for this test a fully refined Cartesian grid with 16 cells.

The standing Alfvén waves test We now start the simulation from an initial perturbed state obtained by adding two propagating waves in opposite directions with the same damping s_r, and let the system evolve. Figure 2.16 displays a snapshot of the evolution of B_{1x}, v_{1nx}, B_{1y}, v_{1ny}, ρ and P along x, after about 4 periods (in order for v_{1nx} and v_{1ny} to be greater than zero) for $\gamma_{AD} = 80$. The excellent agreement between the numerical and the analytical solution is confirmed.

As previously, we determine the time evolution of the pressure thanks to Equation (2.101)

$$P = P_{init} + (\gamma - 1)k^2\eta_{AD}\Big[\frac{e^{2s_r t} - 1}{s_r} + e^{2s_r t}\left(\frac{s_r\cos(2s_i t) + s_i\sin(2s_i t)}{|s|^2}\right) - \frac{s_r}{|s|^2}\Big]. \tag{2.103}$$

Following Choi et al. (2009) it is interesting to study the time variation of the magnetic field in the z direction, B_x, as represented Figure 2.17. The analytical solution is represented by the solid line while the dotted line represents the error and the squares the simulation.

Convergence order We tested the evolution of the precision of the implementation of ambipolar diffusion by examining the evolution of the error with the level of refinement, *i.e* with the mesh size Δx, for Alfvén standing waves and the Barenblatt test. The error ϵ is defined here as the maximum difference between the analytical values and the numerical solution, corrected by the damping factor for Alfvén waves. The error against the cell size follows a power-law, at least in the range studied here (up to 10 periods of the wave). For the standing waves we find

$$\epsilon \propto \Delta x^3. \tag{2.104}$$

For the Alfvén propagating waves

$$\epsilon \propto \Delta x^2. \tag{2.105}$$

For the Barenblatt test

$$\epsilon \propto \Delta x^2. \tag{2.106}$$

A log-log plot of the error as a function of cell size Δx for different times is shown on Figure 2.13 for Alfvén standing waves and propagating waves, and on Figure 2.10 for the Barenblatt test. Note that the evolution of the error follows the power laws found through the modified equation study, in subsection 2.2.1.4.

Estimate of the numerical drift coefficient of ambipolar diffusion As seen in § 2.2.1.4, the dissipation of Alfvén waves is slightly larger than expected according to the analytical values. The spurious dissipation due to the numerical scheme can be estimated as:

$$\frac{1}{\gamma_{mes}} = \frac{1}{\gamma_{AD}} + \frac{1}{\gamma_{num}}, \tag{2.107}$$

where γ_{mes} is the value measured in the numerical simulation, with ${\gamma_{mes}}^{-1} = -\frac{2s_r\rho_i}{k^2 v_A^2}$, and γ_{num} is the drift contribution due to numerical dissipation. Another way to proceed is to set $\gamma_{AD} = \infty$, to examine how the Alfvén waves dissipate, and then to estimate γ_{num} as ${\gamma_{num}}^{-1} = -\frac{2s_r\rho_i}{k^2 v_A^2}$. Both methods give about the same value for γ_{num}. For a level of AMR refinement of 2^4, we get ${\gamma_{num}}^{-1} = 3\times10^{-3}$; for 2^5, ${\gamma_{num}}^{-1} = 5\times10^{-4}$ and for 2^6, ${\gamma_{num}}^{-1} = 6\times10^{-5}$, to be compared with ${\gamma_{AD}}^{-1} = 0.0125$ or 0.033 for the present simulations. As expected, the better the resolution, the smaller the numerical diffusion.

Figure 2.18 is a plot of the dissipation of Alfvén waves with $\gamma_{AD} = \infty$, as explained previously. The red solid line corresponds to the analytical solution corrected with our estimate of the magnitude of the numerical diffusion, as explained in Equation (2.99), while the black solid line corresponds to the uncorrected analytical solution (no diffusion).

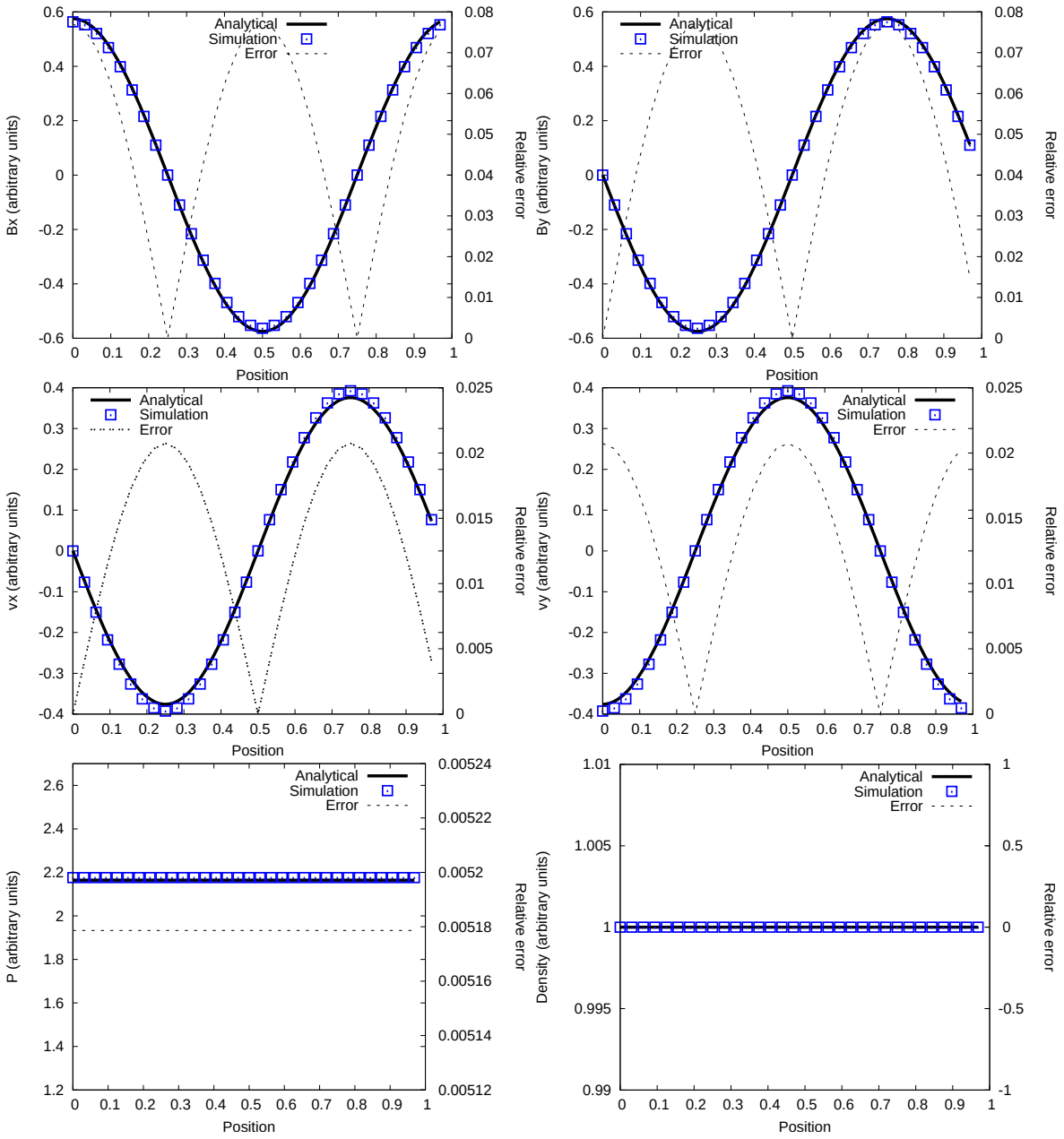

Figure 2.16: The standing Alfvén wave test with ambipolar diffusion ($\gamma_{AD} = 80$) after about four periods. The simulation is represented by squares, while the solid-lines are the exact solutions. The dotted lines represent the relative error. We use for this test a fully refined Cartesian grid with 32 cells.

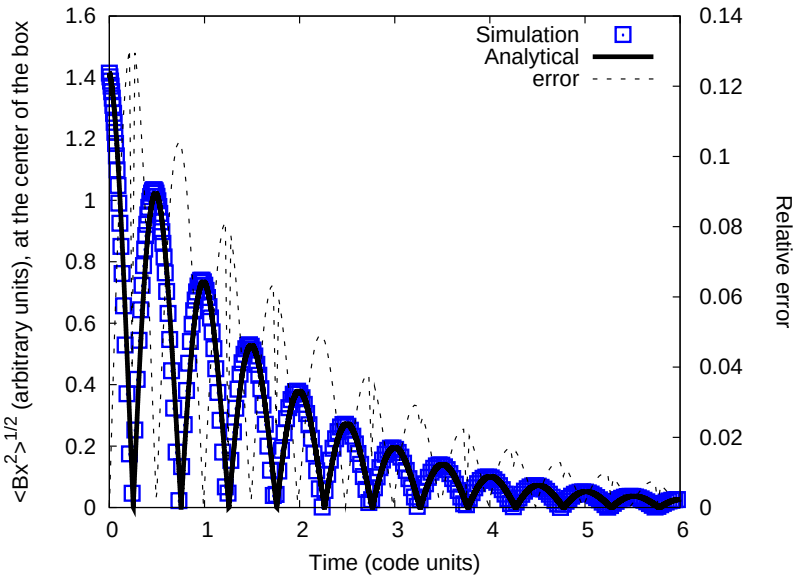

Figure 2.17: Time evolution of $\sqrt{< Bx^2 >}$, the root-mean-square of the magnetic field in the x direction at the center of the box, for Alfvén standing waves with ambipolar diffusion ($\gamma_{AD} = 30$). The squares are the result of the simulation and the solid line is the analytical solution.

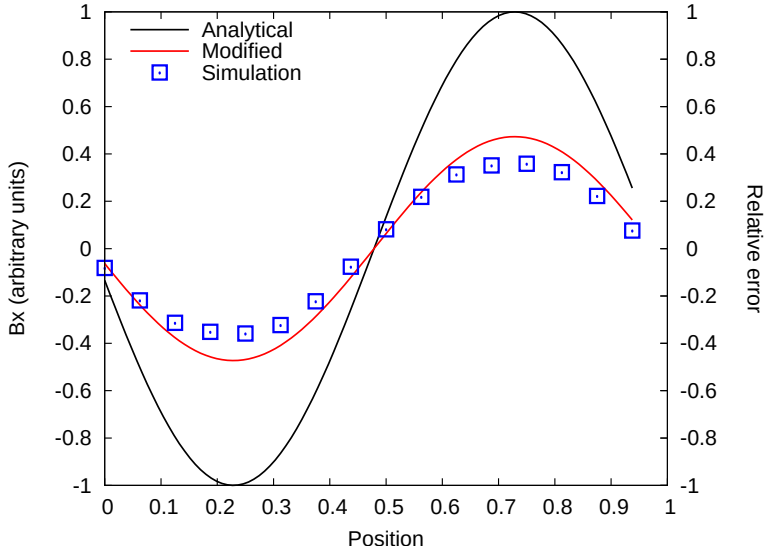

Figure 2.18: Plot of the magnetic field without ambipolar diffusion: $\gamma_{AD} = \infty$. The black solid line shows the analytical solution of the unperturbed Alfven wave, while the red solid line shows the analytical solution with numerical diffusion taken into account (corrected as explained in Equation (2.99) for a level of refinement of 4).

2.2.2 Ohmic diffusion

2.2.2.1 Equations

We now turn to the case of Ohmic diffusion in the MHD equations. Equations (2.20), (2.21), (2.24) and (2.27) remain the same. The energy equation is now:

$$\frac{\partial E_{tot}}{\partial t} + \nabla.\Big(\mathbf{v}(E_{tot} + P_{tot}) - \mathbf{B}(\mathbf{v}.\mathbf{B}) - \mathbf{E}_\Omega \times \mathbf{B}\Big) = 0, \tag{2.108}$$

where E_{tot} and P_{tot} denote the total energy and pressure:

$$E_{tot} = \rho\epsilon + \frac{1}{2}\rho v^2 + \frac{1}{2}B^2 \tag{2.109}$$

$$P_{tot} = (\gamma - 1)\rho\epsilon + \frac{1}{2}B^2. \tag{2.110}$$

The time evolution of $\mathbf{B}$ reads:

$$\frac{\partial \mathbf{B}}{\partial t} = \nabla \times (\mathbf{v} \times \mathbf{B} - \eta_\Omega \nabla \times \mathbf{B}). \tag{2.111}$$

The Lorentz force and the Ohmic diffusivity EMF read:

$$\mathbf{F}_{Lorentz} = (\nabla \times \mathbf{B}) \times \mathbf{B} \tag{2.112}$$

$$\mathbf{E}_\Omega = -\eta_\Omega \nabla \times \mathbf{B}, \tag{2.113}$$

where η_Ω denotes the Ohmic diffusivity.

2.2.2.2 Computation of Ohmic diffusivity

Various authors (Machida et al. (2006), Machida et al. (2007a), Machida et al. (2008), Machida et al. (2009)) have studied the influence of Ohmic diffusion, in particular in the context of molecular cloud's collapse. Their work assumes that the heating from Ohmic resistivity is negligible, and that the approximation $\nabla \times (-\eta_\Omega \nabla \times \mathbf{B}) \simeq \eta_\Omega \Delta \mathbf{B}$ is valid. We choose a more general framework and do not assume either of these two assumptions. We implement in `RAMSES` non-isothermal Ohmic diffusivity, with the exact EMF $\mathbf{E_\Omega} = -\eta_\Omega \nabla \times \mathbf{B}$

To compute the term of Ohmic diffusivity we proceed exactly as in § 2.2.1.2.

The Ohmic diffusion EMF The EMF in the z direction $\mathbf{E_\Omega} \cdot \mathbf{e_z} = -\eta_\Omega(\nabla \times \mathbf{B})_z$ is to be computed at $x_{i-\frac{1}{2}}, y_{j-\frac{1}{2}}, z_k$. Since the EMF writes:

$$E^\Omega_{z;i-\frac{1}{2},j-\frac{1}{2},k} = -\eta_\Omega\Big(\frac{B_{y;i,j-\frac{1}{2},k} - B_{y;i-1,j-\frac{1}{2},k}}{\Delta x} - \frac{B_{x;i-\frac{1}{2},j,k} - B_{x;i-\frac{1}{2},j-1,k}}{\Delta y}\Big), \tag{2.114}$$

it is naturally defined at the right position using the natural definition of the Ohmic field components (see Figure 2.4). η_Ω is computed at $x_{i-\frac{1}{2}}, y_{j-\frac{1}{2}}, z_k$ using the procedure described in § 2.2.1.2 to compute γ_{AD}, ρ and ρ_i.

The Ohmic diffusion energy flux This flux writes $\mathcal{F}_\Omega = \eta_\Omega(\mathbf{J} \times \mathbf{B})$. As explained in § 2.2.1.2 the flux has to be evaluated on each face of the cell, that is at locations $(x_{i\pm\frac{1}{2}}, y_j, z_k)$, $(x_i, y_{j\pm\frac{1}{2}}, z_k)$ and $(x_i, y_j, z_{k\pm\frac{1}{2}})$. The computation of $\mathbf{J}$ and $\mathbf{B}$ at these locations is already explained in § 2.2.1.2.

Computation of the time step in presence of Ohmic diffusion The characteristic Ohmic diffusivity time step, t_Ω, is computed according to

$$t_\Omega = 0.1 \times \frac{\Delta x^2}{\eta_\Omega}, \tag{2.115}$$

where, as for the ambipolar diffusion case, the coefficient 0.1 yields a small enough time step to ensure good code convergence. The computational time step is the minimum between t_Ω and the time step obtained for the ideal MHD case.

2.2.2.3 Tests for the Ohmic diffusion

Test of Ohmic diffusivity alone We first examine the accuracy of the treatment of Ohmic diffusivity alone. We take exactly the same conditions as in § 2.2.1.4 for ambipolar diffusion. We further assume that η_Ω is constant. In that case the induction equation reduces to a diffusion equation with a constant diffusion coefficient, using the divergence-free condition $\nabla \cdot \mathbf{B} = 0$:

$$\frac{\partial \mathbf{B}}{\partial t} = \eta_\Omega \Delta \mathbf{B}. \tag{2.116}$$

The solution to this equation for an initial state given by a Dirac pulse is the well known heat diffusion equation which yields a gaussian distribution with a width spreading as $\sigma \propto \sqrt{t}$. This can easily be studied either for a one dimensional pulse (e.g. $B_y(x)$, $B_x = 0$, $B_z = 0$) or a two dimensional pulse (e.g. $B_y(x, z)$, $B_x = 0$, $B_z = 0$). The results (setting $\eta_\Omega = 1$) are displayed on Figure 2.19. The agreement between the numerical and the analytical results is excellent, always better than about 0.5%. We checked that the results obtained on an AMR grid are as good as the ones obtained on a regular grid corresponding to the highest level of refinement, and that exactly the same results are obtained for any orientation of the magnetic field.

The evolution of the error as a function of the resolution is represented Figure 2.20. For this particular test (heating equation) the spatial scheme is of order 2: $\epsilon \propto \Delta x^2$.

In this case, due to the smoothly varying magnetic field, using a refinement strategy based on ∇B is not very efficient: the AMR runs are using typically the same number of cells as a fully refined grid (at least for our tests between level 5 and 9).

J-shock Proceeding as in § 2.2.1.4 we have tested the accuracy of our treatment of Ohmic diffusivity for the case of an oblique J-shock. For a stationary shock in the x direction (all quantities are supposed to only depend on x) the equations of mass, momentum, energy, magnetic field conservation and the condition $\nabla.\mathbf{B} = 0$ read:

$$\partial_x(\rho v_x) = 0 \tag{2.117}$$

$$\partial_x(\rho v_x^2 + P_{gaz} + \frac{1}{2}B_y^2) = 0 \tag{2.118}$$

$$\partial_x(\rho v_x v_y - B_x B_y) = 0 \tag{2.119}$$

$$\partial_x\left((E_{tot} + P_{tot})v_x - (\mathbf{v}\cdot\mathbf{B})B_x - \eta_\Omega B_y \partial_x B_y\right) = 0 \tag{2.120}$$

$$\partial_x(v_x B_y - v_y B_x - \eta_\Omega \partial_x B_y) = 0 \tag{2.121}$$

$$\partial_x(B_x) = 0. \tag{2.122}$$

This set of equations is solved numerically and provides the benchmark to which the simulation with the RAMSES code will be compared to assess the accuracy of the numerical treatment in the code.

We start from a steep function as initial state for the different variables whose values are the ones taken at infinity ahead of and behind the shock, respectively, in the frame of the shock. These

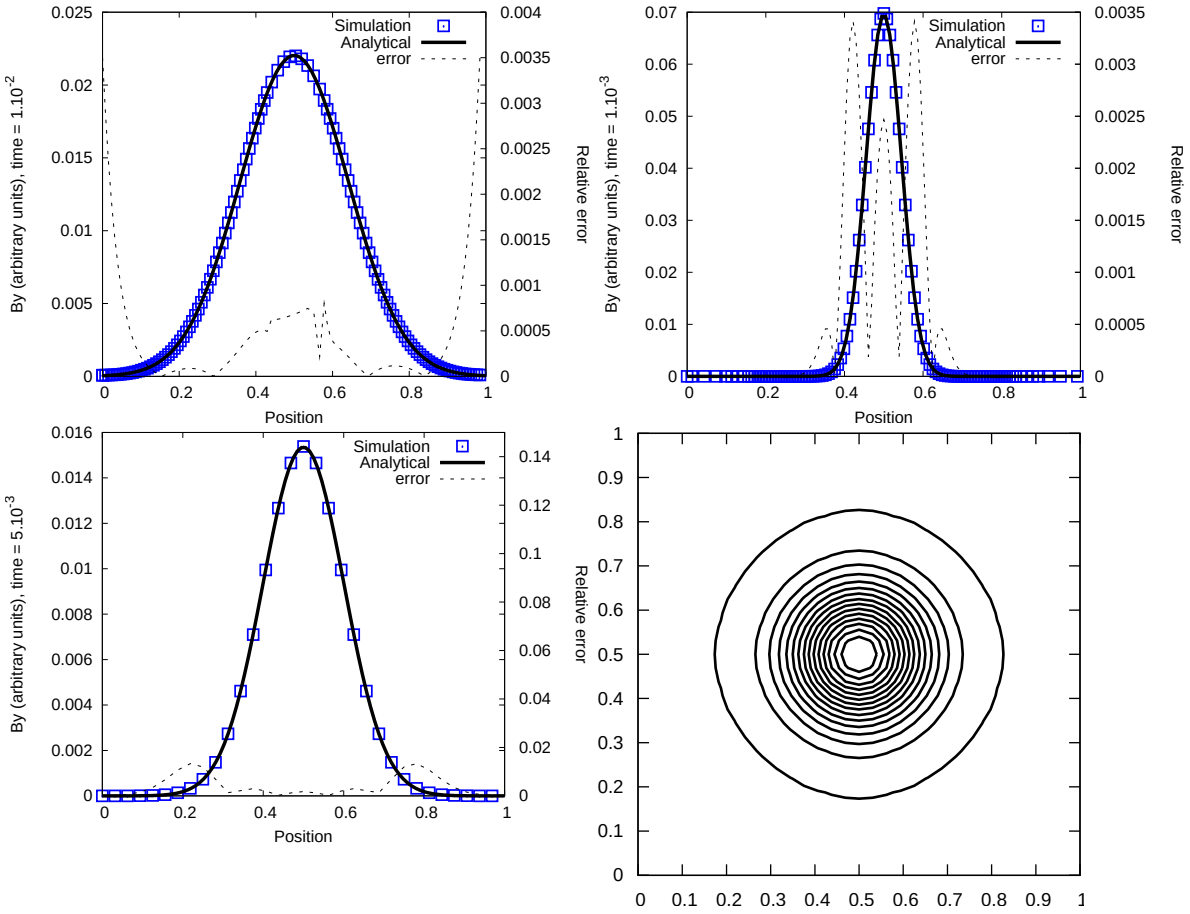

Figure 2.19: Test for Ohmic diffusion only, assuming a Laplacian. The upper panels are snapshots for the 1D test, with an AMR grid with levels from 5 to 7, at times $t = 1.10^{-3}$ on the top left and $t = 1.10^{-2}$ one the top right panel. The solid lines are the analytical solution, while the dashed lines are the relative error. The lower panels represent the 2D test, on a fully refined grid up to level 5, with a contour snapshot on the right and a transverse cut on the left, at $t = 5.10^{-3}$: the symmetry is well preserved.

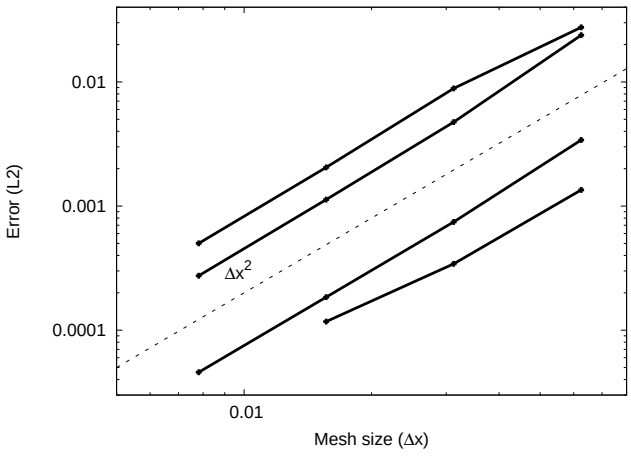

Figure 2.20: Evolution of the error ϵ for the barenblatt test ($\epsilon = \sqrt{\sum_{i=1}^{N} \frac{(By_{\text{numerical}} - By_{\text{analytical}})^2}{N}}$). The dashed line correspond to: $\epsilon \propto \Delta x^2$.

Variable	ρ	v_x	v_y	B_x	B_y	P
Pre-shock value	0.4	3	0	$\frac{\sqrt{2}}{2}$	$\frac{\sqrt{2}}{2}$	0.4
Post-shock value	0.71084	1.68814	0.4299	$\frac{\sqrt{2}}{2}$	1.43667	1.19222

Table 2.2: Initial state used to generate an oblique C-shock, as described in § 2.2.2.3.

values are displayed in Table 2.2. For this test the Ohmic diffusivity coefficient is set to $\eta_\Omega = 0.1$. The results are portrayed on Figure 2.21. As seen in the figure, after a transitory regime the shock becomes stationary, as expected. A very small drift velocity of the shock front persists, of the order of 0.25% of the minimum value of v_x. Identical results are obtained for any orientation of the magnetic field and of the initial velocity.

Such an agreement between the numerical and the analytical solutions, within about 0.2% (except a few points where it can reach 1%) can be considered as very satisfactory and asseses the validity of our treatment when hydrodynamics and Ohmic diffusion are coupled.

The grid is refined if the gradient of magnetic field, pressure, density or velocity is greater than 0.1 (this insures for this test that the error on the AMR grid and on the regular grid are about the same).

Alfvén waves Proceeding as for the ambipolar diffusion study we have examined the behaviour of propagating Alfvén waves as well as of standing waves in an non-isothermal ionized plasma in the case of Ohmic diffusion. Lesaffre and Balbus (2007) derived analytical solutions for the general case of MHD flows with shear, non-zero resistivity η_Ω, viscosity and cooling. In the absence of shear and rotation, these authors showed that torsional Afvén waves are a solution for such flows.

Following closely the notations of Lesaffre and Balbus (2007), the unperturbed state in both studies for a wave propagating in the x direction is defined as:

$$\begin{aligned} P_0 = 0.625, \quad \rho_{0n} = 1, \quad \rho_{0i} = 1, \\ V_{0x} = 0, \quad V_{0y} = 0, \quad V_{0z} = 0, \\ B_{0x} = 0, \quad B_{0y} = 0, \quad B_{0z} = 1. \end{aligned}$$

For the propagating wave study, the perturbed state is chosen such as $\delta b_x = 1$ and $\delta b_y = i\,\delta b_x$ (we necessarily have $\delta b_z = 0$). Furthermore, we have $\delta\rho = 0$ (constant density), but the pressure varies with time, so that $\delta P \neq 0$ (see Lesaffre & Balbus 2007). In the absence of shear, viscosity and rotation, the relation between the perturbed magnetic field, $\delta\mathbf{b} = (\delta b_x\,\mathbf{x} + \delta b_y\,\mathbf{y})e^{st+ikz}$, and the perturbed velocity, $\delta\mathbf{u}$, reads

$$s\,\delta\mathbf{u} = i\frac{B_0 k}{\rho}\delta\mathbf{b}, \tag{2.123}$$

with s the wave angular frequency and k the wave number.

The time evolution of the gaz pressure P is governed by the equation:

$$\partial_t\left(\frac{P}{\gamma-1}\right) + \nabla\cdot\left(\frac{P}{\gamma-1}\delta\mathbf{u}\right) = -P\nabla\cdot(\delta\mathbf{u}) + \eta_\Omega\,\mathbf{J}^2, \tag{2.124}$$

with γ the adiabatic coefficient of the gaz and $\mathbf{J} = \nabla\times\mathbf{B}$ the current.

Since $\delta\mathbf{u}$ only depends on z and has components only in the x and y direction, $\mathrm{div}\,\delta\mathbf{u} = 0$. We finally get

$$\partial_t P = (\gamma-1)\eta_\Omega\,\mathbf{J}^2. \tag{2.125}$$

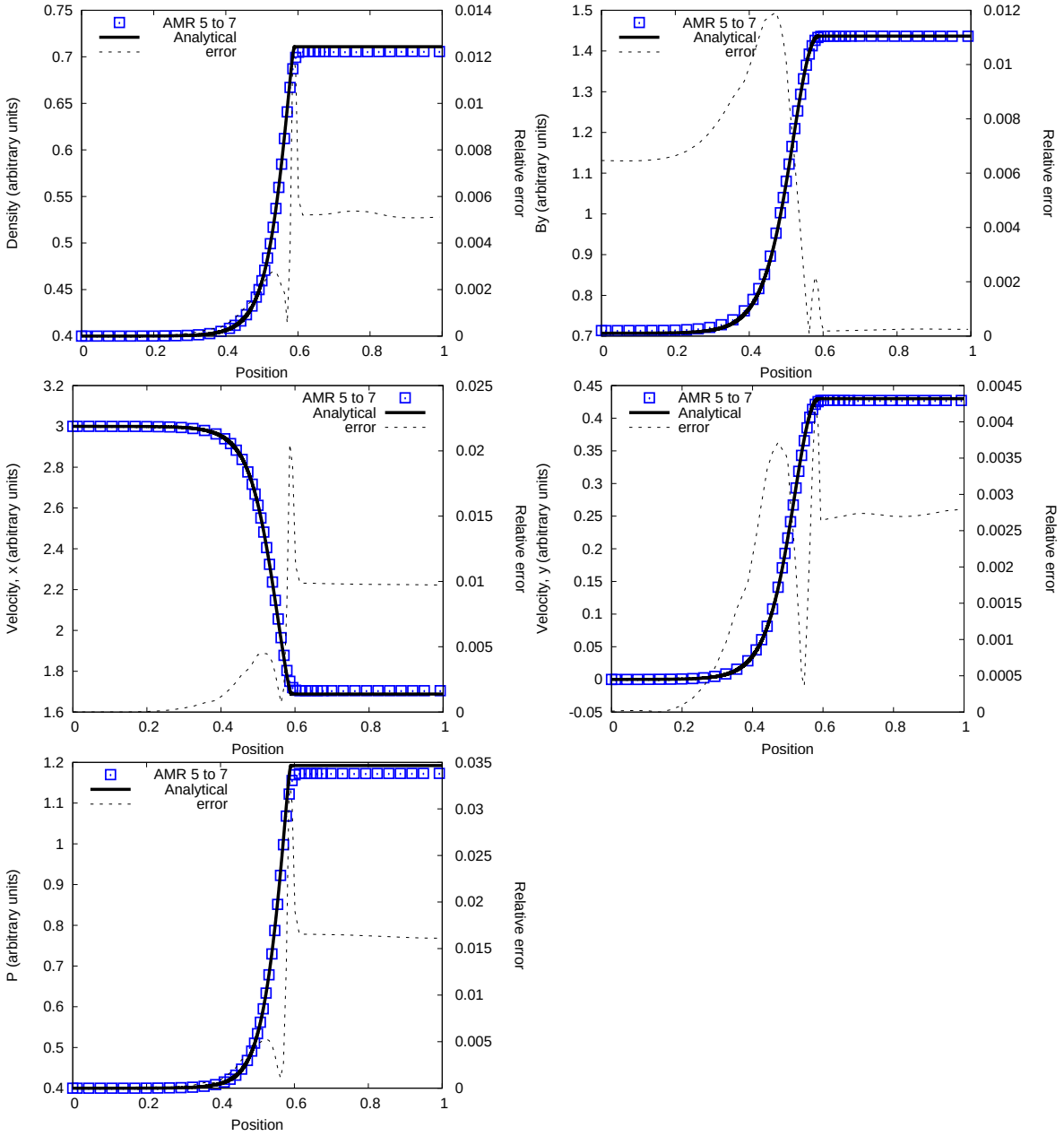

Figure 2.21: Non-isothermal oblique shock with Ohmic diffusion ($\eta_{md} = 0.1$). Same caption as in the previous figures. The level of refinement is from 5 to 7.

The solutions of the dispersion relation read:

$$s = -\frac{\hat{\eta}}{2} \pm \sqrt{(\frac{\hat{\eta}}{2})^2 - k^2 v_A^2}, \tag{2.126}$$

with $\hat{\eta} = k^2\eta_\Omega$. A value $\eta_\Omega = 5 \times 10^{-3}$ yields a moderate damping, with $s_r = -9.8696 \times 10^{-2}$ and $s_i = \pm 1.9844$, whereas a value $\eta_\Omega = 2 \times 10^{-2}$ produces a stronger damping, with $s_r = -3.9478 \times 10^{-1}$ and $s_i = \pm 1.9473$.

Estimating numerical diffusion Proceeding exactly as in § 2.2.1.4 we can derive the leading order error term in the ideal MHD scheme for Alfvén standing, and propagating waves.

Propagating waves We start the simulation from an initial perturbed state with $\delta\mathbf{b} = \delta b_x . \mathcal{R}e\left(e^{ikx}(\mathbf{x} + i\mathbf{y})\right)$ and $\delta\mathbf{u} = \frac{B_0 k}{\rho}\mathcal{R}e\left(\frac{i}{s}e^{ikx}(\mathbf{x} + i\mathbf{y})\right)$. The time evolution of the pressure is:

$$P = P_{ini} + \frac{(\gamma - 1)\eta_\Omega\, k^2\, \delta b_x^2}{2 s_r}(e^{2 s_r t} - 1). \tag{2.127}$$

For the propagating wave test, we have arbitrarily chosen $s_i > 0$ and let the system evolve from the initial state. Figure 2.22 portrays a snapshot of the evolution of $\delta\mathbf{b}_x$, $\delta\mathbf{u}_x$, $\delta\mathbf{b}_y$, $\delta\mathbf{u}_y$, ρ and P along the z-direction after five wave periods (*i.e*, $t = \frac{5 \times 2\pi}{s_i}$), for $\eta_\Omega = 5.10^{-3}$. Once again, the agreement between the numerical and the analytical solution is very satisfactory, at most of the order of a few percents.

Standing waves As for the ambipolar diffusion, we start the simulation from an initial perturbed state obtained by adding two propagating waves with opposite values of s_i and the same value of s_r, and let the system evolve. The evolution of the pressure is (in real notation):

$$P = P_{init} + (\gamma - 1)\eta_\Omega\, k^2\, \delta b_x^2 \Big[\frac{e^{2 s_r t} - 1}{s_r} + e^{2 s_r t}\Big(\frac{s_r \cos(2 s_i t) + s_i \sin(2 s_i t)}{|s|^2}\Big) - \frac{s_r}{|s|^2}\Big]. \tag{2.128}$$

Figure 2.23 shows a snapshot of the evolution of $\delta\mathbf{b}_x$, $\delta\mathbf{u}_x$, $\delta\mathbf{b}_y$, $\delta\mathbf{u}_y$, ρ and P along z after three wave periods ($t = \frac{3 \times 2.\pi}{s_i}$), for $\eta_\Omega = 5 \times 10^{-3}$. As seen, once again, the agreement between the numerical and the analytical solution is very good, of the order of or better than a few percents.

Convergence order We tested the evolution of the precision of the implementation of Ohmic diffusion by examining the evolution of the error with the level of refinement, *i.e* with the mesh size Δx for Alfvén standing waves and the Barenblatt test. The error ϵ is defined here as the maximum difference between the analytical values and the numerical solution, corrected by the damping factor for Alfvén waves, and the error at the center of the box for the Barenblatt test. The error as function of cell size follows a power-law, at least in the range studied here (up to 10 periods of the wave). For the standing waves we find:

$$\epsilon \propto \Delta x^3. \tag{2.129}$$

For the Alfvén propagating waves

$$\epsilon \propto \Delta x^2. \tag{2.130}$$

For the Barenblatt test

$$\epsilon \propto \Delta x^2. \tag{2.131}$$

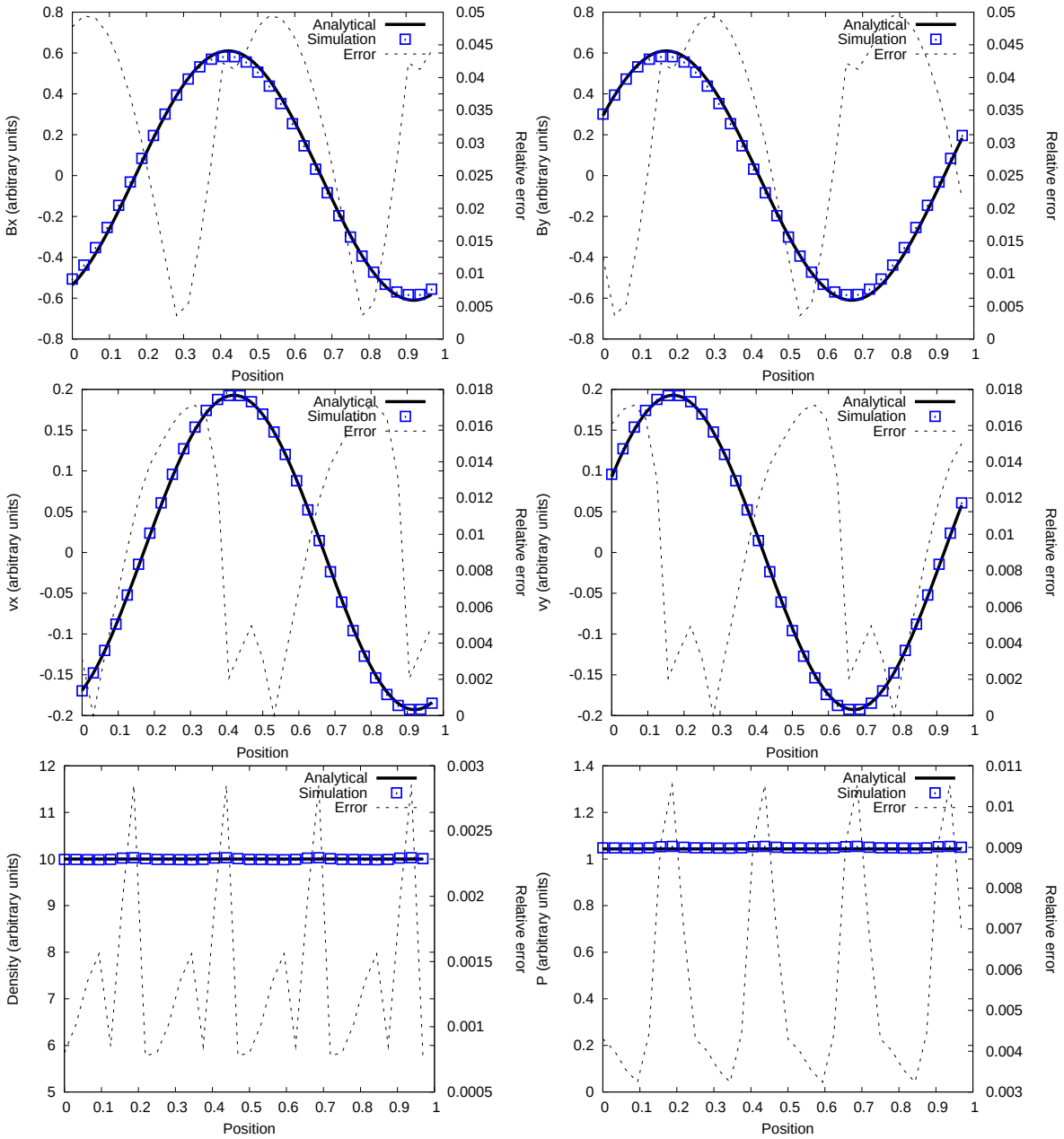

Figure 2.22: Alfvén propagating waves after five periods. The level of AMR refinement is constant and equal to 2^5. The Ohmic diffusivity is $\eta_{md} = 5.10^{-3}$.

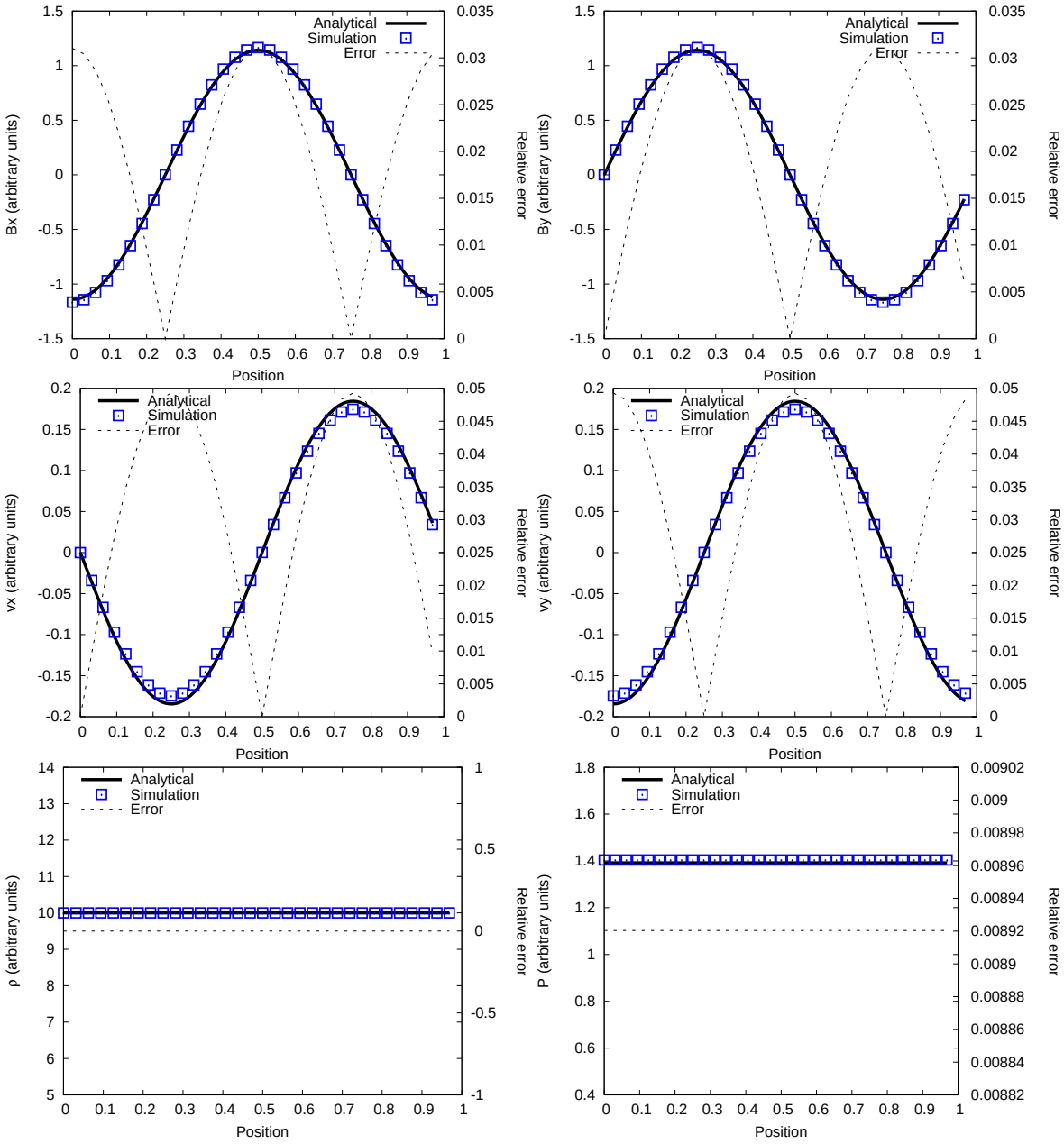

Figure 2.23: Alfvén standing waves after four periods and a half, for $\eta_{md} = 5 \times 10^{-3}$. Same caption as in the previous figures.

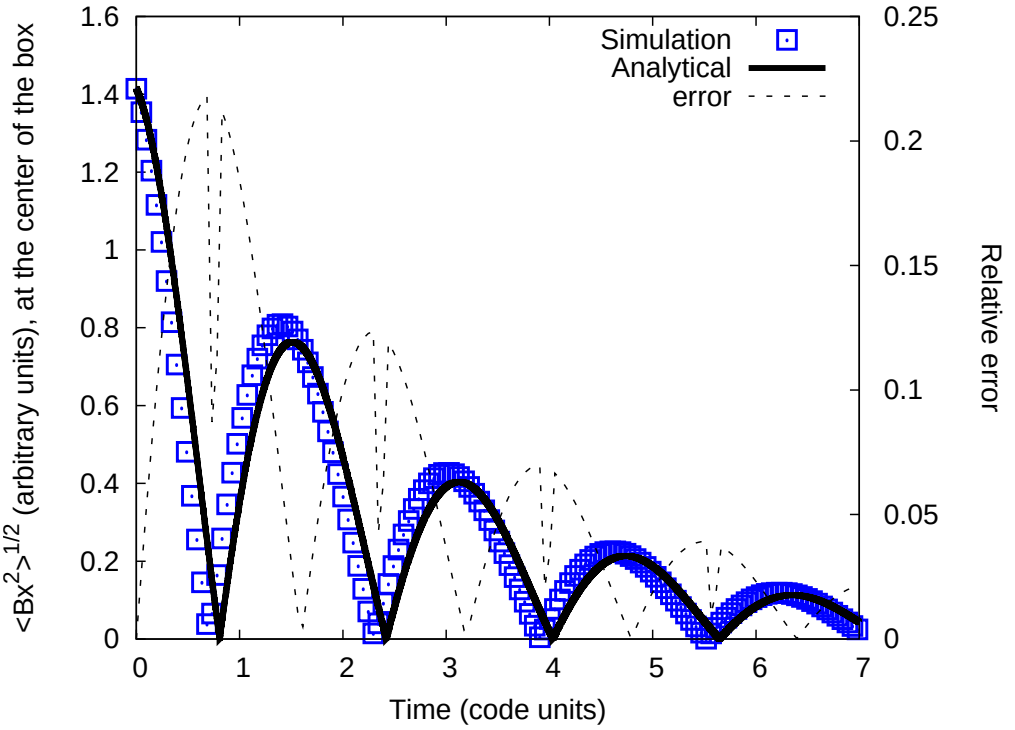

Figure 2.24: Time evolution (expressed in units of the period, $\frac{2.\pi}{s_i}$) of $\sqrt{< Bx^2 >}$, the root-mean-square of the magnetic field in the x direction, for Alfvén standing waves. In this case, $\eta_\Omega = 2 \times 10^{-2}$.

A log-log plot of the error as a function of cell size Δx for different times is given on Figure 2.25 for Alfén standing waves, and on Figure 2.20 for the barenblatt test. The behavior of the error for the propagating waves differs if the mesh size is coarse or fairly refined ($\epsilon \propto \Delta x^1$ or $\epsilon \propto \Delta x^2$ respectively). For the Barenblatt test, the error scales as $\sim \Delta x^2$. In the case of Ohmic diffusion, Equation (2.116) reduces exactly to the Heat equation, whereas in the case of ambipolar diffusion, Equation (2.73) reduces to a non-linear diffusion equation. The error in the two cases scales as $\sim \Delta x^2$.

Estimate of the numerical drift coefficient of Ohmic diffusion As seen in subsection 2.2.2.3, the dissipation of Alfvén waves is slightly larger than expected according to the analytical values. The spurious dissipation due to the numerical scheme can be estimated as:

$$\eta_{mes} = \eta_\Omega + \eta_{num}, \tag{2.132}$$

where η_{mes} is the value measured in the numerical simulation, with $\eta_{mes} = -\frac{2 s_{r,num}}{k^2}$, and η_{num} is the drift contribution due to numerical dissipation. Another way to proceed is to set $\eta_\Omega = 0$, to examine how the Alfvén waves dissipate, and then to estimate η_{num} as $\eta_{num} = -\frac{2 s_{r,num}}{k^2}$. Both methods give about the same value for η_{num}. For a level of AMR refinement of 4, we get $\eta_{num} = 1. \times 10^{-3}$; for 5, $\eta_{num} = 1. \times 10^{-4}$ and for 6, $\eta_{num} = 1.1 \times 10^{-5}$, to be compared with $\eta_\Omega = 0.005$ or 0.02 for the present simulations. As expected, the better the resolution, the smaller the numerical diffusion.

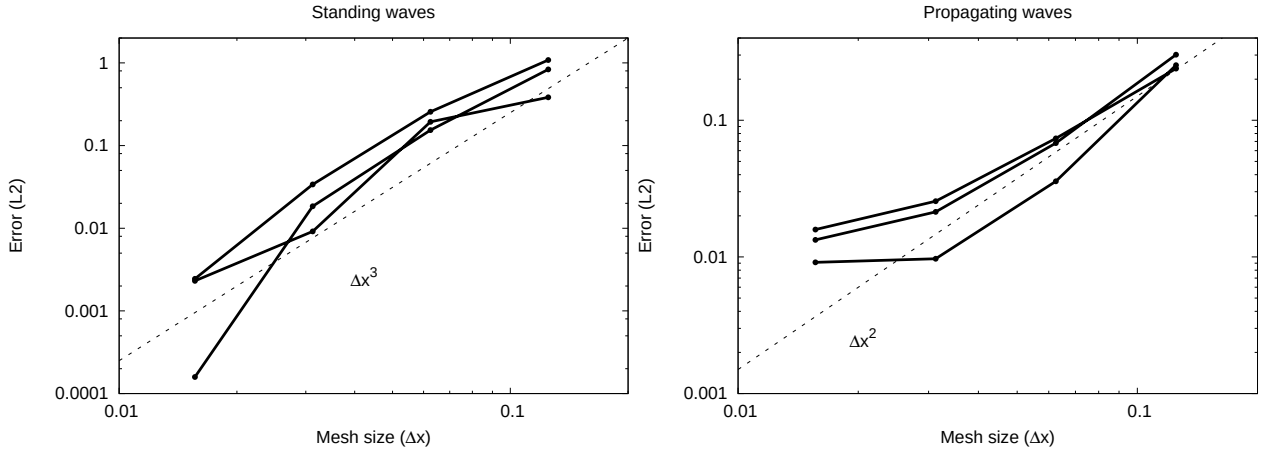

Figure 2.25: Evolution of the error $\epsilon = \sqrt{\sum_{i=1}^{N} \frac{(By_{\text{numerical}} - By_{\text{analytical}})^2}{N}}$ with the mesh size Δx for Alfvén standing waves (left plot) and Alfvén propagating waves (right plot) at different times. The dashed lines correspond to two slopes: $\epsilon \propto \Delta x^3$ for the standing waves and $\epsilon \propto \Delta x^2$ for the propagating waves.

2.2.3 Conclusion

In this chapter we have described a numerical method to implement the treatment of the two important terms of non-ideal MHD, namely ambipolar diffusion and Ohmic dissipation, into the multi-dimensional AMR code `RAMSES`. For ambipolar diffusion, we have used a single fluid approach, which is valid when the Lorentz force and the neutral-ion drag force are comparable, corresponding to a domain of strong coupling between the fluid and the field lines. The situations where such an approximation can be made are numerous, of which cloud collapse or certain protoplanetary disks are two typical examples. The accuracy of our numerical resolution of the MHD equations was examined by performing a diversity of tests, for which either analytical or benchmark solutions exist. For both ambipolar and Ohmic diffusion, we first explored the purely magnetic case, without any coupling to the hydrodynamics. For ambipolar diffusion, this was done by comparing the evolution of a Dirac pulse to the solution provided by Barenblatt while for Ohmic diffusion, the solution is confronted to the well known heat diffusion equation. In a second step, we studied the full MHD case (coupling the fluid to the magnetic field) by considering first an oblique shock, and then the behavior of propagating and standing Alfvén waves. For all these tests the solutions obtained with our method show excellent agreement with the analytical predictions, typically within a few tenths of a percent on average, showcasing the validity and the robustness of our method. We have also carefully analyzed the main source of numerical error using the Modified Equation framework. In order to estimate the spatial resolution that is required to model non-ideal MHD effects reliably. This opens the avenue to a vast domain of astrophysical applications, in particular cloud collapse, pre-stellar core formation and protostellar disks where ambipolar and Ohmic diffusion processes are believed to play a dominant role. Such astrophysical applications of the non-ideal MHD equations with `RAMSES` will be explored chapter 4.

2.3 Multigroup radiation hydrodynamics

Parallel to the study of non-ideal magnetohydrodynamics, an accurate treatment of radiative transfer is of tremendous importance in star formation. Radiative feedback from the dense central object, frequency dependent opacities and cooling and heating terms due to non-ideal MHD effects are expected to play a crucial role in particular in fragmentation studies and in the launching mechanisms

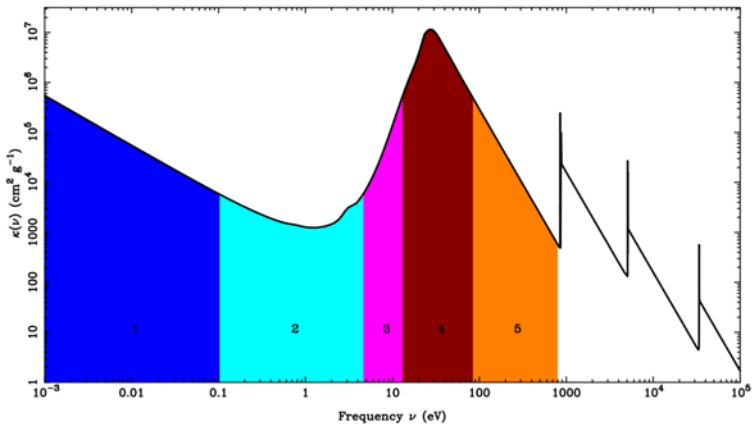

Figure 2.26: Xenon opacities at $\rho = 10^{-3}$ g.cm^{-3} and $T = 1$ eV as a function of frequencies. The colours illustrate the decomposition of the frequency domain into five groups from $\nu = 10^{-3}$ to 770 eV. Taken from Vaytet et al. (2011).

of outflows and jets. Various approximations can be made to treat radiative transfer, the lowest order being the barotropic approximation where we use a prescription for the temperature as a function of density. This approximation however does not allow for the study of heating from non-ideal MHD terms. To focus on this along with the wish to propose a versatile code for further probing the physics of star formation, we used and developed an already existing radiative solver in `RAMSES`. This implementation is only used for second core calculations in this manuscript and reader uninterested in those can skip this section.

2.3.1 The method

We present here succinctly the method used to add multigroup radiative transfer in `RAMSES`. We based the method on the radiation-hydrodynamics solver developed by Commerçon (2009) (see also Commerçon et al. (2011)) and the multigroup solver developed by Vaytet et al. (2011) and González et al. (2007). Multigroup radiative transfer allows for a frequency dependent set of equations, with user defined boundaries for each group. An example of a frequency decomposition is shown Fig. 2.26. Results from Vaytet et al. (2012, 2013a) in 1D simulations showed few differences in the first and early second core formation. However, for those regimes, the grey approximation ($\sim$ 1 group in the multigroup framework) is expected to perform greatly because of the high optical thickness in the infrared regime of the dense parts of the cloud, and the thinness of the surroundings. Using multigroup radiative transfer is expected to have a greater impact for later phases when UV and X-ray radiations are present and matter and radiation are strongly decoupled. Last, in order to investigate 3D non-isotropic effects in particular for radiative shocks (see also the study by Vaytet et al. (2013b) in 1D) we integrated the multigroup radiative transfer using the M1 approximation additionally to the Flux Limited Diffusion approximation. In either cases, we must solve a system of linear equations $Ax = b$ where A is a squared matrix, x is the array of radiative energy (and flux, for the M1 case) and b the source terms.

Flux Limited Diffusion approximation Also called FLD, the Flux Limited Diffusion approximation is an effective way to describe radiative transfer. It only involves one more equation: the first moment of radiative transfer equations (the energy) per group to the previous set of magnetohydrodynamics equations. It cannot account for shades or non-isotropic radiation (because we

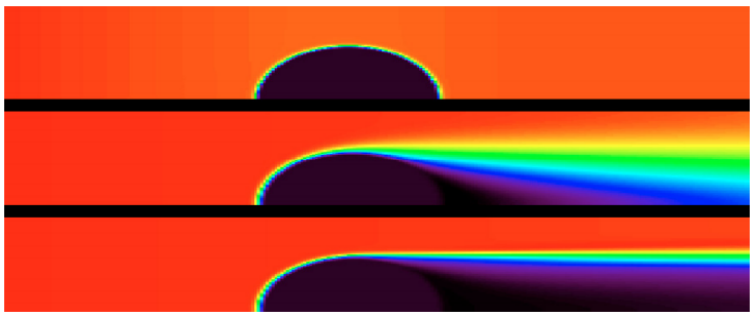

Figure 2.27: Visual comparison between the FLD approximation, the M1 model and the M1 model with accurate eigenvalues. The color map represents the radiative temperature. Taken from González et al. (2007).

lack the vectorial information of the flux) but can be solved efficiently using the conjugate-gradient method (CG). The radiative flux is in this case always collinear to the radiative gradient temperature, explaining the absent shadows and possible propagation around corners. In the multigroup case, exchange terms between groups are dealt with using a relaxation scheme in order to keep the matrix symmetrical. This approximation is valid when the photon mean free path is small compared to other length scales in the system.

M1 approximation A remarkable feature of the M1 model is to take into account high anisotropy factors while remaining computationally efficient. It makes use of the first two moments of radiative transfer equations (energy and flux) and therefore has the vectorial information the FLD approximation lacks. On the other hand in this case the matrix A is no longer symmetrical. Therefore, the bi-conjugate gradient method has to be used, making the method less memory efficient in the case of an AMR grid.

Riemann problem In order to accurately solve for radiative transfer the eigenvalues have to be modified in the Godunov scheme (see Commerçon (2009)). For both the FLD and M1 approximations in the multigroup framework, we kept the same eigenvalues as for the grey approximation. Indeed, in the multigroup case the eigenvalues (the waves speed) tend to be close to the speed of light. This is a problem as it completely freezes the simulation. We therefore chose to code multigroup additions as sources terms to keep the wave fan unaltered.

A visual comparison between these approximations is shown Fig. 2.27.

2.3.2 Radiative shocks

Radiative shocks are part of many astrophysical processes. In stellar formation, they are relevant in stellar accretion shocks, but can be also encountered in jets, supernovæ, etc. Practically, a shock can be created with a flow hitting a wall. If the fluid speed is low, temperature behind and before the shock are very different, with a sharp transition. When the fluid speed is high, temperature is identical behind and before the shock. Behind, the shock, a matter temperature peak appears, due to the matter and radiation coupling. These two cases are denominated subcritical shock for the low velocity case, and supercritical for the high velocity case (see Mihalas and Mihalas (1984a)).

We performed sub- and super-critical shock tests in three dimensions (separately) to validate the method used, using the same setup as Mihalas and Mihalas (1984b). There are still some issues, in

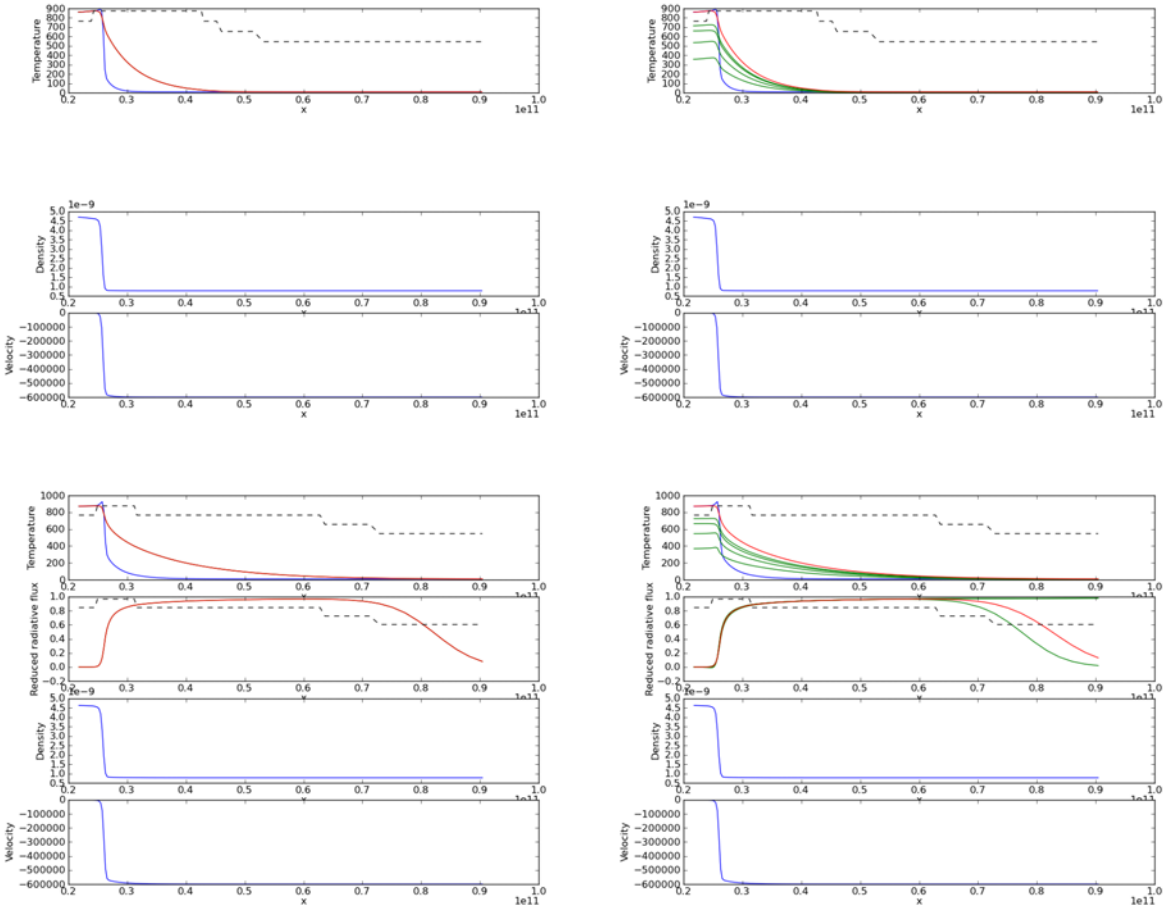

Figure 2.28: Subcritical shock, as described in Mihalas and Mihalas (1984b). Top: FLD, one group on the left, 4 groups on the right. Bottom: M1, one group on the left, 4 groups on the right. Gas temperature is the blue solid line. Radiative temperature is the red solid line. Green lines stand for the radiative temperature for the different groups.

particular with the M1 supercritical shock. However, the multigroup FLD implementation and the M1 for subcritical shocks is very satisfying, as can be seen in Fig. 2.28.

2.4 Notes on the Super Time-Stepping method (STS method)

2.4.1 Theory

Star formation simulations need a huge resolution, yielding stringent restriction on the time-step and in particular when using diffusive terms, in which case the time-step scales as the square of size of a cell. At densities of the order of 10^{-10} g.cm^{-3}, the time-step restriction due to resistive effects can be up to several orders of magnitude, therefore artificially freezing the time integration in the simulation compared to a non-diffusive case. In order to somehow release this restriction, we can use a method called super-time stepping.

General framework Following Alexiades et al. (1996) and Choi et al. (2009), we try and implement the super-time stepping in the AMR code `RAMSES` to solve for ambipolar diffusion. The basic idea is to demand stability over a large number of time steps instead of demanding it for each time step. Therefore, the length of each time step is to be chosen carefully:

$$\tau_j = \Delta t_{expl} \left((-1+\nu) cos(\frac{2j-1}{N}\frac{\Pi}{2}) + 1 + \nu \right)^{-1} \tag{2.133}$$

and then:

$$\lim_{\nu \to 0} \Delta T = \lim_{\nu \to 0} \sum_{j=1,N} \tau_j = N^2 \Delta t_{expl}. \tag{2.134}$$

For details on the mathematics (stability issues, etc.) see Alexiades et al. (1996).

2.4.2 Problems

The problems to tackle are the following:

- Choice of N_{expl} and N_{sts} : should we use a strict inequality, and how ? or in Fortran words: ceiling ? floor ? +1 ?
- The result at each time step does not carry any physical sense. All N time steps have to be done before any physical discussion.
- If $\nu \neq 0$, the sum of time steps doesn't equal $N^2 \Delta t_{expl}$ and therefore additional (or less) time steps have to be done.

Choice of the number of steps In case of totally explicit subcycling, the best choice is:

$$\frac{\Delta T_{cc}}{dt} - 1 < N = ceiling(\frac{\Delta T_{cc}}{dt}) \leq \frac{\Delta T_{cc}}{dt} \tag{2.135}$$

with ΔT_{cc} being the global time step given by the Courant condition, and dt the explicit time step (ambipolar diffusion time step). The last time step still remains to be carefully attended to: the best solution is to truncate it in order to exactly reach the Courant condition time step:

$$dt_{last} = \Delta t_{cc} - \sum_{i=1,N-1} dt. \tag{2.136}$$

For the super time stepping, two choices are possible:

$$N_{sts}^{(1)} = ceiling(\sqrt{\frac{\Delta T_{cc}}{dt}}), \tag{2.137}$$

$$N_{sts}^{(2)} = floor(\sqrt{\frac{\Delta T_{cc}}{dt}}) + 1. \tag{2.138}$$

Both solutions give $N_{sts}^2 \geq ceiling(\frac{\Delta T_{cc}}{dt}) = N$, which is the necessary condition sought (see 2.4.3). A little further, one can find that:

$$N_{sts}^{(1)} \geq N_{sts}^{(2)} \tag{2.139}$$

and therefore $N_{sts}^{(2)}$ is a better solution.

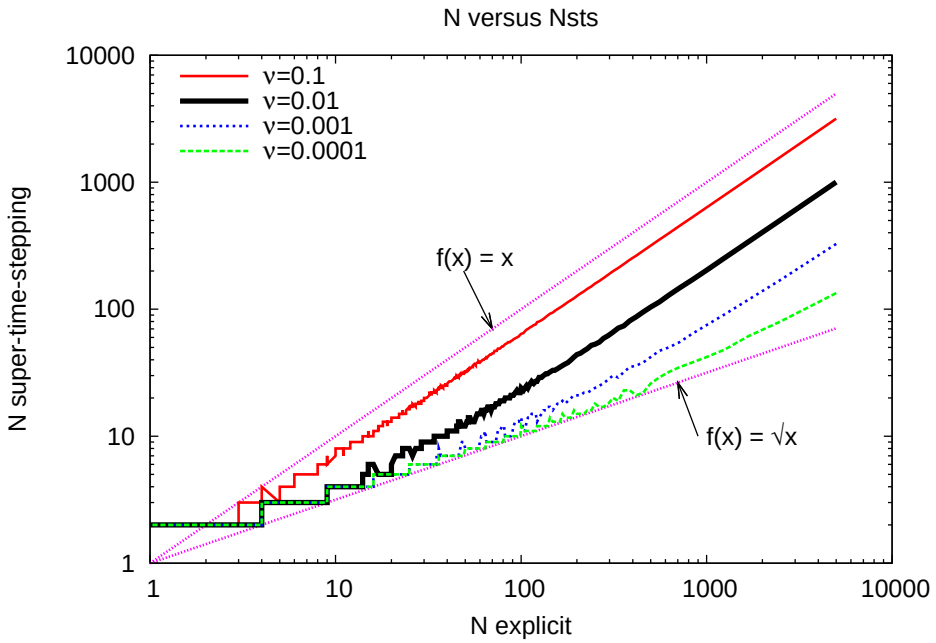

Figure 2.29: Number of super time *vs* explicit time steps, as described in subsection 2.4.2. For large numbers of time steps everything is fine, yet for few time steps the aimed global time step is way overpassed (which cannot be seen here).

Case: $\sum_{j=1,N} \tau_j < N^2 \Delta t_{expl}$ In that case, more time steps have to be performed in order to reach the larger Courant time step. The solution retained is to perform super time step taking as global time step the remaining time:

$$T_{\text{global}} = \Delta T_{cc} - \sum_{j=1,N} \tau_j \tag{2.140}$$

and so until finished (then the gain in computation steps is not exactly $\sqrt{N}$ but slightly worse: see Figure 2.29). Eventually, it will end up with one time step which will be longer that the remaining time. This leads to next subsection: 2.4.2.

Case: $\sum_{j=1,N} \tau_j > N^2 \Delta t_{expl}$ In case the sum of the super time-stepping is larger than the expected global time-step (see Figure 2.30), we shrink it by a factor $\frac{\Delta T_{cc}}{\sum \tau_i}$. That way we keep stability, and we do not overpass the global time-step. If the last time-step is too large, again, we use a shorter time step in order to exactly reach the global needed time-step. The only problem is that it can go endlessly, with shorter and shorter time-step. In order to avoid this problem, we restrict this to the case where there is more than one time step needed. If $N_{sts} = 1$, then we simply take $\tau_{sts} = T_{final} - T_{actual}$.

Tests First, we plot on Figure 2.29 the number of super time steps (N_{sts}) against the number of explicit time steps (N). The method used is the one described in § 2.4.2: when the sum is not large enough, we continue with a new global time corresponding to the remaining time in order to reach the Courant time step. When the number of necessary time steps is small (in the order of 20 or less), the sum of STS steps is way larger than the global Courant time step. Therefore, we need to limit the sum when overpassing the global time step. This is represented Figure 2.30: when the sum is bigger than the global time step, we limit the next step to the difference between global and

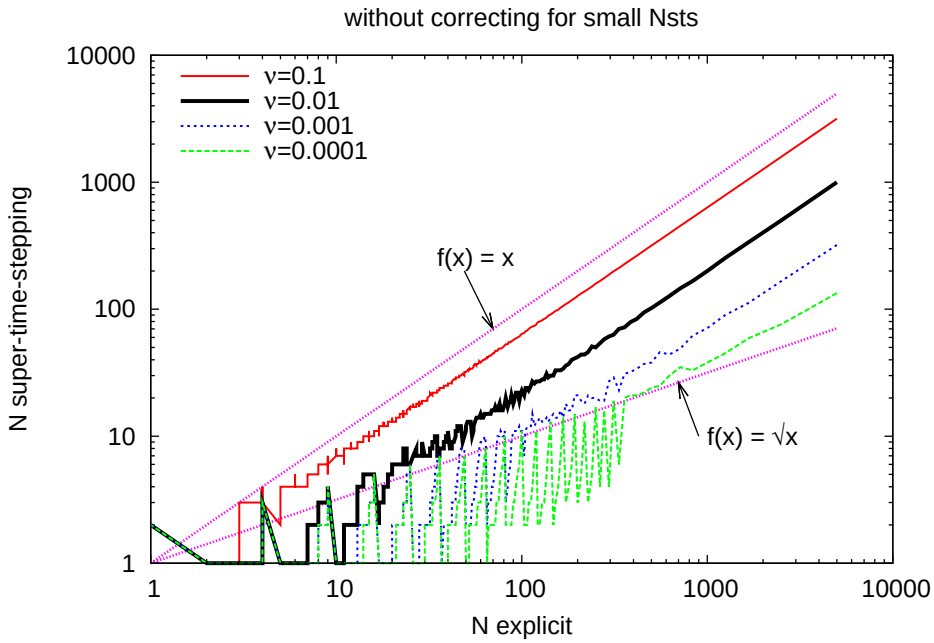

Figure 2.30: Number of super time *vs* explicit time steps, without correcting when $N_{sts} \lesssim 7$.

sum of previous time steps. This leads to an unexpectedly small number of STS steps: the first STS step is too large compared to the aimed sum when $N_{sts} \lesssim 7$. In order to remain stable, we do as explained in subsection 2.4.2, and we keep the right number of STS steps, shrinking them all by the necessary factor, and correcting for the last one if necessary. This is represented Figure 2.31. The gain in computation steps is as expected near $\sqrt{N}$ for $\nu = 0.001$ at about any number of time steps.

2.4.3 Ceiling or floor ?

First, let's focus on $N_{sts}^{(1)} = floor(\sqrt{\frac{\Delta T_{cc}}{dt}}) + 1$. Be $floor(\sqrt{\frac{\Delta T_{cc}}{dt}}) = i$, then:

$$\begin{aligned} i \leq \sqrt{\frac{\Delta T_{cc}}{dt}} < i+1, \\ i^2 \leq \frac{\Delta T_{cc}}{dt} < \underbrace{i^1 + 1 + 2i}_{N_{sts}^{(1)\,2}} \end{aligned} \tag{2.141}$$

so that:

$$N_{sts}^{(1)\,2} \geq ceiling(\frac{\Delta T_{cc}}{dt}) = N. \tag{2.142}$$

For $N_{sts}^{(2)} = ceiling(\sqrt{\frac{\Delta T_{cc}}{dt}})$, the same study gives, with $ceiling(\sqrt{\frac{\Delta T_{cc}}{dt}}) = j$:

$$\begin{aligned} j - 1 < \sqrt{\frac{\Delta T_{cc}}{dt}} \leq j, \\ j^2 + 1 - 2j < \frac{\Delta T_{cc}}{dt} \leq \underbrace{j^2}_{N_{sts}^{(2)\,2}} \end{aligned} \tag{2.143}$$

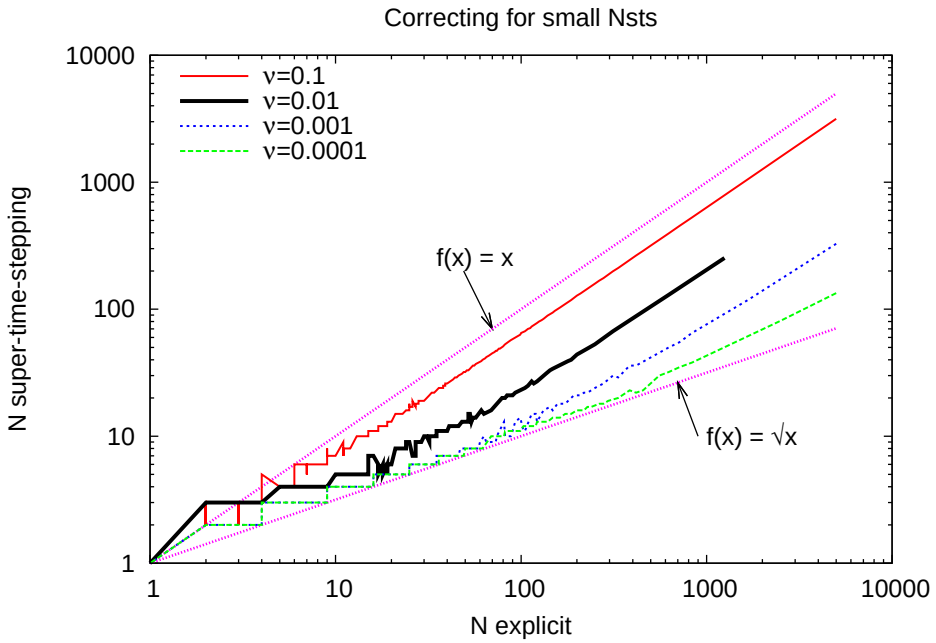

Figure 2.31: Number of super time *vs* explicit time steps, as described in subsection 2.4.2.

so that:

$$N_{sts}^{(2)^2} \geq ceiling(\frac{\Delta T_{cc}}{dt}) = N. \tag{2.144}$$

2.4.4 Conclusion

In order to correctly replace explicit time steps by STS steps, we follow the method explained in subsection 2.4.2 and implement it in `RAMSES`. We choose $\nu = 0.001$ for a significant gain in computation time, keeping good stability performances ($\nu \rightarrow 0$ is the stability limit). Tests for a physical collapse of a $1\,M_{\odot}$, with ambipolar diffusion and a barotropic equation of state leading to the first Larson's core have been made. The results are that using adaptive time-steps (a different time-step for each level of refinement, since coarse levels don't need to be updated with the very constrained same Courant condition as the finest ones) is more efficient than using the STS method by a factor depending on the number of levels of the simulation. One way to improve the overall efficiency of the method would be to use both adaptive time-steps and STS for each level, but this raises some yet unsolved difficulties such as how to keep the divergence-free constraint while updating coarse levels.

2.A The Barenblatt-Pattle solution

Following Grundy and McLaughlin (1982), the solution of Equation (2.73) in general form ($\frac{\partial B_y}{\partial t} = \nabla.\Big(B_y^\beta \nabla B_y\Big)$), where β depends on the problem, is:

$$B_y = \begin{cases} At^\alpha \left[1 - (\frac{r}{\eta_0 t^\delta})^2\right]^{\beta^{-1}} & \text{if} \quad r \leq \eta_0 t^\delta \\ 0 & \text{if} \quad r > \eta_0 t^\delta \end{cases} \tag{2.145}$$

With μ the dimensionality of the problem, the various constants are defined as follow:

$$\alpha = \frac{-\mu}{2+\mu\beta} \tag{2.146}$$

$$\delta = \frac{1}{2+\mu\beta} \tag{2.147}$$

$$A = \left(\frac{\delta\beta\eta_0^2}{2}\right)^{\frac{1}{2}} \tag{2.148}$$

$$\int_{x_1}^{x2} B_{y0}(\mathbf{x})\, d\mathbf{x} = \eta_0^{\mu+2/\beta} (\frac{1}{2}\delta\beta)^{\beta^{-1}} \frac{\Gamma(\frac{1}{2}\mu)\Gamma(1/\beta+1)}{\Gamma(1/\beta+1+\frac{1}{2}\mu)} \tag{2.149}$$

2.B Semi-analytical solution for the isothermal C-shock

Following Mac Low et al. (1995), in the isothermal case with a constant ion density, we reduce the set of MHD equations to:

$$\rho v_x^2 + P + \frac{B_y^2}{2} = C_1 \tag{2.150}$$

$$\rho v_x v_y - B_y B_x = C_2 \tag{2.151}$$

$$b^2 - b_0^2 = 2A^2(D-1)(D^{-1} - M^{-2}) \tag{2.152}$$

$$(D^{-2} - \mathcal{M}^{-2}) L \frac{dD}{dx} = \frac{b}{A}(b^2 + \cos\theta)^{-1} \times \Big[b - D\big(\frac{b-b_0}{A^2}\cos\theta^2 + \sin\theta\big)\Big] \tag{2.153}$$

with C_1 and C_2 derived from the initial state, $A = \frac{v}{v_A}$ the Alfvén Mach number, and $M = \frac{v}{c_s}$ the Mach number; $\theta = 45°$ is the angle between the magnetic field and the velocity field; and $D = \frac{\rho}{\rho_0}$ and $b = \frac{B_y}{B_0}$ are the dimensionless density and magnetic field.

2.C Semi-analytical solution for the non-isothermal C-shock

Following Duffin and Pudritz (2008) and Wardle (1991), and reminding that the set of equations is not exactly the same as ours, we solve the set of equations:

$$\frac{db}{dx} = \frac{\gamma_{AD}\rho_{i0}A^2 r}{v_s b} \tag{2.154}$$

$$\left(\frac{1-\gamma r_n p}{(\gamma-1)r_n}\right)\frac{dp}{dx} = \frac{\gamma_{AD}\rho_{i0} r}{v_s}\left(\frac{1}{r_n}\frac{\gamma}{\gamma-1}p - \frac{S_n+\sin\theta}{b}\right) \tag{2.155}$$

$$S_n = \frac{b-b_0}{A^2}\cos^2\theta \tag{2.156}$$

$$r_n = \frac{1}{1-(p-p_0)-(\frac{b^2-b_0^2}{2A^2})} \tag{2.157}$$

$$r_i = r_n\left(\frac{b^2+\cos^2\theta}{b r_n(S_n+\sin\theta)+\cos^2\theta}\right) \tag{2.158}$$

$$r = 1 - \frac{r_i}{r_n} \tag{2.159}$$

where the dimensionless quantities are $p = \frac{P_n}{\rho_{n0}v_s^2}$, $b = \frac{B_y}{B_0}$, the velocities $v_{nx} = \frac{v_s}{r_n}$, $v_{ny} = \frac{S_n B_0 v_s}{B_x} = \frac{S_n v_s}{b_0}$. p_0 and b_0 are the initial dimensionless pressure and magnetic fields, $\theta = 45°$ is the angle between the pre-shock velocity and the magnetic field, and $A = \frac{v_s}{v_A}$ the Alfvén Mach number.

Chapter 3

Refinements: chemical network and equation of state

"*If research in Astronomy had stopped in 1913, our knowledge of stellar evolution today would be in a satisfactory state*".

Lymann Spitzer, Spitzer (1949)

Contents

Introduction

The increasing computational power and efficiency of numerical methods allow to tackle star formation in its basis. However, many scales remain unattainable and we need to use tabulated data to account for physical effects yet impossible to simulate self-consistently in core collapse simulations.

Non-ideal effects arise when accounting for collisions between the many different particles composing the core and are directly dependent on the relative abundances between species and the (their) kinetic temperature. There are still many great unknowns concerning chemical reaction rates or even the grains size distribution at densities of about the first Larson core and it's an open field of research. We chose to develop our own chemical evolution network code in order to be able to easily change some key parameters (such as the reaction rates, the ionization rate, the temperature and density evolution, the distribution and number of grains...) and compute new abundances or resisitivities immediately. We used a rather simple chemical network for two main reasons: the uncertainties linked to, for example, grains size distribution can dominate the very precise refinements more complex networks would add; the computational time to run a simulation for a given set of parameters was a high priority, since we have the project to integrate it in `RAMSES` to use self-consistent thermodynamics to compute the resisitivities. We present in section 3.1 the chemical evolution network we developed.

The core medium is a complex mixture, constituted mainly of hydrogen and helium. Its thermodynamical properties are of tremendous importance in core collapse calculations: the rise of temperature and pressure due to the gravitational collapse is a direct consequence of the thermodynamics of the gas, while the second collapse is started due to the dissociation of dihydrogen molecules. Developing an accurate equation of state in the conditions of core collapse for a given mixture of hydrogen and helium is a full-time work by itself, and we chose in this case to use raw tabulated data computed by Saumon et al. (1995). We describe in section 3.2 the use of this equation of state. Reader should be advised that this section can be skipped if only interested in first core collapse, barotropic simulations.

3.1 Chemical network for ionisation rates

3.1.1 Theory

3.1.1.1 Chemical network

In order to compute the chemical evolution to assess for the Ohmic, ambipolar and Hall resistivities, we consider a simplified yet relevant reaction scheme. We use the following elements: H, He, C, O and heavy metal elements such as Na, Mg, Al, Ca, Fe, Ni, Si. Since we are studying dense molecular clouds (therefore cold) we assume that the elements are principally found in their molecular form (H_2, CO, O_2, H_2O, OH). The charged particles considered are electrons e, H^+, He^+, C^+, H_3^+, molecular ions m^+ and metal ions M^+. We also consider grains of various sizes and with a charge $\pm e$ or neutral grains. The respective abundance for a given size is initially given using their total surface (in order to separate the size effect from the total recombination surface effects). Details on the chemical network (the many reactions considered with the rate coefficients, the initial abundances, etc.) can be found in Umebayashi and Nakano (1990). We advertise their schematic diagram (see Fig. 3.1), which summarizes every reaction used in this network.

We then solve the complete set of equations for each charged particle (written in dimensionless

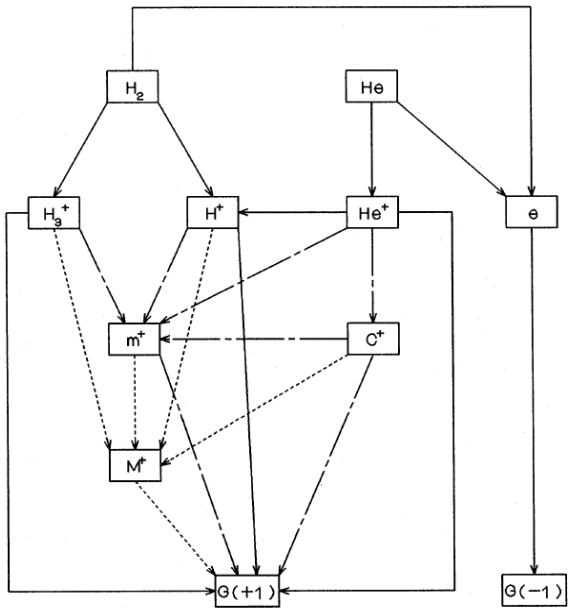

Figure 3.1: Taken from Umebayashi and Nakano (1990). Reactions concerning metals and heavy elements are shown respectively in dashed and dot-dashed lines. Recombination reactions (a cation reacting with an electron) are not shown here.

form):

$$\begin{cases} \dots \\ \frac{dx_i}{d\tilde{t}} = \sum_{j=1}^{N} \left[\alpha_{ij} x_j + \frac{n_H}{2\zeta} \sum_{k=1}^{N} \beta_{ijk} x_j x_k - \frac{n_H}{\zeta} \gamma_{ij} x_j x_i\right] \\ \dots \end{cases} \tag{3.1}$$

where N is the total number of species (both neutrals and charged particles). n_H is the density of neutrals (here: the density of hydrogen molecules). ζ is the ionisation rate for hydrogen, and $\tilde{dt} = dt\zeta$. x_i are the fractional abundances of various particles: $x_i = \frac{n_i}{n_H}$.

α_{ij} represents the ionisation of the specie j into i:

$$j \rightarrow i + e^- \quad \alpha_{ij} \tag{3.2}$$

β_{ijk} represents the reactions between j and k to form i:

$$j + k \rightarrow i + - \quad \beta_{ijk} = \beta_{ikj} \tag{3.3}$$

γ_{ij} represent the reactions between j and k to form another species (it is the same as $\beta_{?ij}$, but we kept it for the sake of clarity as it stands for the destruction of i and j more than the creation of a given specie):

$$i + j \rightarrow - \quad \gamma_{ij} = \gamma_{ji} \tag{3.4}$$

We consider that neutral abundances are constant, with values taken in Umebayashi and Nakano (1990), and we solve for the 6 ions cations (m^+ standing for molecular ions like HCO^+, M^+ accounting for metal ions such as Mg^+, H_3^+, H^+, C^+, He^+), for electrons (e^-), and for grains (described § 3.1.1.2).

The reactions rates are taken from Umebayashi and Nakano (1990), Nishi et al. (1991) for gaz species and Kunz and Mouschovias (2009) for the interactions with and between grains.

3.1.1.2 Such little grains...

We consider bins of size to account for a size distribution (e.g. the MRN distribution), as done in Kunz and Mouschovias (2009)).

The grain surface area is the key factor in the dust opacity, the conductivity of the gas and the collision rate, therefore an accurate description of the grain size distribution is needed. We will ultimately use the standard MRN distribution (Mathis et al. (1977)). The most common distribution is a uniform distribution with:

- the density of each grain is $\rho_s = 2.3$ g.cm^{-3} (dust grain are mainly formed of silicates of such a density)
- a grain size of $a_0 = 0.0375$ μm
- a total mass density for the dust grain which is a fraction of the total density of neutrals $\rho_{\rm g,tot} = 0.01\rho_{\rm n,tot}$

For the MRN distribution, we use a minimum grain size $a_{\rm min}$ and a maximum size $a_{\rm max}$. We also fix the number density of grains with radii between a and $a + da$:

$$dn_{\rm g,tot}(a) = N_{\rm MRN} a^{-3.5}\, da \tag{3.5}$$

Each bin of size is defined by a lower and upper radius, namely $a_{\rm lower}$ and $a_{\rm upper}$, which gives the number density and size for the bin α:

$$n_g^\alpha = n_{\rm g,tot}\zeta^{\frac{2.5(\alpha-1)}{N}}\left(\frac{1-\zeta^{\frac{2.5}{N}}}{1-\zeta^{2.5}}\right) \tag{3.6}$$

$$a_\alpha = a_{\rm min}\zeta^{\frac{(1-\alpha)}{N}}\left[5\left(\frac{1-\zeta^{\frac{0.5}{N}}}{1-\zeta^{\frac{2.5}{N}}}\right)\right]^{\frac{1}{2}} \tag{3.7}$$

with

$$n_{\rm g,tot} = \left(\frac{\rho_{\rm g,tot}}{\frac{4}{3}\pi\rho_s a_{\rm min}^3}\right)\left[\frac{1}{5}\left(\frac{1-\zeta^{2.5}}{1-\zeta^{0.5}}\right)\right] \tag{3.8}$$

$$\zeta = \frac{a_{\rm min}}{a_{\rm max}} \tag{3.9}$$

Lastly, we constrain the factor $N_{\rm MRN}$ by choosing the total grain density $\rho_{\rm g,tot}$ so that the total surface area remain the same as for the fiducial uniform distribution model. In order to do so, we choose $\rho_{\rm g,tot}^{\rm (MRN)} = \frac{a_{\rm min}}{a_0}\zeta^{-0.5}0.01\rho_{\rm n,tot}$. In the following we took for the minimum and maximum radii:

$$a_{\rm min} = 0.0181\,\mu{\rm m} \tag{3.10}$$

$$a_{\rm max} = 0.9049\,\mu{\rm m} \tag{3.11}$$

Since small grains contribute to most of the total surface area (because they are small and in very high number compared to bigger grain, due to the MRN distribution), and since the fiducial size for the uniform distribution is closer to $a_{\rm min}$ than to $a_{\rm max}$, we get for the total grain density $\rho_{\rm g,tot}^{\rm (MRN)} = 0.341\rho_{\rm n,tot}$ instead of $\rho_{\rm g,tot}^{\rm (fiducial)} = 0.01\rho_{\rm n,tot}$.

We find that contrarily to their assessment, 5 bins in size is not enough to reach a relative precision of the order of 1% for *every* species considered. It is sufficient, although, to reach this precision when we only consider the error on the grains (neutral grains g_0, and charged grains g_+ and g_-), as can be seen Figure 3.2. The reference case chosen is 50 bins. The error for other species than grains is, when reaching a density $\geq 10^8$ cm^{-3}, converging towards unity, probably because at this stage grains are the dominant species and therefore the relative error on the very faint gas molecules is fairly high yet with no consequence since they only scarcely participate to the resistivity at this stage.

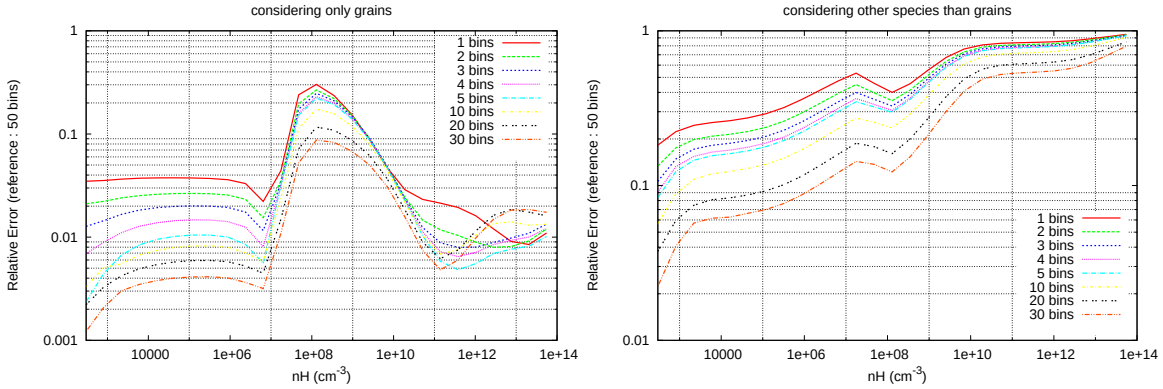

Figure 3.2: Relative error in the species abundances ($= \frac{||\mathbf{x}_\alpha - \mathbf{x_{ref}}||}{||\mathbf{x_{ref}}||}$ where the norm $||\ ||$ stands for $\sqrt{x_1^2 + ... + x_N^2}$), for the grains only (left panel), or for other species (right panel).

3.1.1.3 Numerical methods

In this subsection we describe the numerical methods we chose to focus on, and highlight their advantages and drawbacks.

Explicit method The fully explicit method is the simplest method we can think of to solve this set of equations. The idea is to evaluate at time t_n the right hand side of Equations (3.1): $\sum_{j=1}^{N} \left[\alpha_{ij} x_j + \frac{n_H}{2\zeta} \sum_{k=1}^{N} \beta_{ijk} x_j x_k - \frac{n_H}{\zeta} \gamma_{ij} x_j x_i\right] = F_i(\mathbf{x})$, and then to update the values of every x_i accordingly:

$$x_i^{n+1} = x_i^n + \tilde{dt} \times F_i(\mathbf{x^n}) \tag{3.12}$$

The time step has to be limited in order to stay stable:

$$\tilde{dt} = \epsilon \frac{||\mathbf{x^n}||}{||\mathbf{F}(\mathbf{x^n})} \tag{3.13}$$

with $\epsilon = 1 \times 10^{-2}$ controlling the relative variation per time step allowed.

This method is robust, and is stable provided the time step is well chosen. Oscillations can sometimes occur for the least present species, but the feedback on the most abundant species is negligible. Using this method, we can also perform non-equilibrium chemistry in order to follow a given simulation.

The drawbacks are the stringent constraint on the time step, and the related issue which is the impossibility to find the *exact* equilibrium.

Implicit method (Newton Raphson) This method *should* be able to find the equilibrium state but cannot be used to follow a non-equilibrium simulation as there is no time dependence.

We want to solve the set of non-linear equations:

$$0 = F_i(\mathbf{x}) \tag{3.14}$$

In order to do this, we write the Taylor expansion of $\mathbf{F}$:

$$F_i(\mathbf{x} + \delta\mathbf{x}) = F_i(\mathbf{x}) + J_{ij}\delta x^j + o(||\delta\mathbf{x}||) \tag{3.15}$$

with $J_{ij} = \frac{\partial F_i}{\partial x_j}$ and set each $F_i(\mathbf{x} + \delta\mathbf{x})$ to be equal to zero. We then only have to solve for the correction $\delta\mathbf{x}$ in the equation:

$$J\delta\mathbf{x} = -\mathbf{F} \tag{3.16}$$

A good initial guess has to be input. This step seems crucial and very difficult as even taking the solution given by the fully explicit method results in a very wrong $\delta\mathbf{x}$ (greater in norm than $\mathbf{x}$). This is at a dead-end right now (but since it cannot account for time evolution, I think it will stay that way).

Semi-implicit method in time An interesting idea would be to linearize the set of equations in time by writing:

$$\begin{aligned} x_i^{n+1}x_j^{n+1} &= (x_i^n + \frac{\partial x_i^n}{\partial dt}dt + o(dt))(x_j^n + \frac{\partial x_j^n}{\partial dt}dt + o(dt)) \\ &= x_i^n x_j^n + x_i^n\frac{\partial x_j^n}{\partial dt}dt + x_j^n\frac{\partial x_i^n}{\partial dt}dt + o(dt||\mathbf{x^n}||) \\ &= x_i^{n+1}x_j^n + x_j^{n+1}x_i^n - x_i^n x_j^n + o(dt||\mathbf{x^n}||) \end{aligned} \tag{3.17}$$

Then, we have to rewrite the whole system (see 3.B), and solve it.

This method works, but the constraint on dt is as stringent as for the explicit method, as we now need:

$$o(dt||\mathbf{x^n}||) \ll x_i^n x_j^n \tag{3.18}$$

Semi-implicit method in *space* This is the method which is currently implemented. It is much faster (even though one has to be careful when using semi-implicit schemes: the precision of the scheme has to be taken into account as much as the time-step when time integration is at stake) than a fully explicit scheme, is more stable and can be used to *find* the equilibrium state (something an explicit scheme cannot).

The idea in this scheme is to Taylor expand the right-hand side of Equations (3.1):

$$\begin{aligned} x_i^{n+1} &= x_i^n + \tilde{dt}F_i(\mathbf{x^{n+1}}) \\ &= x_i^n + \tilde{dt}\big[F_i(\mathbf{x^n}) + J_{ij}^n\delta x^j + o(||\delta\mathbf{x}||)\big] \end{aligned} \tag{3.19}$$

so that finally, in matrix form:

$$(Id - \tilde{dt}J^n)\delta\mathbf{x} = \tilde{dt}\mathbf{F}(\mathbf{x^n}) \tag{3.20}$$

By constraining the time step in the same way as in the explicit time step (see Equation (3.13)), we have both good precision and a faster way to reach the equilibrium.

The matrix on the left-hand side of Equation (3.20) is singular (mainly because of the neutral grains, but is also very close to singular without the grains and PLU decomposition fails). In order to solve this system we use SVD decomposition, describe in Press et al. (2007)

An issue is that when reaching the equilibrium up to the machine precision, the matrix becomes more and more singular (up to the machine precision, again). In order to avoid this problem while still taking the last abundances from $n_H - dn_H$ as a starting point for every new density, we demand for $\mathbf{x_{init}}$ to be at the ionisation equilibrium, as for every $\delta\mathbf{x}$ (this is also used as a way to assess that the calculation is going well and no numerical instability has developed).

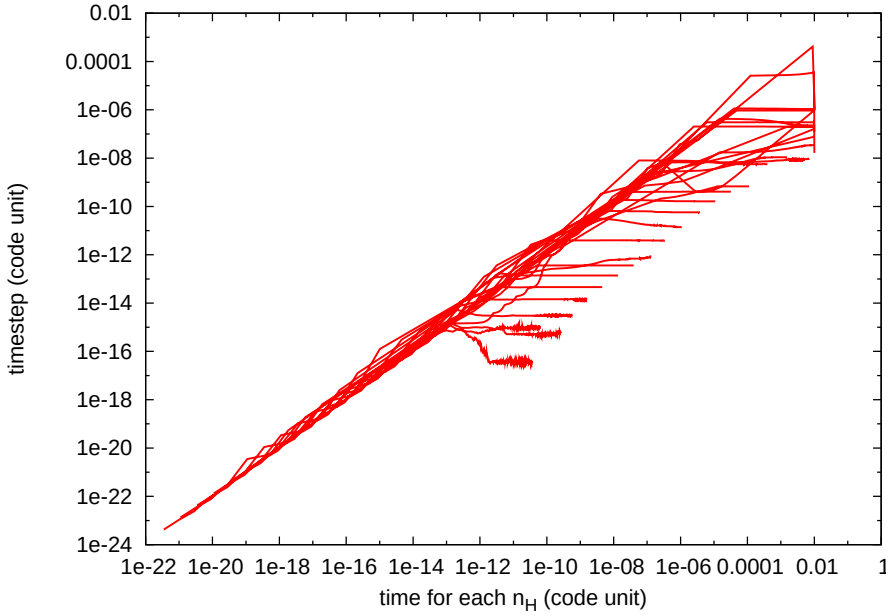

Figure 3.3: The time-step evolution versus the total integration time for each step of hydrogen number density n_H. When the plateau is reached, we can hope that equilibrium has been reached, and the calculation is stopped for this given density, proceeding to the next density step using the previous abundances as a new initial condition.

Numerical convergence In order to test for the accuracy of the calculation, we chose not to put a stringent criterion on the relative error, yet for the very faint species such a criterion is not very suited. We thus chose to stop the integration when the time-step reached a final value, meaning that only the faint species were still evolving. This can be seen Fig. 3.3.

Another convergence test is to take a look at the fractional abundances for a number of species at each density step. The x-axis are plotted in log and therefore are good indicators of the dynamical evolution of the elements. It is not hard proof, but can be used to justify that we jump to the next step. An overview of what it looks like can be seen Fig. 3.4.

3.1.2 Results

3.1.2.1 Retrieve previous work

Umebayashi and Nakano (1990) We first try to recover their Figures 2 and 4, corresponding to the simpliest cases with one bin size for grains. Our results can be seen on Figure 3.5 (done with the explicit method, in that time). It is very similar and satisfying.

Kunz and Mouschovias (2009) The next step is to add bin size for grains, more accurate collision rates for grains, as in Kunz and Mouschovias (2009). Details on the implementation of bin sizes can be found §3.1.1.2. Results concerning the accuracy can be seen Figure 3.2. We will discuss the accuracy on the final resistivities in §3.1.2.4 rather than trying to explain the differences now. Indeed, even though the global fractional abundance remains very similar (we implemented the bins that way !!!), a few bins cannot account accurately for the effect on the final conductivity, as most of the surface is due to the smallest grains. Figure 3.6 represents the fractional abundances of various species and of the grains (as a sum over all the bins) using 50 bins and no temperature evolution ($T = 10K$ and $\zeta = 1.10^{-17}s^{-1}$ for the whole density range). In order to implement inelastic

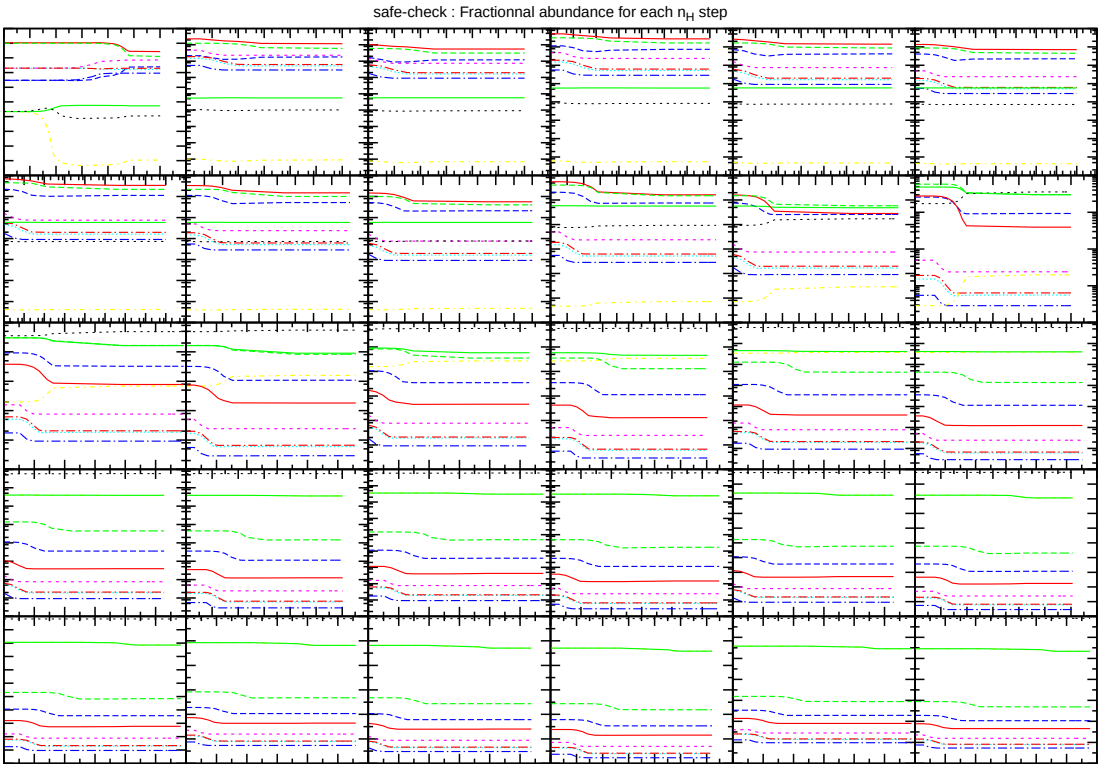

Figure 3.4: Time evolution for several density steps, used as a safe-check. The x-axis (representing time integration) is in logscale to better retrace the dynamical evolution of the abundances.

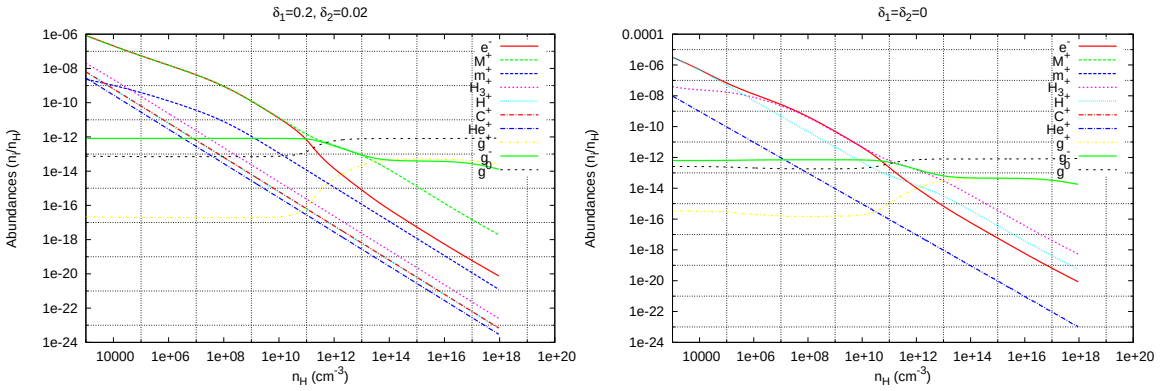

Figure 3.5: Abundances of various charged particles, to be compared to Figures 2 and 4 from Umebayashi and Nakano (1990). Left: $\delta_1 = 0.2$ and $\delta_2 = 0.02$. Right: $\delta_1 = \delta_2 = 0$.

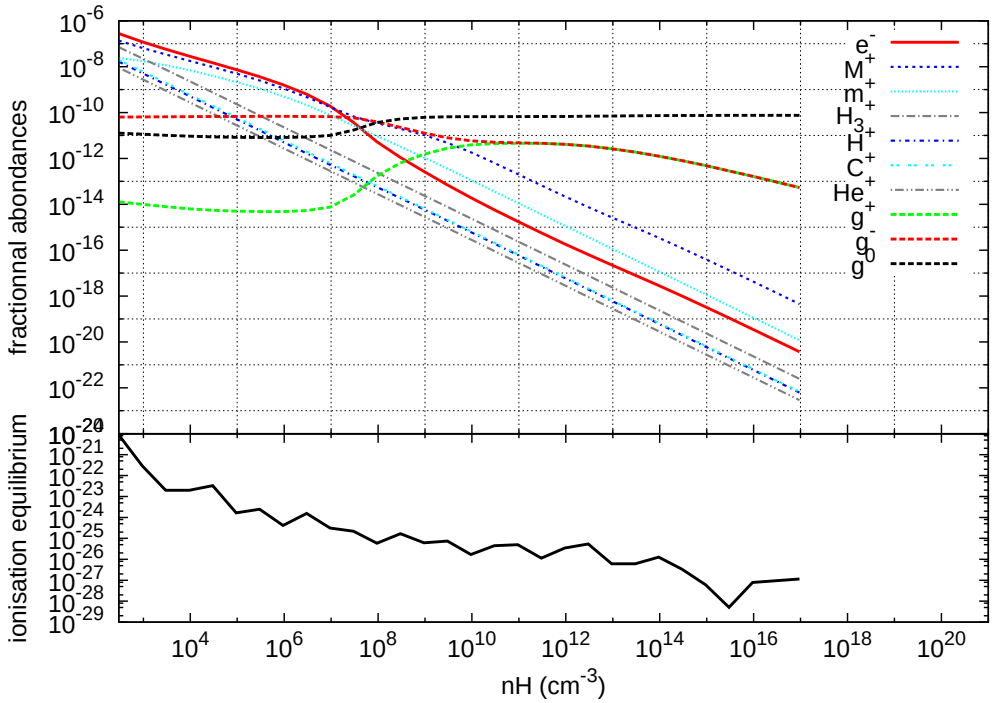

Figure 3.6: Fractional abundances using 50 bins. On the bottom is plotted the ionisation equilibrium ($\sum_{species>0} x_s - \sum_{species<0} x_s$), to check that the calculation is going well. This ionisation should remain equal to zero (up to machine precision).

collisions, one can refer to Appendix 3.C.

3.1.2.2 Temperature

We use a barotropic equation of states to account for the temperature evolution of the gas (see Figure 3.7). This equation is computed following the density at the center of a collapsing core in radiation hydrodynamics calculations. It cannot describe accurately the temperature in jets and outflows, or in the disk (or any three dimensional effect), but it is a good approximation for the temperature as a function of density only (and it is widely used). We use a smoothed version of the piecewise equation to avoid sharp transitions:

$$T = T_0 \sqrt{1 + (\frac{n_H}{n_1})^{2g_1}} (1 + (\frac{n_H}{n_2})^{g_2})(1 + (\frac{n_H}{n_3})^{g_3}) \tag{3.21}$$

with

$$\begin{aligned} n_1 &= 10^{11}\ cm^{-3} \\ n_2 &= 10^{16}\ cm^{-3} \\ n_3 &= 10^{21}\ cm^{-3} \\ g_1 &= 0.4 \\ g_2 &= -0.3 \\ g_3 &= 0.4 \end{aligned} \tag{3.22}$$

and $T_0 = 10\ K$.

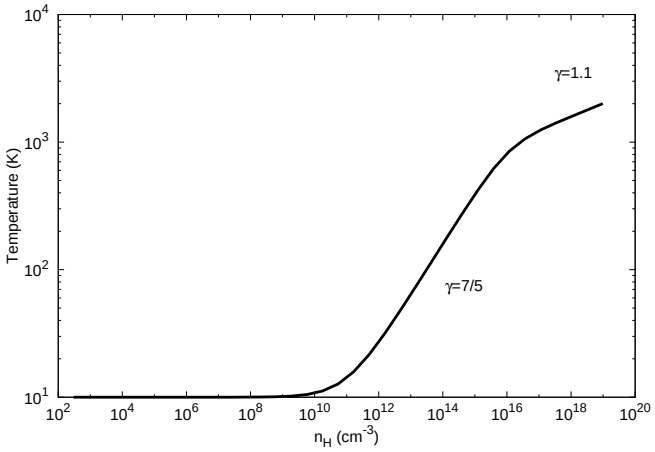

Figure 3.7: Piecewise barotropic equation of state used to evolve the temperature.

The results are shown Figure 3.8. Taking into account the temperature does not change which species are dominant but it substantially changes the abundances (in particular for electrons e^-, ions M^+ and charged grains g^+ and g^-. At a density $n_H = 10^{18}\ cm^{-3}$ the abundance of the charged grains is two order of magnitudes lower when taking into account the temperature even with a model as simple as a barotropic evolution.

3.1.2.3 Non-equilibrium chemistry

As first suggested thanks to a discussion with Ugo Hincelin, and confirmed with Patrick Hennebelle, a non-equilibrium chemistry is something to study precisely. In order to probe this effect, we use data from a spherical hydrodynamical collapse and input the evolution in temperature and density in our evolution code. We knowledgeably overestimate non-equilibrium effects by using a faster model of collapse compared to magnetized models to increase non-equilibrium differences.

With our simplified chemical network, using a time-dependant evolution since $n_H > 10^7$ cm^{-3}, we cannot highlight any significant difference from the equilibrium case, as can be seen Fig 3.9.

Conductivities We calculate the conductivities with the following formulae:

$$\sigma_{\parallel} = \sum_s \sigma_s \tag{3.23}$$

$$\sigma_{\perp} = \sum_s \frac{\sigma_s}{1 + (\omega_s \tau_{sn})^2} \tag{3.24}$$

$$\sigma_H = -\sum_s \frac{\sigma_s \omega_s \tau_s n}{1 + (\omega_s \tau_{sn})^2} \tag{3.25}$$

with:

$$\sigma_s = \frac{n_s q_s^2 \tau_{sn}}{m_s} \tag{3.26}$$

$$w_s = \frac{q_s B}{m_s c} \tag{3.27}$$

$$\tau_{sn} = \frac{1}{a_{sH_e}} \frac{m_s + m_{H_2}}{m_{H_2}} \frac{1}{n_{H_2} < \sigma_{coll} w >_{sH_2}} \tag{3.28}$$

where s stands for any charged particle. The factor a_{sH_e} accounts for collisions with helium atoms and is equal to 1.14 for ions, 1.16 for electrons and 1.28 for grains. The rate constant $< \sigma_{coll} w >_{sH_2}$

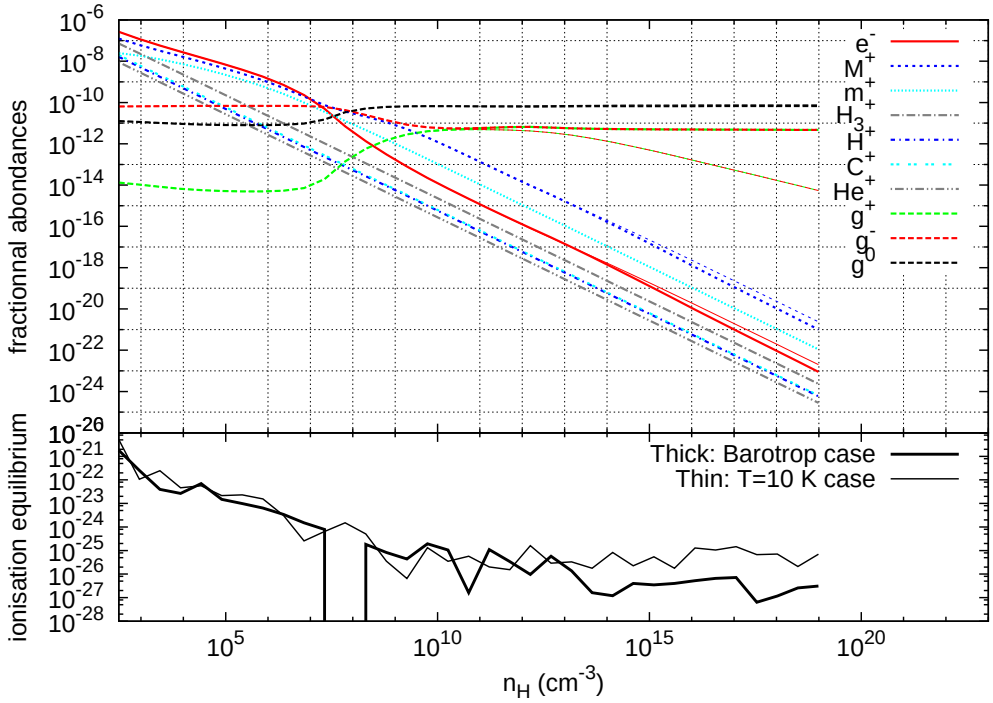

Figure 3.8: Fractional abundances using 5 bins. Thick lines (solid, dashed and dotted) stand for the barotropic case while thin lines (in particular for e^-, M^+ and charged grains g^+ and g^-) are the already presented constant $T = 10\ K$ case. On the bottom is plotted the ionisation equilibrium ($\sum_{species>0} x_s - \sum_{species<0} x_s$) for both cases.

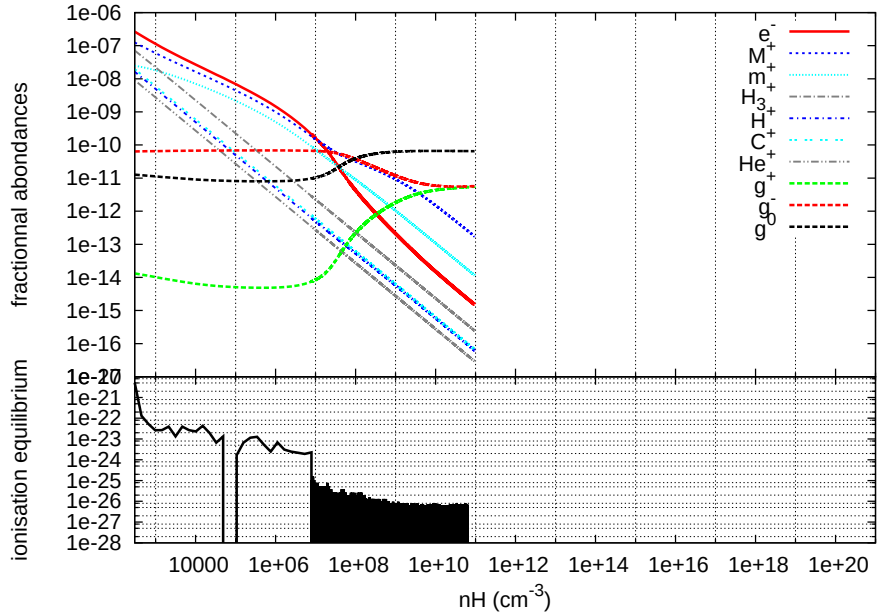

Figure 3.9: Fractional abundances using a time-dependant scheme, with a free-falling model.

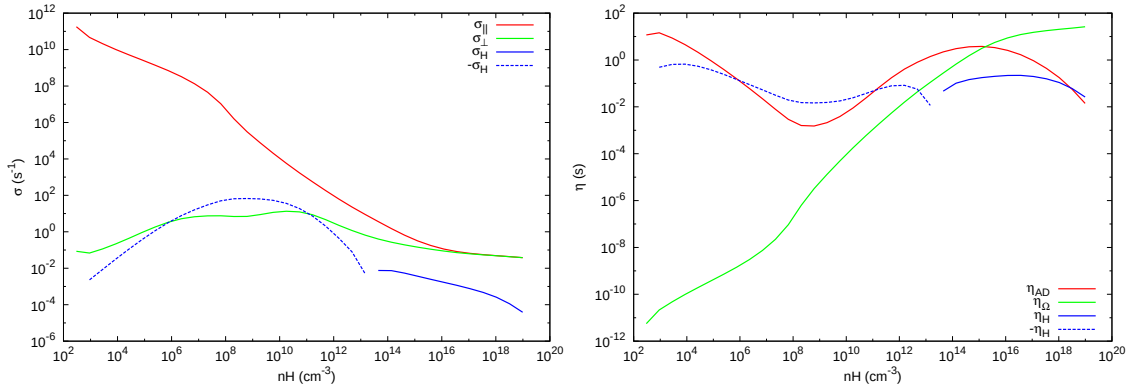

Figure 3.10: Left: conductivities as a function of the density. Solid lines represent positive values, while dashed lines represent negative values. Right: resistivities, with the same solid/dashed code as previously. Theses plots were made using the barotropic equation of states described in § 3.1.2.2, a ionisation rate $\zeta = 10^{-17}\ s^{-1}$ and 50 bins of grains.

for collisions between a particle s and molecular ions (m^+, H_3^+ etc.) or metal ions (M^+) is equal to $1.69 \times 10^{-9}\text{cm}^3\ \text{s}^{-1}$, $1.3 \times 10^{-9}\ \text{cm}^3\ \text{s}^{-1}$ for electrons, and $\pi r_g^2 \sqrt{\frac{8K_bT}{\pi m_{H_2}}}$ for grains.

Note that only ω_s can be negative, through the charge q_s. This has a tremendous importance when calculating the conductivities, as the hall conductivity σ_H can be either positive or negative.

A graphical review of this discussion can be seen Figure 3.10, where solid lines are positive values, and dashed lines are negative values.

3.1.2.4 Resistivities

Generalized Ohm's law Following Kunz and Mouschovias (2009) and Nakano et al. (2002), we obtain the following induction equation:

$$\begin{aligned}\frac{\partial \mathbf{B}}{\partial t} =& \nabla \times \Bigg[\mathbf{v} \times \mathbf{B} \\ & -\eta_\Omega (\nabla \times \mathbf{B}) \\ & -\eta_H \left\{ (\nabla \times \mathbf{B}) \times \frac{\mathbf{B}}{B} \right\} \\ & -\eta_{AD} \frac{\mathbf{B}}{B} \times \left\{ (\nabla \times \mathbf{B}) \times \frac{\mathbf{B}}{B} \right\} \Bigg]\end{aligned} \tag{3.29}$$

with the diffusivities defined as:

$$\eta_\Omega = \frac{1}{\sigma_\parallel} \tag{3.30}$$

$$\eta_H = \frac{\sigma_H}{\sigma_\perp^2 + \sigma_H^2} \tag{3.31}$$

$$\eta_{AD} = \frac{\sigma_\perp}{\sigma_\perp^2 + \sigma_H^2} - \frac{1}{\sigma_\parallel} \tag{3.32}$$

We note that the Hall resistivity can be negative, as it is of the same sign as σ_H. On the other hand, the ambipolar diffusion resistiviy is always positive:

- At low densities, $\sigma_\parallel \gg \sigma_\perp$ and then $\eta_{AD} \simeq \frac{\sigma_\perp}{\sigma_\perp^2+\sigma_H^2}$.
- At high densities, when the grains are the main charged particles, $\sigma_\parallel \simeq \sigma_\perp$, and $\sigma_\perp \gg \sigma_H$ which results in $\eta_{AD} \simeq \frac{1}{\sigma_\perp} - \frac{1}{\sigma_\parallel}$
- In a broader point of view, it is difficult to assess that $\eta_{AD} \geq 0$ throughout the whole range of densities. Indeed, if the Hall resistivity is high enough, we can have $\eta_{AD} \leq 0$

Comparison with previous work In order to derive conductivities without coupling the evolution code with an hydrodynamical code, we use a simple law to describe the evolution of the magnetic field (obtained through conservation of the magnetic flux). Following Li et al. (2011) the magnetic field to compute the resistivity is assumed to be only dependant on the density, as $B(n_H) = 1.43 \times 10^{-7}\sqrt{n_H}G$.

Figure 3.10 can be directly compared to Figures 7(a) and 7(b) of Kunz and Mouschovias (2010).

On the other hand, there is a very confusing problem when comparing with Li et al. (2011). In particular, their Figure 3 and the description going with it are in contradiction with our results (and in contradiction with Kunz and Mouschovias (2010)). They find negative ambipolar resistivity (and at high density, they find $\eta_{AD} \simeq \eta_\Omega$. In our case, $\sigma_H \ll 1$ which leads to $\eta_{AD} \simeq \frac{1}{\sigma_\perp} - \frac{1}{\sigma_\parallel}$ and a drop in the ambipolar resistivity (we see this Figure 3.10 or in Kunz and Mouschovias (2010)). We have no explanation for this since both the abundances and the conductivities they find are similar to ours (without the temperature dependency).

A comparison with previous approximations for the resisitivities are represented Fig. 3.11.

3.1.2.5 Ionisation rate

We use a constant ionisation rate equal to the fiducial value $\zeta = 1.10^{-17}s^{-1}$. The uncertainty on the ionisation rate is one of the flaws that could be improved greatly. Some work in progress show that complex phenomena happen when looking in the details of the ionization rate. Due to the pileup of toroidal field, the cosmic-rays can stay in the disk longer. Pioneering work has been done by Padovani and Galli (2013). They consider cosmic-rays propagation in an idealized magnetic field shaped in an hourglass, fitted for core collapse. Two effects compete when integrating the cosmic-rays propagation along filed lines: magnetic focusing which increases the ionisation rate, and magnetic mirroring that prevents cosmic-rays to reach deep parts of the cloud. They find that mirroring always dominates in this topology of the field. Depending on the mass-to-flux ratio and the magnetic flux tube considered, the ionisation rate is divided by up to a factor 5.

We tried to compute abundances and resistivities using $\zeta = 5.10^{-18}s^{-1}$ and $\zeta = 1.10^{-18}s^{-1}$. Results for the resistivities are shown Fig. 3.12. For both ambipolar diffusion and Ohmic dissipation, reducing the ionisation rate yields overall larger resistivities. The Hall effect, on the contrary, is diminished. Using the fiducial value $\zeta = 1.10^{-17}s^{-1}$ therefore underestimates the effects from ambipolar diffusion and Ohmic dissipation.

3.2 An accurate equation of state

3.2.1 Justification

The second collapse begins in the dihydrogen dissociation phase. An accurate description of the equation of state of a mixture of dihydrogen and other elements (helium and hydrogen mostly) allow for a more detailed study of this and every phase of the collapse. Instead of using an ideal gas equation of state, the low-temperature addition to the Saumon-Chabrier equation of state (see Saumon et al. (1995)) allows to self-consistently describe the thermodynamical evolution of a collapsing cloud.

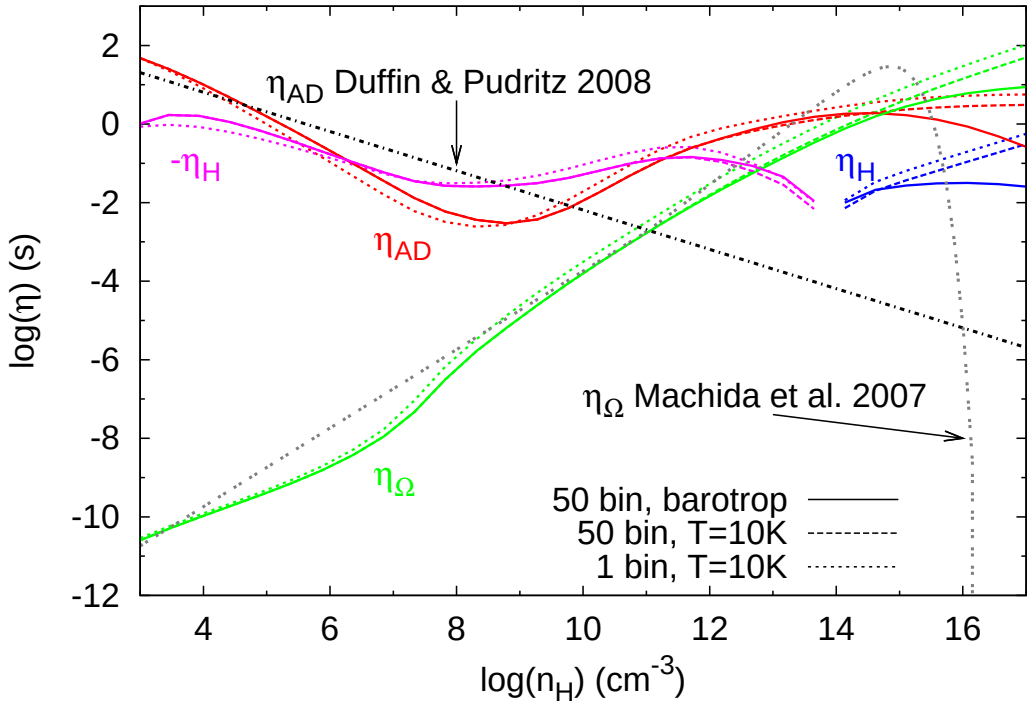

Figure 3.11: Resistivities for various cases and comparison with previous work. Thick lines correspond to the barotropic case, with 50 bins. Dashed lines correspond to the case with a constant temperature $T = 10\ K$, with 50 bins. Dotted lines correspond to the case with a constant temperature $T = 10\ K$, with 1 bin. Lines are color-coded to represent various resistivities: red (respectively green, purple and blue) is the ambipolar (respectively Ohmic, Hall (positive) and Hall (negative)) resistivity. Ambipolar resistivity taken from Duffin and Pudritz (2008) is plotted as the black dash-dotted line. Ohmic resistivity taken from Machida et al. (2007b) is plotted as the grey double-dotted line.

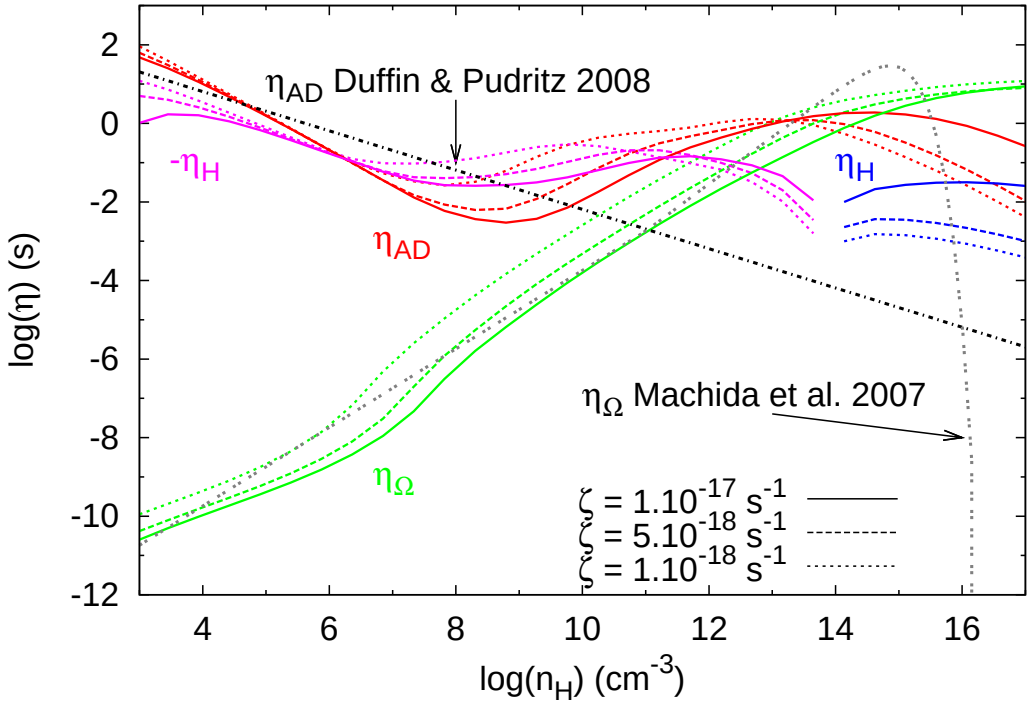

Figure 3.12: Resistivities for different ionisation rates. Solid lines: fiducial value $\zeta_{\rm ref} = 1.10^{-17} s^{-1}$. Long dashed lines: $\zeta = \frac{zeta_{\rm ref}}{2} = 5.10^{-18} s^{-1}$. Short dashed lines: $\zeta = \frac{zeta_{\rm ref}}{10} = 1.10^{-18} s^{-1}$.

3.2.2 Implementation

Using an equation of states supposes to solve for the energy equation. Therefore, it replaces the barotropic equation of state we used until then. There are still two different cases: when using the equation of state with or without radiative transfer.

Case with radiative transfer In this case, the set of equations (including the energy equation) is solved at each time step. The need for an equation of state comes from the expression of the pressure P and the heat capacity at constant volume C_V, which appear in various equations in the radiative solver (details can be found in Commerçon et al. (2010)). These variables are determined using the EOS, as a function of the density and specific energy. In order to update the internal energy at the end of the radiative step, we translate the energy in terms of temperature and density.

The cooling is naturally taken into account through the energy equation, and the total energy $(\rho e + e_{\rm kinetic} + e_{\rm magnetic} + e_{\rm radiative})$ is correctly updated without anymore work.

Case without radiative transfer The energy equation is solved, without the radiative transfer terms. Then, an artificial cooling can be used to describe approximately the effects of radiative transfer (like cooling described in Neufeld et al. (1995)).

Until now, a barotropic equation of state was used, and the total energy was updated at each time step according to this equation.

Now, we want to use an accurate EOS. The idea is to force the gas to stay at 10 K during the isothermal collapse (until the density reaches $\rho_c \simeq 3.810^{-13} g.cm^{-3}$), by setting the internal energy to the needed value. Then, as the adiabatic phase begins, we don't overwrite the total energy: the equation of energy is the correct one even without transfer, as long as the opacity is high enough for

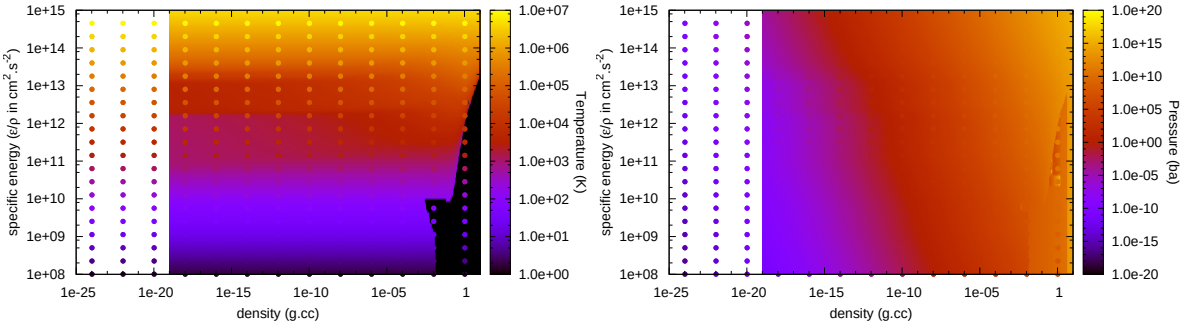

Figure 3.13: Comparison between ideal gas (colored dots) and Saumon et al. (1995) (colormap) for two thermodynamical variables. Left: temperature. Right: pressure.

the evolution to be adiabatic.

$$\text{If } \rho < \rho_c \text{ then } \rho e_{tot} = \frac{T_{cloud}\ nH\ k_b}{\gamma - 1} + e_{kin} + e_{mag} \tag{3.33}$$

$$\text{If } \rho \geq \rho_c \text{ then } \rho e_{tot} = \rho e_{tot}^{\text{given by the godunov solver}} \tag{3.34}$$

In the case of an ideal gas EOS, the pressure is calculated using $P = (\gamma - 1)\rho e_{int}$, which gives the correct value in both the adiabatic case $\rho \geq \rho_c$ and isothermal case $\rho < \rho_c$. When using a complex EOS, the assumption is made that during the isothermal collapse the gas is close to an ideal gas, as we use it to overwrite the internal energy which is then used to calculate the pressure. This is close to be true, as can be seen in Figure 3.13.

3.2.3 Tests

The first tests were performed without magnetic fields, and with no rotation. The initial setup is an homogeneous sphere sitting in a less dense environment.

3.2.3.1 Direct implementation of the EOS, without radiative transfert or cooling

We first tried to use the ideal gas EOS, as this should be easily compared with previous cases up to the first Larson core. We used a smoothing function to go from the isothermal to adiabatic phase.

The tests were unsuccessful, as can be seen Fig. 3.14. The isothermal phase is correctly described but as soon as the the gas begins to warm up, problems arise. The heat is traped in the cloud and results in an unphysical heating of all the dense regions.

Absence of radiative transfer along with an equation of states lead to problems Neither an ideal gas nor a complex EOS can work on their own. We need to add some cooling (either using a full radiative solver or cooling functions).

Without transfer or cooling, there are two problems:

- On the one hand we have to artificially keep the gas at 10K at the beginning, overwriting the internal energy with a hacked value corresponding to 10K at a given density. On the other hand, we make the assumption that when the density reaches the threshold, then the total energy given by the Godunov solver is the correct one, and we just use it at the next time step.

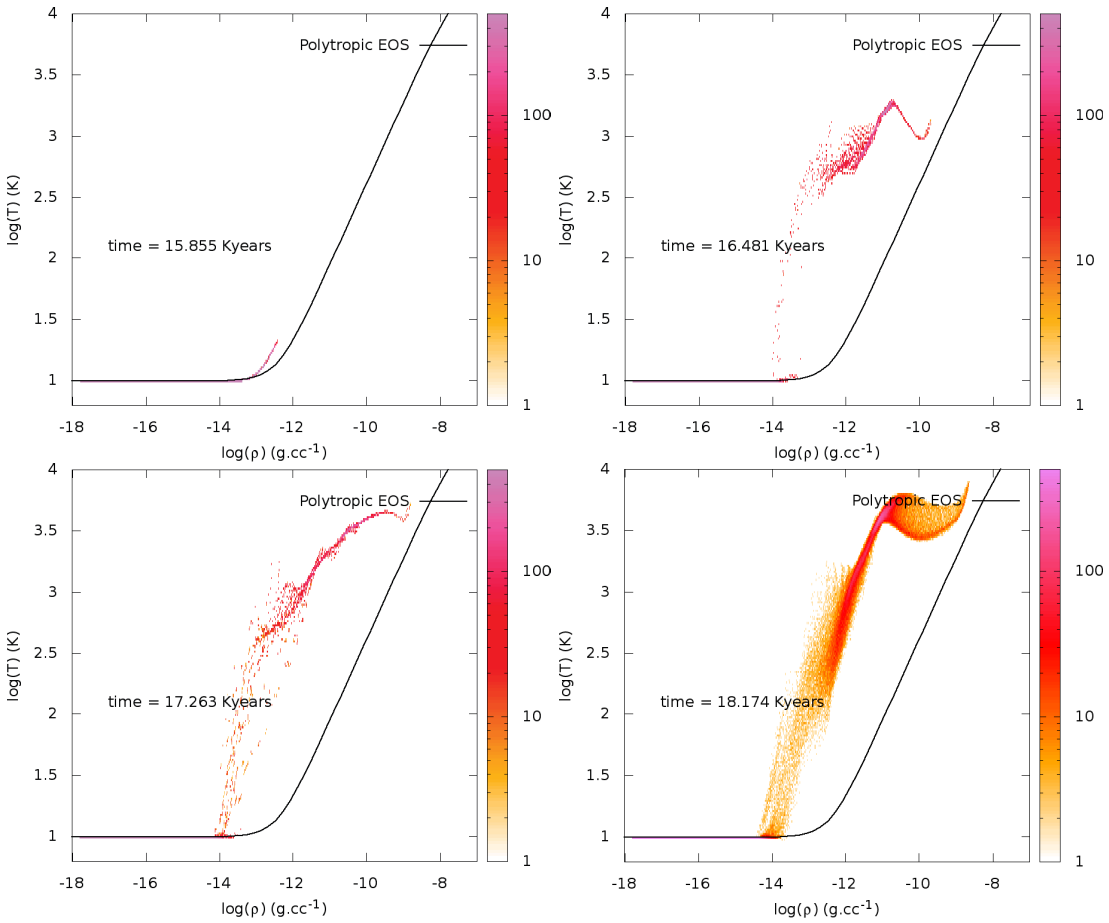

Figure 3.14: ideal gas EOS. Pressure versus density at various times. The color scale represent the number of cells at a given density and temperature.

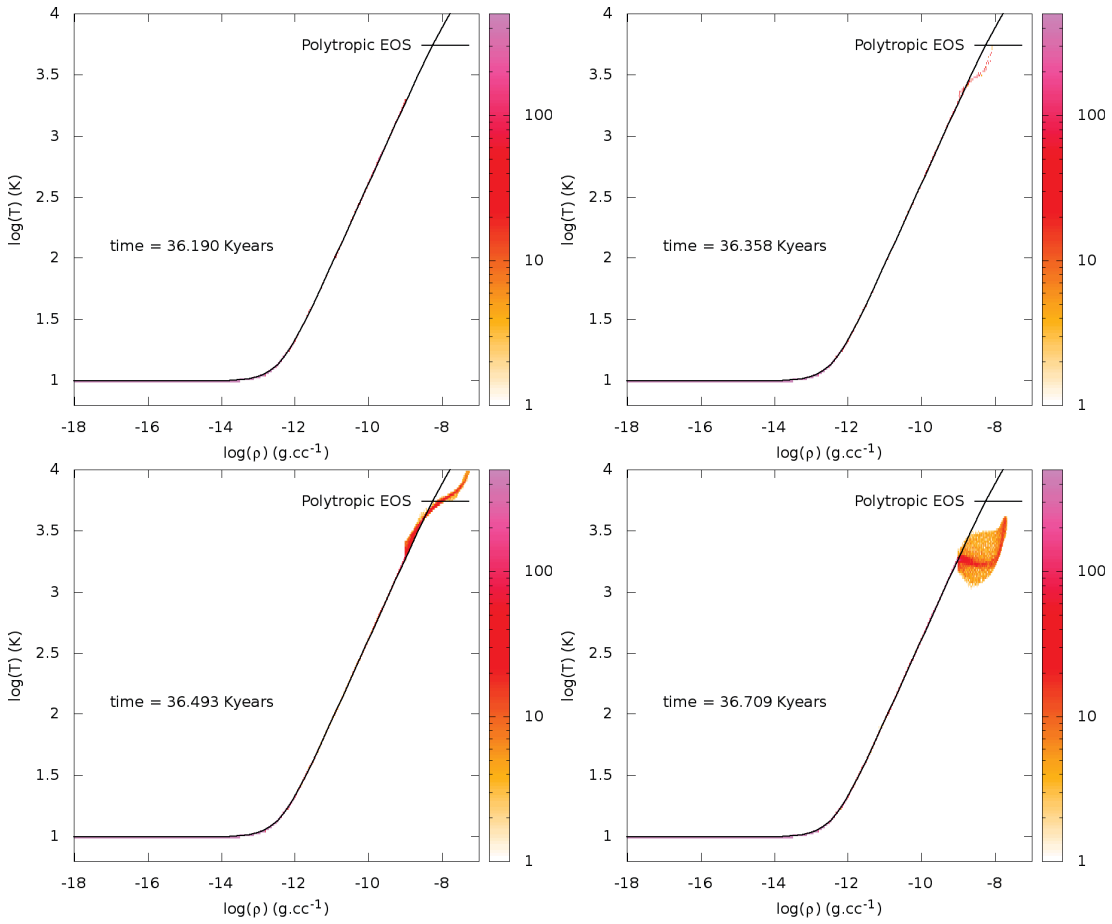

Figure 3.15: ideal gas EOS. Pressure versus density at various times. The color scale represent the number of cells at a given density and temperature. Result when the switching density threshold is set to $\rho = 10^{-8} g.cm^{-3}$, using a barotropic law for the pressure.

- This might not be so simple: if the first accretion shock moves a little, then we can have cells at a lower density but already through the shock, or the contrary. Which means that going from isothermal to adiabatic evolution should probably not be defined by a threshold.

We also tried to overwrite the internal energy up to $\rho = 10^{-8}$ g.cm^{-3}, using the usual barotropic law. Above, we switch to using the raw energy without overwriting it. We thought it might avoid the issue of the shock, as well as being more advanced on the adiabatic part of the collapse, but it doesn't seem to work well either. The plots are on Figure 3.15. We correctly retrieve the collapse while overwriting the internal energy, which is exactly what is done when using the barotropic law. Again, as soon as we relax the constraints and hope for an adiabatic evolution for the densest parts, the temperature goes off-track. We can conclude that even if qualified and considered adiabatic, the latter stages of the collapse can't be accurately describe using an equation of state without transfer or cooling.

3.2.3.2 Solving the full radiation hydrodynamics set of equation

The arrow of eigenvalues used for the radiative case doesn't need to be changed when using an equation of states compared to the ideal gas case. It is enough to calculate the equivalent heat

capacity C_V using the equation of states chosen. For an ideal gas, $C_V = \frac{e}{T}$. This relationship fails to describe a real gas and we use the more general formula:

$$C_v = \frac{\partial e}{\partial T}\Big]_V \tag{3.35}$$

The radiation hydrodynamics solver uses a constant ratio of specific heats $\gamma = \frac{5}{3}$. In the real case when using a realistic equation of state, this can be changed to use the exact value for the ratio of specific heats. This value is then used to compute the waves speed for the Riemann solver. However, our tests led to the conclusion that using a constant value $\gamma = \frac{5}{3}$ was only adding some diffusivity. Since radiation hydrodynamics are very time-consuming we chose for a start to keep the constant value $\gamma = \frac{5}{3}$ to be able to carry out simulations up to the second Larson core.

For details on the radiation hydrodynamics itself, refer to § 2.3.

3.2.3.3 Refining the grid

In order to follow the collapse up to the second core, we have to cautiously define the refinement criterion. The Jeans length scales linearly with the sound speed $c_s = \sqrt{\frac{\gamma P}{\rho}}$ and with $\rho^{-\frac{1}{2}}$. As the collapse proceeds and reaches dihydrogen dissociation, the pressure increases by ~ 1 order of magnitude (same as the temperature) while density increases by ~ 4 orders of magnitude, compared to the first core. The ratio of specific heats changes from a monoatomic gas of dihydrogen to a diatomic gas of hydrogen molecules, but its order of magnitude is unchanged. Therefore the sound speed drops by ~ 1 to 2 orders of magnitude. Finally, the Jeans length drops by about 3 to 4 orders of magnitude. According to Vaytet et al. (2013a), the second cores is ~ 4 orders of magnitude smaller than the first core. Accordingly, the resolution is lower for the second compared to the first core. Note that the mass inside a cell (or Jeans length) is not constant: $M \propto \frac{T^{\frac{3}{2}}}{\rho^2}$. One way to add resolution in the cores while keeping low resolution for the outer parts is to get rid of the temperature dependency. Computing the sound speed using the external temperature T= 10K increases the resolution for regions where T> 10K. In this case, $M \propto \frac{1}{\rho^2}$.

More numerical tests have to be performed in order to define an appropriate refinement criterion. Both adding resolution everywhere or using an isothermal sound speed with a lower global resolution seem to work. The later is more difficult to control *a priori* but may when properly used end up with a lower computational cost, since resolution is theoretically added only when the temperature is significantly higher than 10K.

3.2.4 Outflow temperature

We conducted two simulations with radiative transfer, until after the formation of the outflow. As explained in § 4.2, the outflow is more clearly visible in the aligned non turbulent case, with a mass-to-flux ratio greater than 2. We used $\mu = 5$, no turbulence, a ratio of rotational to gravitational energy of 30% to easily create outflows and a ratio of thermal to gravitational energy of 30%.

First, we show Fig. 3.16 the temperature histogram in function of density, to validate the method used. We didn't follow these simulations up to the second core, because we focused on outflow properties.

Heating in the outflow has been studied by Panoglou et al. (2012). They found that the main contributor is the heating due to ambipolar diffusion. We can simulate this using the non-ideal MHD along with radiative transfer and an accurate equation of states for the first time in a full three dimensional code. We plot Fig. 3.17 the evolution (from left to right) of the outflow temperature

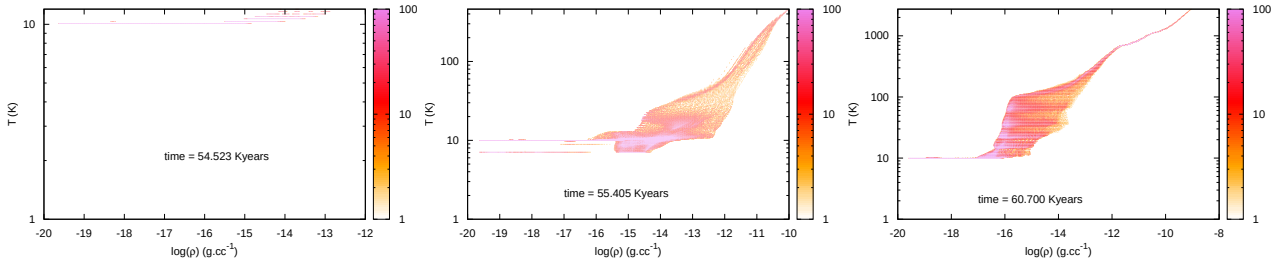

Figure 3.16: Temperature as a function of density. The colormap show the number of cells at a given (T, ρ). We show three differents times (evolution from left to right), up to H_2 dissociation, in the case of ideal MHD.

and density. At a given time, the outflow in the ideal MHD case is more developed than in the AD case, as will be pointed out in § 4.2. We chose to represent also an earlier time for the ideal MHD case to better compare with the AD case, when the outflow is of the same height. The conclusion is clearly visible on the two right plots: the outflow cavity has a different temperature in both cases. Its temperature is close to 10 K everywhere in the AD case, with a slight increase at the edge of the cavity where $T \sim 12$ K. In the ideal MHD case, the edge of the cavity is at the same temperature $T \sim 12$ K, but the inner parts are colder by a few degrees: $T \gtrsim 7$ K. The coldest part are also located in different regions: right above the core in the AD case, and closer to the edge on the ideal MHD case. In the AD case, it is located where the outflow cavity is less dense than in the ideal MHD case. At a time matching the one of the AD case, the temperature in the ideal MHD case rises but is still lower than in the AD case at the same time, even though comparison is more difficult due to the very different evolution. We can conclude that this heating effect is relevant, because the coldest case (ideal MHD) is also the densest case, where we would expect greater temperature when using a barotropic equation of states. Therefore, ambipolar diffusion indeed has an important effect on the heating of the gas in the outflow cavity, as reported by Panoglou et al. (2012). We also note in both cases a very thin needle of low temperature, from ~ 100 a.u. above and below the core and with a radius ~ 10 a.u. and growing as a function of the height. This is not physical and is a consequence of the azimuthal mean: there are no refined cells at this height, and therefore no temperature data.

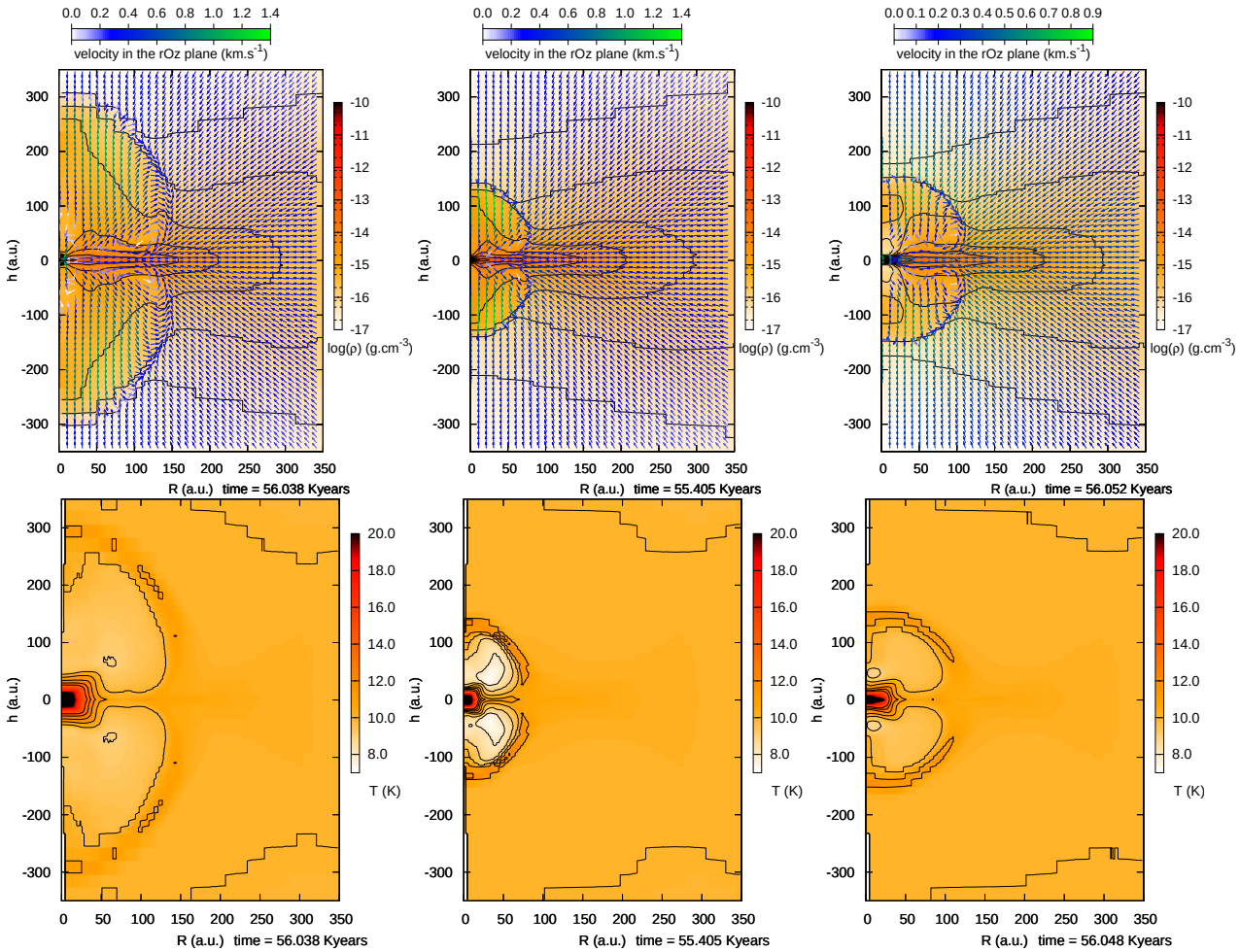

Figure 3.17: Top: density/velocity maps. Bottom: temperature maps. From left to right: (left) ideal MHD case at 56 kyears; (middle) ideal MHD case at 55.4 kyears, when outflow cavity is of the same size as for the AD case; (right) AD case.

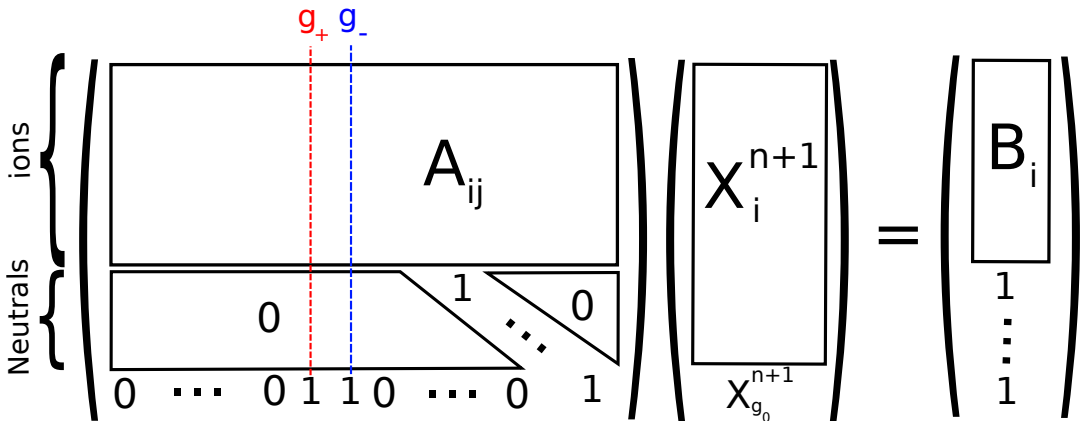

Figure 3.18: Matrix visualisation of the system to solve after linearisation in time.

3.A Jacobian matrix

The Jacobian general expression (for charged particles only, neutral grains are taken care of separately) is the following:

$$\begin{aligned} J_{ij} &= \frac{\partial F_i}{\partial x_j} \\ &= \alpha_{ij} + \sum_{k=1}^{N} \beta_{ijk} x_k - \gamma_{ij} x_i - \delta_{ij} \sum_{k=1}^{N} \gamma_{ik} x_k. \end{aligned} \tag{3.36}$$

The Jacobian expression for neutral grains in the bin α is the following:

$$J_{g_0^\alpha j} = -J_{g_+^\alpha j} - J_{g_-^\alpha j}. \tag{3.37}$$

This makes the Jacobian matrix J singular, and is a major issue when performing newton-Raphson iteration. Nevertheless, it's not a problem for the semi implicit method, and we won't focus on how to calculate a non-singular Jacobian only for the purpose of the implicit method (a simple solution is to restraint the calculated species to charged particles only and then at the end of the iteration update neutral grains).

3.B Linearised system

The linearised system looks like Figure 3.18, with:

$$A_{ij} = \delta_{ij} - \tilde{dt}\big[\alpha_{ij} - \frac{n_H}{\zeta}\gamma_{ij} x_i^n + \frac{n_H}{\zeta} \sum_{k=1}^{N} (\beta_{ijk} - \gamma_{ik}\delta_{ij}) x_k^n\big], \tag{3.38}$$

$$B_i = \frac{n_H}{\zeta}\big[\sum_{j=1}^{N} \gamma_{ij} x_j^n x_i^n - \frac{1}{2}\sum_{j=1}^{N}\sum_{k=1}^{N} \beta_{ijk} x_j^n x_k^n\big]\tilde{dt} + x_i^n. \tag{3.39}$$

3.C Inelastic collisions

In this appendix, we add a few comments in order to implement multiple bins of different sizes and inelastic collisions, as described in Kunz and Mouschovias (2009).

Using their definitions for Ψ_1, Ψ_2 and Ψ_3, we get:

$$\zeta_s = \frac{\varrho_s}{1+\varrho_s}\left(1 - \frac{\Psi_1}{\omega_s\tau_{sn}}\right), \tag{3.40}$$

$$\bar{\omega}_s = \frac{\varrho_s}{1+\varrho_s}\left(1 + \frac{\zeta_s}{\varrho_s} - \frac{\Psi_2 + \Psi_3\Psi_1}{(\omega_s\tau_{sn})^2}\right), \tag{3.41}$$

$$\begin{aligned}\varphi_s = &\frac{\varrho_s(2+\varrho_s)}{(1+\varrho_s)^2}\left(1 - \frac{\Psi_{2,s} + \Psi_3\Psi_{1,s}}{(\omega_s\tau_{sn})^2}\right), \\ &+ \frac{\varrho_s}{(1+\varrho_s)^2}\left(\frac{\Psi_{2,s} + \Psi_3\Psi_{1,s}}{(\omega_s\tau_{sn})^2} - \frac{\Psi_{1,s}}{\omega_s\tau_{sn}}\right).\end{aligned} \tag{3.42}$$

We also needed to redefine the matrix A and ϑ (e.g. the non-diagonal terms) since in the multibin case we can't put $\omega_k\tau_{sk}$ in factor:

$$[A]_{sk} = [1 + \omega_s^2\tau_{sn}^2(1-\varphi_s)]\delta_{sk} + \theta_{sk}(1-\delta_{sk}), \tag{3.43}$$

$$\theta_{sk} = \frac{\omega_s\tau_{sn}}{1+\varrho_s}\left(\frac{\varrho_s}{1+\varrho_s}\Psi_{1,k}\right) + \frac{\varrho_s}{1+\varrho_s}\left(\Psi_{2,k} + \Psi_3\Psi_{1,k}\right), \tag{3.44}$$

$$\vartheta_{g_\pm g_\mp} = \frac{\varrho_\pm}{1+\varrho_\pm}\frac{\tau_0}{\tau_{g_0 n}}\frac{1}{1+\varrho_\mp}\left[\frac{\frac{1}{1+\varrho_\mp} - \frac{1}{1+\varrho_\pm}}{\frac{\tau_0}{\tau_{g_0 n}} + \sum_k \frac{\tau_0}{\tau_{k,inel}}\frac{1}{1+\varrho_k}} + \frac{\frac{\tau_0}{\tau_{\mp,inel}}\frac{\varrho_\mp}{(1+\varrho_\mp)^2} - \frac{\tau_0}{\tau_{\pm,inel}}\frac{\varrho_\pm}{(1+\varrho_\pm)^2}}{[\frac{\tau_0}{\tau_{g_0 n}} + \sum_k \frac{\tau_0}{\tau_{k,inel}}\frac{1}{1+\varrho_k}]^2}\right]. \tag{3.45}$$

These expressions are not too demanding to compute, since for a given temperature they can be calculated once and for all.

Perpendicular components of the current density We have to solve

$$C^\perp\frac{c}{B}\mathbf{E}_{\mathbf{n},\perp} - C^H\frac{c}{B}\mathbf{E}_\mathbf{n}\times\mathbf{b} = \mathbf{A}\mathbf{W}_\perp \tag{3.46}$$

with

$$[A]_{sk} = [1 + \omega_s^2\tau_{sn}^2(1-\varphi_s)]\delta_{sk} + \theta_{sk}(1-\delta_{sk}), \tag{3.47}$$

$$[C^\perp]_s = \omega_s\tau_{sn}(1-\zeta_s), \tag{3.48}$$

$$[C^H]_s = -(\omega_s\tau_{sn})^2(1-\bar{\omega}_s). \tag{3.49}$$

This is in fact two Kramer's systems of equation, yielding the solution:

$$\omega_{\mathbf{s},\perp} = \frac{D_s^\perp}{D}\frac{c}{B}\mathbf{E}_{\mathbf{n},\perp} - \frac{D_s^H}{D}\frac{c}{B}\mathbf{E}_\mathbf{n}\times\mathbf{b} \tag{3.50}$$

with

$$D = det[\mathbf{A}], \tag{3.51}$$

$$D_s^\perp = det[\mathbf{A}_\mathbf{s}^\perp], \tag{3.52}$$

$$D_s^H = det[\mathbf{A}_\mathbf{s}^\mathbf{H}]. \tag{3.53}$$

where $\mathbf{A}_\mathbf{s}^\perp$ (resp. $\mathbf{A}_\mathbf{s}^\mathbf{H}$) is the matrix $\mathbf{A}$ with the sth column being replaced by $\mathbf{C}_\perp$ (resp. $\mathbf{C}_\mathbf{H}$). The perpendicular component of the current density is therefore:

$$\mathbf{j}_\perp = \sum_s n_s q_s \omega_{\mathbf{s},\perp} \tag{3.54}$$

$$= \sum_s \frac{D_s^\perp}{D}\frac{c}{B}\mathbf{E}_{\mathbf{n},\perp} - \frac{D_s^H}{D}\frac{c}{B}\mathbf{E}_\mathbf{n}. \tag{3.55}$$

In the simpler case where no inelastic collisions are considered, $\mathbf{A}$ is reduced to a diagonal matrix:

$$[A]_{sk} = [1 + \omega_s^2 \tau_{sn}^2]\delta_{sk} = a_s \delta_{sk} \tag{3.56}$$

and then, $\sum_s \frac{n_s q_s D_s^\perp}{D} = \sum_s \frac{a_1 ... a_{s-1} C_s^\perp a_{s+1} ... a_N}{\prod_k a_k} = \sum_s \frac{C_s^\perp}{a_s}$ (and the same for the Hall part), which is the standard form of the conductivities. On the other hand, when taking into account bin sizes, the sum cannot be simplified since its expression is:

$$\sum_s \frac{n_s q_s D_s^\perp}{D} = \sum_s \frac{\sum_i C_i^\perp \mathrm{Cof}_A(i,s)}{\sum_j [A]_{j,s} \mathrm{Cof}_A(j,s)}. \tag{3.57}$$

Multiplying by a diagonal matrix $[D_A]_{ij} = \frac{1}{a_{ij}}\delta_{ij}$ is useful as it will remind us of the standard form. Indeed, $\frac{det[D_A \mathbf{A}_\mathbf{s}^\perp]}{det[D_A \mathbf{A}]} = \frac{det[\mathbf{A}_\mathbf{s}^\perp]}{det[\mathbf{A}]}$ and

$$\begin{aligned} \sum_s \frac{n_s q_s D_s^\perp}{D} &= \sum_s \frac{\sum_i \frac{C_i^\perp}{1+\omega_i^2 \tau_{in}^2 (1-\varphi_i)} \mathrm{Cof}_{D_A \mathbf{A}_\mathbf{s}^\perp (i,s)}}{det[D_A \mathbf{A}]}, \\ &= \sum_s \frac{C_s^\perp}{1 + \omega_s^2 \tau_{sn}^2 (1-\varphi_s)} \sum_i \frac{\mathrm{Cof}_{D_A \mathbf{A}_\mathbf{s}^\perp (s,i)}}{det[D_A \mathbf{A}]}. \end{aligned} \tag{3.58}$$

Finally, we get

$$\begin{aligned} \mathbf{j}_\perp &= \sum_s \frac{D_s^\perp}{D} \frac{c}{B} \mathbf{E}_{\mathbf{n},\perp} - \frac{D_s^H}{D} \frac{c}{B} \mathbf{E}_\mathbf{n} \\ &= \sum_s \frac{\sigma_s (1-\zeta_s)}{1 + \omega_s^2 \tau_{sn}^2 (1-\varphi_s)} \Upsilon_s(\perp) \mathbf{E}_{\mathbf{n},\perp} + \sum_s \frac{\sigma_s \omega_s \tau_{sn} (1-\bar{\omega_s})}{1 + \omega_s^2 \tau_{sn}^2 (1-\varphi_s)} \Upsilon_s(\mathrm{H}) \mathbf{E}_\mathbf{n} \times \mathbf{b} \end{aligned} \tag{3.59}$$

with

$$\Upsilon_s(\perp) = \sum_i \frac{\mathrm{Cof}_{D_A \mathbf{A}_\mathbf{s}^\perp (s,i)}}{det[D_A \mathbf{A}]}, \tag{3.60}$$

$$\Upsilon_s(\mathrm{H}) = \sum_i \frac{\mathrm{Cof}_{D_A \mathbf{A}_\mathbf{s}^\mathbf{H} (s,i)}}{det[D_A \mathbf{A}]}. \tag{3.61}$$

Chapter 4

Numerical experiments

"*It is surrounded by a thin flat ring, inclined to the ecliptic, and nowhere touches the body of the planet.*"

Christiaan Huygens, original Latin: "Annulo cingitur, tenui, plano, nusquam cohaerente, ad eclipticam inclinato," De Saturni luna observato nova, 1656.

Contents

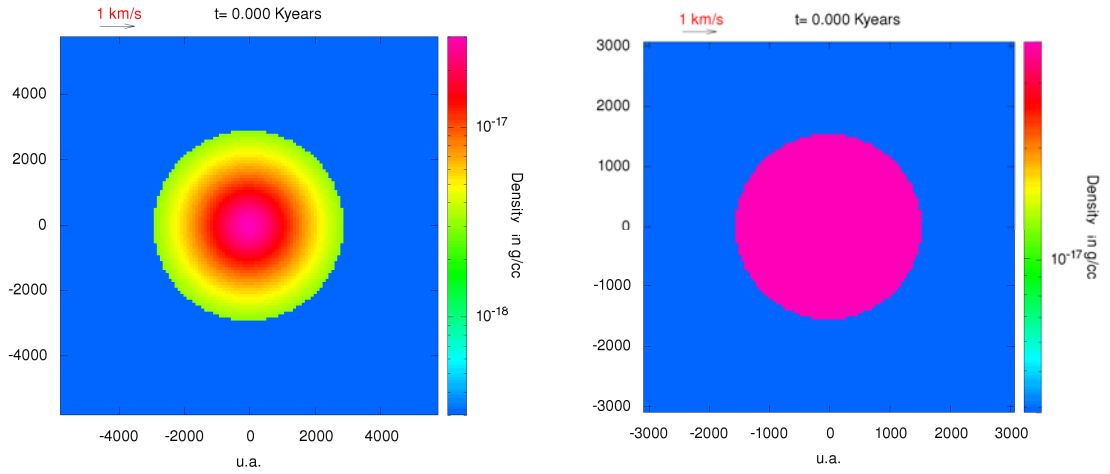

Figure 4.1: Initial density map for both a Bonner-Ebert (left) and a constant density profile (right).

Introduction

In this chapter we present simulations conducted during this thesis. We begin with a note on magnetic fields related to the question of initial conditions. Then we focus on a detailed study of the first core formation and the consequences of using non-ideal MHD. We follow by presenting second Larson core simulations in ideal and non-ideal MHD. Finally, we show a study on the kinetic ABC dynamo.

4.1 Initial conditions in magnetic clouds

We introduce or discuss in this chapter some fundamental notions in numerical core collapse simulations. We explore the difficulties lying in the definition of something as simple as the mass-to-flux ratio, the consequences of a different initial density profile and highlight some of the results concerning angular momentum transfer in an ideal MHD and non-ideal MHD framework. Physical results of non-ideal magnetohydrodynamics effects on first core simulations are presented § 4.2.

4.1.1 General setup

We seek to make understandable comparisons between two widely used initial density profiles in star formation studies. In particular, we highlight differences in the degree and the measure of magnetization in both cases. We also discuss the use of the mass-to-flux ratio as an indicator for stability, and how to derive a quantity to measure the magnetic strength in any topology of the field. We won't focus on consequences for the physics of the collapse and the protostars in this discussion, as this will be discussed § 4.2.1.

The first case is a Bonnor-Ebert profile, characterized by a density scaling as r^2 with a flatter profile at the center. The ratio of thermal to gravitational energy controls the stability of the initial cloud against gravitational collapse. The other initial condition used is a flat density, with a mass greater than the Jeans mass, again to allow gravitational collapse. The density maps corresponding to these density profiles can be seen Fig. 4.1

In both cases, the dense core is embedded in a medium several times (usually ten times) less dense. The size of the box is set to be twice the diameter of the instable core.

The initial magnetic field is along the z-direction. Its intensity is only dependent on the cylindrical radius r, which ensures that the divergence free condition is verified for initial conditions. Indeed, since $\mathbf{B} = B(r)\mathbf{e_z}$,

$$\nabla \cdot \mathbf{B} = \frac{\partial B(r)}{\partial z} = 0. \tag{4.1}$$

In the case of the Bonnor-Ebert profile, the intensity of the magnetic field scales as $B(r) \propto \frac{\Sigma(r)}{\Sigma_{max}}$, where Σ is the column density. This setup tries to mimic the fact that the field lines strengthen up while the collapse is occurring, dragged by the infalling matter. For the flat profile the magnetic field is constant in the core, and divided by the same number as the density outside of the core.

The first difficulty arises when calculating the mass-to-flux ratio. As explained in § 1.1.3 it serves as a global indicator for stability through magnetic support against collapse in the case of a uniformly dense sphere embedded in a homogeneous magnetic field. We define a radius dependent indicator that we call $\mu(r)$, defined as:

$$\mu(r) = \frac{(\frac{M(r)}{\phi(r)})}{(\frac{M}{\phi})_{crit}} \tag{4.2}$$

with $M(r)$ the mass in a sphere of radius r, and $\phi(r)$ the magnetic flux permeating the sphere, weighted by the critical ratio $(\frac{M}{\phi})_{crit} = \frac{0.53}{3\pi}\sqrt{\frac{5}{G}}$, with G the gravitational constant. We derive the evolution of this indicator for the two different initial conditions.

4.1.1.1 Homogeneous profile

For this profile, we get $\mu(r) \propto r$ for $r < r_{\rm core}$. At $r = r_{\rm core}$, $\mu(r) = \mu_{\text{Mouschovias and Spitzer (1976)}}$. In that case, the analytical result for the critical mass to flux ratio can theoretically be probed by numerical experiments, since the conditions match the ones of the analytical derivation of Mouschovias and Spitzer (1976). Practically, the boundary conditions given by the surrounding medium (the computational box isn't infinite) and the thermodynamical pressure modify the result. Since there are no reasons for the jump in density at $r \gtrsim r_{\rm core}$ to compensate for the jump in magnetic strength if not defined through column density ratio, we expect a similar jump in $\mu(r)$.

Another point of interest is that this initial condition accurately describes the folding of the field lines while the cloud is collapsing. Starting with a relatively low density ($n_H = 1.\ 10^7$ cm^{-3}) and straight lines, one can follow the evolving geometry of the field lines before reaching the first core. As pointed out in a recent paper (Joos et al. (2012)), assuming different geometries for the field lines have a critical impact on the efficiency of angular momentum transport due to magnetic braking.

4.1.1.2 Bonnor-Ebert profile

In that case, we note $r_{\rm core}$ the radius of the core and r_0 the radius of the flat inner density, where $\rho = \rho_0$. At a radius r, we note $h(r)$ the height of the dense core. Then, $M(r) = \iiint \rho(r) r^2 \sin\theta \, d\theta d\phi dr = M_0 + \alpha(r - r_0)$, where $M_0 = \frac{4}{3}\pi r_0^3 \rho_0$ is the mass contained in $r \leq r_0$. This leads with $B(r) \propto \frac{\Sigma(r)}{\Sigma_{max}}$ to[1]

$$\mu(r) \propto \frac{M_0 r + \alpha(r - r_0)r}{\arctan \frac{\sqrt{r_{\rm core}^2 - r^2}}{r}}. \tag{4.3}$$

where α is a proportionality coefficient. This expression is approximate, but it gives an idea of $\mu(r)$ in the core. For $h(r) >> r > r_0$, we obtain $\mu(r) \propto r$. For $r \lesssim r_{\rm core}$, we obtain $\mu(r) \propto \frac{1}{\sqrt{r_{\rm core} - r}}$.

[1] We neglect the outer cloud and the flat inner part for the column density.

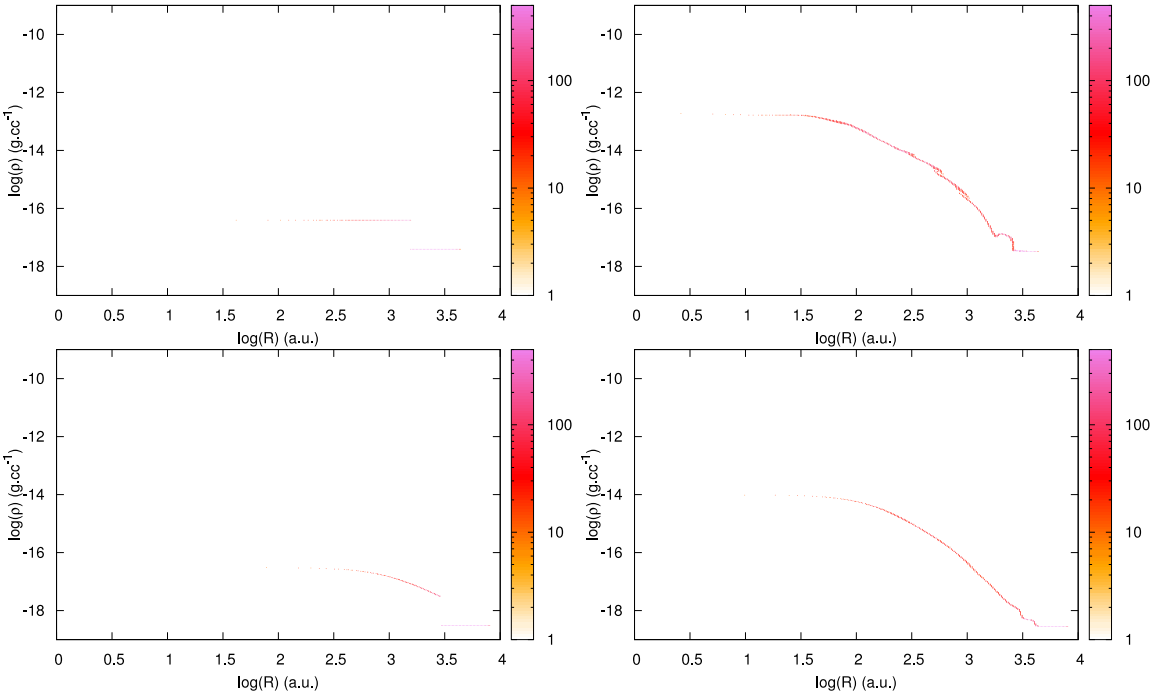

Figure 4.2: *top*: density profile in the equatorial plane starting with a flat homogeneous profile (left) and after a few time-steps. *Bottom*: same as top, for a Bonnor-Ebert initial profile. The colorscale represents the number of cells in a given range of density at a given radius.

There is no easy way to directly compare the magnetic strength in that case with the homogeneous case.

Observed protostellar cores have density profiles that match extremely well Bonnor-Ebert ones (see Fig. 1.6). Accordingly, taking the same kind of slightly unstable density profile as an initial condition for cloud collapse seems reasonable. However, the simple $B(r)$ geometry chosen for the magnetic field doesn't fit what is observed or simulated: the field lines are linked to the infalling matter and it's not possible to observe such a profile permeated with straight field lines. One could argue that as for the homogeneous case, it's sufficient to start with low enough density (meaning an early stage of core collapse), but then the box size will be too large to be able to follow the collapse long enough.

It should also be noted that even in the homogeneous case, the density quickly tends towards a Bonnor-Ebert profile (see Fig. 4.2), with field lines stretched as expected.

4.1.2 Mass to flux ratio

The magnetic field acts as a means to support the core against collapse. Would the field be too strong, the collapse will not occur. To quantify the point at which the magnetic field becomes a hindrance for the collapse, Mouschovias and Spitzer (1976) focused on the particular case of a homogeneous spherical cloud permeated by a uniform magnetic field and found that there is a critical mass-to-flux ratio below which the collapse is prevented. This study was based on global stability. The quantity $\mu(r)$ defined in § 4.4.1 measures the magnetization of a core. The higher, the less magnetized. For a flat density profile, we recall $\mu(r = r_{\rm core}) = \mu$ defined as in Mouschovias and Spitzer (1976). For more details on the mass-to-flux ratio, see § 1.1.3.

One way to define an initial setup with realistic density profiles along with coherent value of

the magnetic field is to imagine the collapse of cylinders which drag the field lines while collapsing, yielding a density profile similar to the one observed (Bonnor-Ebert profile) with a magnetic field depending on the radius as $B_z(r) = \frac{\Sigma(r)}{\Sigma_{\rm center}} B_{\rm center}$. In this case, one can define a constant ratio taking into account all the matter in a given flux tube: $\mu_{\rm BE}$ as

$$\mu_{\rm BE}(r \leq r_{\rm core}) = \frac{\frac{\int_0^r dM}{\int_0^r d\phi_B}}{(\frac{M}{\phi})_{crit}} = \frac{\frac{\Sigma_{\rm center}}{B_{\rm center}}}{(\frac{M}{\phi})_{crit}}. \tag{4.4}$$

4.1.2.1 A critical value

The most resilient choice (and one that we can justify) is to clearly separate the indicator of stability and the magnetization of a core. μ and $\mu_{\rm BE}$ are indicators to assess the stability of a cloud (in any given initial setup). To quantitatively describe the stability of a given setup, one can always input any coefficient to control the magnetic strength and probe the stability limit. We can then give a value which can be looked at as a *critical* value above which collapse occurs, and below which the cloud is stable. This value will depend on every parameter of the run, such as the rotational, thermal or turbulent support (or anything else contributing to the equilibrium of the cloud). For example, we conducted tests for both setups with the following outcomes:

- in the flat density case, without rotation and with 30% of thermal support ($\frac{E_{\rm thermal}}{E_{\rm gravitational}} = 0.3$) we found that $\mu = 2$ is the critical value for collapse to occur.
- in the BE density profile case, without rotation and with 50% of thermal support we find a critical value $\mu_{\rm BE} = 1.4$.

What must be emphasized is that neither μ nor $\mu_{\rm BE}$ are absolute indicators for numerical simulations. They are a useful means to compare our work with other authors or to adjust the strength of the magnetic field but shouldn't be used to demonstrate anything else. In order to study the evolution of the magnetic support, other quantities more reliable from one numerical setup to another have to be used.

4.1.2.2 Measuring the magnetic support

To define a quantity able to measure the magnetic support in 3D simulations, we can follow the idea of the mass-to-flux ratio and modify it accordingly:

$$\tilde{\mu} = \frac{\frac{M(r)}{<\phi(r)>}}{\text{any normalisation value}} \tag{4.5}$$

where $M(r)$ is the mass in a sphere of radius r and $<\phi(r)>$ is the mean magnetic field in the same sphere of radius r times the area of a cylinder which encloses the sphere ($<\phi(r)> = <||\mathbf{B}||>_{\rm sphere} \pi r^2$). In order to retrieve previous work, it's useful to choose the normalization value to be the same as in Mouschovias and Spitzer (1976). Fig. 4.3 shows $\tilde{\mu}(r)$ for the two profiles. For the flat density profile, we retrieve $\tilde{\mu}(r = r_{\rm core}) = \mu$. This indicator is not perfect as inhomogeneities in the field are smoothed out through the averaging of the flux, but it is resilient and can be used to compare simulations between themselves even though the setup is different. In the following, we will be mostly using $\mu_{\rm BE}$ or μ as parameters to describe our setup, and then plotting $\tilde{\mu}$ for the time evolution of the magnetization of spheres of various radii.

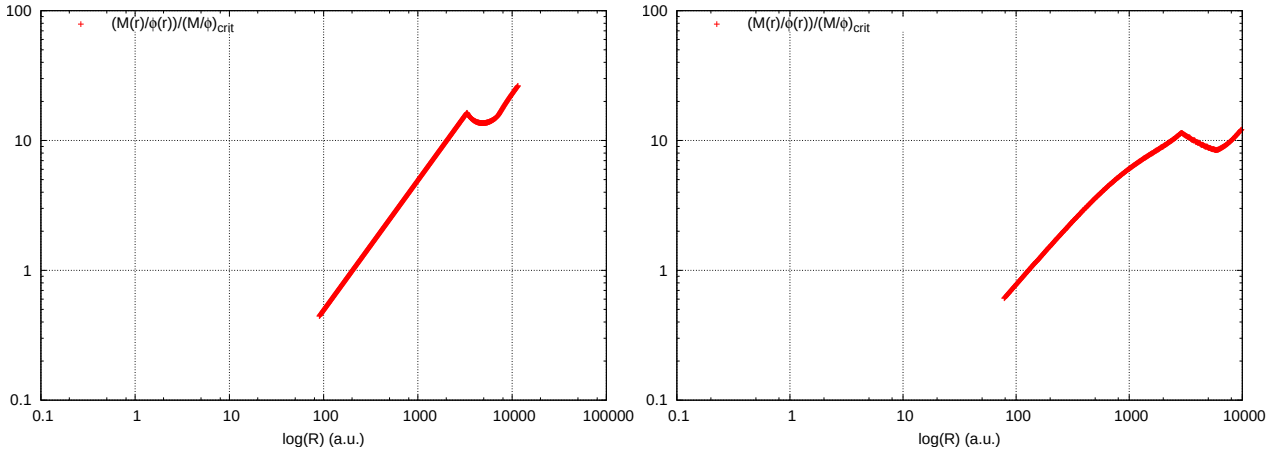

Figure 4.3: We represent here $\tilde{\mu}$ instead of μ. Left: flat density profile with $\mu = 11.6$. Right: realistic BE profile, with $\mu_{\rm BE} = 5$.

4.1.2.3 Note on the flat density profile

It has been pointed out in one dimensional analytical studies of dense core formation by Falle and Hartquist (2002); van Loo et al. (2008) that density inhomogeneities can arise from slow magnetohydrodynamics waves (the density grows linearly with time), without generating any significant difference in the magnetic field strength. This is in contradiction with the commonly used setup where magnetic flux conservation results in a stronger field in the dense core than in the surrounding medium. Since the formation of dense cores is still an active research field we may assume that any of the two scenarios is valid (or even that both scenarios can happen, one because of turbulent motions and compressible flows and the other through slow magnetohydrodynamics waves). The question is: does it make any difference at the scale of the first and second Larson cores ? We performed two runs in order to tackle this issue. Both have $\tilde{\mu}(r_{\rm core}) = 5$ in the core and 3% of rotation ($\frac{E_{\rm rotational}}{E_{\rm gravitational}} = 0.01$) along with 35% of thermal support. In one case the field is uniform through the whole computation domain, and in the other the magnetic flux conservation is taken into account to calculate the magnitude of the field from which the density enhanced (the dense core) arose. The results are shown Figs. 4.4 and 4.5. In Fig. 4.4 we plot an early time (before the first core formation) to probe for differences in the large-scale part of the cloud that can possibly chain-react and have consequences on the small scales. We also represent a later time, after the first core formation, to check for differences. In Fig. 4.5 we show density/velocity and magnetic field intensity maps around the first core, when an outflow has been launched. The main conclusion is that either a uniform or non-uniform initial magnetic field gives the same result concerning the first Larson core, magnetic fields repartition and structures like the outflow. Differences can be pointed out in the faint medium (for densities below 10^{-18} g.cm^{-3}) in both density and magnetic field repartition, but these differences remain unable to cascade down to the dense parts.

The major discrepancy concerns the magnetic support. When trying to probe almost stable initial configurations, the non-uniform case has a need for more instability than the uniform case as the magnetic pressure (or rather the gradient of magnetic pressure) is stronger at the edge of the core resulting in an outward expansion at first. This is not too much of a problem since almost stable initial conditions are not supposed to be studied in a small box (both for a uniform and non-uniform field) with interactions with the boundary of the box: they require large scale simulations.

The other tricky part is the angular momentum transport via magnetic braking. Alfvén waves can transport angular momentum from the dense parts to the surrounding gas. Yet because of

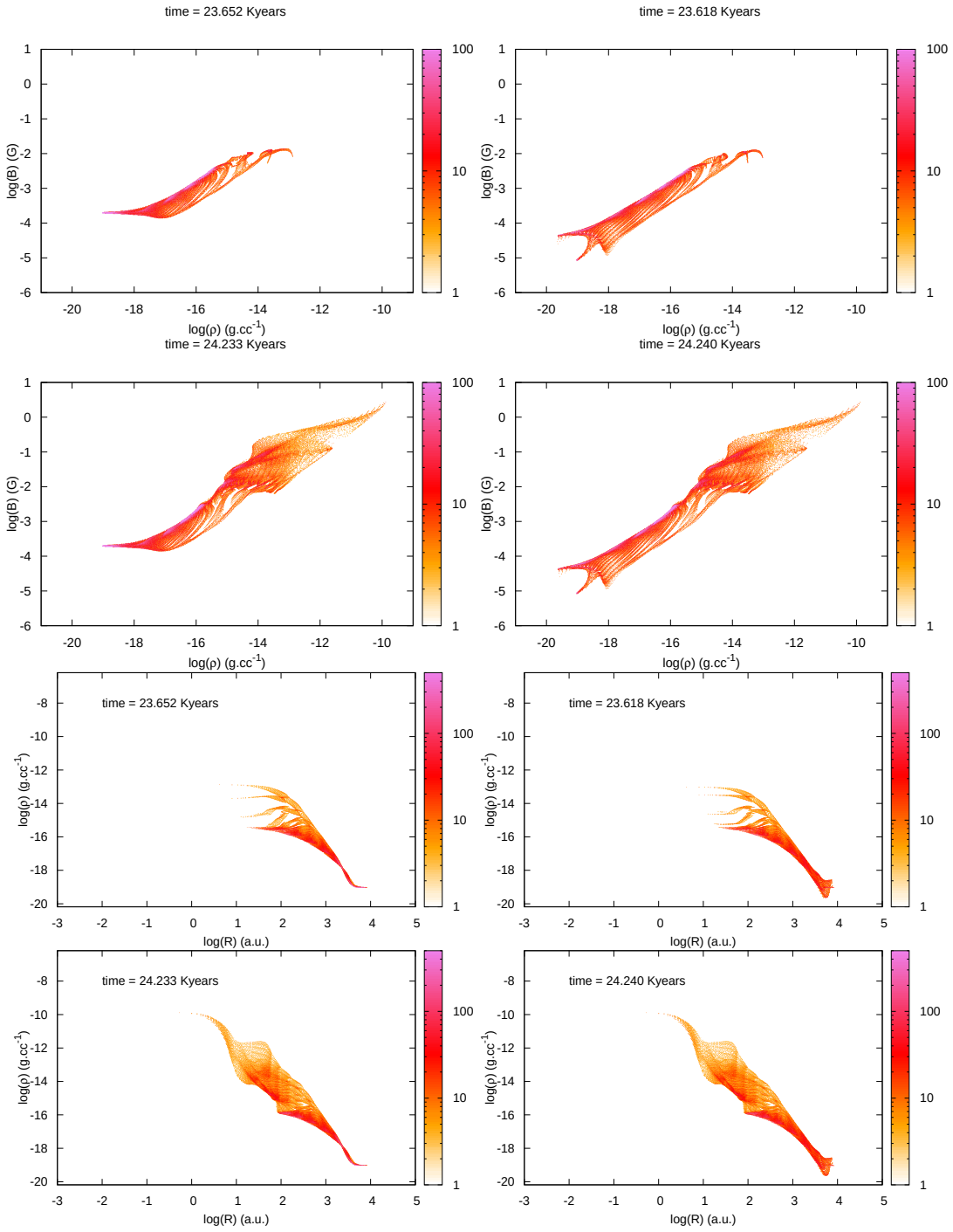

Figure 4.4: Scatter plots (along with a colorbar representing the number of cells at a given density/magnetic field versus density). Left: uniform magnetic field through the whole box. Right: non-uniform magnetic field, $\propto \frac{\Sigma}{\Sigma_{\max}}$. The top four plots show the magnetic field magnitude in function of density. The bottom four plots show the density as a function of the radius. Time evolves from top to bottom in each group of plots. Again, the colorbar represent the number of cells at a given B/ρ: the pink parts of the plot are where most cells are.

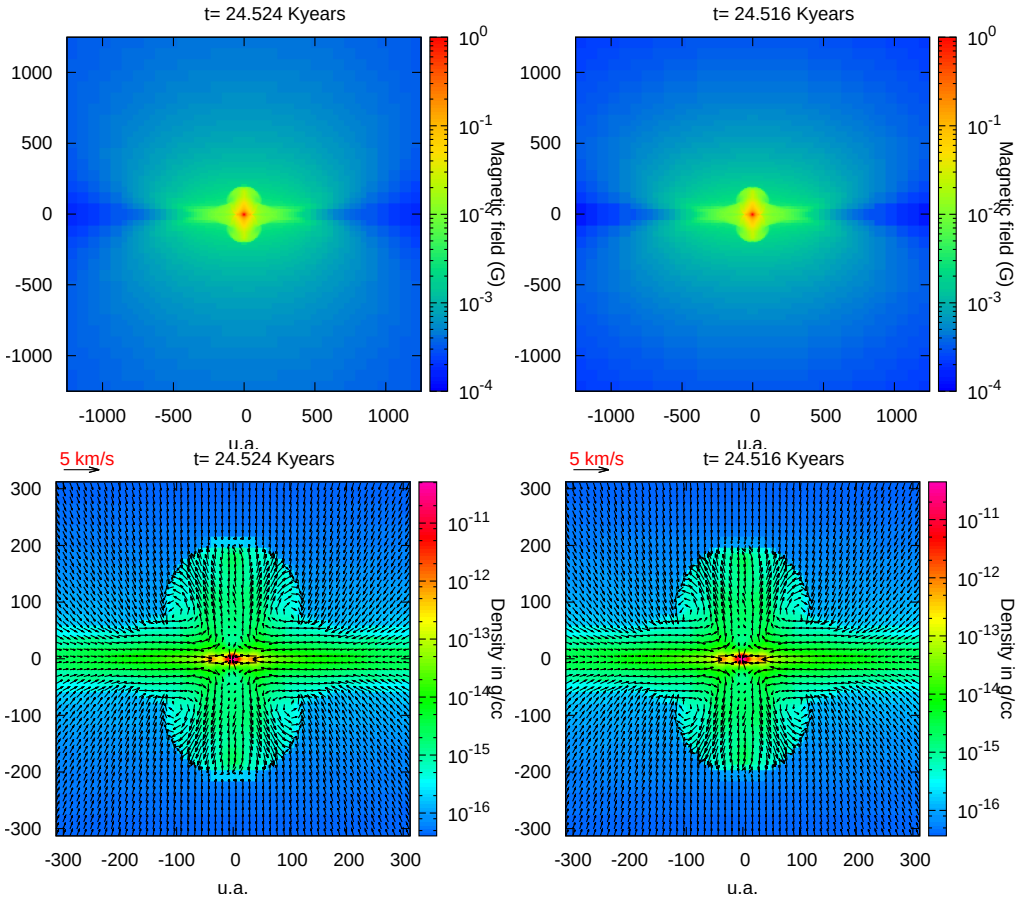

Figure 4.5: Colormap plots for the magnitude of the field and the density. Left: uniform magnetic field through the whole box. Right: non-uniform magnetic field, $\propto \frac{\Sigma}{\Sigma_{\max}}$.

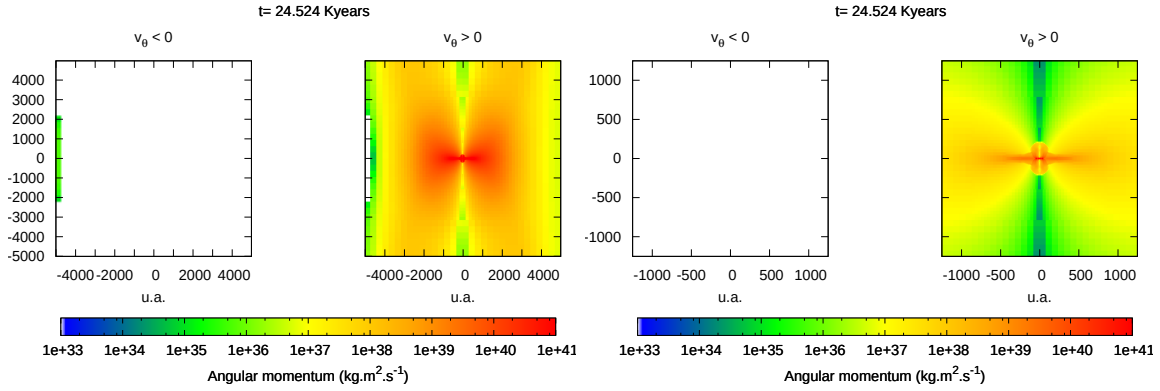

Figure 4.6: Colormap plots of the angular momentum for the full box and a zoomed in region around the first core, for a uniform magnetic field through the whole box.

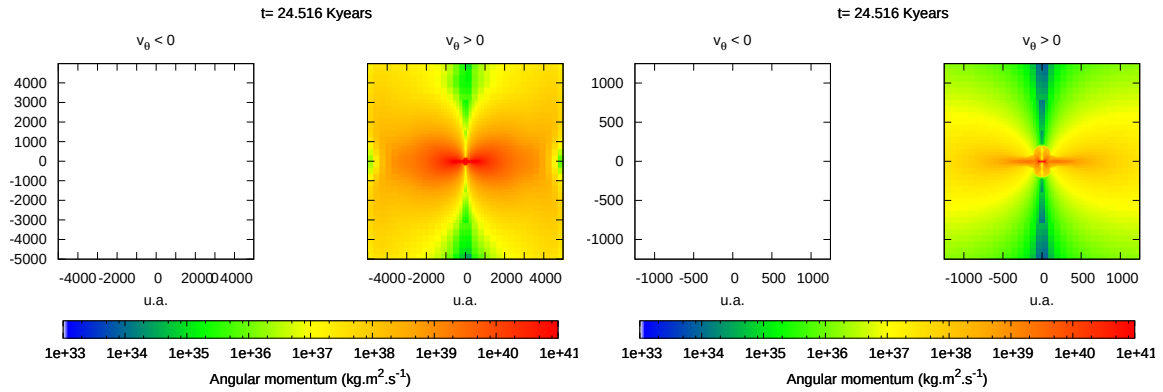

Figure 4.7: Colormap plots of the angular momentum for the full box and a zoomed in region around the first core, for a non-uniform magnetic field, $\propto \frac{\Sigma}{\Sigma_{\max}}$.

the strong magnetization in the uniform case, magnetic tension resists the motion and can yield different behaviors at large scales such as those presented in Figs. 4.6 compared to the non-uniform case Fig. 4.7. At the scale of the first core there is no noticeable difference for the angular momentum repartition. As a conclusion, both setups are valid.

4.1.3 Angular momentum transport and ideal MHD

As we add more and more physics to numerical codes, we seek to reach the point where outputs from numerical experiments can be treated more as observations than as precise phenomenum study. Following this trend, we have to discuss whether a simulation accurately describes the physics at stake or is polluted by numerical effects. It must be emphasized that even if some simulations lack some of the required physics, studying them is still very insightful in order to understand the role of a particular effect. Ideal MHD simulations used to be both: they were first the state of the art of numerical experiments and then with the ever-growing computational power at our disposal, we began to look at them as incomplete yet useful tools to probe star formation processes.

We now present some of the limitations of such simulations and finally discuss their usefulness in the actual context of turbulent star formation.

4.1.3.1 Ideal MHD

3D full scale simulations are expensive in terms of computational time, which explains the many 1D (spherical) and 2D (axisymmetrical) studies carried out in the past two decades. Yet very insightful, they have trouble describing intrinsic 3D effects such as inhomogeneity, anisotropy and turbulence. We shall first describe some classical ideal MHD simulations.

We use a barotropic equation of state to account for heating due to the increasing density. We restrict ourselves to the case where $T \propto T_0(1 + \frac{n_H}{n_{\text{threshold}}}^{\gamma-1})$ with $n_{\text{threshold}} = 10^{-13}$ g.cm^{-3}, $\gamma = \frac{5}{3}$ the ratio of specific heats and $T_0 = 10$ K the temperature of the molecular cloud. We aim to study the first core formation and evolution. In other words, we will integrate over more than one freefall time without taking into account the fact that the second Larson core will have formed by then and produced some feedback on the first core scale or even on the disk and outflows. We will discuss this later in the chapter § 4.3 (see also Vaytet et al. (2013a)). In the following simulations we used an initial BE density profile, 1% of rotation ($\frac{E_{\text{rotational}}}{E_{\text{gravitational}}} = 0.01$) and a thermal support $\frac{E_{\text{thermal}}}{E_{\text{gravitational}}} = 0.3$.

We first present a classical simulation with the magnetic field lines initially aligned with the axis of solid body rotation. $\mu_{\rm BE} = 5.4$, corresponding to a weakly magnetized core compared to observations (see Crutcher (2009) for a discussion of the mass-to-flux ratio and its measurements in molecular clouds). The main results were no fragmentation and some troublesome difficulties to form disks (which led to the *fragmentation crisis*, see for example Hennebelle and Teyssier (2008); Machida et al. (2009)). On an analytical point of view, Galli et al. (2012) showed that under some circumstances the magnetic braking could be so efficient as to completely stop the rotation of the star and even make it counter-rotate. This phenomenum has been seen in numerical simulations as well (see for example Krasnopolsky et al. (2010)). We retrieve the same conclusion, as can be seen in Fig. 4.8 where we represent the angular momentum in a colormap distinguishing between the rotation and counter-rotation (the reference is the initial solid-body rotation). The counter-rotation starts in the core, and then propagates outwards through a couter-rotating outflow. Another counter-counter-rotation follow when the magnetic braking becomes once again too effective. This goes on until the removal of all the angular momentum, yielding an almost stable core with a mass $M_{\rm core} \simeq M_{\rm Jeans}$. This can in some more magnetized cases be concomitant with the launching of a faster outflow than expected in the first core (see for example the density/velocity map for a simulation with $\mu_{\rm BE} = 2$, Fig. 4.9), due to the disentanglement of the magnetic field lines, allowing for an easy escape of the matter pushed out from the inner regions by the high magnetic pressure.

As a preliminary conclusion, we can say that one must be careful when carrying out first core simulations in ideal MHD. Ambipolar diffusion and turbulence (see also chapter 4.2.4.1) seem to effectively reduce or remove the spurious counter-rotation. We emphasize the *first core* because as noted previously at the time when the couter-rotation happens ($t \gtrsim t_{\rm freefall}$) the second core is already formed, providing complicated feedback on every scale. Recent studies (Joos et al. (2012); Krumholz et al. (2013) or § 4.2.4.2) pinpointed the strong impact of misaligned configurations (magnetic field lines and axis of solid body rotation not aligned). We focus on these configurations now.

4.1.3.2 Misaligned configuration

The aligned case is now known to be very peculiar. From a theoretical point of view (see Joos et al. (2012)) it gives the highest efficiency for magnetic braking, because of the fanning out geometry of the field lines and the strong pileup of toroidal field in the disk-plane. In a statistical point of view, it is very unlikely to have a perfectly aligned magnetic field and rotation axis (providing there is no evolution towards this configuration as an equilibrium configuration) and it has been shown numerically that even a slight misalignment (less than twenty degrees) can lead to significant discrepancies in the angular momentum removal (Joos et al. (2012)). Numerical experiments of collapsing cores (see Matsumoto and Tomisaka (2004)) demonstrate that angular momentum is ultimately and at small scales aligned with the magnetic field direction regardless of the initial angle between the two. This does not contradicts the initial idea of a peculiar aligned case: the important parameter is the initial angle in the cloud core between the direction of the field and the angular momentum. They indeed retrieve important differences in the evolution of the angular momentum in the misaligned cases during the collapse. Last, observations by Goodman et al. (1993) reveal uncorrelated orientation of the axis of rotation in dense cores and of the cloud-scale magnetic field, supporting our point.

We present Fig. 4.10 the same experiment as previously, with angles between the initially parallel magnetic field lines and the axis of solid-body rotation. There is still counter-rotation after the creation of the first core, but the spatial extent is more limited than in the aligned case. As the collapse proceeds, the counter-rotation outflow propagates outwards. The main difference takes place at a longer time, when a quasi steady-state configuration is reached. We call it quasi steady-state for several reasons. First, we are limited by smaller and smaller time-steps, making the evolution of the large scales frozen. Second, we use a barotropic equation of state that doesn't account for H_2

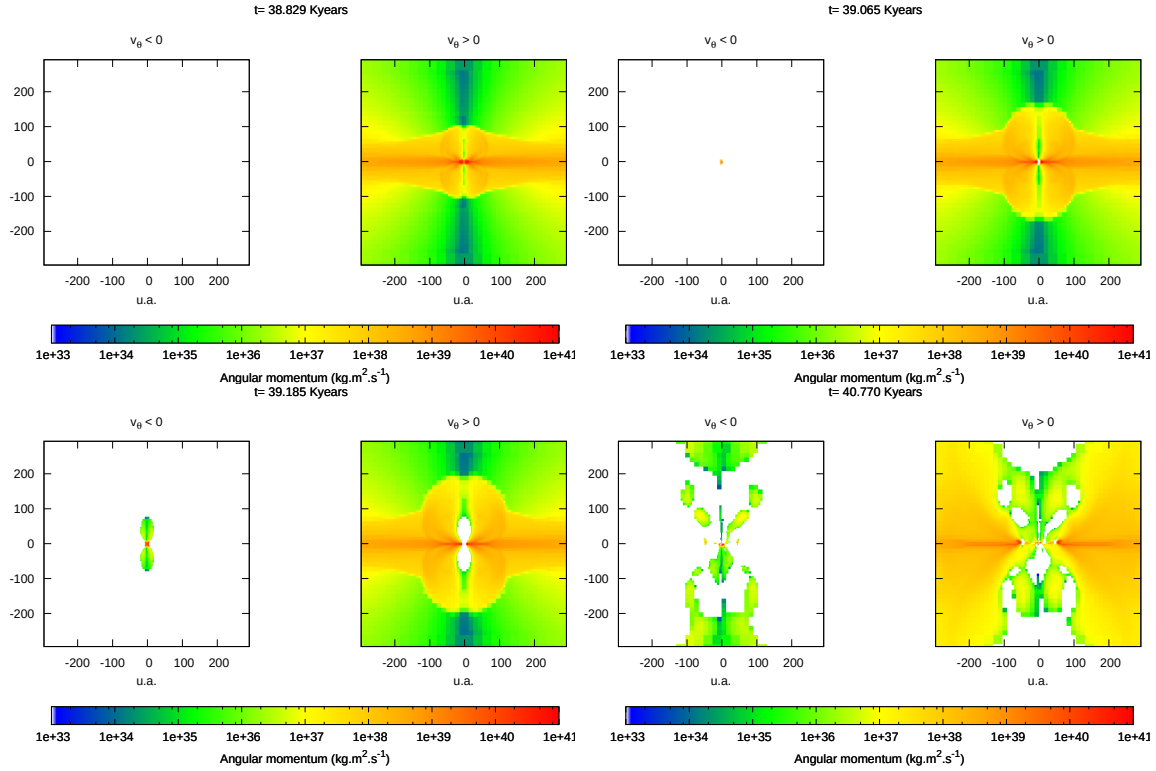

Figure 4.8: Four time steps for an ideal MHD simulation in the aligned case. The angular momentum is plotted in the left or right panel according to the sign of the azimuthal speed v_θ in cylindrical coordinates.

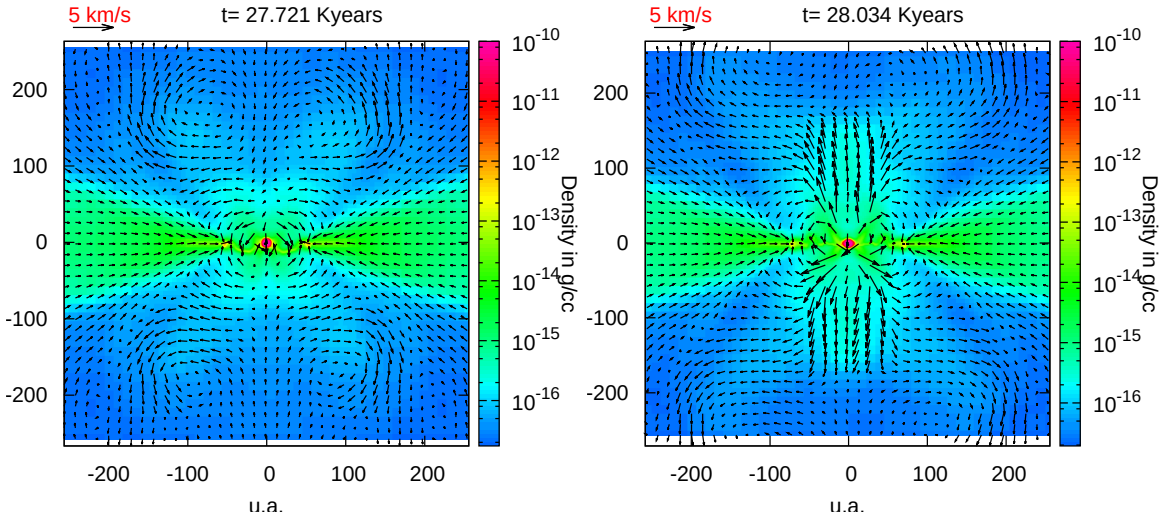

Figure 4.9: $\mu_{\rm BE} = 2$, a fast outflow is launched when the core starts to counter rotate.

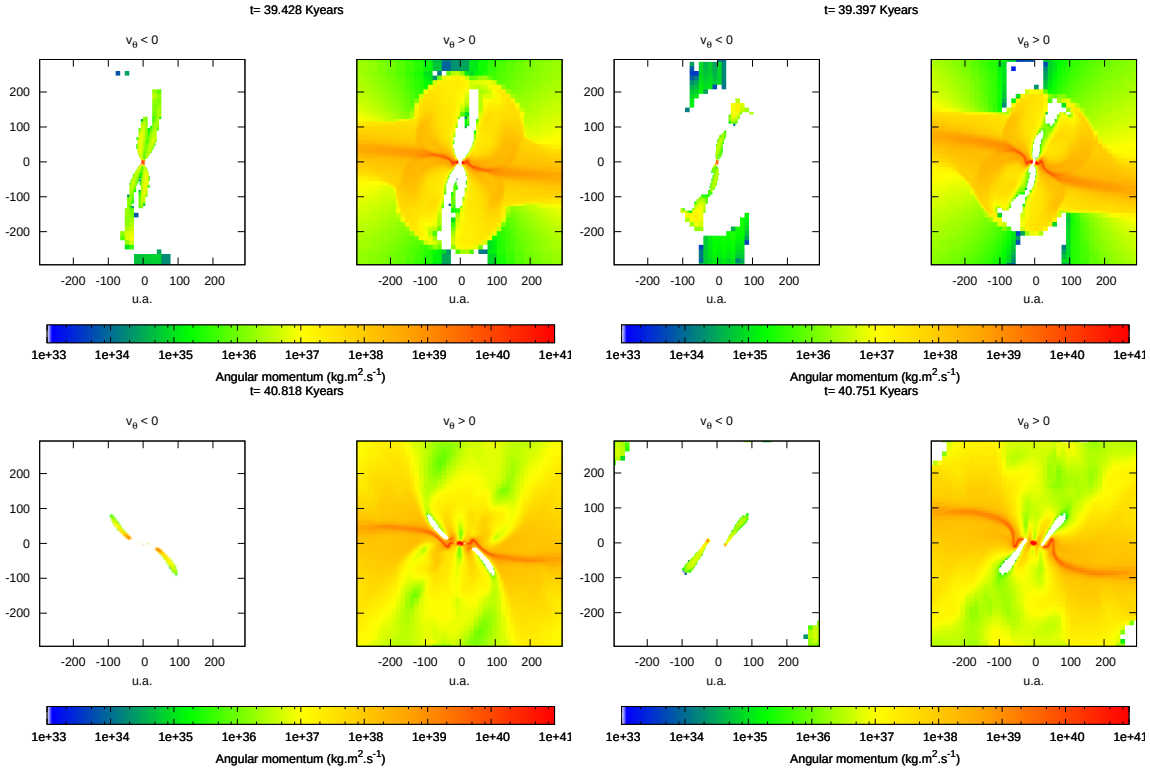

Figure 4.10: Angular momentum maps, $\mu_{\rm BE} = 2$. Left: angle of 10 degrees. Right: angle of 20 degrees. From top to bottom: time evolution.

dissociation, therefore we will never probe the small scale physics that will dominate later in more evolved protostars (e.g. second core formation, disk-star interactions, jets launching, etc.). This configuration seems much more physically relevant, as almost all the cloud and the core rotate in the same way. These simulations didn't end up in a total removal of the angular momentum as previously, because of the less efficient magnetic braking.

4.1.3.3 Weaker magnetic field

We have shown that misaligned magnetic fields help reduce the spurious counter-rotation. We will now explore the effect of a weaker magnetic field.

For weaker magnetic fields, we find that the area surrounding the core is unaffected by this spurious effect, the counter-rotation being limited to the outer part of the faint outflow. We find that a massive disk and substructures can form in the misaligned case (we retrieve the same results as in Joos et al. (2012)). In the aligned case, there is almost no counter-rotation for $\mu_{\rm BE} \gtrsim 5$. An illustration is displayed Fig. 4.11.

4.1.3.4 Ambipolar diffusion

Ambipolar diffusion has been shown to have a stabilizing effect as well as helping to dissolve density gradients in turbulent motions (Zweibel (2002)). Adding the ambipolar diffusion term with the calculated resistivities prevents the counter-rotation of the core and outflow even for the highly magnetized $\mu_{\rm BE} = 2$ case. In the weakly magnetized case ($\mu_{\rm BE} = 5$) we witness fragmentation even in the aligned case. Fig. 4.12 shows these results.

Ambipolar diffusion helps to prevent the counter-rotation to occur in the first Larson core and

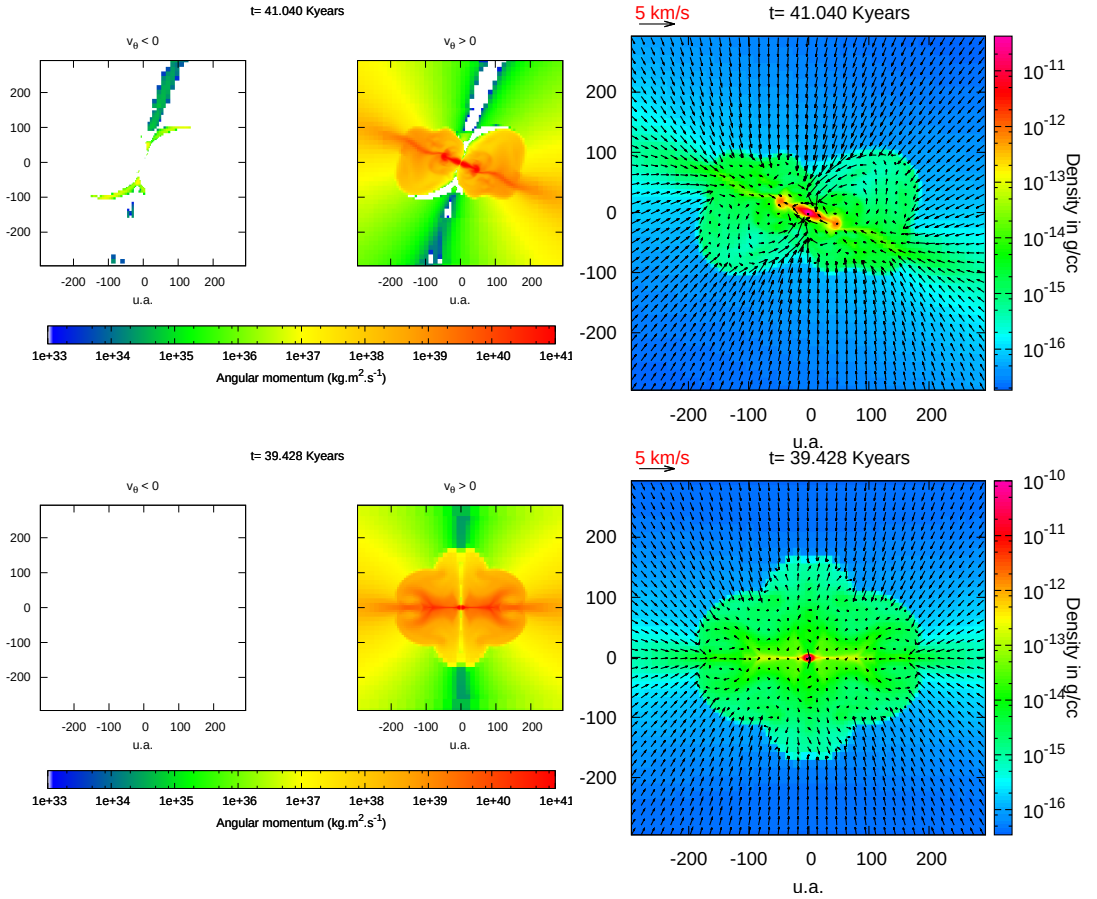

Figure 4.11: Weaker magnetic field configuration: $\mu_{\rm BE} = 5$. Top panels: misaligned case by 20 degrees. Bottom panels: aligned case. Left: angular momentum map. Right: density map.

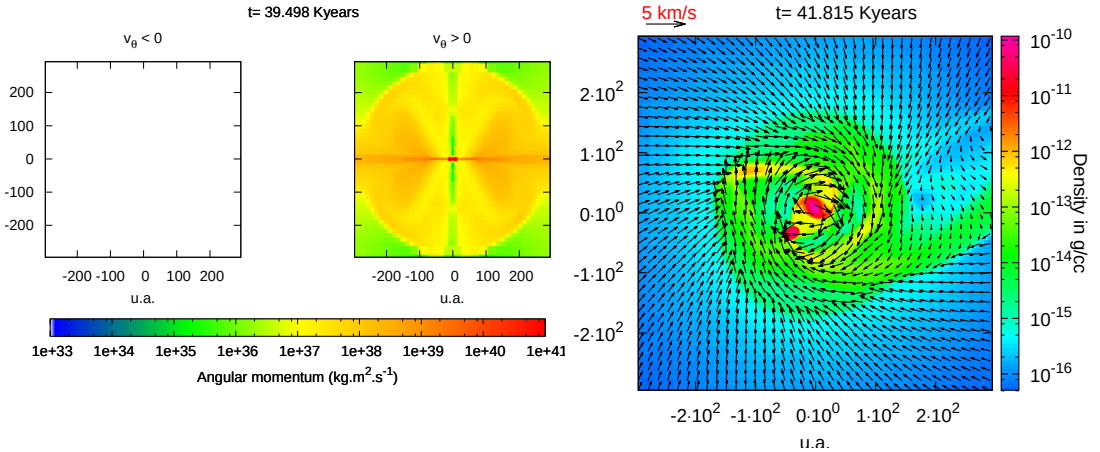

Figure 4.12: Same experiment with ambipolar diffusion. Left: angular momentum map for $\mu_{\rm BE} = 2$. Right: density map in the disk-plane with $\mu_{\rm BE} = 5$.

the outflow, even at high magnetization ($\mu_{\rm BE} = 2$). This can also be achieved by using weaker magnetization ($\mu_{\rm BE} \gtrsim 5$) or misaligned configurations (angle $\gtrsim 5 - 10$ degrees). In order to study angular momentum transport and disk formation and fragmentation, one should be confident to be in one of those cases. It should be noted that there are cases where counter-rotation may occur within a valid framework: see Sauty et al. (2012) for more details.

4.1.4 Conclusion

In this chapter, we have highlighted some of the issues that arise when carrying out numerical simulations of magnetized core collapse and we have clarified some of the terms we will use hereafter. We have also given a glimpse at the angular momentum/magnetic flux conservation in real numerical simulations, and tried to focus on showing that it is indeed a very complicated problem with counter rotation zones appearing in ideal MHD simulations. We can now move on to more detailed studies of first core simulations.

4.2 First core simulations

4.2.1 Introduction

The role of magnetic fields and their impact on star formation on possibly every scale is an old subject of interest since the precursory work by Mestel and Spitzer (1956). Followed many studies from a grand variety of points of view: theoretical studies such as Mouschovias and Spitzer (1976) and Pinto et al. (2008); linear analysis of waves (Balsara (1996); Falle and Hartquist (2002)); non-linear studies (van Loo et al. (2008)); and finally numerical studies (Basu et al. (2009); Hennebelle and Ciardi (2009); Hennebelle et al. (2011); Hennebelle and Fromang (2008); Joos et al. (2012); Kunz and Mouschovias (2010) and many others). The angular momentum transport along with the *fragmentation crisis* (see Hennebelle and Teyssier (2008)) and the disk formation are nowadays investigated extensively, mainly thanks to the huge increase of computational resources in the last few years along with recent observations of class 0 dense cores: Matrà et al. (2012); Maury et al. (2010); Sicilia-Aguilar et al. (2013). Many physical effects are supposed to play a major role in solving this crisis. Ambipolar diffusion, first highlighted by Mestel and Spitzer (1956) is one possible effect at play that could help solving this issue. It consists of a drift of neutrals through the magnetic field via collisions with charged particles, enabling an effective diffusion of the magnetic field while neutral matter continues to pile up on the central object. Microphysics at stake in dense cores (Kunz and Mouschovias (2009); Nakano et al. (2002)) and complex ionization processes (see recent developments by Padovani and Galli (2013)) add uncertainties on the value of the resistivities (both ambipolar and Ohmic). For example, Machida and Matsumoto (2011)) showed that using abnormally high resistivities can lead to massive disk formation, a result that was argued by Li et al. (2011).

Recent breakthroughs have been made studying the effect of the angle between the magnetic field and the axis of the initial solid body rotation of the core (Joos et al. (2012)) or turbulent cores (both in the low mass end by Joos et al. (2013); Li et al. (2013) or in the high mass end Seifried et al. (2013)). They showed that both the angle and the turbulence have a strong impact on the disk formation. Turbulent diffusion has also been studied by Leão et al. (2012) and Lazarian (2013) with many consequences amongst which the optimistic fact that turbulent numerical simulations can under some conditions accurately describe diffusion in astrophysical fluids with unachievable Lundquist numbers.

Early disk formation is a critical matter as it has many consequences such as fragmentation and binaries formation, which are still unknown processes. Nonetheless, there is no strong evidence from

an observational point of view for massive disks around Class 0 protostars (see in particular Maury et al. (2010)).

In this context of uncertainty, we focus on the effect of ambipolar diffusion in low mass star formation. First, we will present the setup and justify the choices we made. Then we will focus on the global influence of ambipolar diffusion on first core simulations. We will finally present direct comparison between ideal MHD runs and resistive ones with ambipolar diffusion (hereafter AD case), with the underlying concern of disk formation and angular momentum transport.

4.2.2 The setup

4.2.2.1 Numerical setup

We conducted 3D numerical experiments using the AMR code `RAMSES` (Teyssier (2002); Teyssier et al. (2006)) along with its extension to non-ideal MHD (Masson et al. (2012)). `RAMSES` allows to solve the complete set of MHD equation (self-gravity, Euler's set of equation and the induction equation with non-ideal terms) using the constraint transport method, preserving the divergence-free condition for the magnetic field. We emphasize that we treat the exact expression for the ambipolar diffusion instead of replacing it by a Laplace operator (as done in Duffin and Pudritz (2008) for example), yielding important consequences on the topology of the field[2]. In the one-fluid, low ionization framework (Shu et al. (1987)) the induction equation is

$$\partial_t \mathbf{B} = \nabla \times \Big[\mathbf{v_n} \times \mathbf{B} + \frac{\big[(\nabla \times \mathbf{B}) \times \mathbf{B}\big] \times \mathbf{B}}{\gamma \rho \rho_i}\Big], \tag{4.6}$$

where $\mathbf{v_n}$ is the neutral fluid velocity, ρ the neutral density, ρ_i the ionization and γ the drift coefficient between ions and neutrals. Equation 4.6 can be rewritten in the form

$$\partial_t \mathbf{B} = \nabla \times \Big[\bar{\mathbf{v}} \times \mathbf{B}\Big]. \tag{4.7}$$

Contrarily to a Laplace operator (such as $\partial_t \mathbf{B} = \nabla \times \Big[\mathbf{v_n} \times \mathbf{B} - \frac{B^2}{\gamma \rho_i \rho} \Delta \mathbf{B}\Big]$) reconnection does not occur since it is just another *flux-freezing* condition at a different speed $\bar{\mathbf{v}}$. It is worth noting that this remains true only in the already mentioned one-fluid approximation, as pointed out by Tsap et al. (2012).

The use of the AMR allows for dynamical refinement based on the Jeans length, carrying a constant number of cells per Jeans length throughout the collapse (10 cells per Jeans length in most cases). It is therefore suited for fragmentation studies and disk formation in a turbulent medium where nested grids would be difficult to use.

Since we focus on the magnetic fields and non-ideal MHD terms, we use a barotropic equation of state instead of solving for radiative transfer

$$\frac{P}{\rho} = c_s^2 \sqrt{1 + \big(\frac{n_H}{10^{-13}\,\mathrm{g.cm^{-3}}}\big)^{\frac{4}{3}}}. \tag{4.8}$$

After an isothermal collapse up to $n_H \simeq 10^{-13}\,\mathrm{g.cm^{-3}}$, the adiabatic phase takes place. In that phase, the polytropic index n is equal to the ratio of specific heats γ: $n = \frac{5}{3} > n_{\mathrm{critic}} = \frac{4}{3}$, stoping the collapse while accreting matter onto the first core. Without a realistic equation of state (Saumon et al. (1995)) and radiative transfer, or without using a more realistic barotropic equation of state, the simulation continues accreting matter indefinitely. Any interaction with jets launched at the scale of the second Larson core are beyond the scope of this study, meaning that there might be significant differences at several times the free-fall time.

[2]Refer to appendix 1.B and section § 4.4 for more details

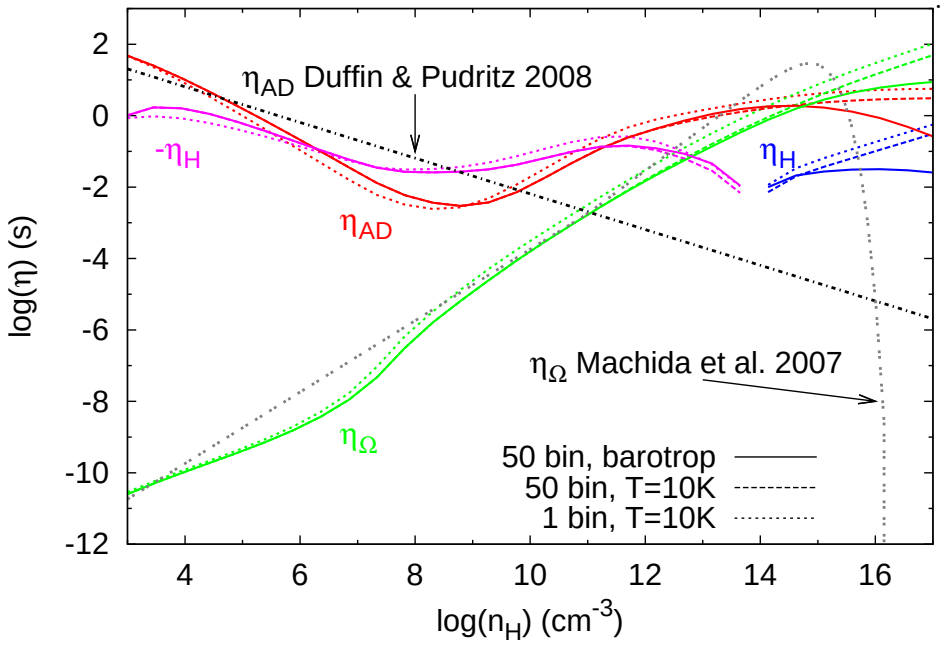

Figure 4.13: Resistivities for various cases and comparison with previous work. Thick lines correspond to the barotropic case, with 50 bins in size for the grains. Dashed lines correspond to the case with a constant temperature $T = 10\ K$, with 50 bins. Dotted lines correspond to the case with a constant temperature $T = 10\ K$, with 1 bin. Lines are color-coded to represent various resistivities: red (respectively green, purple and blue) is the ambipolar (respectively Ohmic, Hall (positive) and Hall (negative)) resistivity. Ambipolar resistivity taken from Duffin and Pudritz (2008) is plotted as the black dash-dotted line. Ohmic resistivity taken from Machida et al. (2007b) is plotted as the grey double-dotted line.

The ambipolar resistivity is calculated using a simplified chemical network, following work by Nakano et al. (2002) and further refined through insightful discution with M. Kunz (Kunz and Mouschovias (2009, 2010)). The complete explanations can be found § 3.1. The final resistivities are calculated using a non-equilibrium semi-implicit code assuming the same barotropic law for the temperature as in equation 4.8. Following Li et al. (2011) the magnetic field to compute the resistivity is assumed to be only dependant on the density, as $B(n_H) = 1.43 \times 10^{-7}\sqrt{n_H}$. A comparison with previously used resistivities is represented Fig. 4.13.

At high density ($n_H \simeq 10^{16}$ cm^{-3}) we artificially changed the Ohmic resistivity to account for the ionization of alkali metals (Machida et al. (2007a)), rendering Ohmic diffusion inefficient.

4.2.2.2 Initial condition

We consider a dense core of 1 $M_\odot$ embedded in a ten times less dense environment. The initial density profile of the core is assumed to follow a Bonnor-Elbert density profile:

$$\rho(r) = \frac{\rho_0}{1 + (\frac{r}{r_0})^2}, \tag{4.9}$$

with the ratio of the thermal over gravitational energy $\epsilon_{\rm therm} = 0.25$, yielding an inner radius $r_0 = 1000$ a.u. and $\rho_0 = 3 \times 10^{-17}$ g.cm^{-3}. Using a BE profile instead of a flat density is both more and less realistic. On the one hand, it fits density profiles from observation (see Andre et al. (2000); Belloche et al. (2002) and has analytical basis (Hunter (1977); Li and Shu (1996)). On the

other hand, we are simulating a magnetized medium permeated with straight parallel field lines, and it is hardly possible to end up with a BE density profile without bending the field lines while the density enhancement (the dense core) forms. Some authors (van Loo et al. (2008)) found some non-linear enhancement of density in simulated turbulent molecular sheets via slow mode magnetic waves which let the magnetic field unchanged, but it remains unclear if this process is happening. Our own tests tend to prove that the initial density profile is not a critical matter, as can be seen in a more detailed discussion in § 4.1.

4.2.3 Preliminary remarks

Stabilizing effect We found a recurrent effect from ambipolar diffusion which tends to smooth every strong gradient, yielding more stable simulations in particular concerning the interchange instability, as described by Krasnopolsky et al. (2012). Fig. 4.14 shows colormaps of the density overlayed with velocity vectors in the cut plane. The free-fall time for both simulations is the same ($t_{\rm ff} = \frac{1}{4}\sqrt{\frac{3\pi}{2G\rho_{\rm moy}}} = 27635$ years) and the maps are for a very similar evolution time, enabling direct comparison between the two. It is very clear on the first top two figures that the interchange instability is well developed in the ideal MHD case while not in the resistive case. This is due to the strong pileup of magnetic field in the ideal MHD case on the central object, only counteracted by numerical diffusion. For the resisitive case the redistribution of magnetic field occurs in larger scales yielding much less constraints on the core and where the accretion flux can come from. It is worth noticing that Krasnopolsky et al. (2012) explored the interchange instability in simulations taking into account ambipolar diffusion and concluded that the instability should occur in 3D, yet we do not see the same complex structures in our case. The most plausible explanation is that strong gradient are smoothed out by ambipolar diffusion.

Ambipolar diffusion has consequences on the momentum equation, the induction equation and the energy equation. Since we are using a barotropic equation of state instead of solving for the full radiation MHD equations, the energy equation is not solved. Fig. 4.15 displays a colormap of the magnetic field intensity for a cut orthogonal to the disk-plane, for both ideal MHD (left) and non-ideal MHD (right). As expected, there is a huge diffusion of the magnetic flux from within the first core to its surroundings. What is worth noticing is that the ideal MHD seems to be solved too accurately, meaning that numerical resistivity is not important enough to remove the flux from the central object leading to unphysical magnetic pressure and magnetic breaking. Material to support this assumption is displayed on the two bottom plot of Fig. 4.15: at high density in the ideal MHD case (left) the magnetic flux falls down instead of following the same trend (a power law of index $\frac{2}{3}$), which is possibly explainable through numerical resistivity and/or reconnection. The result is a shift of the central object, usually along the direction of the field lines (direction of least resistance).

In order to study this effect and its resilience, we carried out several simulations both in ideal and non-ideal MHD, with or without turbulence and changing the angle between the initial magnetic field lines and the axis of solid-body rotation.

4.2.4 Results

We first describe the results for the fiducial, aligned case. We keep in mind that there are limitations to this simple case, but it is worth studying in order to compare to previous results. Then we show a more general setup with an angle between the rotation axis and the initial direction of the magnetic field lines. Finally, we try and extract valuable informations from turbulent simulations.

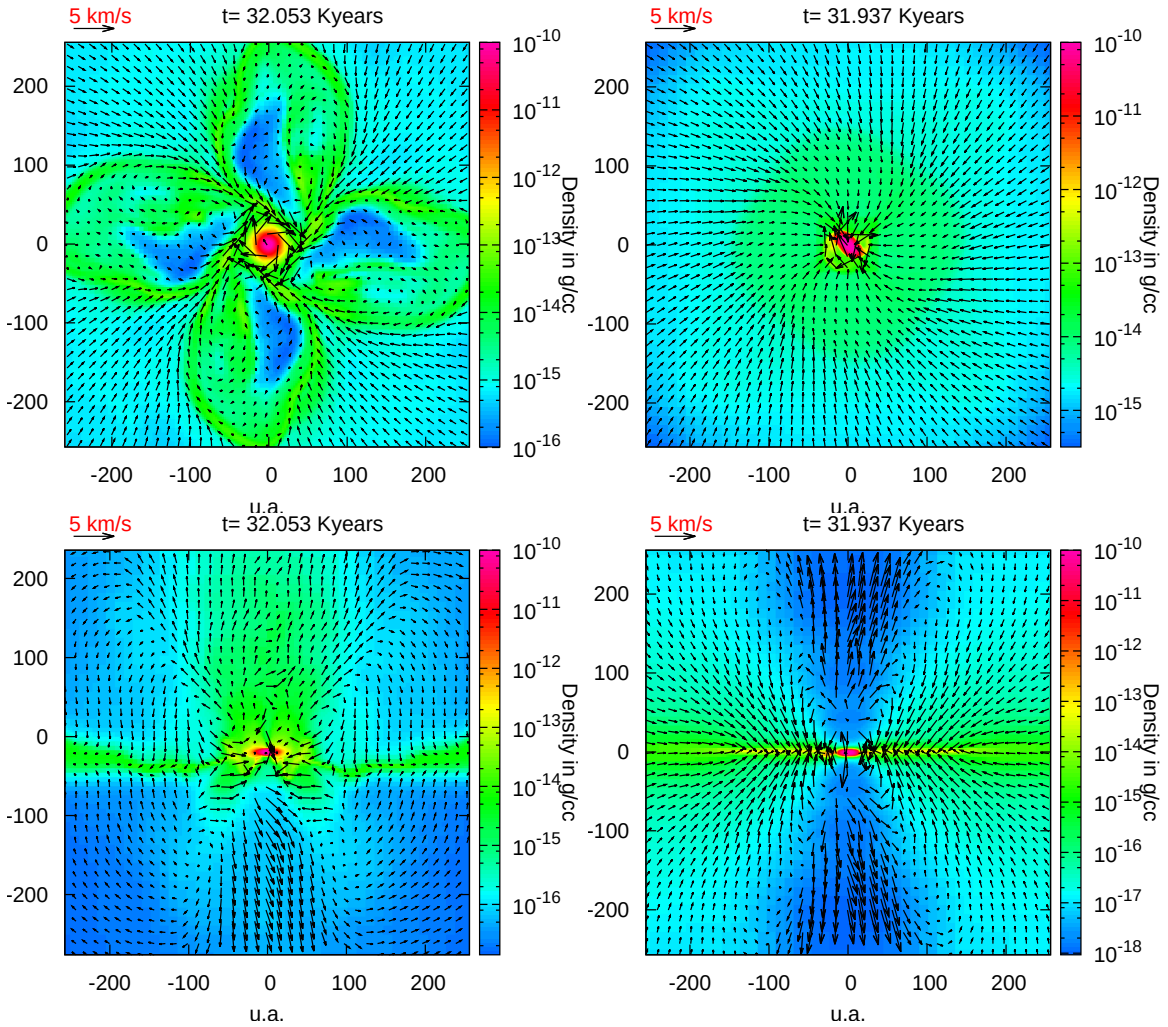

Figure 4.14: Left: ideal MHD. Right: non-ideal MHD, taking into account ambipolar diffusion. The top two figures represent a cut along the plane of the disk (or pseudo-disk in this aligned case), and the bottom two are an orthogonal cut. In those cases, $\mu = 2$ and the ratio of the rotational energy other gravitational energy is 3% while the thermal support is 0.25.

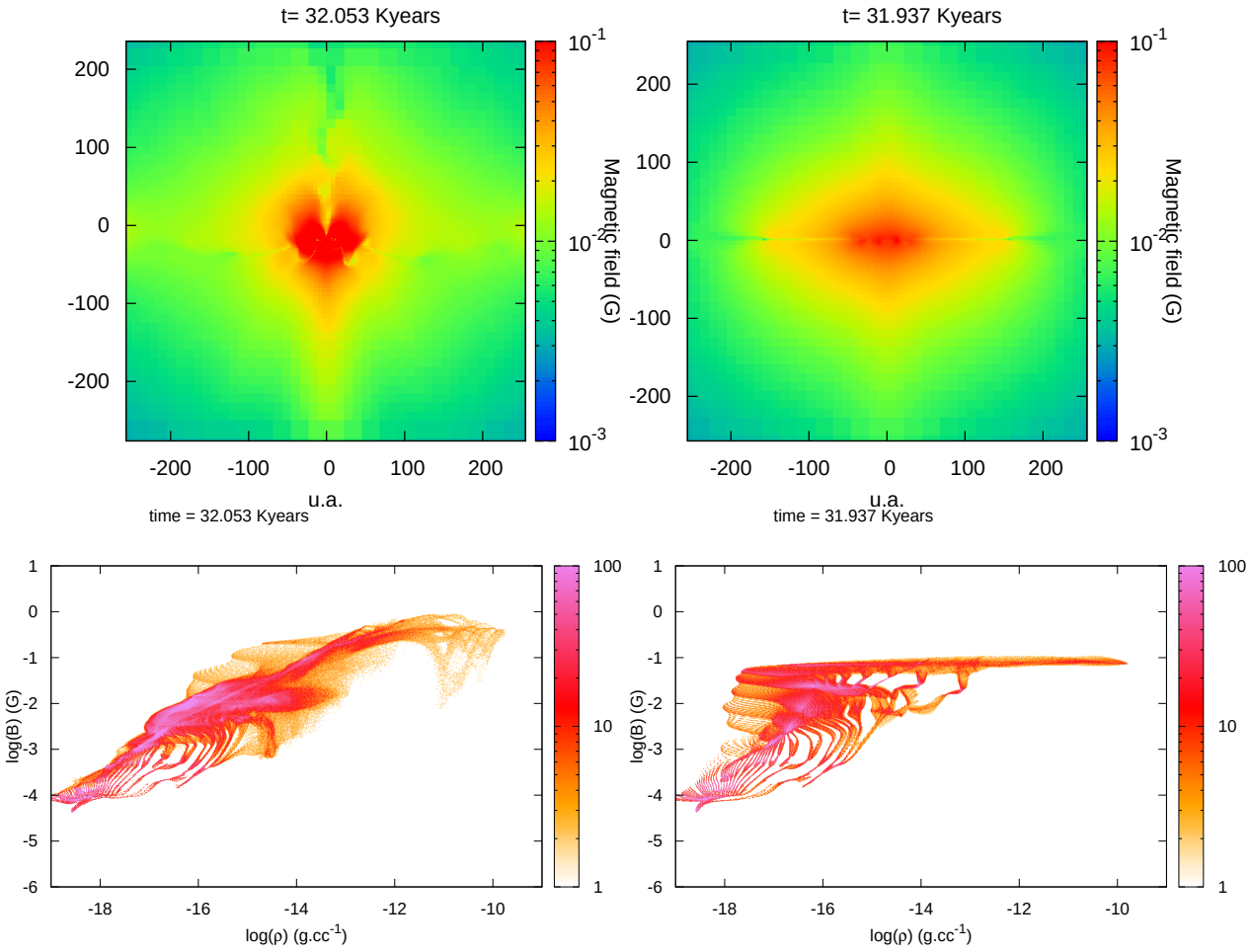

Figure 4.15: Left: ideal MHD. Right: non-ideal MHD, taking into account ambipolar diffusion. The top two figures represent a cut orthogonal to the plane of the disk (or pseudo-disk in this aligned case), and the bottom are scatter plots of the magnetic field magnitude versus the density. In both cases, $\mu = 2$ and the ratio of the rotational energy other gravitational energy is 3% while the thermal support is 0.25.

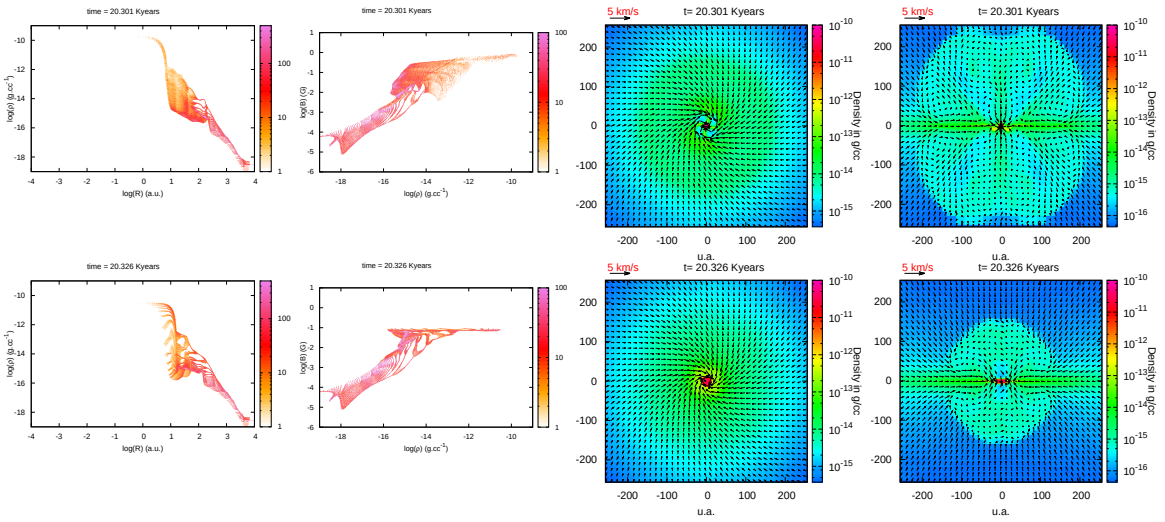

Figure 4.16: $\mu = 5$, aligned case. Top: ideal MHD. Bottom: Ambipolar diffusion. All plots are taken at about the same time (right after the first core formation), $t = 20.3$ kyears. From left to right: scatter plot of density versus radius with the number of cells at a given density/radius color coded; magnetic field magnitude versus density, number of cells color coded; density/velocity cut in the equatorial plane; density/velocity cut in a transverse plane.

4.2.4.1 Aligned, classical case

This case uses the described setup, with a ratio of rotational over gravitational energy $\frac{E_{\rm rot}}{E_{\rm grav}} = 0.03$, hereafter referred to as 3% of rotational support. The initial axis of solid body rotation is aligned with the direction of the magnetic field. We present two cases, a somewhat weak magnetized case ($\mu_{\rm BE} = 5$) and a more magnetized case, closer to critical and observations ($\mu_{\rm BE} = 2$).

$\mu_{\rm BE} = 5$, weakly magnetized case

First core formation Approximately when the first core forms, an outflow is launched. It occurs at the same time for both ideal MHD and AD simulations ($t \sim 19$ kyears). The core is similar, slightly bigger in the AD case (in both cases $R_{\rm core} \sim 10$ a.u.). Then accretion continues, and differences begin to appear more clearly. Both cases at $t \sim 19$ kyears are shown Fig. 4.16. We retrieve the strong accretion from the interchange instability in the ideal case, and a more steady accreting flow in the AD case. From densities of the order of 10^{-15} g.cm^{-3}, the magnetic pileup is hindered by magnetic field redistribution in the AD case. This yields a flat plateau at $B \simeq 10^{-1}$ G, more than one order of magnitude less than in the ideal case. The accretion shock (radius of the first core) seems to be related to a uniform magnetic field in both cases. The thinner part of the plateau begins at $\rho \sim 10^{-13}$ g.cm^{-3} in the AD case. In the ideal MHD case it occurs for higher densities, $\rho > 10^{-12}$ g.cm^{-3}.

To better compare the general trends and differences, we plot azimuthally integrated flow variables. The direction of the axis of reference (z-axis) is given by the direction of the mean angular momentum in a 100 a.u. sphere. This is represented Fig. 4.17. The angular momentum flux for the Lorentz force is a flux depending on the toroidal magnetic field that appears when writing the conservation of the angular momentum with Euler equation. Details can be found in Joos et al.

(2012), we recall here the final expression:

$$\frac{\partial \rho v_\theta r}{\partial t} + \boldsymbol{\nabla} \cdot \cdot r \left[\rho v_\theta \mathbf{v} + (P + \frac{B^2}{8\pi} - \frac{g^2}{8\pi G})\mathbf{e}_\theta - \frac{B_\theta}{4\pi}\mathbf{B} + \frac{g_\phi}{4\pi G}\mathbf{g} \right] = 0 \tag{4.10}$$

in a cylindrical coordinate system. We therefore define the angular momentum flux for the Lorentz force as $\mathbf{F_l} = -\frac{B_\theta r}{4\pi}\mathbf{B}$. The accretion is indeed different. There is a moderately strong outward velocity field at about 40 degrees in the ideal MHD case absent from the AD case. The accretion flow comes from both the midplane and the vertical direction in both cases. The most striking difference is a faster growth rate of the magnetic cavity (magnetic tower) in the ideal MHD case. We explain this through the same interchange instability and a stronger pileup of toroidal field in the ideal case: the stronger pileup allows for more pressure and tension which makes the tower grow, while the cavities due to the filamentary accretion (see Krasnopolsky et al. (2012)) allow for a stronger outflow. When looking at the Alfvén speed and magnetic field repartition, the structure is very similar. The pileup is stronger in the ideal MHD case but the topology remains the same. We can note a faster Alfvén speed in regions of about 50 a.u. immediately above and below the core in the AD case. Moreover, the shape of the fast Alfvén speed region is more needle-shaped in the AD case, evidence for a less developed magnetic cavity. Last, in the angular momentum maps, more differences arise. In two different regions in the ideal MHD case, we note an inward angular momentum flux for the Lorentz force. It occurs when the field lines are entangled enough so that they are folded (regions above and below the equatorial plane, at about 20 degrees), because of the vectorial component of the flux along $\mathbf{B}$. It also occurs in counter-rotating regions, marked in blue in the small box on the top right of the plot, same axis as the main frame. The intensity of the transport of angular momentum is non-negligible in those regions but globally the transport is outwards, dominated by transport along the equatorial plane. For the AD case, transport is always pointing outwards and dominates in the radial direction in the midplane but is also less intense, while the angular momentum close to the core is one order of magnitude higher than in the ideal MHD case.

Last, we want to compare the evolution of magnetization versus radius in both cases, right after the first core formation. What we call magnetization is the inverse of the ratio of the mass of a sphere of radius r over the mean magnetic flux in the sphere, normalized by a critical value[3] (high magnetization means low mass-to-flux ratio). This is represented Fig. 4.18. It is very clear from these plots that flux redistribution occurs in the surroundings of the first core. It is even more accurate to talk about neutral matter slipping through the field lines than magnetic field redistribution since the pileup of magnetic field never occurs as much as in the ideal case. The whole collapsing cloud does not bring as much field lines as in the ideal MHD case when collapsing, yielding much less magnetization. At the time of formation of the first core (second-to-last plot) there is one order of magnitude of difference between ideal MHD and the case with ambipolar diffusion. Naturally, this leads to a less efficient braking: magnetization is effectively ten times smaller in regions of interest in regard of magnetic braking. This is the same order of magnitude as in the angular momentum flux, Fig. 4.17. After the first core formation, in regions of high density the magnetization decreases gradually in the ideal MHD case to resemble more and more the AD case. In a perfectly ideal framework, we expect the magnetization to evolve even in a perfect coupling case: geometry effects and a different definition of the magnetization are required in order to represent flux freezing with constant quantities. In this case it is not clear if numerical resistivity is responsible for the increasing mass-to-flux ratio at small radius (of the order of the first core size or less). It is clear however that the AD case shows an overall magnetization about one order of magnitude weaker than the ideal MHD case.

[3]See 4.1.2.2 for more details and a full discussion of this issue.

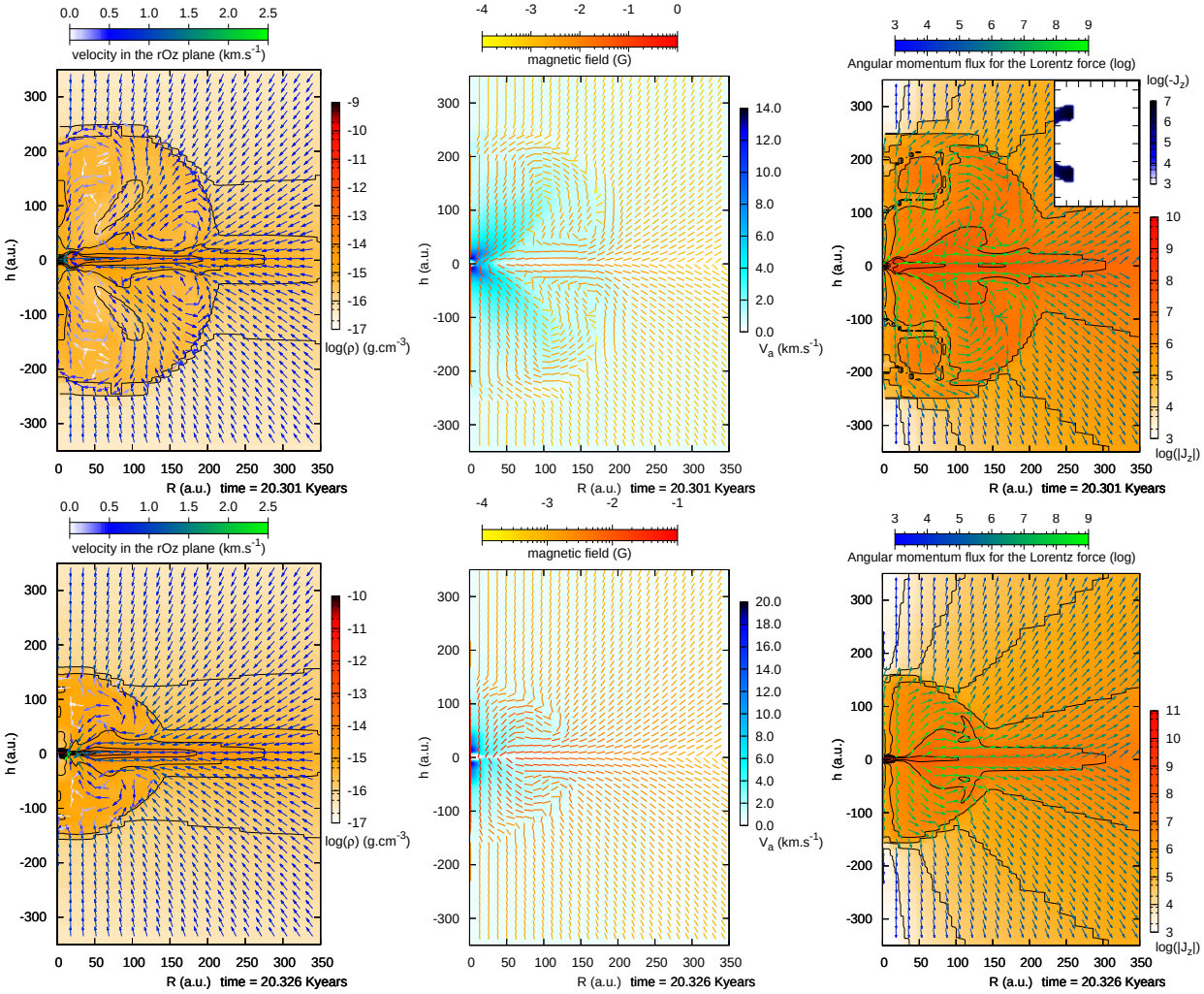

Figure 4.17: $\mu = 5$, aligned case. Top: ideal MHD. Bottom: Ambipolar diffusion. All plots are taken at about the same time (right after the first core formation), $t = 20.3$ kyears. From left to right: density/velocity plot, with both density and the vector field color coded and isocontours for density; Alfvén speed and the magnetic vector field, again both colorcoded; the angular momentum in a given volume (to account for density and the AMR) in colormap and the angular momentum flux for the Lorentz force in vectors.

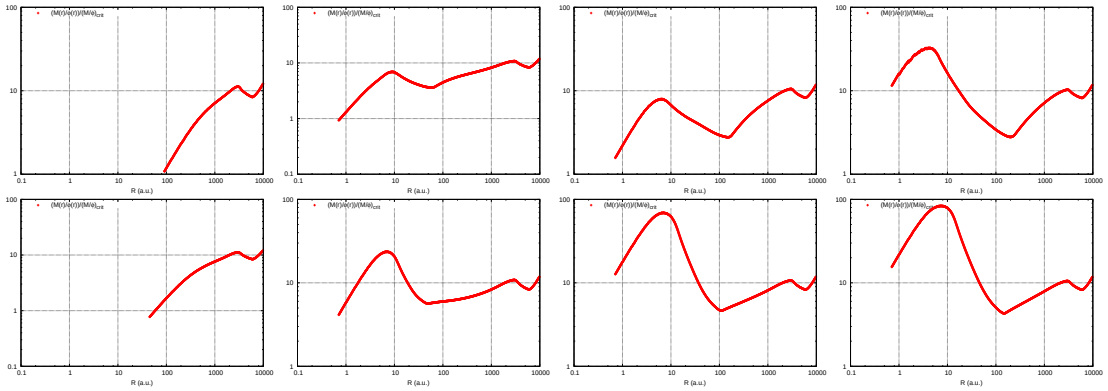

Figure 4.18: $\mu = 5$, aligned case. Top: ideal MHD. Bottom: Ambipolar diffusion. From left to right: inverse of the magnetization (spherically averaged mass-to-flux to ratio) versus radius as time passes (same for top and bottom panels), until after the formation of the first core ($t \sim 19$ kyears). From left to right, time=11.7; 19.0; 19.7; 20.3 kyears.

Long term evolution By long term evolution, we mean that we integrated longer than the time to form the second core. Consequently, the physical framework is fragile since we forget all about the feedback from the second core. We wish to draw conclusion on additional effects associated with ambipolar diffusion that were hidden at early times. It also allows for a study of disks, or so-called disks, because they form and grow only at long times. In those simulations, many factors are to be taken into account and modify the picture of the rotationally supported Keplerian disk. First, magnetic pressure adds support, yielding possible slower velocities than Keplerian in the disk. The natural pileup of matter in strong field regions can also be misleading as they are not rotationally supported. We use some stringent criteria to define the *disk*, as in Joos et al. (2012). It should be remembered that these criteria are fallible, meaning they allow for direct comparison between different cases but should not be considered as definite criteria for a disk. This particular point is more detailed in appendix 4.A

Fig. 4.19 summarizes the long term evolution of the specific angular momentum, disk mass and magnetization. The red solid curve appears when structures (cells) of length < 10 a.u. are created in the AMR grid, it is therefore a good indicator of the first core formation. Before it, we can see the consequence of the collapse and the geometrical non-conservation of the mass-to-flux ratio in the rising curves for $R > 100$ a.u.. At the first core creation, we see kinks in the $R = 100$ a.u. curve. It is a spurious effect of the shape of the magnetization versus radius: it corresponds to the local minimum of magnetization (see Fig. 4.18, top raw, last plot on the right at 250 a.u.) crossing the $R = 100$ a.u. boundary, yielding rapid change in the global curve. In the ideal MHD case after some strong variation associated with the expansion of the outflow, the magnetization reaches what appears to be an equilibrium at every scale. At the scale of the core, we reach $\tilde{\mu}(r = 10 \text{ a.u.}) \sim 10$, while for larger radius the equilibrium value is common to every curve, ~ 5. For the AD case, the behavior at large scales is similar to the ideal MHD case with slightly superior values. It is sadly not possible yet to know if equilibrium has been reached in this case. The most noticeable difference concerns the magnetization at a small radius, comparable to the size of the core. In this case, the mean mass-to-flux ratio increases almost linearly in log/linear scale until the end of the simulation, for almost 10000 years after the first core formation. The increase is of exponential nature, $\log(\tilde{\mu}(r = 10 \text{ a.u.})) \sim 0.4t$, ending almost two orders of magnitude higher than in the ideal MHD case. This is supposedly very important in second core studies, as the drop in magnetization occurs quickly after the first core formation when second core formation is supposed to form. On the other hand the evolution of the specific angular momentum (in respect to the center part of

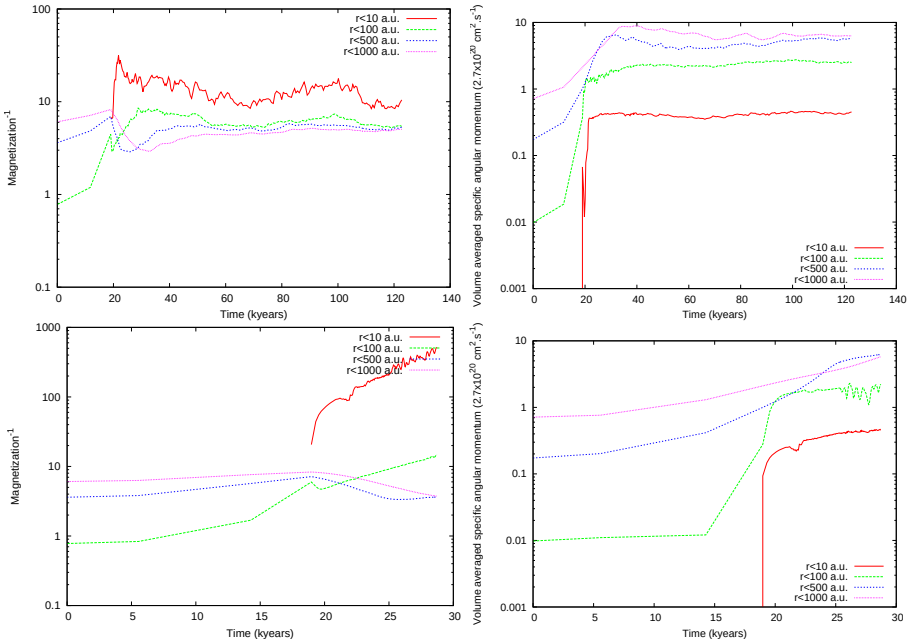

Figure 4.19: $\mu = 5$, aligned case. Top: ideal MHD. Bottom: Ambipolar diffusion. From left to right: inverse of the magnetization (average of the mass-to-flux ratio in a sphere of given radius) versus time for various control spheres; specific angular momentum versus time for various control spheres, in respect to the densest part of the cloud.

the cloud) is different in both cases. The order of magnitude is similar, but the evolution of the specific angular momentum at small scales is different. What we call specific angular momentum is the volume averaged quantity, different from the mass averaged angular momentum. We recall both definitions, with V the control volume (sphere of radius r) and M the mass inside the volume V of density $\rho(r)$:

$$\mathbf{J}_{\text{specific}} = \frac{1}{V} \iiint_{V=\text{volume of the sphere of radius } r} \mathbf{r} \times \mathbf{v}(\mathbf{r}) \mathrm{d}V, \tag{4.11}$$

$$\mathbf{J}_{\text{mass averaged}} = \frac{1}{M} \iiint_{V=\text{volume of the sphere of radius } r} \mathbf{r} \times \mathbf{v}(\mathbf{r}) \rho(r) \mathrm{d}V. \tag{4.12}$$

The mass averaged angular momentum traces the rotational energy, while the specific angular momentum traces the rotation regardless of the mass. We are investigating rotationally supported disks, and therefore are more interested in the latter. We represented Fig. 4.19 on the right the evolution of the specific angular momentum for the whole simulation in the MHD case, thus the abscissa do not match in each plot. In the ideal MHD case, we note a significant drop in the angular momentum at low radius ($r < 10$ a.u.) right after the first core formation. At this stage, the specific angular momentum is several times higher in the AD case. After this drop, from 20 to 30 kyears, we note less noticeable differences. In the ideal MHD case, the specific angular momentum quickly increases until it reaches about the same value as in the AD case. The rotation then increases exponentially in both 10 and 100 a.u. spheres. In the AD case, the increase is similar for the core ($r < 10$ a.u.) but specific angular momentum in the 100 a.u. sphere remains steady.

Last, we want to point out another possibly unphysical behavior. The launching of the outflow precedes a displacement of the core of dozens of a.u. to less magnetized regions. This is due to the combination of two effects: first numerical resistivity can release of the flux-freezing constraint;

second, the core moves along the mean direction of the magnetic field with time. This allows for a release of the magnetic pressure as the core moves (up to dozens of a.u.) freely[4] towards regions where pileup did not occur. Evidence for this is gathered Fig. 4.20. The $(0, 0)$ coordinates correspond to the center of the box, where the core initially forms. After the fast outflow is launched (different from the growing magnetic tower) the core moves up to a less dense/magnetized region. Its consequences appear in the $B(\rho)$ plot (middle column) as in the most dense part of the core, magnetic field drops while the regions right next to it see their magnetic energy increase (respectively decrease) because they correspond to the former center of the box (respectively magnetic cavity). On the last column is represented the Alfvén speed and magnetic field. In this case, we integrated azimuthally with the densest cell as center around the angular momentum in 100 a.u. direction, therefore the $(0, 0)$ coordinates follow the center of the core. It is very clear that from top to bottom, the core moves upwards and explore the outflow cavity, yielding a more complex and entangled topology of the field along with very different Alfvén speed above and below. These regions used to be very different: strongly magnetized where the core used to be and a low density, less magnetized magnetic cavity. It is interesting to note that this configuration, with strong anisotropy, seems to be in a steady-state. We link the displacement of the core with the drop in specific angular momentum Fig. 4.19 for the ideal MHD case. Right after, the configuration is less constrained and the evolution of the specific angular approaches the one of the AD case, explaining the similar evolution. However, it is unlikely that this is physically relevant, as no displacement of the core is observed with diffusive effects.

Disk formation and evolution Even in this aligned case, we can form disk-like structures with a dominant rotational support. These structures are called disks, not to be confounded with pseudo-disks due to the pileup of magnetic field lines. Again, we emphasize that all the forthcoming discussion is based on arbitrary criteria and allows for comparison, but is not a definite definition of a rotationally supported disk. The evolution of the disk mass is displayed Fig. 4.21. We are interested in this paragraph only in the solid lines. The main conclusion is that disk formation occurs earlier in the AD case than in ideal MHD. We lack time integration to conclude on the final mass of the disk in the AD case but evidence point to the displayed result: there is a great stability in every flow variable at the end of the time integration for the AD case. It is safe enough to suppose that steady-state is almost achieved, with $M_{\rm disk} \sim 0.2 M_\odot$. For the ideal MHD case, on the other hand, strong variations occur even at later times, due to the continuous pileup of magnetic field. Thus, we finally reach a steady value ($M_{\rm disk} \sim 0.1 M_\odot$) but care is to be taken while talking of equilibrium, as it is unclear if it is physically relevant (see § 4.2.1 where we show that the core moves along the initial direction of the field lines, at late times).

We compare in Fig. 4.22 the last time step for the AD case with the ideal MHD case at the same time. The most striking feature is the turbulent behavior of the ideal MHD case compared to the well organized AD case. This is clear in every of the three (density, Alfvén speed, angular momentum) plots. It is insightful since it allows to better visualize what is considered as a disk in both cases. Additionally, we note that we conserve the growing magnetic tower (hourglass shape) in the AD case while the ideal MHD case shows no clear evidence of magnetic cavities, neither in the Alfvén speed nor density maps. Fig. 4.23 also adds more insight by displaying the intensity of the magnetic field, and the toroidal magnetic field for cells that fit the criteria of Joos et al. (2012). We can conclude that in the AD case, we indeed form a disk-like structure with strong rotational support. On the ideal MHD case, on the other hand, the structure differs from a flat, rotationally supported disk. Both the total and toroidal component of the magnetic field are more than two orders of magnitude lower in the AD case than in the ideal MHD case, explaining the increased magnetic braking and the shape of the disk. Indeed, magnetic pressure becomes non-negligible as support against collapse and the shape of the disk suffers accordingly. One way to improve this

[4]Up to the assumption of parallel field lines.

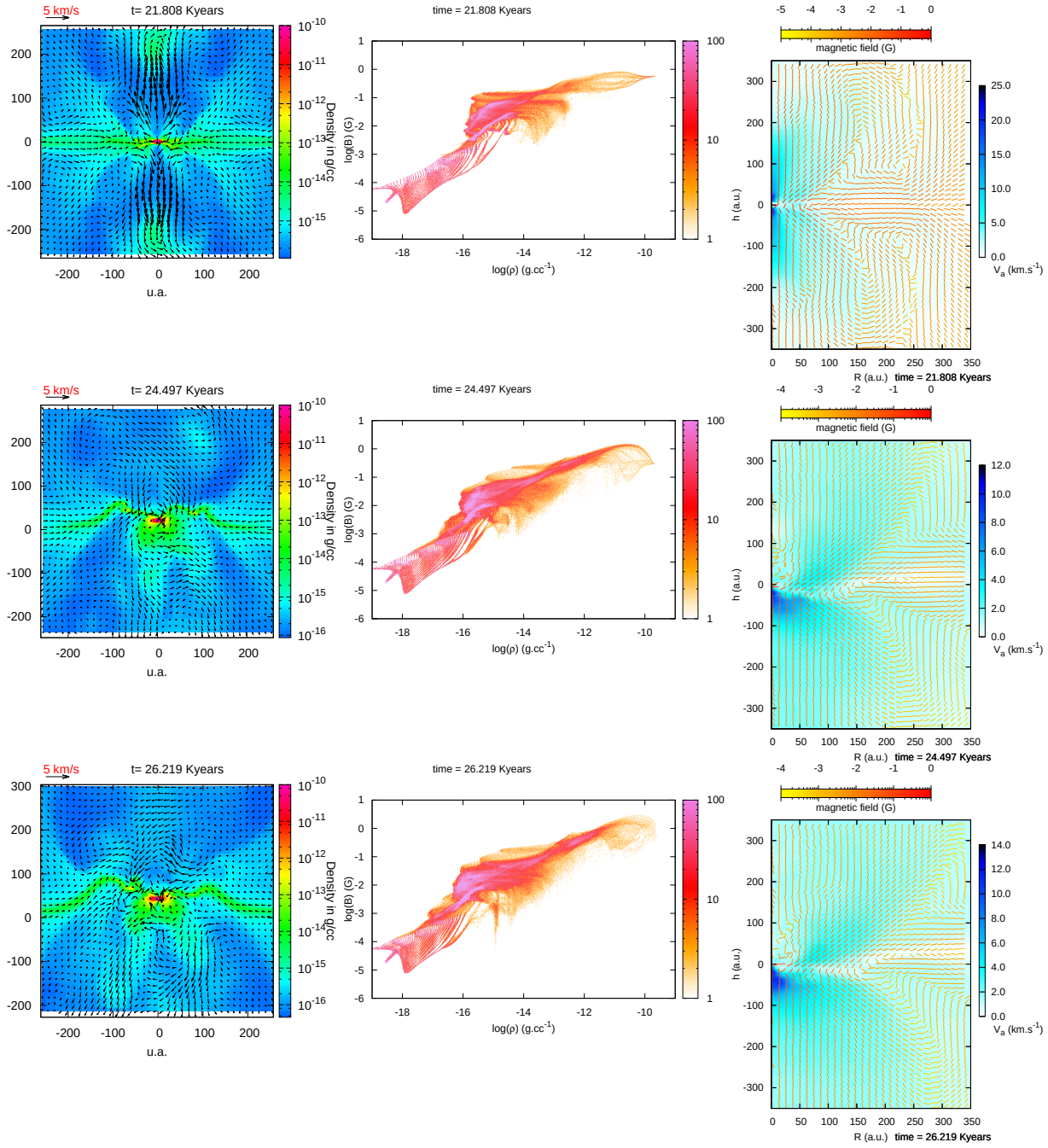

Figure 4.20: $\mu = 5$, aligned case. From left to right: time evolution in the ideal MHD case (same time for each column of plots). Top: magnetic field versus density. Middle: cut in the xOz plane (perpendicular to the disk plane) representing density/velocity maps. Bottom: Alfvén speed map with the magnetic field direction and intensity as noheaded vectors.

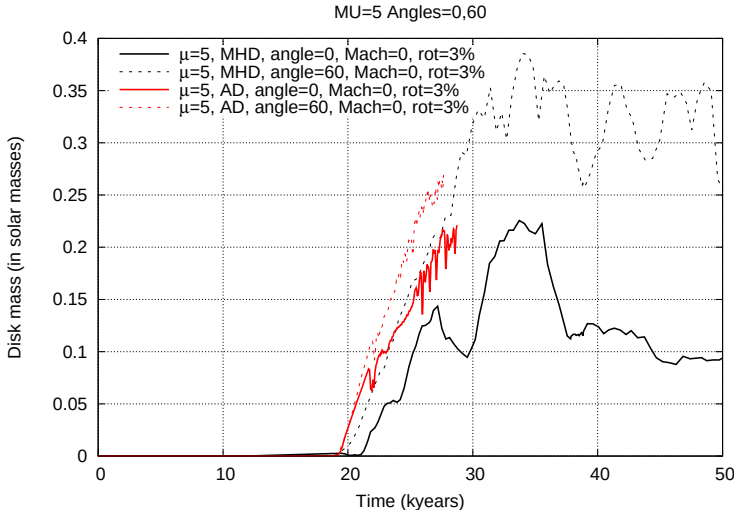

Figure 4.21: $\mu = 5$, aligned case and misaligned case. Evolution of the mass of matter abiding by the criteria of Joos et al. (2012) as a function of time. The mass is in solar masses. Solid lines stand for the aligned case while dashed lines stand for the non-aligned case, with an angle of 60 degrees between the rotation axis and the initial magnetic field direction.

would be to use a much more stringent criteria for the rotational support, but will then lead to more statistical errors: we are clearly taking into account non-Keplerian supported regions. However, one has to remember that these regions are more than 5 orders of magnitude less dense, yielding a minor fraction of the accounted mass. If we sharpen the disk-criteria, we will end up with less mass, and therefore any error will have a much higher statistical importance (and occur in higher density regions). We finally chose to keep these criteria, remembering that they stand as ad-hoc criteria more than they exactly identify rotationally supported disks.

$\mu_{\mathbf{BE}} = 2$, a more magnetized case

First core formation In this more realistic case, we expect even more differences than in the weakly magnetized case. We also expect abnormalities in the ideal MHD case because of an increased pileup compared to the previous case. We note some differences in the outflow and magnetic cavity in both cases. There is outflowing fluid but it does not end up in higher density bubbles as in the previous case. Accretion is filamentary in the idea MHD case and remains smooth in the AD case. The main difference is a very fast outflow launched in the ideal MHD case a few kyears after the first core formation. This arises due to a very high pileup of magnetic energy at low radius (< 5 a.u.) which is then released as a collimated outflow (see Fig. 4.24). Again, this does not happen in the AD case where the magnetic pileup stops in the same plateau at $B \sim 10^{-1}$ G. On the contrary in the ideal MHD case the magnetic field rises up to $\sim 10^{1}$ G before the launching of the outflow and then we witness oscillations in the magnetic energy as the energy is released and then pileups again. This is summarized Fig. 4.25. This fast outflow is of unphysical nature, and results concerning long-term evolution have to be taken with care (see § 4.2.3). After the fast outflow event, most of the magnetic and rotational energy is evacuated and the surroundings of the core evolve to a more stable configuration. This configuration allows for a rotational structure to form, abiding by the criteria chosen for the disk.

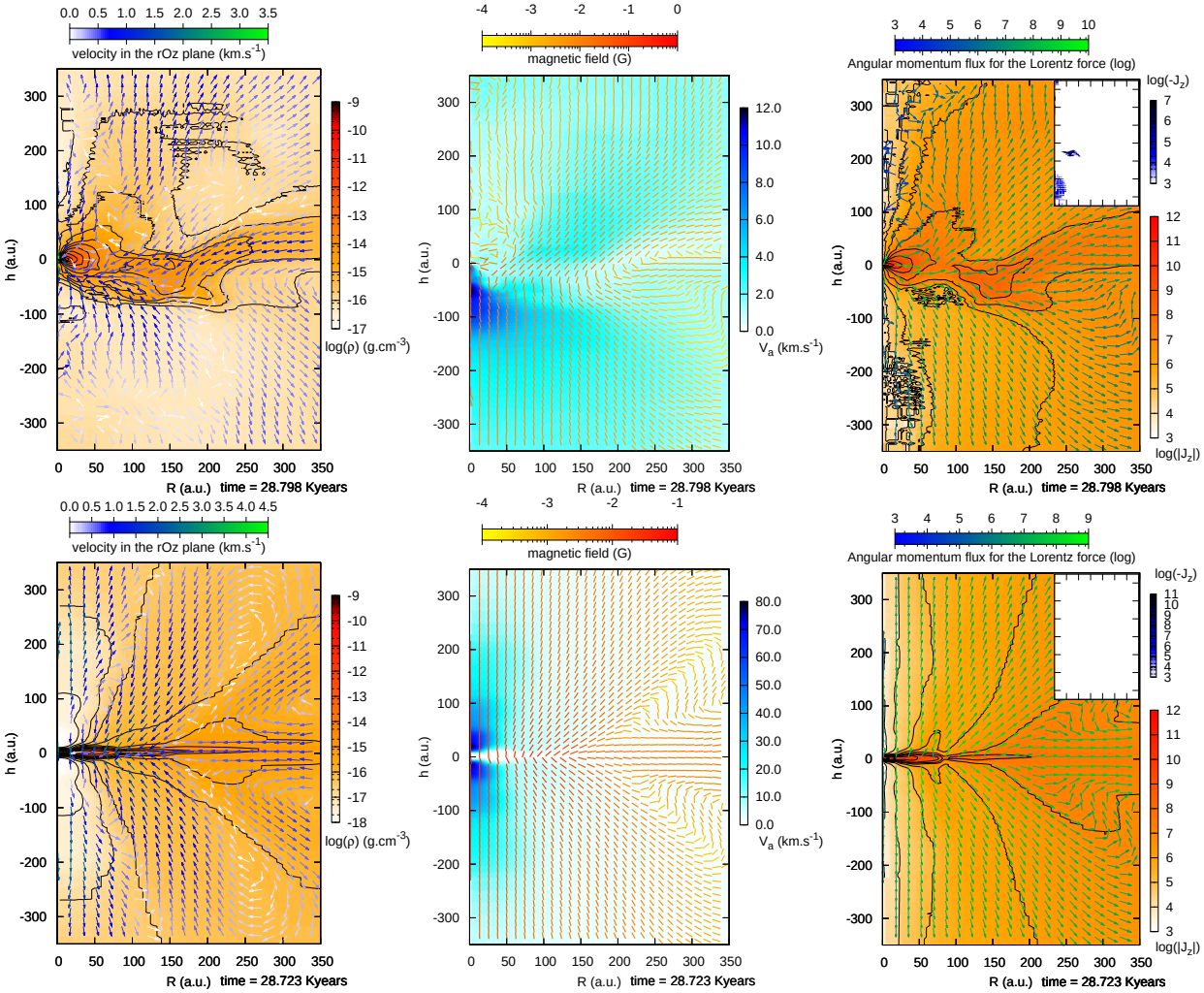

Figure 4.22: $\mu = 5$, aligned case. Top: ideal MHD. Bottom: Ambipolar diffusion. All the plots correspond to the time of the last output in the AD case. From left to right: density/velocity azimuthally integrated; Alfvén speed and magnetic field; angular momentum and flux from the Lorentz force; toroidal component of the magnetic field for cells abiding by the criteria of Joos et al. (2012).

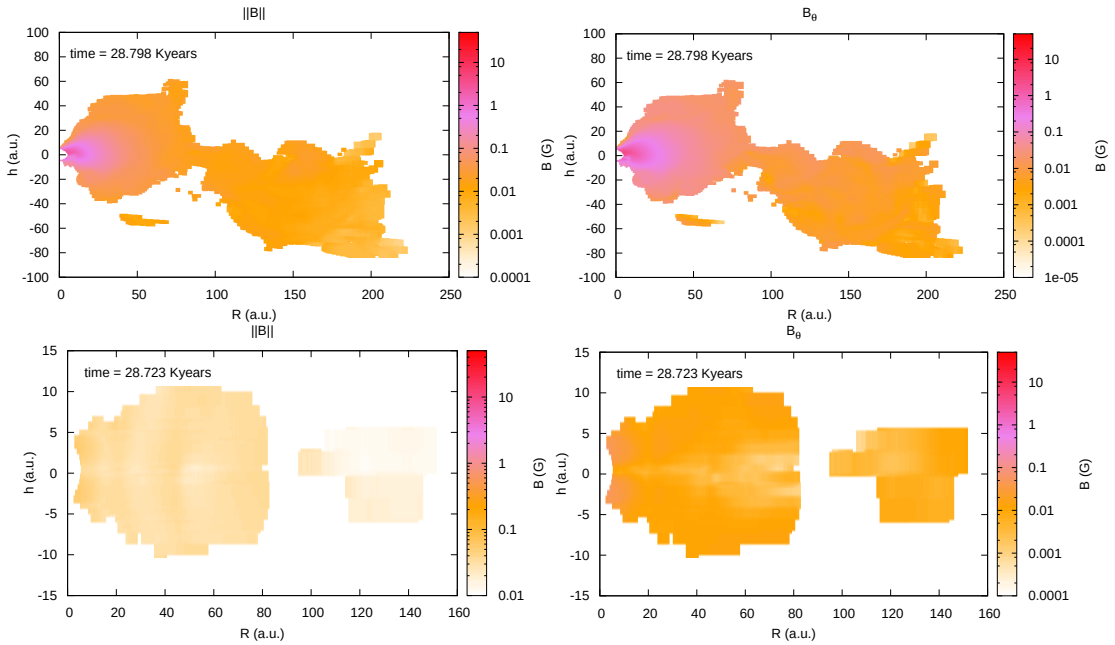

Figure 4.23: $\mu = 5$, aligned case. Top: ideal MHD. Bottom: Ambipolar diffusion. All the plots correspond to the time of the last output in the AD case. From left to right: magnetic field intensity; toroidal magnetic field intensity; restraining ourselves in all cases to cells abiding by the criteria of Joos et al. (2012).

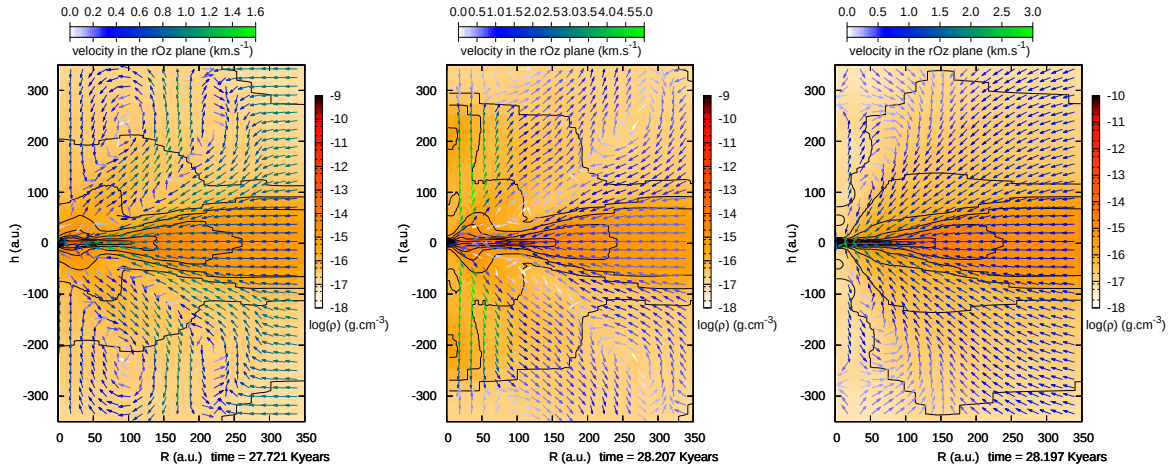

Figure 4.24: $\mu = 2$, aligned case. Two left columns: ideal MHD. Right: Ambipolar diffusion, density/velocity field. Two left columns: time evolution in the ideal MHD case of the density/velocity field from after the first core formation to the time when a fast outflow is launched.

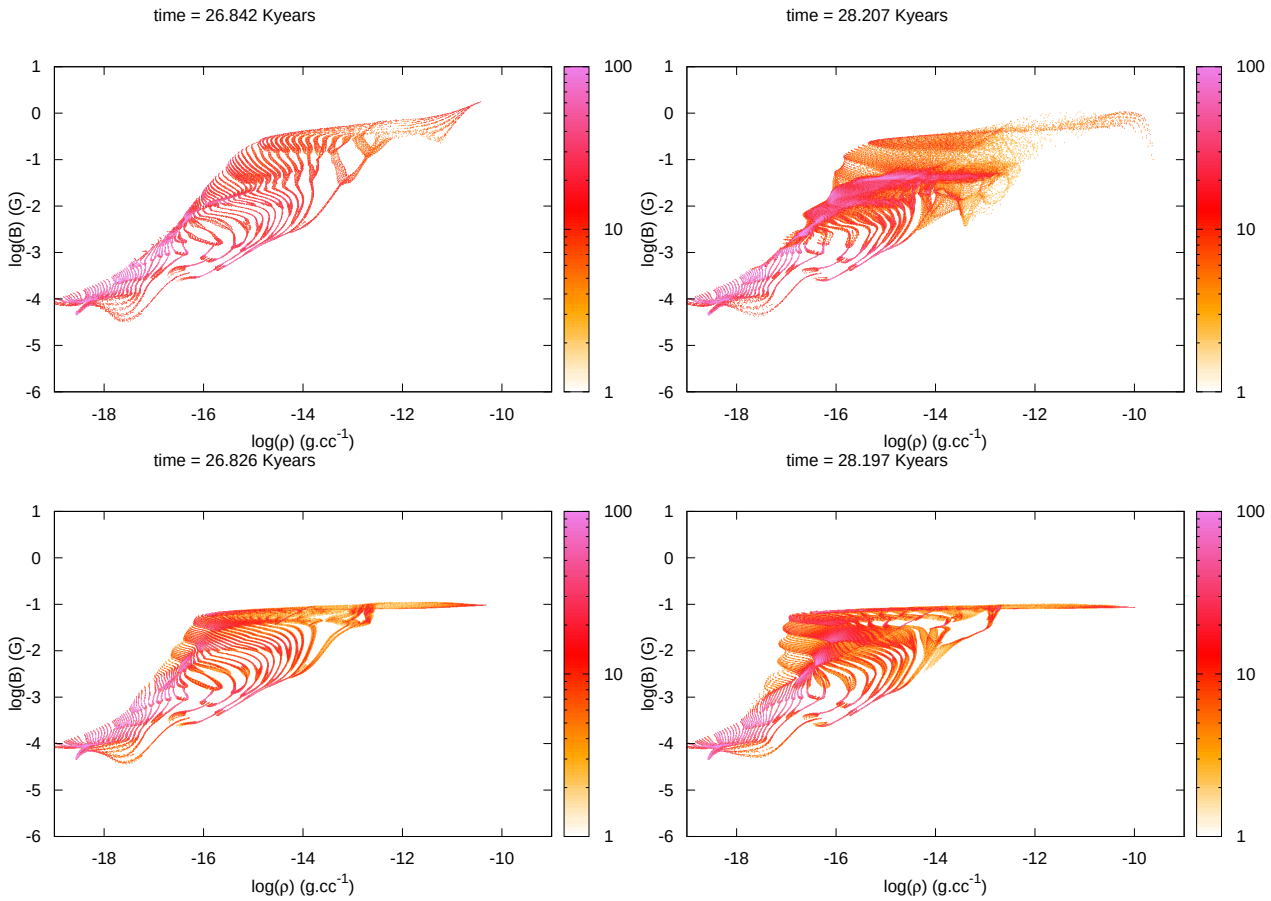

Figure 4.25: $\mu = 2$, aligned case. Top: ideal MHD. Bottom: Ambipolar diffusion. Evolution of the magnetic field versus density from the first core formation to the time when a fast outflow is launched.

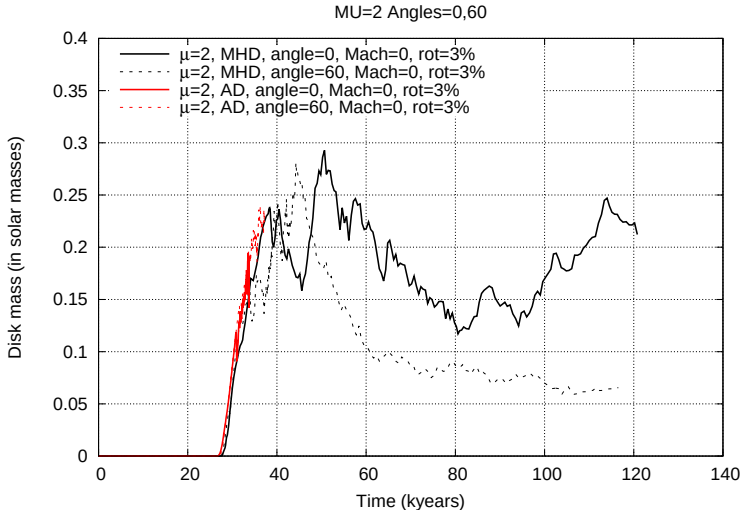

Figure 4.26: $\mu = 2$, aligned case and misaligned case. Evolution of the mass of matter abiding by the criteria of Joos et al. (2012) as a function of time. The mass is in solar masses. Solid lines stand for the aligned case while dashed lines stand for the non-aligned case, with an angle of 60 degrees between the rotation axis and the initial magnetic field direction.

Long term evolution and disk formation In the long term evolution, we first look at the disk mass as a function of time, represented Fig. 4.26. The disk appears earlier in the AD case than the ideal MHD case, as expected. The disk evolution is very similar to the previous $\mu_{\rm BE} = 5$ study for the AD case. It is due to the very similar magnetic field repartition in both cases. Ambipolar diffusion effectively prevents the magnetic field pileup, therefore making both runs very similar in the AD case. On the other hand, after the removing of a grand fraction of the magnetic energy and angular momentum in the ideal MHD case, a quite massive disk (two times more massive than in the previous $\mu_{\rm BE} = 5$ case) forms. This, again, is very probably unphysical, and explains the complex structure of the so-called disk. The evolution of the magnetization is represented Fig. 4.27. Regarding the magnetization, an equilibrium is reached after the outflow event at about 28 kyears. After the displacement of the core in the ideal MHD case, the cloud evolves toward the same steady-state configuration as in the weakly magnetized case. We note the same drop in the specific angular momentum for the ideal MHD case as previously, evidence for the displacement of the core and the release of stringent constraints due to the pileup of magnetic energy. After this event, both cases evolve again in a similar way with the building of a disk. Last, we show a snapshot of a late output Fig. 4.28. The disk structure is well defined in the AD case but as foreseen, it is very complex in the MHD case. Two separate structures abide by the criteria for a rotationally supported disk[5], as can be seen Fig. 4.29. The structure resembles a disk in the AD case. In the ideal MHD case, even the part of the disk at small radius is more extended in the vertical than in the radial direction. Both the magnitude and the toroidal component of the magnetic field are more than one order of magnitude higher in the ideal MHD case than in the AD case, yielding a pressure support from the magnetic fields two orders of magnitude higher in the ideal MHD case.

Conclusions for the fiducial, aligned case The main conclusions for the aligned cases concern the stability and symmetry improvement added with the ambipolar diffusion. In the ideal MHD case, seemingly unphysical structures appear and govern the late evolution of the protostar and the disk. These structures arise from an important pileup of magnetic field close to the central

[5]Even though at larger radius the structure is of low density, the mass of the disk is wrong by an unknown factor

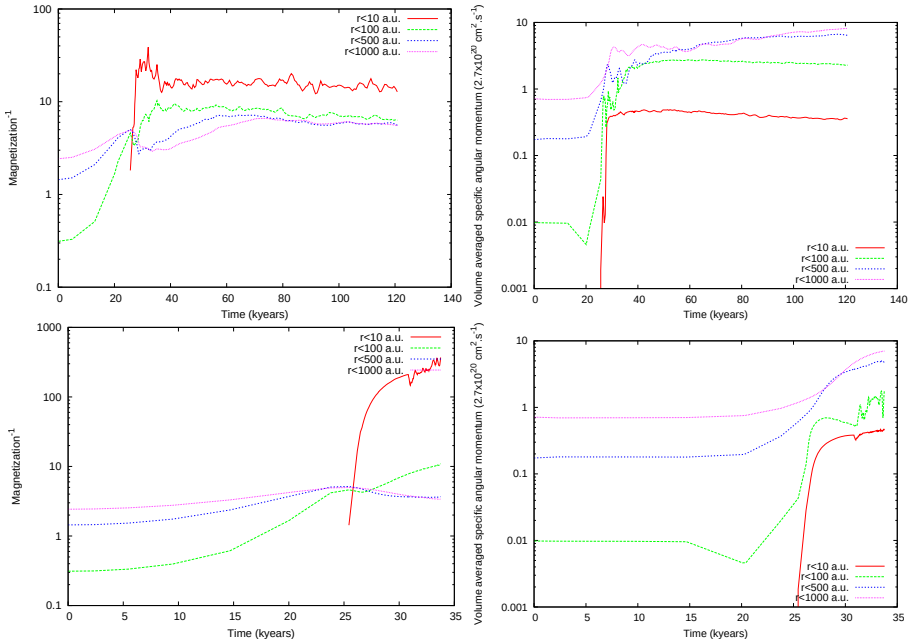

Figure 4.27: $\mu = 2$, aligned case. Top: ideal MHD. Bottom: Ambipolar diffusion. Inverse of the magnetization (average of the mass-to-flux ratio in a sphere of given radius) versus time for various control spheres; specific angular momentum versus time for various control spheres, in respect to the densest part of the cloud.

object. Numerical diffusivity probably has a minor role as resolution increases with density thanks to the AMR grid, and cannot help to release the magnetic energy. When the energy is released, a new equilibrium is able to develop but has probably not much to do with the inputed initial conditions. On the other hand, adding ambipolar diffusion effectively fights this effect even for high magnetization ($\mu_{\rm BE} = 2$). There are even only few differences between the $\mu_{\rm BE} = 2$ and $\mu_{\rm BE} = 5$ cases in particular in the repartition of magnetic field in terms of density and the size and mass of the disk-like structure.

4.2.4.2 Misaligned case

In this case we explore the differences that arise from using ambipolar diffusion when there is initially an angle between the axis of solid body rotation and the direction of the field lines. In this case, disk and pseudo-disk can form and break the cylindrical symmetry. A pseudo-disk is a flattened structure denser than its surroundings. It is the result of the stretching of the field lines that pileup as collapse proceeds. Matter gathers mostly along the field lines, creating overdensity regions where the field is stronger. Although they look like disks, these flattened structures are not rotationally supported and called *pseudo-diks* (see Galli and Shu (1993) and Hennebelle and Ciardi (2009) for more details). The disk (respectively pseudo-disk) forms perpendicular to the axis of rotation (respectively perpendicular to the mean direction of the magnetic field). In the aligned case, both structures are confounded, while in a misaligned case they are distinct: we expect the symmetry to be broken, yielding a fully three dimensional study. To represent and study the rotating structures around the core, we chose to still use a cylindrical coordinate system and azimuthally averaged quantities with the z-axis being the direction of the mean angular momentum in a sphere of 100 a.u. around the densest cell.

Based on our own tests and previous studies (see Joos et al. (2012); Li et al. (2013)) we use an

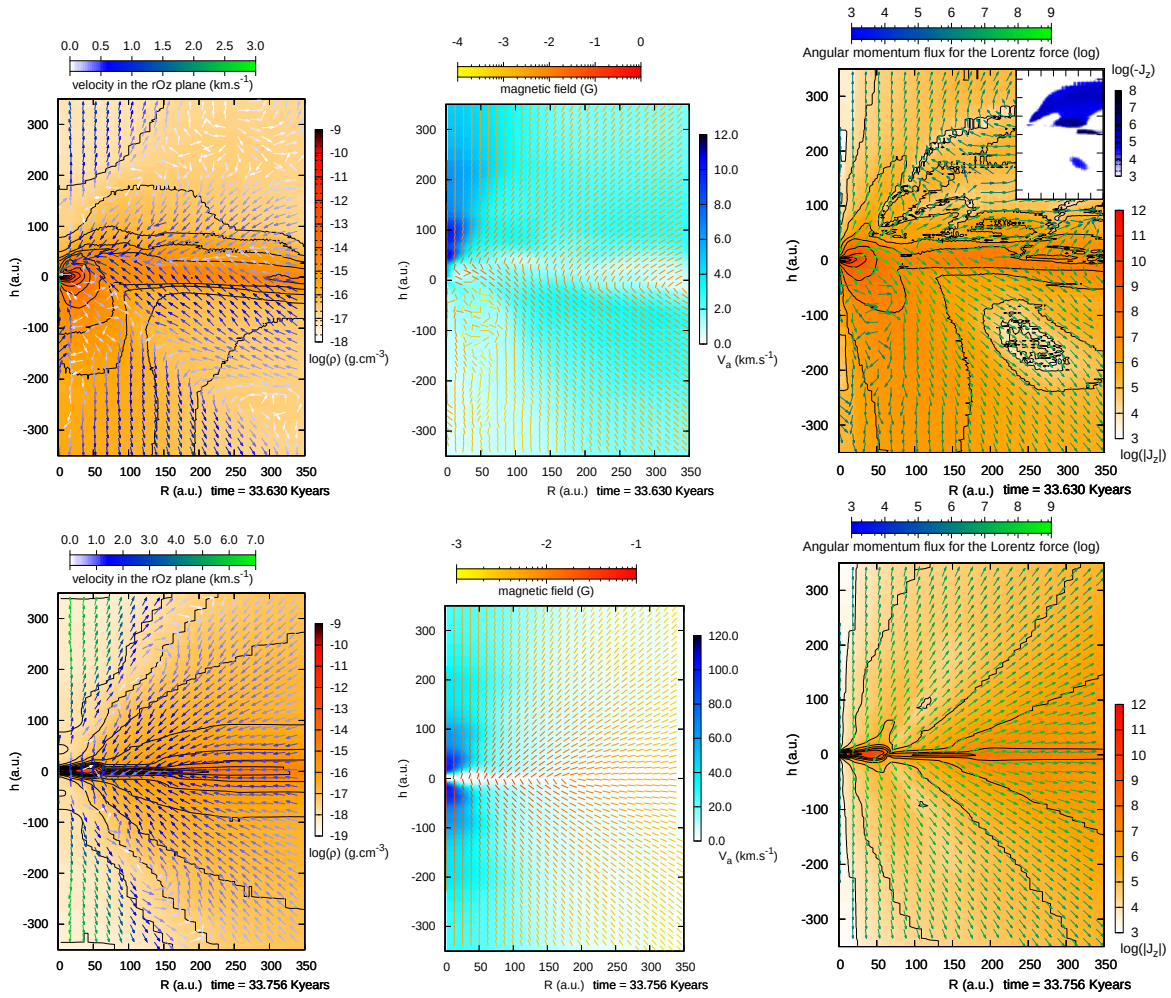

Figure 4.28: $\mu = 2$, aligned case. Top: ideal MHD. Bottom: Ambipolar diffusion. Snapshot at a late time. From left to right: density/velocity map; Alfvén speed and magnetic field; angular momentum and flux from the Lorentz force.

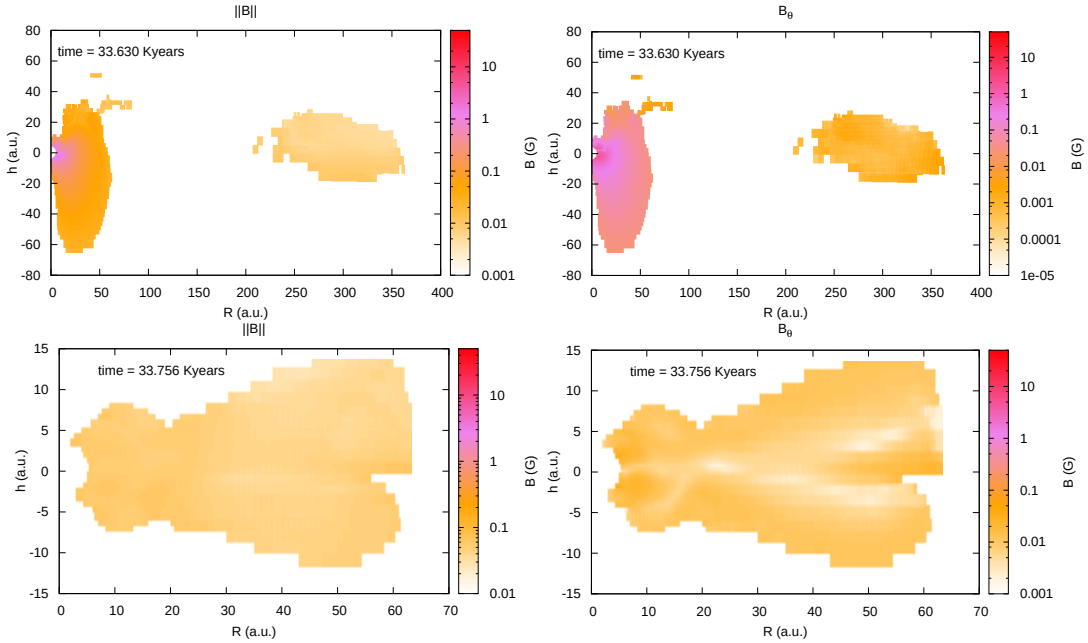

Figure 4.29: $\mu = 2$, aligned case. Top: ideal MHD. Bottom: Ambipolar diffusion. All the plots correspond to the time of the last output in the AD case. From left to right: magnetic field intensity; toroidal magnetic field intensity; restraining ourselves in all cases to cells abiding by the criteria of Joos et al. (2012).

angle of 60 degrees between the axis of rotation and the initial direction of the magnetic field. Theses studies show that results are qualitatively similar as long as we leave the perfectly aligned case by only a few degrees. The extreme case when both axis are perpendicular being possibly special too, we chose a more average angle. Again, we will present two cases, a weakly magnetized case with $\mu_{\rm BE} = 5$, and a strongly magnetized case with $\mu_{\rm BE} = 2$.

$\mu_{\rm BE} = 5$, weakly magnetized case

First core formation In this case, first core formation occurs very similarly in ideal MHD and with ambipolar diffusion. As can be seen on the two tops plots Fig. 4.30, the time of formation is the same ($t \sim 18.9$ kyears) and the size is the same ($R_{\rm core} = 10$ a.u.). In the more diffuse medium, the density repartition is also very close in both cases. About 1000 years after the first core formation, differences appear. The first core in the ideal MHD case is well defined and shrinks a little ($R_{\rm core} \sim 0.8$ a.u.). On the other hand, in the AD case, the core stays with $R_{\rm core} = 10$ a.u. but is more flattened, explaining the thicker repartition of density versus radius. The magnetic field repartition at the first core formation (bottom plots in Fig. 4.30) is also very much alike the aligned case. We retrieve the same features: a plateau in the AD case at $B = 10^{-1}$ G and the evidence for flux-freezing in the ideal MHD case with a maximum $B > 1$ G in the densest parts of the cloud. The scatter-plot is more smooth than in the aligned case (Fig.4.16) because of the non-axisymmetry. Evidence for axi-symmetry lies in the thin spider-web structures that can be seen in scatter plots, more evidently in the aligned case (clearly seen Fig. 4.25). These structures arise at every grid refinement and they are the testimony of the history of a given cell in the AMR grid. Mixing is stronger in the misaligned case, as noted before, because of its intrinsic three dimensional nature. In the aligned case, mixing occurs but the history of each cell (even after several refinements) is kept longer.

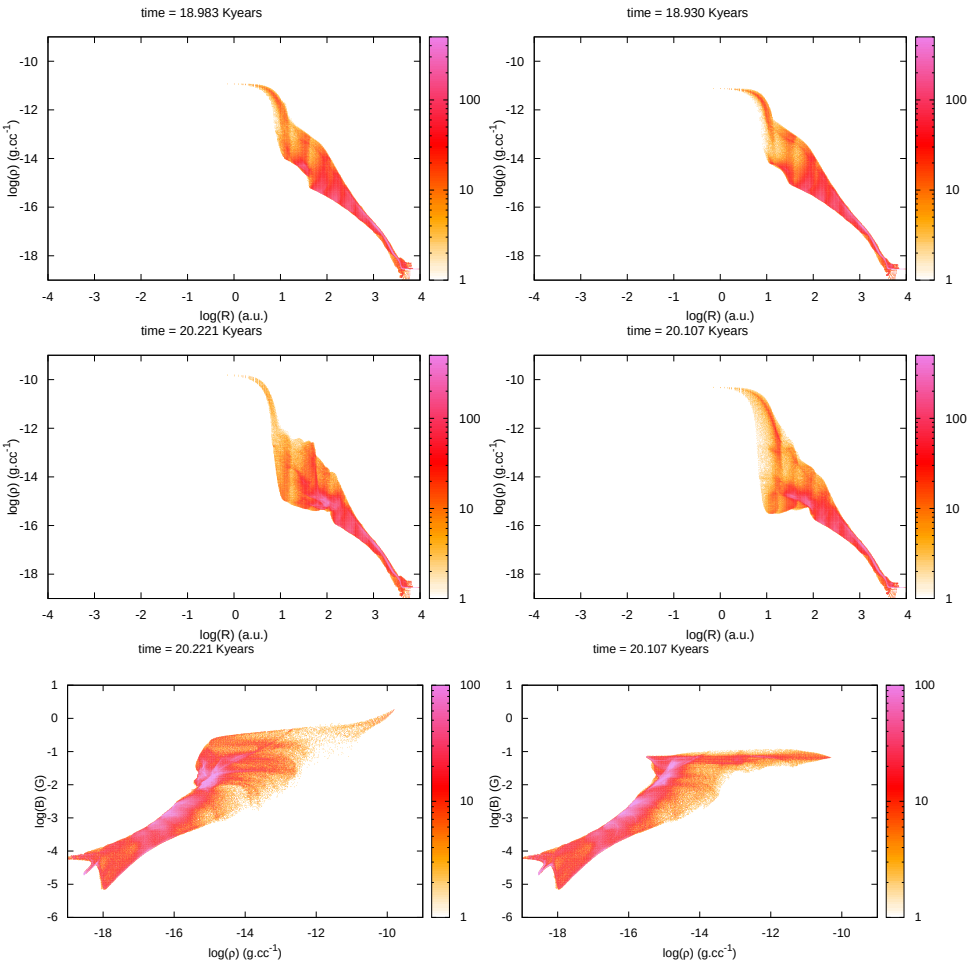

Figure 4.30: $\mu = 5$, misaligned case. Left: ideal MHD. Right: Ambipolar diffusion. Top two raws: evolution of the density versus radius from the first core formation to ~ 1.2 kyears after. Bottom plots: magnetic field intensity versus density, ~ 1.2 kyears after first core formation.

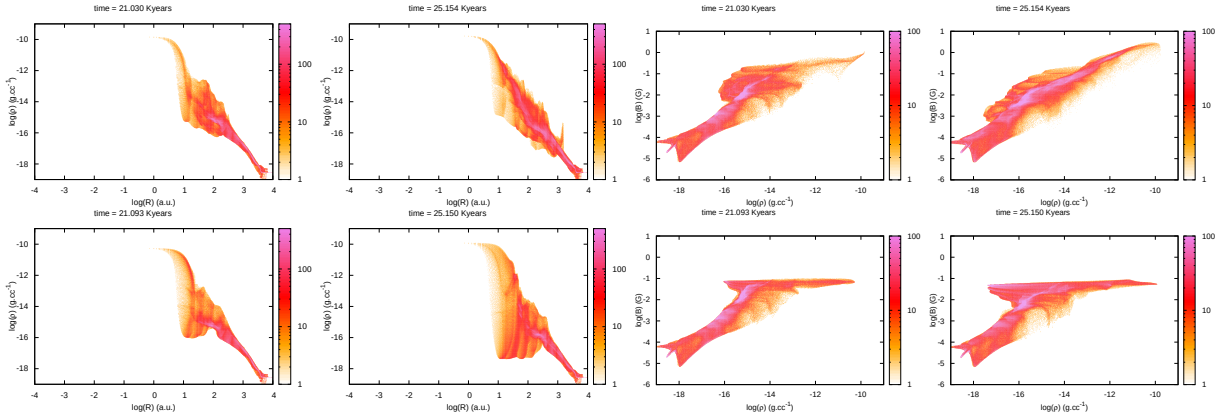

Figure 4.31: $\mu = 5$, misaligned case. Top: ideal MHD. Bottom: Ambipolar diffusion. From left to right: (two left columns) evolution of the density versus radius from after the first core formation to a late time (last output from the AD case), followed (two right columns) by magnetic field intensity versus density evolution.

Long term evolution The ideal MHD case long term evolution differs significantly from the previous aligned case. First, there is less counter-rotating regions (see also § 4.1) which is an encouraging sign to interpret our results. We witness neither significant oscillations of the magnetic energy in high density regions nor displacement of the core, even at very long time (several times the free-fall time). Fig. 4.31 shows scatter plots for both ideal and non-ideal MHD at the time of the last output in the AD case. Focusing on the four plots on the left (density/radius) we note interesting features. First, the broad dense structure in the AD case broadens even more. This structure corresponds to the disk-like structure for the high density (above $\rho = 10^{-14}$ g.cm^{-3}, between $r \sim 5$ to $r \sim 80$ a.u.) and the magnetic cavity for the less dense parts (below $\rho = 10^{-14}$ g.cm^{-3}). In the ideal MHD case, both regions (especially the less dense one) are shrinked because of the flux freezing that prevents mixing between regions. Another proof for this is the slope in the magnetic energy that closely approaches the theoretical $B \propto \rho^{\frac{2}{3}}$ (up to topology issues and mixing) while in the AD case the plateau is kept throughout the whole simulation. We witness an important relocation of the magnetic energy in low density regions (bottom right plot) in the AD case. We represent Fig. 4.32 the density/velocity and Alfvén speed/magnetic field maps for the same late times as Fig. 4.31 to investigate these regions. They are located above and below the core relative to the plane of the disk, in the magnetic tower cavity (see Fig. 4.32, bottom right plot). Although there is no significant ($\gtrsim$ a few a.u.) displacement of the core, we witness qualitatively the same breaking of symmetry as in the aligned case (top right plot). Quantitatively, the change in magnetic field and density (or Alfvén speed) is restrained in this misaligned case. However, when looking at the evolution of density (two right columns) it is very interesting to note that the beginning of outflow in the MHD case (top left plot) is destroyed when symmetry is broken, leading to a complex velocity and density field (top raw, second column from the left). For the AD case, things happen differently: the outflow develops only at a later time, but remains present until the end of the simulation. Last, substructures appear at late time in the ideal MHD case (this is less clear in the AD case), as can be seen in Fig. 4.31 on the second column from the left. Localized regions denser than their surroundings are effectively traced using the scatter plot $\rho(r)$, where they appear as thin spikes of higher density than the background medium. These spikes might lead to fragmentation at later times, but we did not witness it by the time we ended the simulation after about 3 free-fall times.

We now focus on the evolution of the magnetization in four control spheres of various radius (10, 100, 500 and 1000 a.u.), as shown Fig. 4.33 on the left. For $r \geq 500$ a.u., magnetization is similar

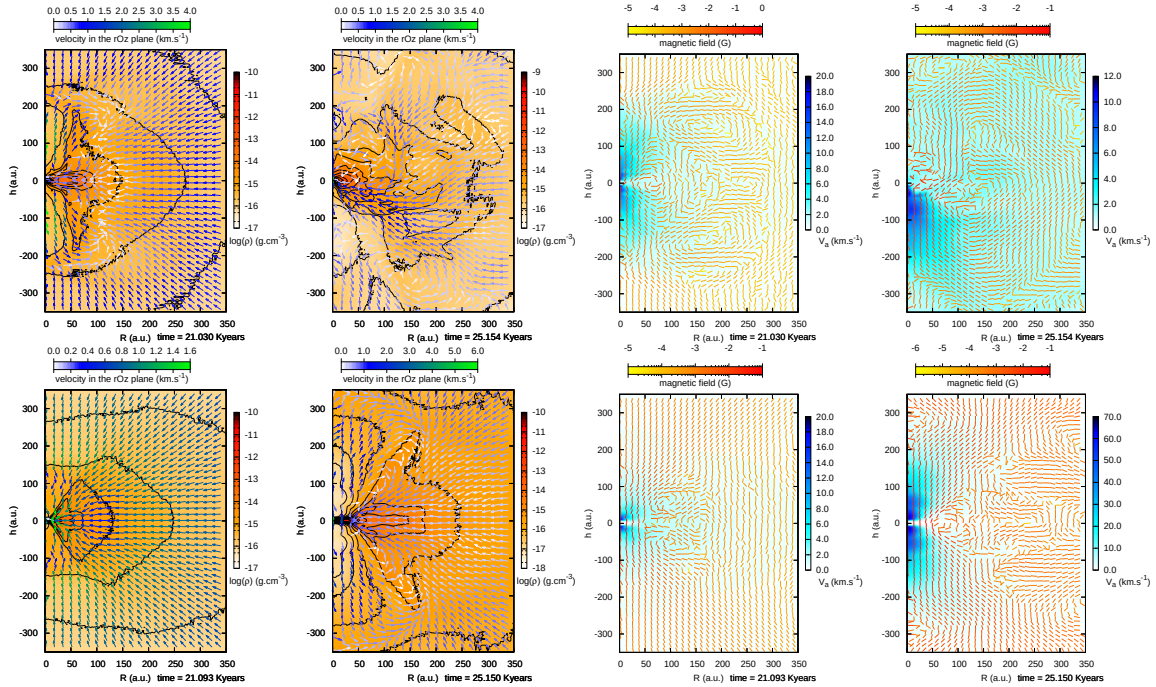

Figure 4.32: $\mu = 5$, misaligned case. Top: ideal MHD. Bottom: Ambipolar diffusion. From left to right: (two left columns) evolution of the density/velocity from after the first core formation to a late time (last output from the AD case), followed (two right columns) by Alfvén speed maps and magnetic field intensity evolution.

in the AD and ideal MHD case. For smaller scales, we retrieve the previous results: magnetization is weaker by a factor of about 3 at 100 a.u. and by several orders of magnitude at the scale of the core. The first exponential growth of the magnetization at $r = 10$ a.u. when the first core forms is extremely similar in both cases, as had be noted previously in the $\rho(r)$ and $B(\rho)$ scatter plots. The brutal drop in the ideal MHD case corresponds to the small displacement of the core and the breaking of symmetry. In the AD case, we still have an exponential growth, with about the same slope as in the aligned case: $\log(< \mu_{\rm BE} >_{r=10\,\rm a.u.}) \sim 0.4t$. Again, we highlight that the steady state reached after the displacement of the core in the ideal MHD case is maybe not of physical nature, and that conclusions regarding long-term evolution in this case must be regarded carefully. Last, it is worth noting that in the ideal MHD case, the overall magnetization is weaker than in the aligned case. Two effects play in the same direction. First the magnetic pileup is weaker because collapse can occur along field lines more easily than when collapse is occurring perpendicular to the mean field. Second, the magnetic braking time is theoretically longer meaning the magnetic braking is weaker. This last effect will have consequences on the disk formation, but also account for less magnetic pileup because infalling matter has a higher azimuthal velocity and does not fall directly towards the core. We represent the evolution of the specific angular momentum on the right of Fig. 4.33. In the ideal MHD case, the displacement of the core is reduced to less than a dozens a.u. and therefore is not visible on the 10 a.u. curve. We can still note a more visible trend: in the AD case specific angular momentum is more effectively kept at smaller radius ($r < 100$ a.u.) while is it pushed outwards in the MHD case (more specific angular momentum for $r > 500$ a.u.).

Disk formation and evolution The disk mass evolution is represented in Fig. 4.21. Again, we use the criteria described in appendix 4.A or in Joos et al. (2012). In both cases, the disk mass

is higher than in the aligned case (dashed lines compared to solid lines). The disk mass in the steady state for the ideal MHD case is about three times the one in the aligned case. We did not reach equilibrium in the AD case, but it is already clear too that the disk will be more massive by a non-negligible factor in the AD case. We represent Fig. 4.34 the shape and repartition of the magnetic field intensity and the toroidal field intensity. In the ideal MHD case the magnetization is comparable although somewhat weaker (by less than an order of magnitude) than in the aligned case, but most importantly the disk now resembles a rotationally supported disk. Moreover, the disk is in one part, there are no cells at large radius abiding by the criteria as in the aligned case. For the AD case the disk is well defined with weaker magnetic field (both total and regarding the toroidal component) by about two orders of magnitude compared to the ideal MHD case. There are remarkable structure at $r \sim 50$ a.u. and $r = 130$ a.u., the first of which matches the edge of the outflow cavity. The structure at $r = 130$ a.u. is believed to be evidence for the non-axisymmetry more than any physically relevant phenomena. It is also interesting to note that there is a lack of toroidal field in the very small radius region, which was not visible in the aligned case. This accounts for weaker magnetic braking and allows for more massive disks to form. Last, we focus on the angular momentum maps. We trace Fig. 4.35 the evolution of the angular momentum since the first core formation and at the two times presented Fig. 4.32. The results look much more similar. In both cases, the transport of angular momentum through the Lorentz force occurs primarily along the disk plane, because of the pileup of angular momentum. The transport is stronger in the ideal MHD case, but more steady in the AD case. Compared to the aligned case, the ideal MHD case seems to look smoother with only few counter-rotating regions, mostly in the turbulent regions of the outflow. These regions does not account for a significant fraction of the angular momentum, contrarily to previously. Moreover, they are also visible in some of the AD case plots and shouldn't be regarded as issues. At the end, the disk is well seable in the AD case (bottom right plot). On this last plot, we notice that iso-angular momentum cylinders appear at low radius (vertical isolines in the plot). We do not have explanations for the formation of such structures yet, but it corresponds to corotation regions since density is almost constant along cylinders too (see Fig. 4.32 bottom line, second plot from the left). This supports the orders of magnitude calculation from Joos et al. (2012) and the few remarks added § 1.C.

$\mu_{\mathbf{BE}} = 2$, a more magnetized case

First core formation The first core forms at $t \sim 26.5$ kyears. It initially sizes $r \gtrsim 10$ a.u. in both ideal MHD and AD cases and shrinks to $r \sim 8$ a.u. shortly after (~ 0.5 kyears). Compared to $\mu_{\rm BE} = 5$ the core is more spherical. Fig. 4.36 shows the flow variables at the time of creation of the first core. Ambipolar diffusion has not yet introduced significant differences at this stage. The angular momentum flux for the Lorentz force is a little higher in the ideal MHD case and there are two small counter-rotating regions that are not correlated to a change of topology in the magnetic field. Close to the core, the topology is slightly different with less pileup in the AD case: it's the region where ambioplar diffusion can effectively diffuse the field.

Long term evolution The main conclusions from the $\mu_{\rm BE} = 5$ hold in this case, yet are less evident. The misalignment is effectively reducing the unwanted effects such as counter-rotation and displacement of the core in the ideal MHD case compared to the aligned case. However we now note some counter-rotation even in the AD case (see Fig.4.41), meaning that the diffusion is now struggling to remove enough magnetic flux to prevent counter-rotation. There is still an oscillation in $B(\rho)$ after the first core formation that occurs in the ideal MHD case while not in the AD case, where the plateau is still very well defined at $B \simeq 10^{-1}$ G (see Fig. 4.37). The oscillation in $B(\rho)$ is concomitant with a slight displacement of core as can be seen Fig 4.38 with the breaking of the symmetry. It quickly

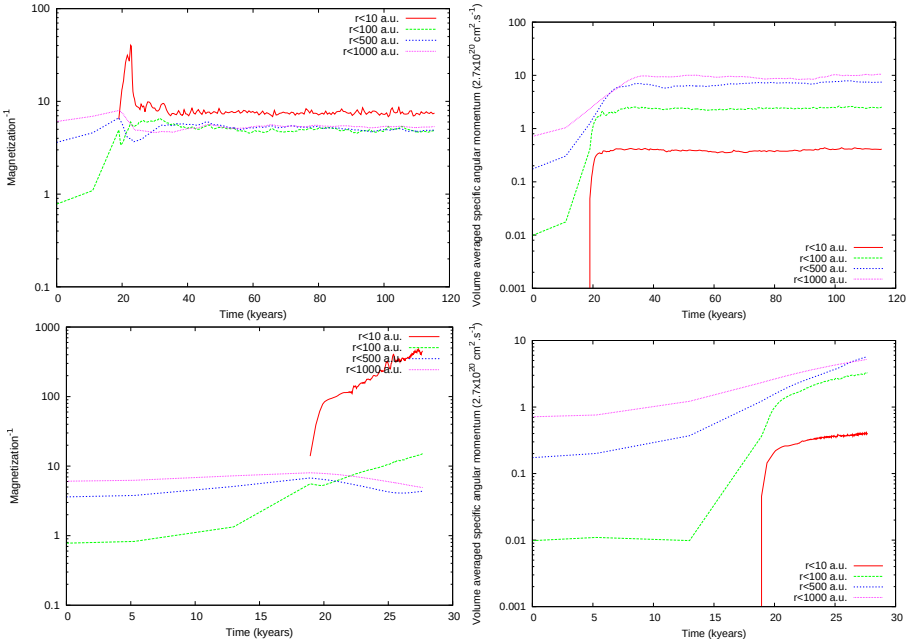

Figure 4.33: $\mu = 5$, misaligned case. Top: ideal MHD case. Bottom: AD case. Evolution of the magnetization in four control spheres of various radius; specific angular momentum versus time for various control spheres, in respect to the densest part of the cloud.

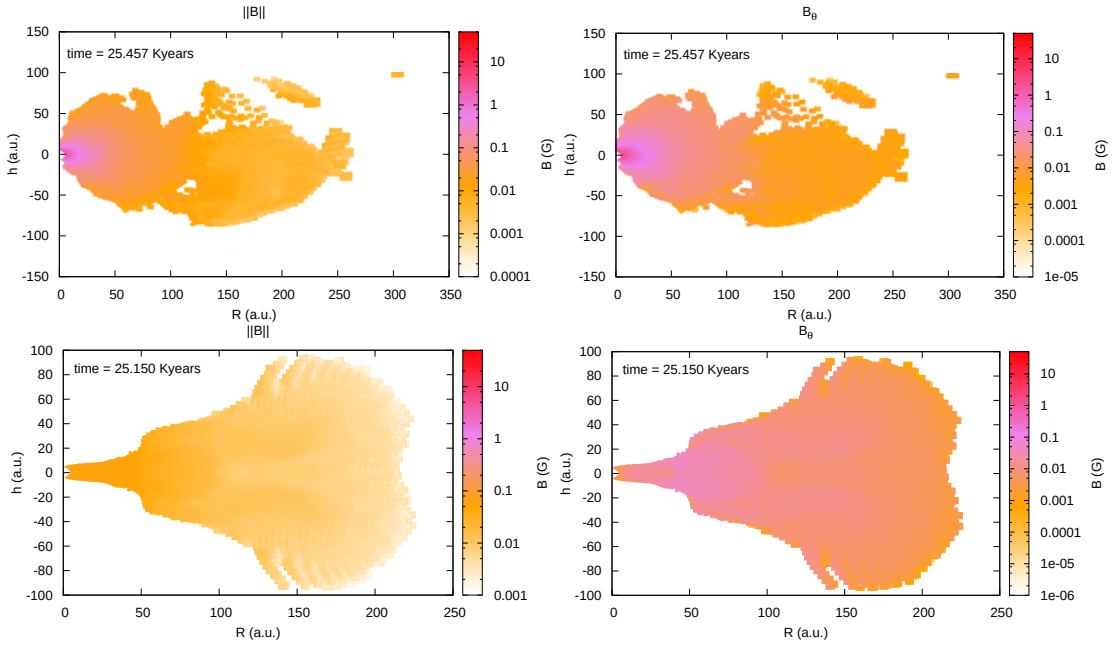

Figure 4.34: $\mu = 5$, misaligned case. Top: ideal MHD. Bottom: Ambipolar diffusion. All the plots correspond to the time of the last output in the AD case. From left to right: magnetic field intensity; toroidal magnetic field intensity; restraining ourselves in all cases to cells abiding by the criteria of Joos et al. (2012).

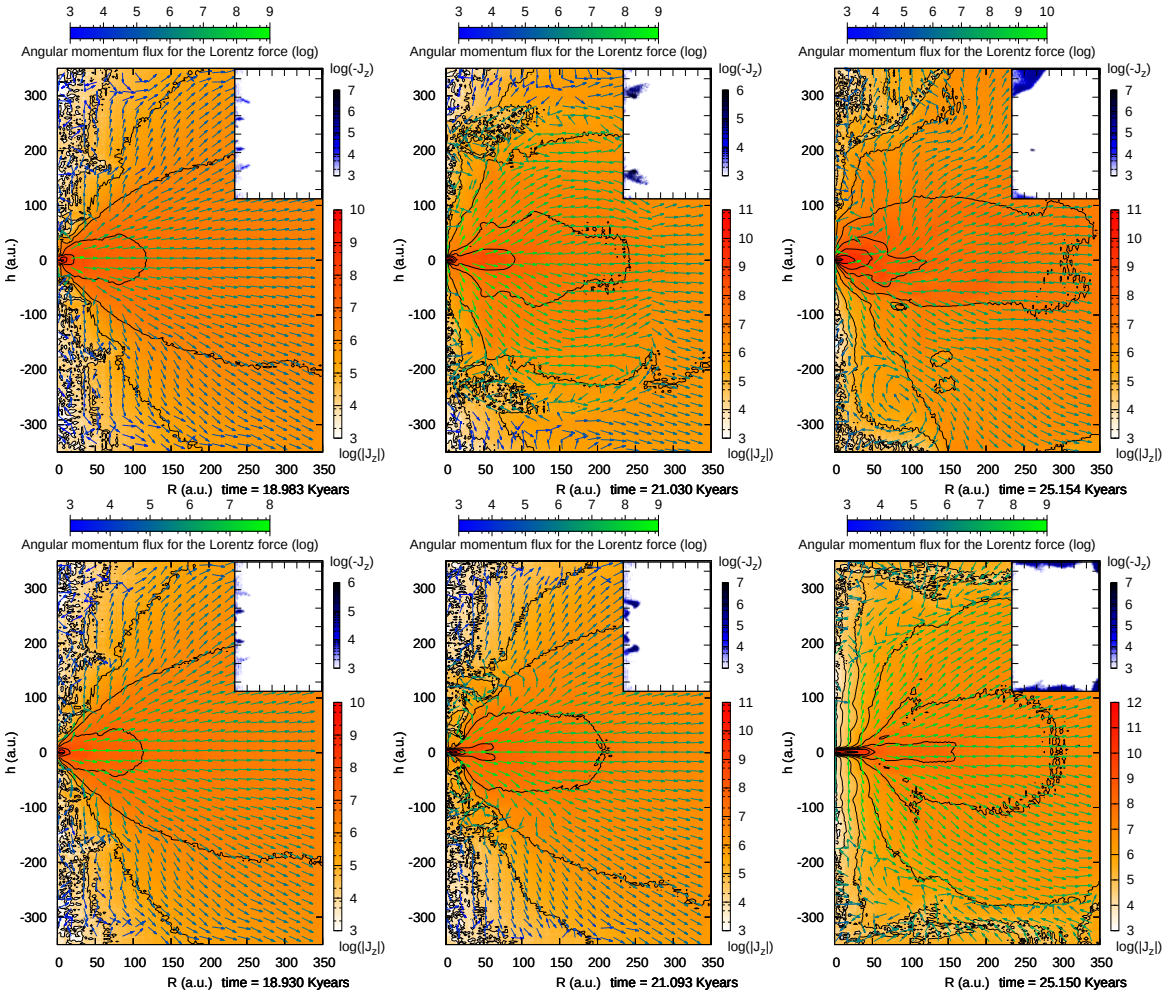

Figure 4.35: $\mu = 5$, misaligned case. Top: ideal MHD. Bottom: Ambipolar diffusion. From left to right: (two left columns) evolution of the angular momentum/angular momentum flux for the Lorentz force from the first core formation to a late time (last output from the AD case).

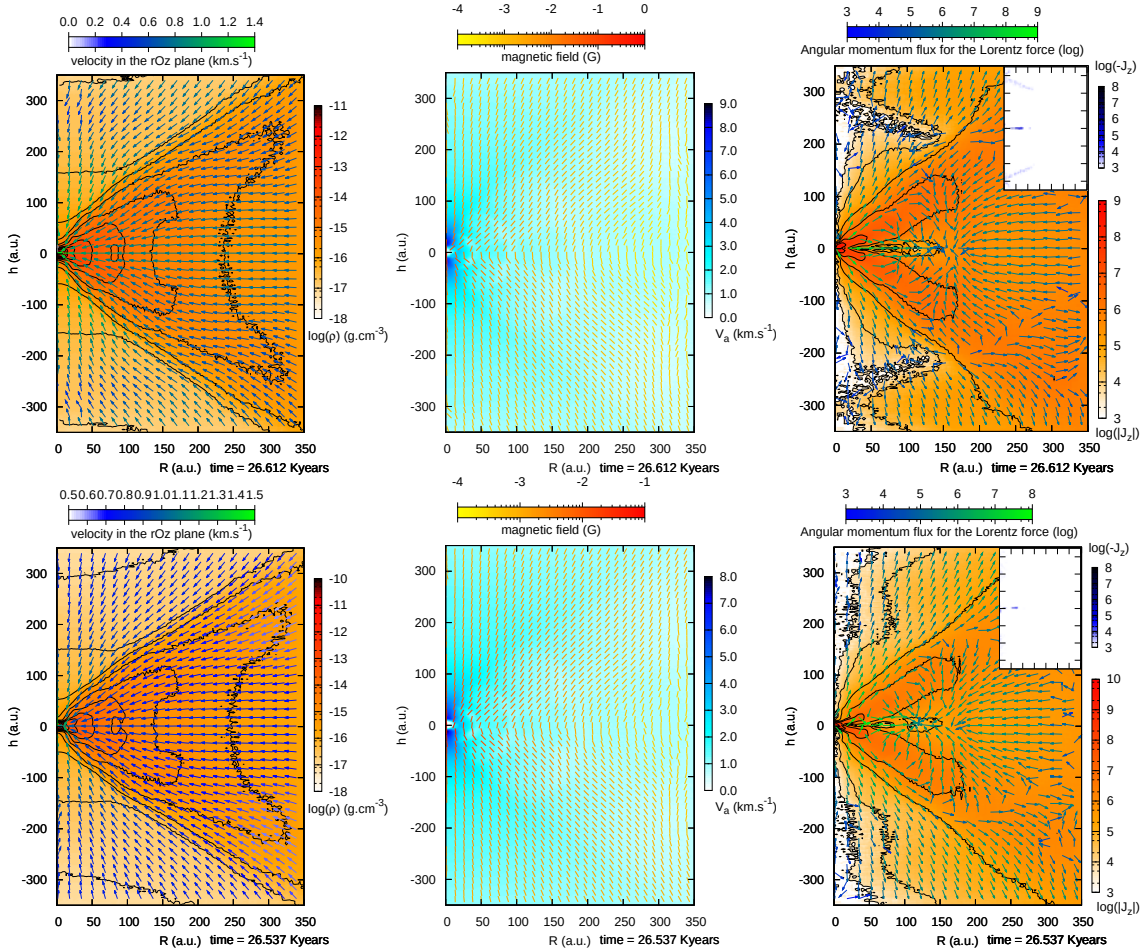

Figure 4.36: $\mu = 2$, misaligned case. Top: ideal MHD. Bottom: Ambipolar diffusion. From left to right: density/velocity map; Alfvén speed/magnetic field map; angular momentum/angular momentum flux for the Lorentz force. All plots correspond to the time of formation of the first Larson core, $t \sim 26.5$ kyears.

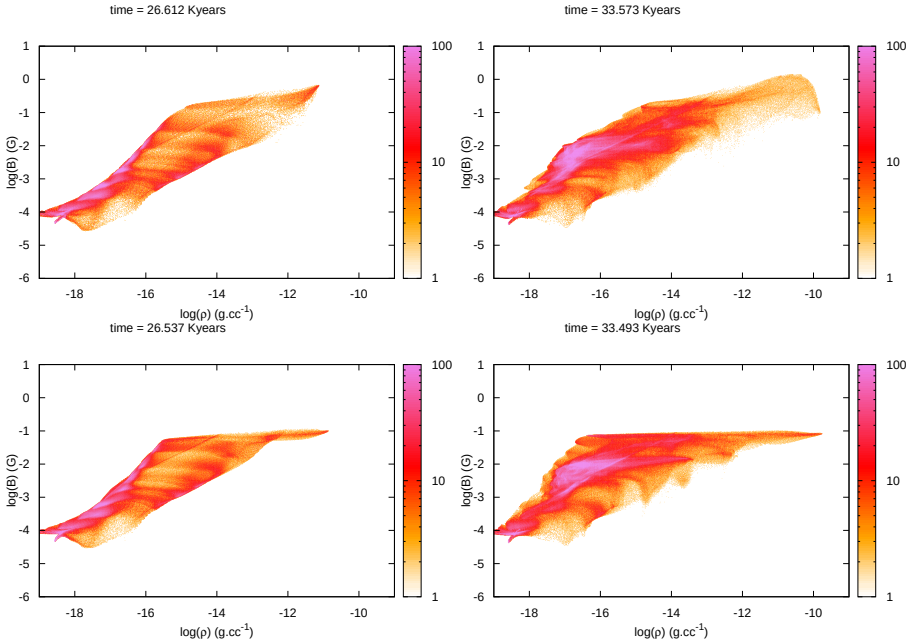

Figure 4.37: $\mu = 2$, misaligned case. Top: ideal MHD. Bottom: Ambipolar diffusion. From left to right: evolution of $B(\rho)$ scatter plots, at the time of the first core formation and 7 Kyears after.

stabilizes and a rotationally supported disk is created, as in the weaker magnetized case. In the ideal MHD case, there are no clear outflows as in the aligned strongly magnetized one. In the AD case, outflowing gas appears about 7 Kyears after the first core formation but it does not yield well defined magnetic cavity or density structure. The evolution of the magnetization is displayed Fig. 4.39 on the left. We see that the weak magnetization in the ideal MHD case for both 10 and 100 a.u. control volumes is kept longer and drops when the displacement and symmetry breaking occur, as in the previous case. The equilibrium value, once again, should not be interpreted with too much details as it is the probable result of an unphysical release of the magnetic energy. It is both encouraging and confusing to note that we seem to describe the relevant physics (without displacement of the core) longer in this more magnetized case than in the previous case (see Fig. 4.33). We explain this behavior with the more magnetized environment surrounding the core, making it harder to release the energy by moving to already highly magnetized regions. In the AD case, the behavior is changed and the smooth exponential growth is replaced by a saturation and then some oscillations around a weak magnetization, still one order of magnitude weaker than in the ideal MHD case for small scales. Evolution of the specific angular momentum is displayed Fig. 4.39 on the right. On every scale, specific angular momentum is extremely similar in both cases. The AD case is still smoother than the ideal MHD case, but both the order of magnitude and the evolution are almost identical. We note an apparent transfer of specific angular momentum from large scales to the scale of the disk (100 a.u.) a few kyears after the first core formation in both cases. The explanation for the variability of the specific angular momentum in the AD case lies in the counter-rotating parts of the flow. These parts account for negative angular momentum, yielding quantitative variations in the specific angular momentum even though the amount of angular momentum in these regions remains negligible due to the low density.

Disk formation and evolution We represented the disk mass evolution Fig. 4.26 in dashed lines. The effect of the angle is not obvious in this case. In the ideal MHD case, the disk is formed earlier and is at first slightly bigger, before stabilizing around $M_{\rm disk} \sim 0.2 M_{\odot}$ for both the aligned

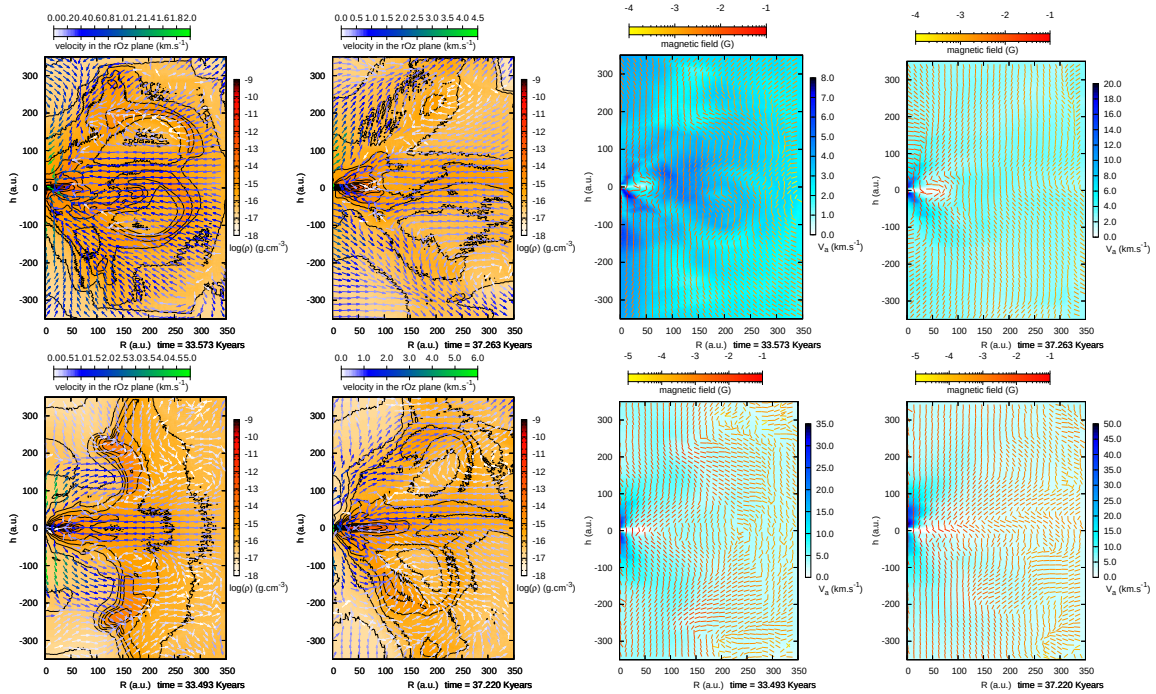

Figure 4.38: $\mu = 2$, misaligned case. Top: ideal MHD. Bottom: Ambipolar diffusion. From left to right: (two left columns) evolution of the density/velocity from 7 Kyears after the first core formation to a late time (last output from the AD case), followed (two right columns) by Alfvén speed maps and magnetic field intensity evolution.

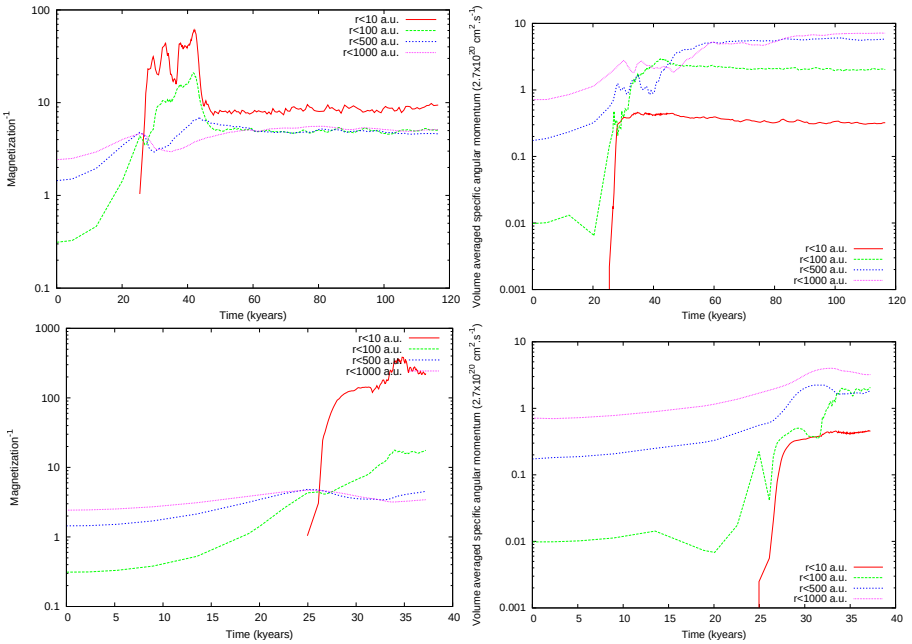

Figure 4.39: $\mu = 2$, misaligned case. Left: ideal MHD case. Right: AD case. Evolution of the magnetization in four control spheres of various radius; specific angular momentum versus time for various control spheres, in respect to the densest part of the cloud.

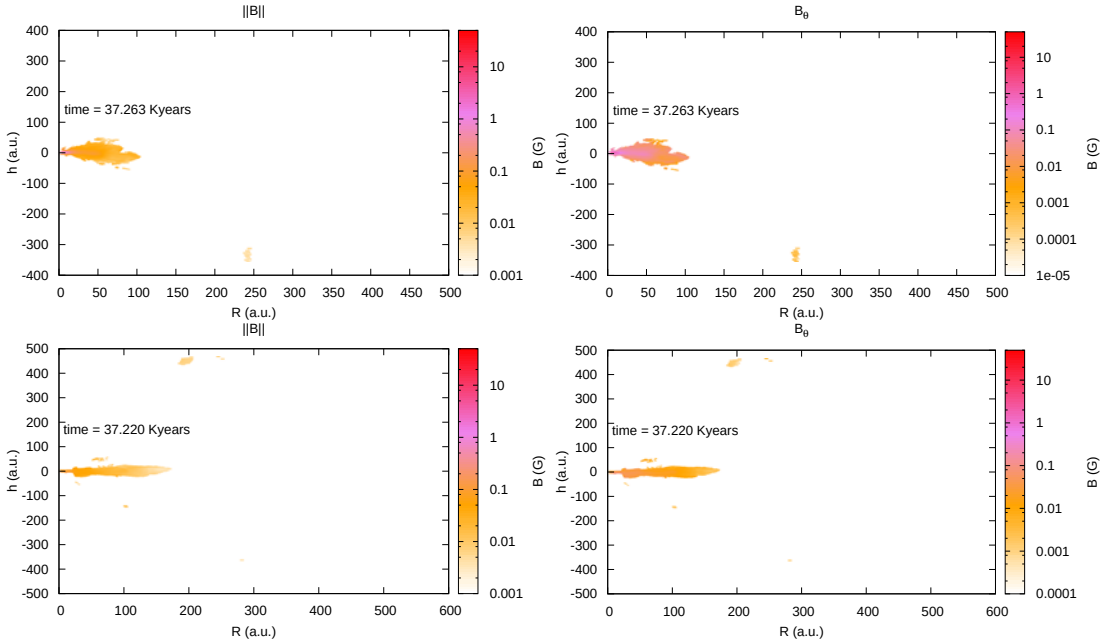

Figure 4.40: $\mu = 2$, misaligned case. Top: ideal MHD. Bottom: Ambipolar diffusion. All the plots correspond to the time of the last output in the AD case. From left to right: magnetic field intensity; toroidal magnetic field intensity; restraining ourselves in all cases to cells abiding by the criteria of Joos et al. (2012).

and misaligned cases. It suggests that the disk formation is facilitated in this misaligned setup. Therefore, the disks forms and grows quicker at first before the magnetic energy is released and a steady state regime almost similar to the one in the aligned case is reached yielding a disk mass about the same. For the AD case, the magnetic flux is effectively diffused yielding almost the same $B(\rho)$. The angle yields more complex flow motions, and a less stable growth but the broad picture remains the same, with similar parameters for the disk.

Last, we look at the details of the disk structure. This is plotted Fig. 4.40. For both cases, the disk is well defined with few cells that fit the disk criteria at much larger radius (for example at $h \sim -300$ a.u. and $r \sim 250$ a.u. in the top left plot). These substructures are obviously not part of the disk, but account for a negligible part of the computed disk-mass as they lie in low density regions. In the ideal MHD case, the disk structure is satisfying, with still a high magnetic pileup at small radius (about one order of magnitude higher than in the AD case both in intensity and for the toroidal component). In the AD case the disk structure is qualitatively different from the previous case. We retrieve a change of height at $r \sim 30$ a.u. corresponding to the outflow cavity. However, the disk is much more flattened than in the $\mu_{\rm BE} = 5$ case. The magnetic pileup is stronger (by a factor ~ 2 to 5) in this case, especially at large radius $r > 100$ a.u.. We expect the intrinsic 3D effects responsible for the disk-structure at large radius in the $\mu_{\rm BE} = 5$ case to be less important compared to magnetic effects, yielding a more flattened structure, similar to a pseudo-disk. However, this structure is flattened but still matches the criteria for the disk, meaning that it is rotationally supported.

4.2.4.3 Turbulent case

We have explored in details differences between the ideal MHD and a resistive case with ambipolar diffusion in the fiducial aligned case, and in a more general misaligned case. We highlighted the

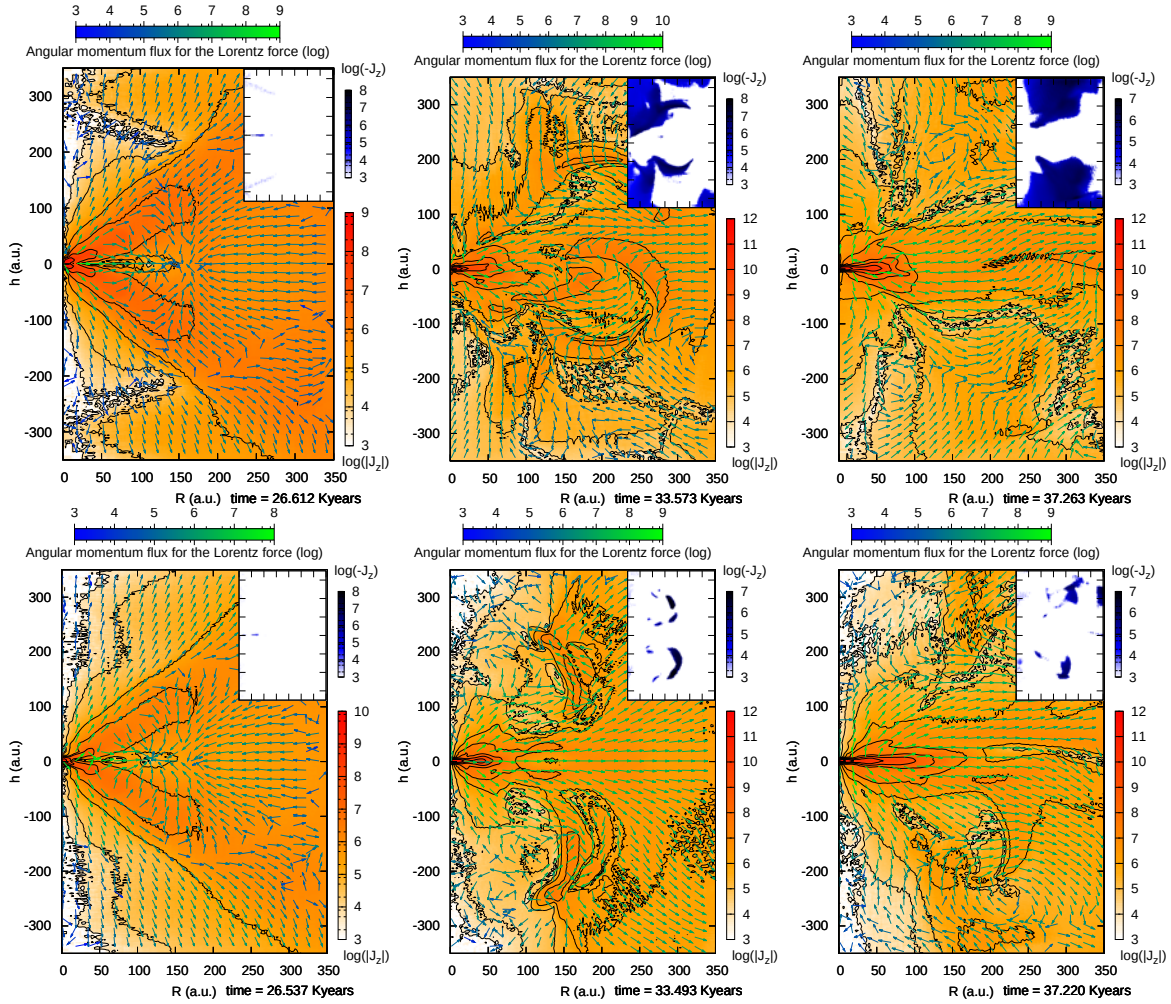

Figure 4.41: $\mu = 2$, misaligned case. Top: ideal MHD. Bottom: Ambipolar diffusion. From left to right: (two left columns) evolution of the angular momentum/angular momentum flux for the Lorentz force from the first core formation to a late time (last output from the AD case).

stabilizing effect of the ambipolar diffusion along with the beneficial effect of a misalignment for the ideal MHD case. We now focus on the most general case of a turbulent core. According to Goodman et al. (1998), dense cores show signs of coherence instead of being fully turbulent. Nevertheless, they still experience fast random motions (suprathermal line width-size), making a random velocity field relevant. We use to generate the initial conditions a turbulent velocity field with a Kolmogorov power spectrum and random phases (see Levrier (2004) for more details). Finally, we insist on the fact that the degree of turbulence does not seem to greatly influence the results: above a threshold, still to be determined, the results are qualitatively in agreement for low and highly turbulent runs. The initial velocity field we use has a non-zero angular momentum, therefore we do not add solid body rotation initially but rather let the angular momentum conservation do its job. Comparing quantitatively to the solid body rotation cases is not trivial and will be achieved by computing the average angular momentum in various control volumes. As previously, we will present for each setup two cases: one weakly magnetized with $\mu_{\rm BE} = 5$ and another more realistic, with $\mu_{\rm BE} = 2$.

$\mu_{\rm BE} = 5$, Mach number= 1.4, weakly magnetized case We present the most turbulent of our runs first. In this case, the Mach number ($M = \frac{v_{\rm rms}}{c_s}$) is $M = 1.4$, corresponding to supersonic turbulence. It is probably over-evaluating turbulence in one solar masses cores, because the classical power law for turbulent motions scales with the mass of the clump. However and as pointed out several times coherence in dense cores, especially low mass cores, is a complex and active field of research and may revisit this picture with new elements. In the meantime, we conduct experiments with more extreme conditions to probe for the effect of non-ideal MHD.

First core formation Properties of the first core resemble the non-turbulent ones. It forms at about 20 kyears, and measures ~ 10 a.u., as can be seen Fig. 4.42. However, the surroundings of the core are very different. First, the mixing is increased, and the spider-web like structures tracing the history of AMR grid cells have disappeared. Second, the $B(\rho)$ scatter plots are very similar in the ideal MHD and AD case, with a less marked plateau for the latter and less pileup (at the time of the first core formation) in the ideal case. Last, the magnetization differs from previous cases. The magnetic flux is effectively reduced in the 1 to 10 a.u. scale, yielding a mass-to-flux ratio above 10 in these regions. We recall that in the aligned, $\mu_{\rm BE} = 5$ case, the mass-to-flux ratio was almost one order of magnitude lower (see Fig. 4.18). On the contrary in the AD case, magnetization is almost exactly identical to the aligned, $\mu_{\rm BE} = 5$ case.

Structural details for the density, magnetic field and angular momentum when the first core forms are displayed Fig. 4.43. Again, both cases are extremely similar. The ideal MHD case is slightly denser, yielding an angular momentum map a little more intense. However, the topology of every flow variable is almost indistinguishable between both cases. It is also very different from the non-turbulent runs. The magnetic field is not organized except at very small scales, of the order of the first core (dozens of a.u.). We do not see any strong organization in either angular momentum or density maps apart from the elongated structures and accretion in a plane perpendicular to the mean angular momentum. On the last column to the right, we plotted the angular momentum maps for the aligned, $\mu_{\rm BE} = 5$ case. Even at the early time of first core formation, in the non-turbulent case angular momentum in regions of the scale of hundreds of a.u. surrounding the disk has been effectively removed. On the contrary, in the turbulent case angular momentum in regions surrounding the disk is still present. This is expected to significantly reduce magnetic braking, since co-rotation will be achieved more easily in the case of faster rotating surroundings.

Long term evolution The long term evolution (see Fig. 4.44) supports the idea that turbulence helps to describe the relevant physics in the ideal MHD case. At small scales, we still see quantitative differences in the magnetization. Since the first core formation at $t = 10$ kyears and

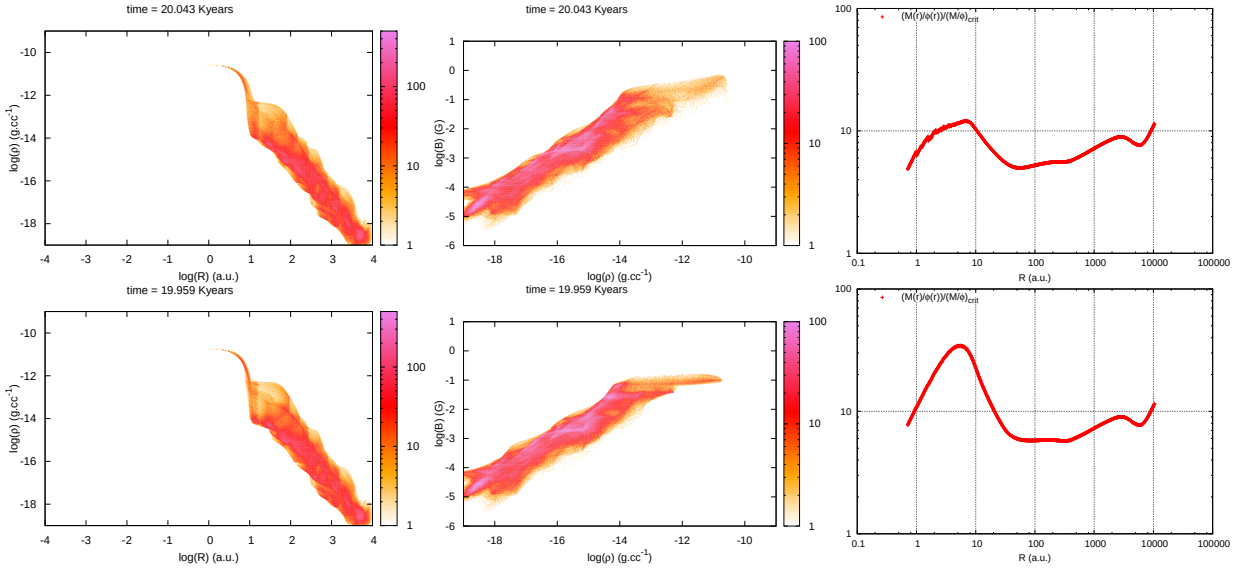

Figure 4.42: $\mu = 5$, turbulent Mach number $M = 1.4$. Top: ideal MHD. Bottom: Ambipolar diffusion. All plots are taken at about the same time (at the first core formation), $t \simeq 20$ kyears. From left to right: scatter plot of density versus radius with the number of cells at a given density/radius color coded; magnetic field magnitude versus density, number of cells color coded; magnetization as a function of radius.

until $t \sim 30$ kyears, the evolution of the magnetization and of the specific angular momentum is nearly identical for the ideal MHD case and the AD case. The topology of the flow variables at the first core formation is indeed almost identical in both cases (see Fig. 4.43). Quantitatively, magnetic field, density and angular momentum are slightly superior in the ideal MHD case. The increased magnetic braking is compensated by the increased angular momentum, itself explained by a larger density. All these effects compensate and yield identical evolution of the specific angular momentum (even inside the first core). It is worth noting that the ideal MHD configuration, with larger magnetic energy and density, is more likely to be unstable. There are no noticeable displacement of the core in this setup for the ideal MHD case, yet we see some strong variations in both magnetization and specific angular momentum. At $t \lesssim 30$ kyears, we notice a big drop in the mass-to-flux ratio at scale of 100 a.u. and less. This change in magnetization still has no visible consequence on the specific angular momentum. We also note that the drop is less steep compared to the previous cases. It is not known if this will happen in the AD case, since the simulation did not reach this point. We will focus on this point in a later paragraph, see § 4.2.4.3 for more details. Last thing to note, the steady-state configuration in the ideal MHD case (and the last time-step in the AD case) appear extremely similar to the steady-states obtained in the previous cases. These steady-states were obtained after a displacement of the core and the release of a large part of the magnetic energy. Moreover, in this case the specific angular momentum is only a consequence of the initial turbulent velocity field. It is qualitatively of the same order of magnitude as the imposed solid body rotation (see Fig. 4.44 on the right, at $t = 0$ kyears) but quantitatively different. However, the steady-state appears to be quantitatively the same both in magnetization and angular momentum.

We compare the flow variables at the time of the last output of the AD case, displayed Fig 4.47 in colormaps and Fig. 4.45 for the scatter-plots. The drop in the magnetization in the ideal MHD has not taken place yet at this time. The resemblance between the AD case and the ideal MHD case is striking in these plots. We retrieve all the features that we emphasized in the AD cases that were absent from the ideal MHD case in previous simulations. First, we focus on the density versus

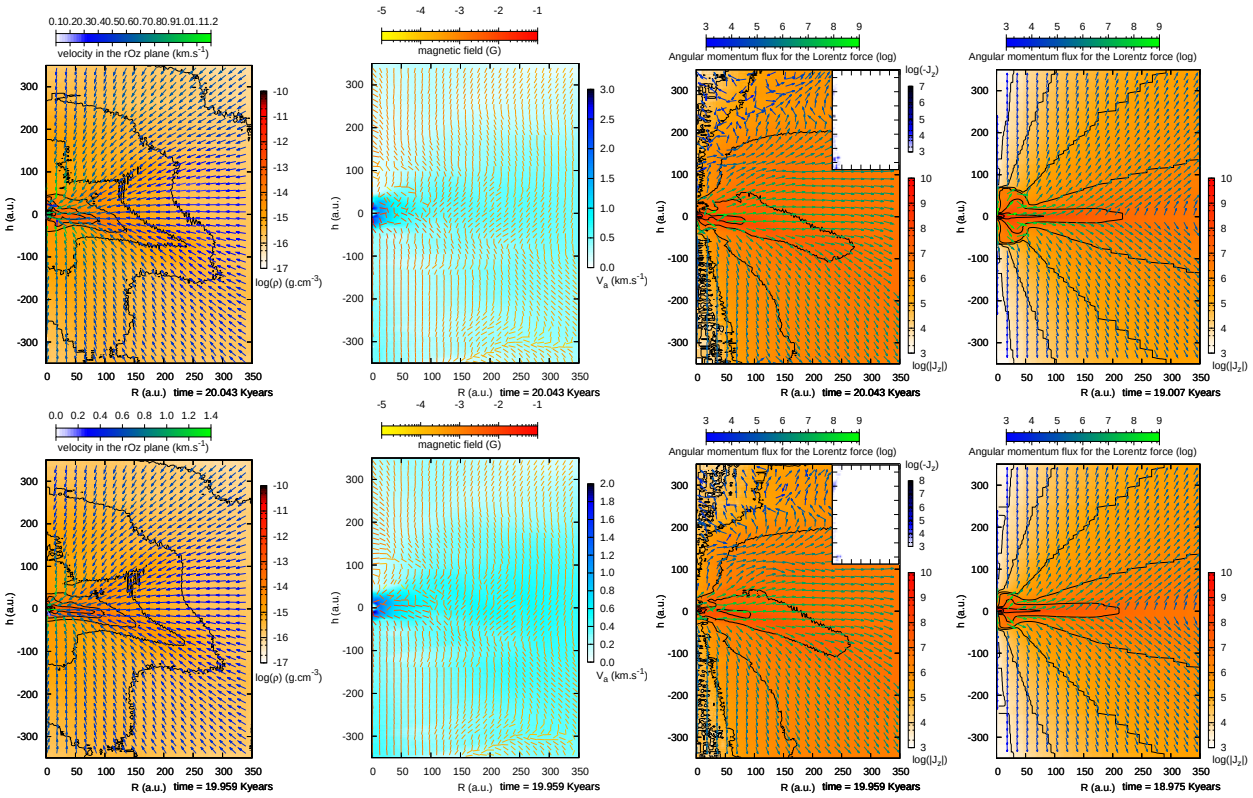

Figure 4.43: Three left columns: $\mu = 5$, turbulent Mach number $M = 1.4$. Top: ideal MHD. Bottom: Ambipolar diffusion. All plots are taken at about the same time (at the first core formation), $t \simeq 20$ kyears. From left to right: density/velocity maps; Alfvén speed/magnetic field maps; angular momentum/angular momentum flux for the Lorentz force. We added (last column on the right) the angular momentum colormap in the previous $\mu = 5$, aligned case, for the sake of comparison.

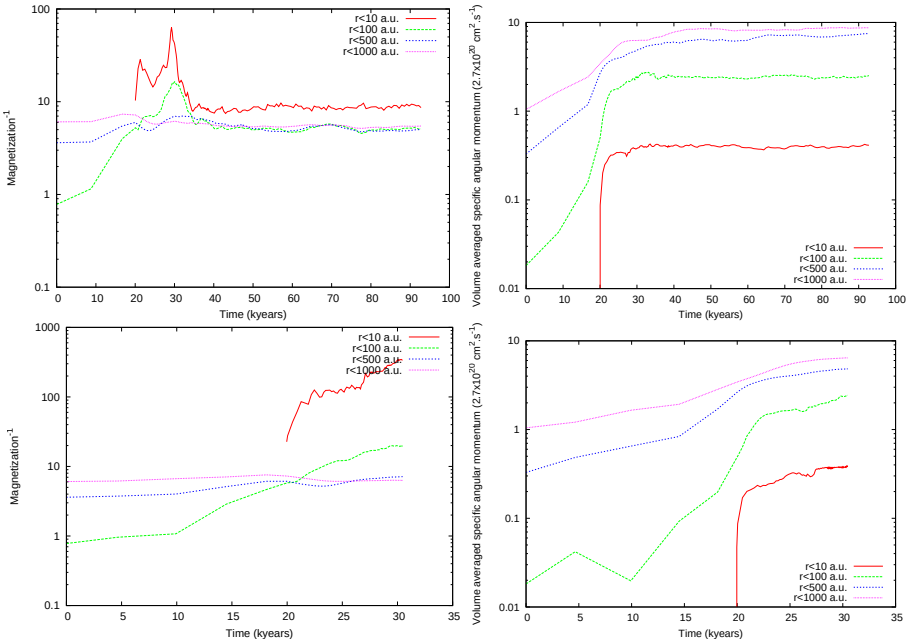

Figure 4.44: $\mu = 5$, turbulent Mach number $M = 1.4$. Top: ideal MHD case. Bottom: AD case. Evolution of the magnetization in four control spheres of various radius; specific angular momentum versus time for various control spheres, in respect to the densest part of the cloud.

radius plot (left column). We note substructure of equivalent size and radius in both cases. The most remarkable feature is the low density from 10 to 100 a.u., typical of the magnetic cavity in the AD case. Because of flux freezing, without turbulence, the outflow cavity in the ideal MHD case is more dense than in the AD case: see Fig. 4.46 where we rescaled the colormaps. It yields on $\rho(r)$ maps for the ideal MHD case very specific areas that are unexplored in aligned or misaligned configuration, namely low density at low radius regions (see for example Fig. 4.31, the two columns on the left). A direct consequence is visible on $B(\rho)$ plots, where low density regions are more magnetized in the ideal MHD case than previously (again, see for example Fig. 4.31, the two columns on the right). Additionally, in the ideal MHD case, the peak of magnetic field at high density is less marked and a plateau is appearing similar to the one of the AD case, at $\rho < 10^{-13}$ g.cm^{-3}. Again, there is almost no difference between the AD case and the ideal MHD case when focusing on the pink parts of the plots, tracing where most cells lie. In this case, the plateau begins at $\rho \sim 10^{-17}$ g.cm^{-3} and grows with a slope $B \propto \rho^{0.1}$ in the AD case, and $B \propto \rho^{0.2}$ in the ideal MHD case. There are still some unexplained behaviors at the densest part in the ideal MHD case, but which impact less on the whole evolution of the cloud. Last, the magnetization is also very close between the two cases. We see the consequence of the high magnetic field in the densest parts, as the magnetization is still several times higher at small scales ($\lesssim 100$ a.u.) in the ideal MHD case. We can still note that in this case, the mass-to-flux ratio in the ideal MHD case remains superior to 10 up until $r \simeq 300$ a.u.. Details on the scale of a few hundreds of astronomical units are shown Fig. 4.47. Again, both cases (ideal MHD and AD case) are almost identical. We note the beginning of a small anisotropy in the ideal MHD case (most visible in the Alfvén speed map) and an slightly larger density and angular momemtum. However, the details of the structures are almost identical. This observation is both encouraging and discouraging, since we use the AD case as a reference to assess the validity of ideal MHD runs but we also show that ambipolar diffusion does not add much physics compared to the ideal MHD framework when using turbulent initial conditions. The robustness of such a conclusion yet remains to be thorougly tested: we first focus on the disk formation and then on the later evolution and drop

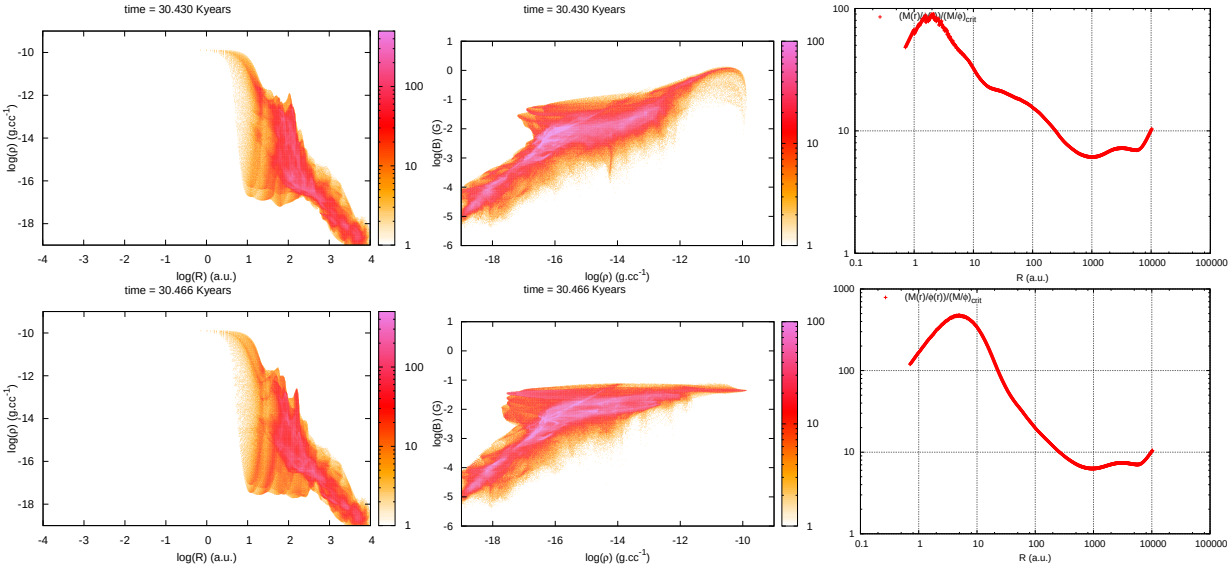

Figure 4.45: $\mu = 5$, turbulent Mach number $M = 1.4$. Top: ideal MHD. Bottom: Ambipolar diffusion. All plots are taken at about the same time (last output from the AD run), $t \simeq 20$ kyears. From left to right: scatter plot of density versus radius with the number of cells at a given density/radius color coded; magnetic field magnitude versus density, number of cells color coded; magnetization as a function of radius.

in mass-to-flux ratio at 100 a.u. in the ideal MHD case.

Disk formation and evolution We show Fig. 4.48 the evolution of the total mass in the disk, using the criteria from Joos et al. (2012). As expected from the previous remarks, the disk mass evolution is almost identical in the ideal MHD case and the AD case. However, the magnetization in the disk is rather different, as can be seen Fig. 4.49. There is still a pileup resulting in magnetic field (either the total magnitude or the toroidal component) more than one order of magnitude larger in the ideal MHD case at small radius ($r < 20$ a.u.). A new feature compared to previous cases is also visible: at large radius ($r > 50$ a.u.) the field permeating the disk is one to two orders of magnitude weaker in the ideal MHD case. This is evidence of the action of ambipolar diffusion, diffusing the flux outwards (or equivalently allowing matter to collapse onto the central object without dragging the field lines). The same explanation holds for the toroidal component of the field. In both cases, the toroidal component is the main component of the magnetic field. These differences do not show up on the disk mass evolution because even in the ideal MHD case at this stage because magnetic fields are not strong enough to slow down the rotation below the threshold value (we recall the details of the criteria and threshold value in appendix 4.A). The disk is about 50 a.u. more extended in the AD case, and of about the same height. This, along with a larger density for the ideal MHD case, explain that we observe the same disk mass evolution. We do not know yet if the fact that a larger density, a larger angular momentum and a smaller disk exactly compensate to give the same specific angular momentum (i.e. rotation speed) and disk mass is a coincidence or a robust feature.

Detailed study of the drop in magnetization in the ideal MHD case We plot Fig. 4.50 the time evolution of the density/velocity fields and the Alfvén speed/magnetic field from $t = 30$ kyears (corresponding to a global maximum in the mass-to-flux ratio at 100 a.u.) to $t \simeq 35$ kyears, time when the steady-states is reached. In the rotationally supported disk, the pileup of the toroidal component of the field continues resulting in the disk being thicker and thicker. Another consequence

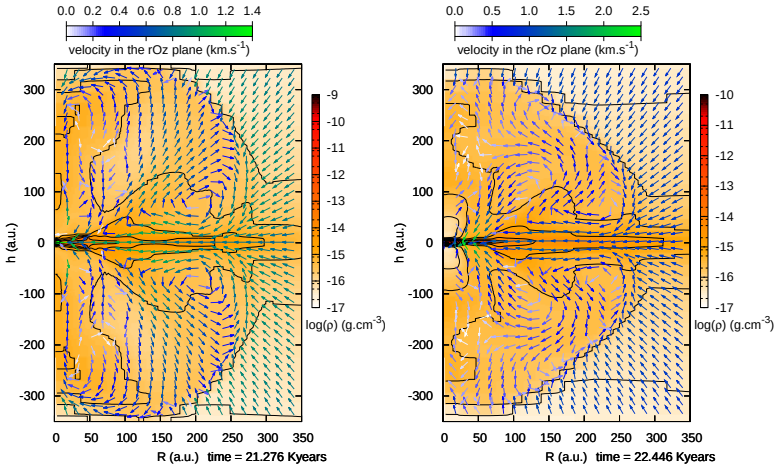

Figure 4.46: $\mu = 5$, aligned case. Left: ideal MHD. Right: Ambipolar diffusion. Density/velocity plot after the first core formation, before any displacement of the core.

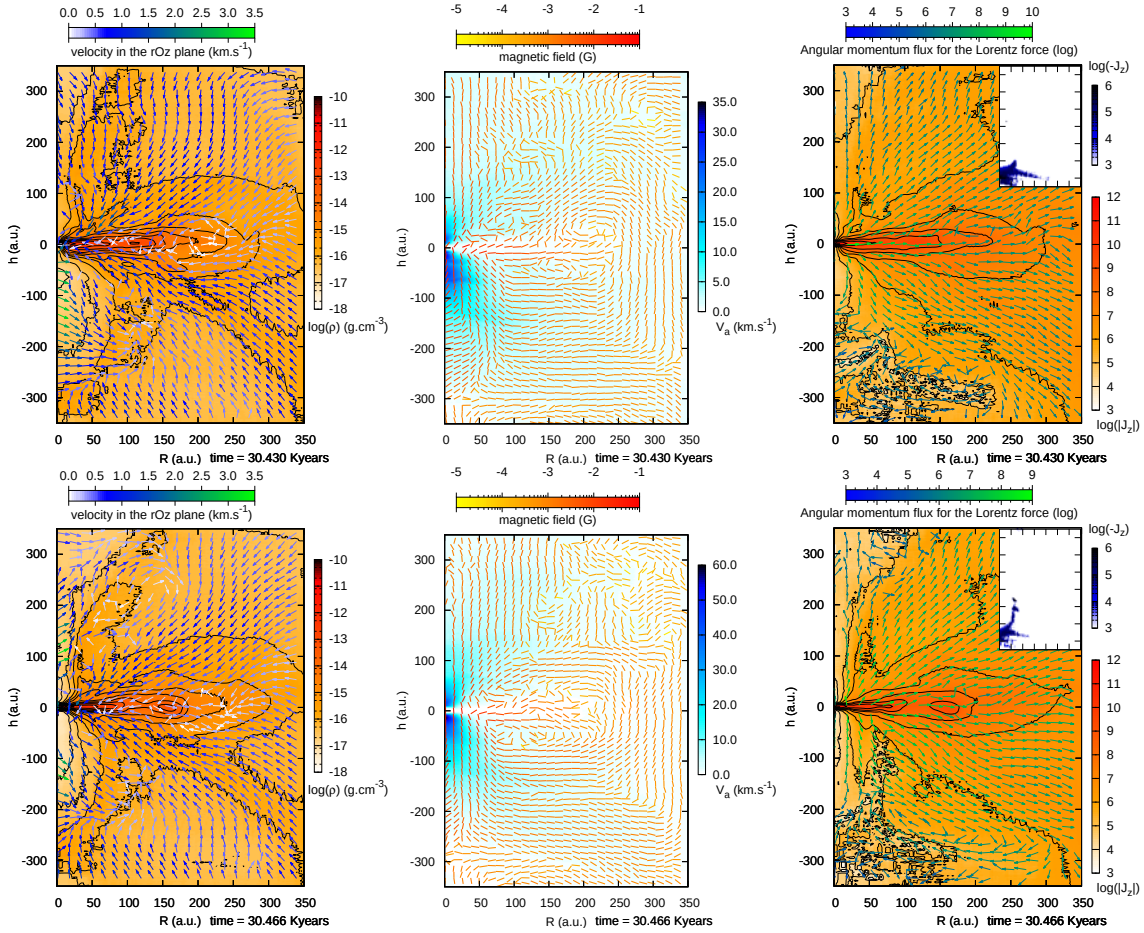

Figure 4.47: $\mu = 5$, turbulent Mach number $M = 1.4$. Top: ideal MHD. Bottom: Ambipolar diffusion. From left to right: density/velocity map; Alfvén speed/magnetic field map; angular momentum/angular momentum flux for the Lorentz force. All plots correspond to the last output in the AD case, $t \sim 30.4$ kyears.

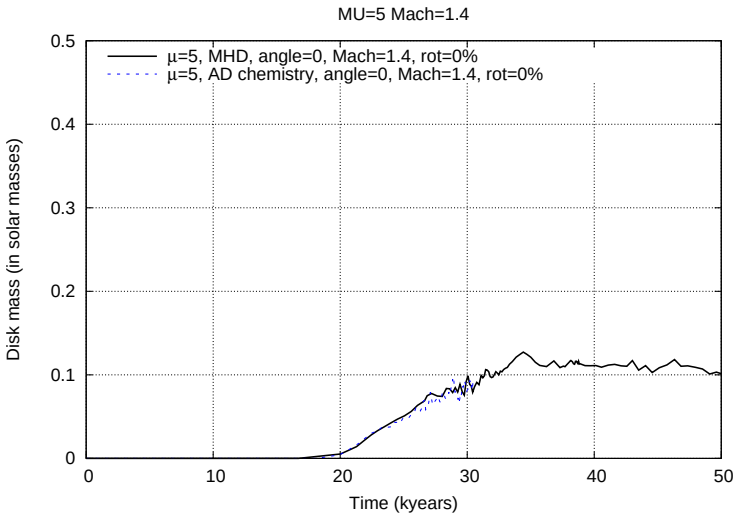

Figure 4.48: $\mu = 5$, turbulent Mach number $M = 1.4$. Evolution of the mass of matter abiding by the criteria of Joos et al. (2012) as a function of time. The mass is in solar masses. Solid lines stand for the ideal MHD case and dashed lines stand for the AD case.

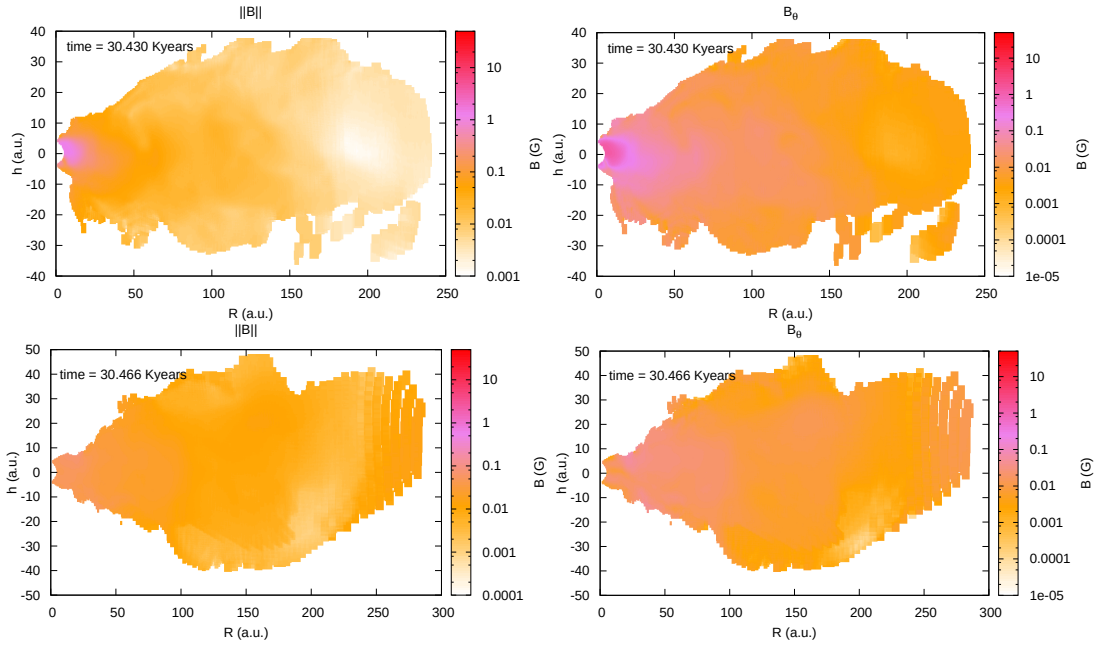

Figure 4.49: $\mu = 5$, turbulent Mach number $M = 1.4$. Top: ideal MHD. Bottom: Ambipolar diffusion. All the plots correspond to the time of the last output in the AD case. From left to right: magnetic field intensity; toroidal magnetic field intensity; restraining ourselves in all cases to cells abiding by the criteria of Joos et al. (2012).

of this pileup of magnetic flux is the increase of density in the surroundings of the core. A weak outflow is also emptying the regions above and below the core to the profit of the disk. These effects are competing, but it is clear that the pileup of the toroidal component of the magnetic field is responsible for the increase in size of the disk and the decrease of the mass-to-flux ratio. Therefore, we hypothesize that this drop in magnetization will not happen in the AD case. Even in this highly turbulent run, there remains issues of magnetic pileup at the densest part of the cloud, while the rest of the cloud looks surprisingly similar to the AD case.

$\mu_{\mathbf{BE}} = 5$, Mach number= 0.9, weakly magnetized case We now present a similar simulation, with subsonic turbulence (Mach number= 0.9). The conclusions from the previous supersonic case hold, and there are no qualitative differences between the two cases.

We first represent the evolution of the magnetization and specific angular momentum Fig. 4.51. Both in magnetization and specific angular mometum, the time evolution as well as the evolution when the first core forms are almost indistinguishable from the more turbulent $M = 1.4$ case. We do not show here the details of the density or magnetic field, because they also are almost indistinguishable from the previous case. It is interesting, as the initial rotational velocity (values of the specific angular momentum at $t = 0$ kyears) are lower in this case but reach the same values as previously.

We represent the disk mass evolution Fig. 4.52. The disk mass is slightly larger in this less turbulent case. We retrieve the same behavior in the ideal MHD case: the disk mass increases linearly until The disk mass is slightly larger in this less turbulent case. We retrieve the same behavior in the ideal MHD case: the disk mass increases linearly until the steady-state is reached, after the disk inflated due to pileup of toroidal magnetic field. The first core formation occurs earlier in this case, because the turbulent support is slightly less important. The event in the ideal MHD case corresponding to the drop in magnetization at about $t \sim 30$ kyears is still linked to the pileup of magnetic field, yet this drop happens even more slowly in this less turbulent case. It allows the disk to accrete more matter before reaching a steady state, which can explain the larger mass compared to the more turbulent case. The main conclusion is still that the ideal MHD and AD case are almost identical in every point of view, at least up to the drop in magnetization.

This is important, as it proves the major importance of turbulence in ideal MHD runs and emphasize the fact that supersonic or subsonic turbulence both appear to yield the same robust result.

$\mu_{\mathbf{BE}} = 2$, Mach number= 0.9 Last, we focus on the most extreme run we conducted. We used subsonic turbulence and $\mu_{\mathrm{BE}} = 2$ to probe the robustness of the previous conclusions. In this case, the first core forms later (t$\sim$ 25 kyears) due to the increased magnetic support.

Concerning the magnetization (Fig. 4.53 on the left), the evolution before the steady-state is identical to the previous $\mu_{\mathrm{BE}} = 5$ case, with a rescaling of 5 kyears. The drop in magnetization is still present, leading to a steady state in the ideal MHD case which characteristics are again identical to all previous cases. We still retrieve in the ideal MHD case the peak in magnetization in a 100 a.u. sphere linked to the drop at larger radius, absent from the non-turbulent runs. In this case, the steady-state is reached more abruptly compared to the weaker magnetized one. There are however strong variations in the specific angular momentum (Fig. 4.53 on the right) both in the AD and ideal MHD cases. These variations arise because in both case there are counter-rotating regions developing above and below the plane of the disk, as shown Fig. 4.54. The fact that the specific angular momentum at $t \simeq 35$ kyears is equal for the large scale (in spheres of radius 100 a.u., 500 a.u. and 1000 a.u.) both in the ideal MHD case and the AD case seems to be a coincidence due to the counter-rotating regions propagating outwards. We do not have any satisfying explanation for this behavior.

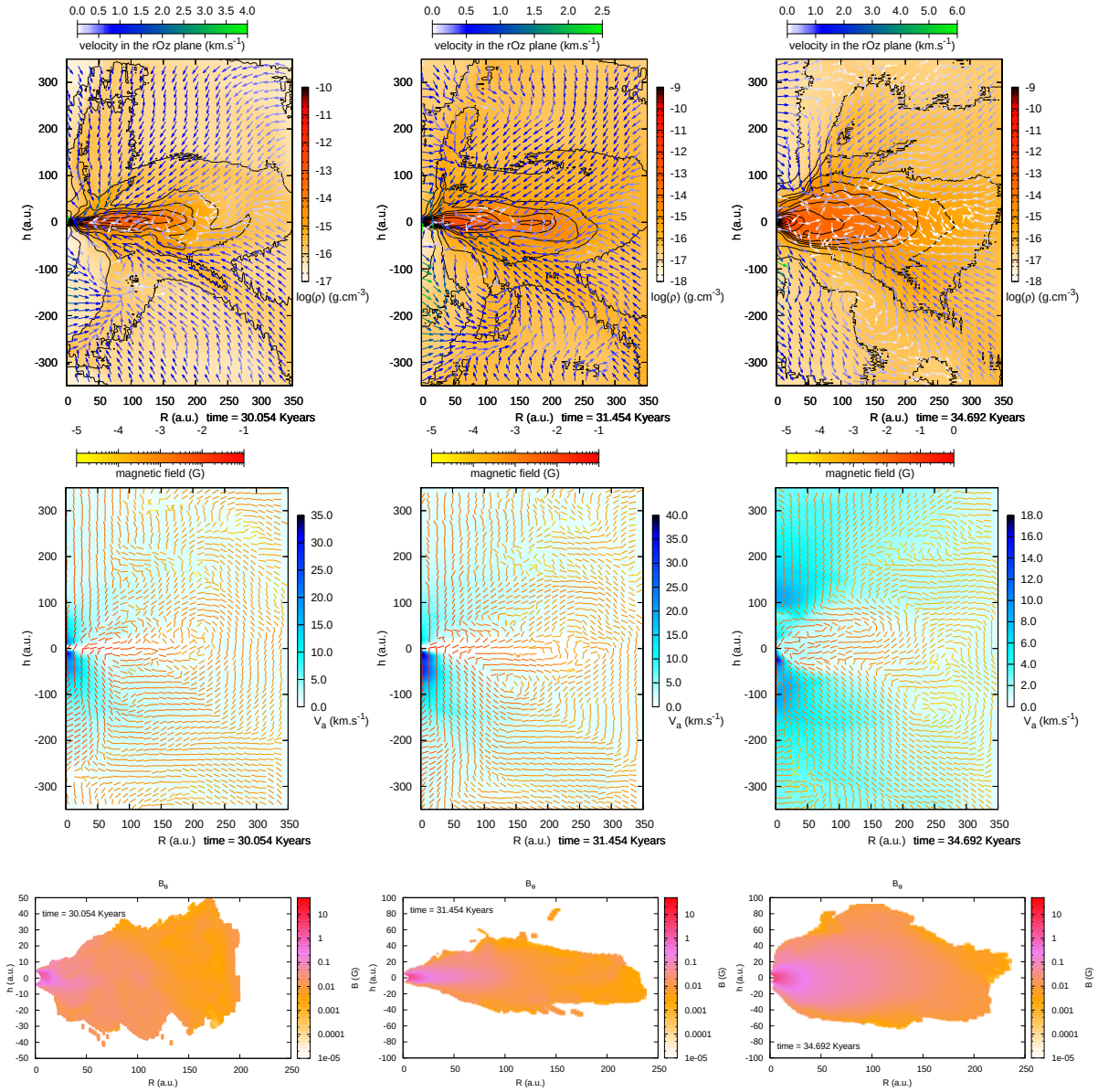

Figure 4.50: $\mu = 5$, turbulent Mach number $M = 1.4$. Ideal MHD case. Top: density/velocity map. Middle: Alfvén speed/magnetic field map. Bottom: toroidal component of the magnetic field. From left to right: time evolution.

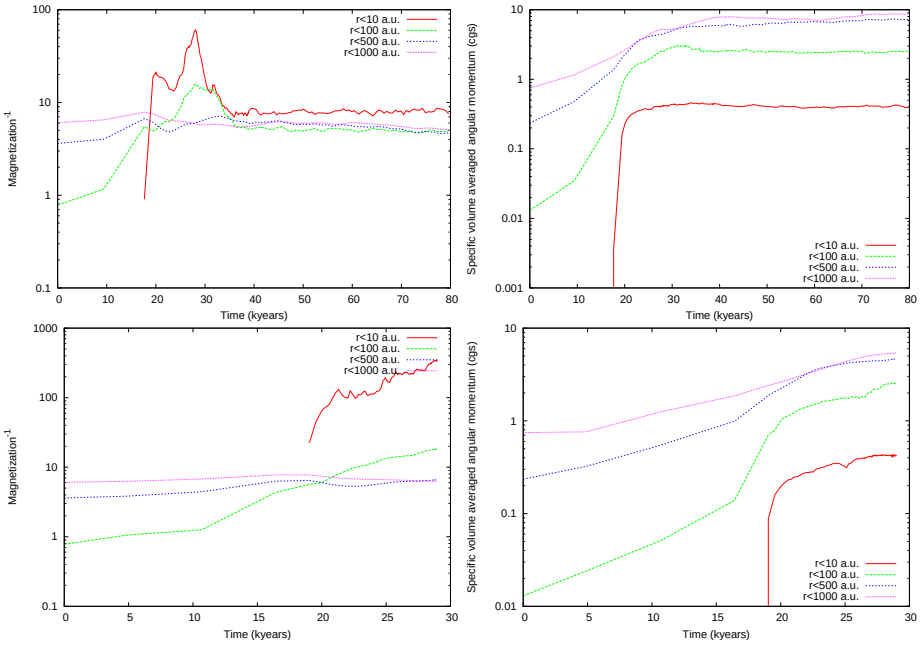

Figure 4.51: $\mu = 5$, turbulent Mach number $M = 0.9$. Top: ideal MHD case. Bottom: AD case. Evolution of the magnetization in four control spheres of various radius; specific angular momentum versus time for various control spheres, in respect to the densest part of the cloud.

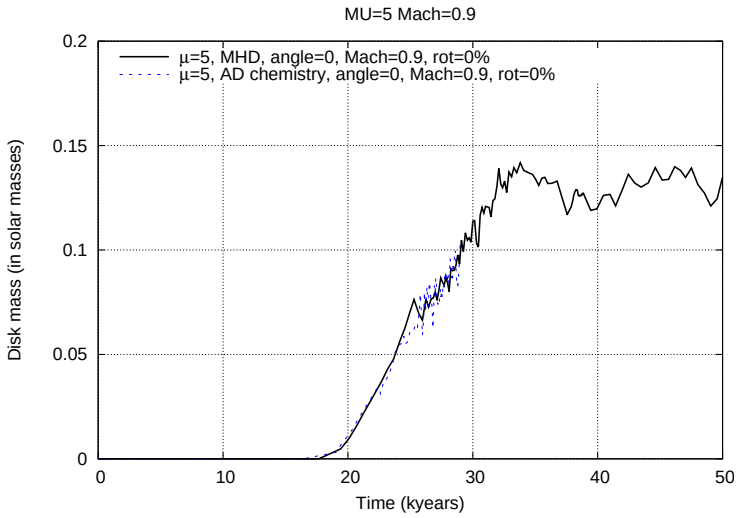

Figure 4.52: $\mu = 5$, turbulent Mach number $M = 0.9$. Evolution of the mass of matter abiding by the criteria of Joos et al. (2012) as a function of time. The mass is in solar masses. Solid lines stand for the ideal MHD case and dashed lines stand for the AD case.

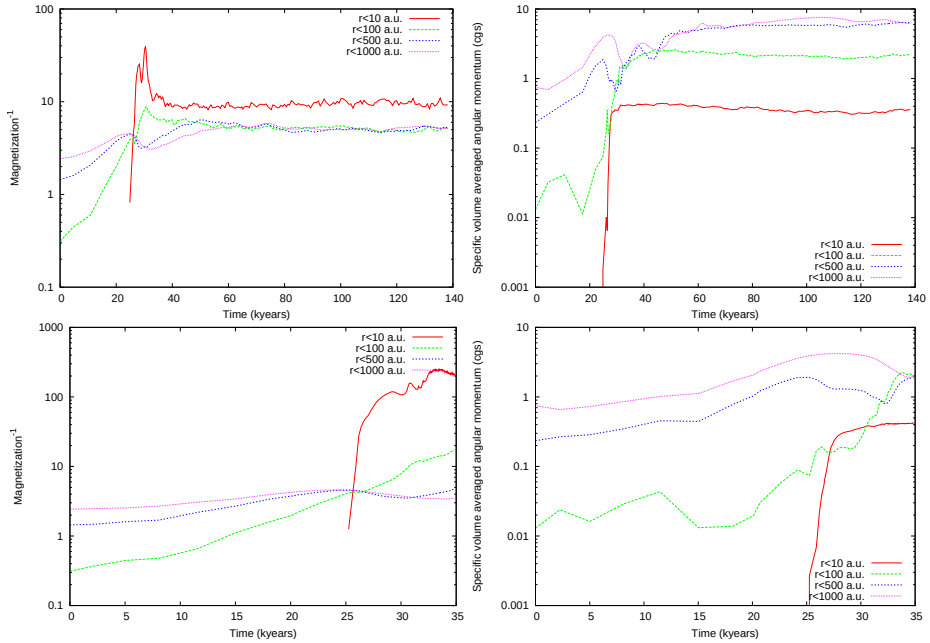

Figure 4.53: $\mu = 2$, turbulent Mach number $M = 0.9$. Top: ideal MHD case. Bottom: AD case. Evolution of the magnetization in four control spheres of various radius; specific angular momentum versus time for various control spheres, in respect to the densest part of the cloud.

This strongly magnetized case yields more complex behaviors for all flow variables, in particular in the ideal MHD case. Turbulence is not strong enough compared to the magnetic fields to diffuse enough of the magnetic field. It is interesting to note that even though in the AD case, the colormaps and the magnetic field look smoother, there is still significant counter-rotating regions. This is not surprising compared to the strongly magnetized case without turbulence, as the initial velocity field is of random nature and naturally leads to counter rotating regions.

The disk is thinner in the AD case, as expected: the pileup of toroidal magnetic field is more important than in the weakly magnetized case, yielding an inflated disk in the ideal MHD case, as can be seenFig. 4.55. In the AD case, there is no strong pileup of either magnetic field or just the toroidal component, explaining the very flat aspect of the disk in this case. We note a strong breaking of the symmetry in the AD case, with a part of the disk-cells only present below the plane of the disk. It corresponds to a spiral arm, but again does not account for a significant fraction of the disk mass. We represent Fig. 4.56 the disk evolution in this case. It is important to note that the disk mass evolution is identical for the ideal MHD case and the AD case, but the disk is not similar. It is a dense elongated structure in the AD case, while it is inflated and more diffuse in the ideal MHD case.

Last, we show Fig. 4.57 the ratio of the magnetic pressure ($\frac{B^2}{8\pi}$) to the rotational support ($\frac{\rho v_\theta^2}{2}$). We note that even in the strongly magnetized case (bottom right panel) with ideal MHD, we retrieve a rotational support that dominates in the plane of the disk in a flat structure extended (> 50 a.u.). This structure is comparable in size to the one in the turbulent weakly magnetized case with ambipolar diffusion (top left panel). We show also the fiducial aligned strongly magnetized case (bottom left panel) for comparison: in this case the disk support is mostly magnetic.

This strongly magnetized case is peculiar, as we begin to separate the effect of turbulence from the effect due to ambipolar diffusion. Turbulence helps to smooth gradients in both cases, and yields counter-rotating regions. Ambipolar diffusion consequences can be seen in a region around the first core, and when looking at the shape of the disk. In this case, we still see no differences in the disk

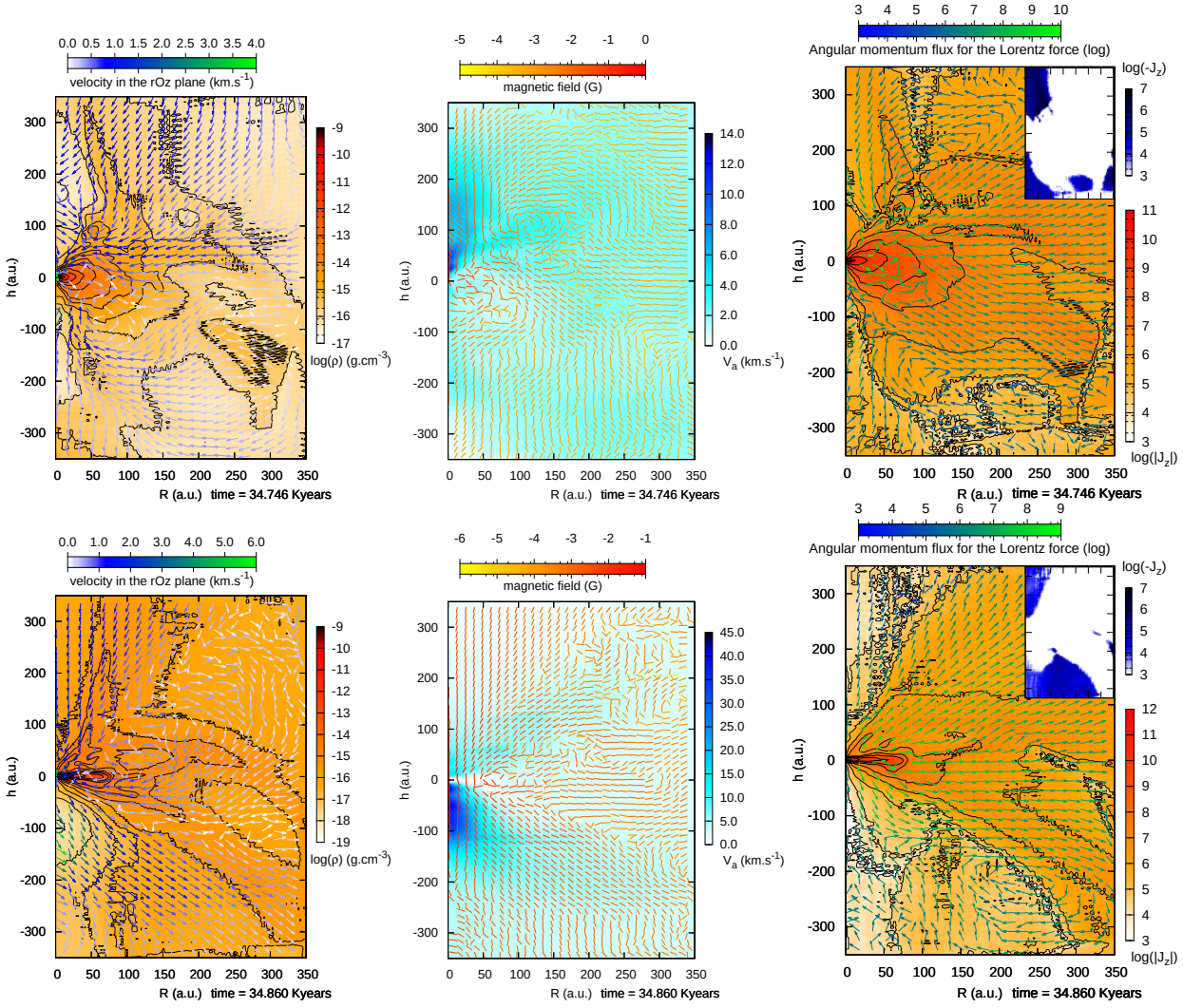

Figure 4.54: $\mu = 2$, turbulent Mach number $M = 0.9$. Top: ideal MHD case. Bottom: AD case. All plots are taken at about the same time, $t \simeq 35$ kyears. From left to right: density/velocity maps; Alfvén speed/magnetic field maps; angular momentum/angular momentum flux for the Lorentz force.

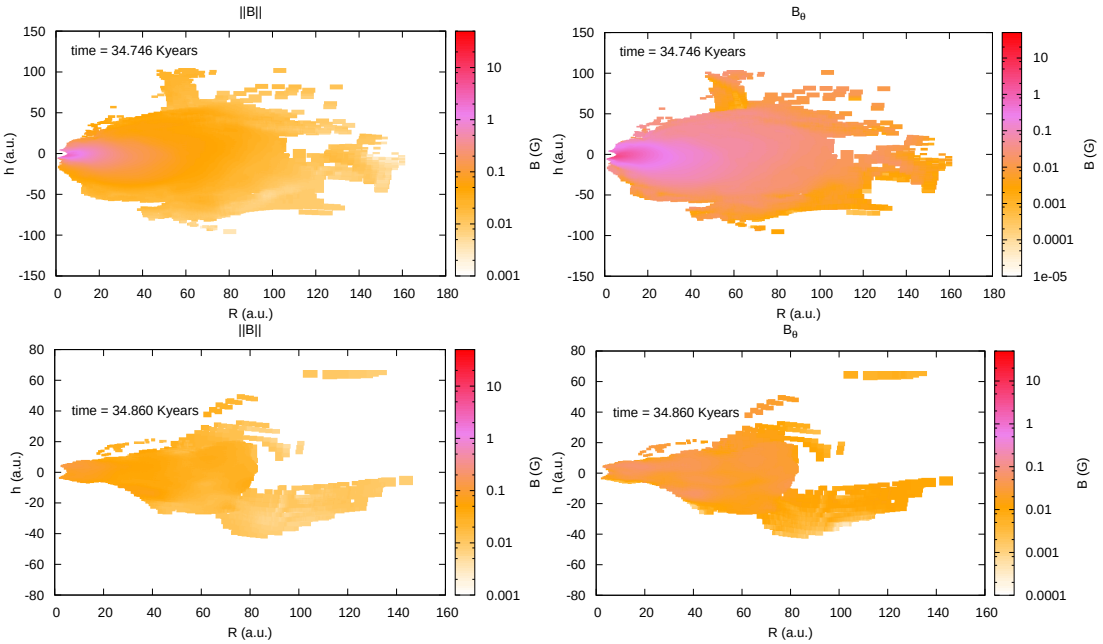

Figure 4.55: $\mu = 2$, turbulent Mach number $M = 0.9$. Top: Ideal MHD case. Bottom: AD case. From left to right: magnetic field intensity in the disk; toroidal component of the magnetic field in the disk. All plots correspond to the last output in the AD case.

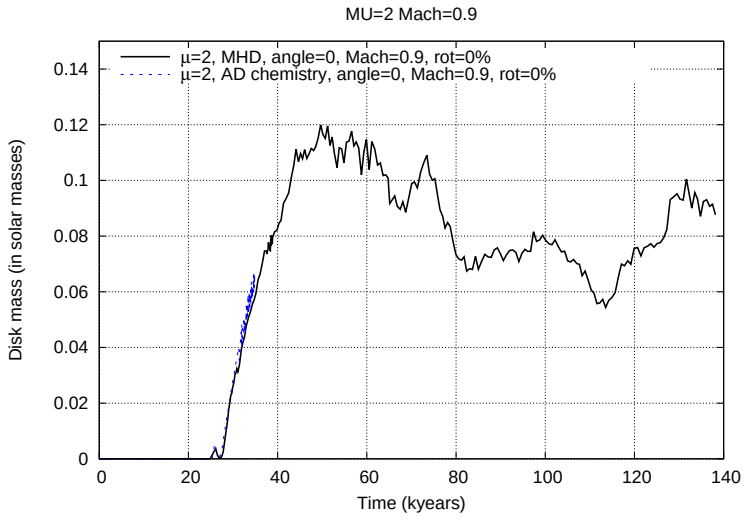

Figure 4.56: $\mu = 2$, turbulent Mach number $M = 0.9$. Evolution of the mass of matter abiding by the criteria of Joos et al. (2012) as a function of time. The mass is in solar masses. Solid lines stand for the ideal MHD case and dashed lines stand for the AD case.

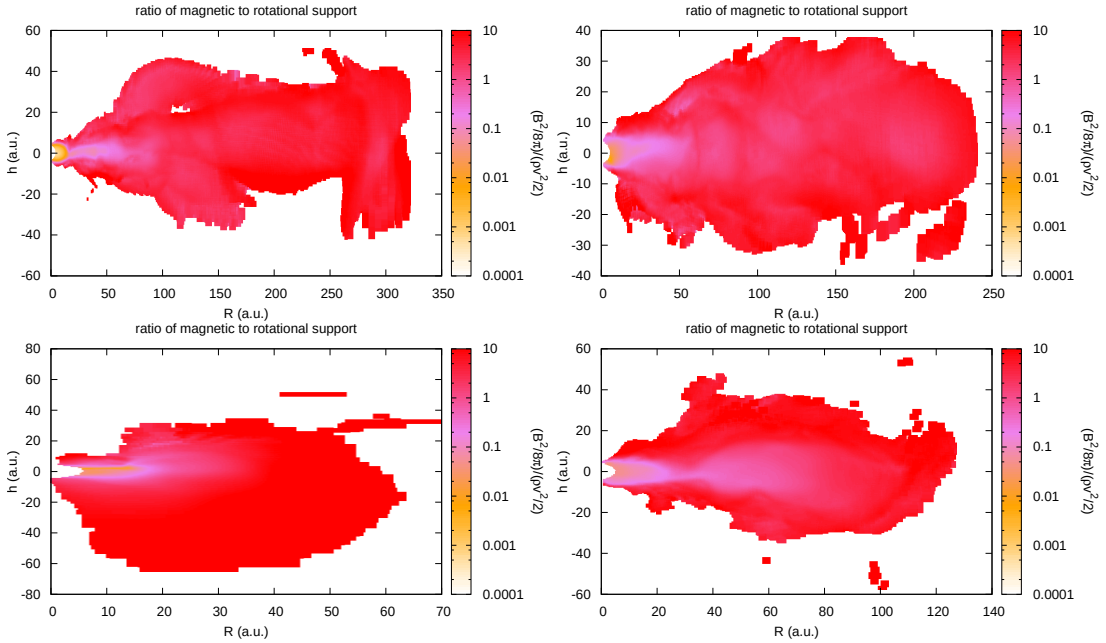

Figure 4.57: Ration of the magnetic pressure ($\frac{B^2}{8\pi}$) to the rotational support ($\frac{\rho v_\theta^2}{2}$). Top left: turbulent (Mach= 1.4) AD case, $\mu = 5$. Top right: turbulent (Mach= 1.4) ideal MHD case, $\mu = 5$. Bottom left: aligned ideal MHD case, $\mu = 2$. Bottom right: turbulent (Mach= 1.4) ideal MHD case, $\mu = 2$.

mass evolution, but contrarily to the previous cases where the disk evolution was indeed comparable in this case the disk shape is very different.

4.2.5 Summary tables and comparison notes with previous work

The main properties of each case are summarized respectively table 4.2 and 4.3 for $\mu_{\rm BE} = 5$ and table 4.4 and 4.5 for $\mu_{\rm BE} = 2$ cases. We recall that the aligned and misaligned cases have no turbulence (Mach= 0) and a rotational to gravitational energy ratio of 3%. Turbulent cases have no initial solid body rotation and the non-zero average angular momentum is a result of the turbulent velocity field used as initial condition.

In the first four rows in tables 4.2 to 4.5 we focus on the disk properties at late time (corresponding to the last output in the AD case). Several details have to be kept in mind while reading these tables. First, the last output in the AD case, used for the disk statistics presented in the tables 4.2, 4.3, 4.4 and 4.5 has sometimes reached a time posterior to the release of magnetic energy in the MHD case. It has been emphasized previously that due to an accumulation of magnetic energy in the first core, a spurious release of most of the energy occurs in the ideal MHD case yielding a state almost similar for all cases. Therefore, the disk properties for the ideal MHD case are subject to caution. Joos et al. (2012) also did observe the same phenomena of core displacement and release of magnetic energy and stopped the time integration before it had dramatic consequences on the core surroundings, explaining the lower masses found in the aligned case in particular, in which the magnetic pileup is the strongest. However, it is hard to evaluate when exactly the simulation is no longer describing the relevant physics in an astrophysical context explaining our choice to describe the outcome of the simulation at a later time but using additional caution. We added for clarity a table (table 4.1) recalling the various times after first core formation ($\sim 20 \times 10^3$ years) at which we witness magnetic flux leakage in the core in the ideal MHD simulations. The magnetic pileup, and the following release of magnetic energy in the ideal MHD case lead to the formation of massive disks that were previously

unable to form in strongly magnetized cores, but it is not in contradiction with previous results: we are simply exploring longer time-scales. What we call a rotationally supported disk is a family of cells that verify arbitrary criteria (see 4.A). We find larger, more massive disks than observed (see for example Maury et al. (2010)) even in the ideal MHD case in strongly magnetized environments, but those disks are mainly supported by the magnetic pressure while they still verify the arbitrary criteria we used. It offers an easy comparison between related simulations but the disk mass and radius we find is very dependent on the criteria and threshold chosen, and while this is of theoretical interest since we believe it is not a numerical issue, we strongly advise against drawing observational consequences. Last, we have to keep in mind that we integrated past the second core formation without taking into account the fast jet that will pierce the first core, the flattened geometry of the first core in second simulations (see Machida et al. (2006)) and the flux redistribution inside the first core due to Ohmic dissipation. All these phenomena are important physics that our description of the first core and disk formation and evolution lacks and that will need to be studied self-consistently in second Larson core simulations. We emphasized this definition issue by adding the affix *inflated* when the (pseudo-)disk is supported by magnetic pressure and *flat* when the disk is resembling a Keplerian disk in the summary tables.

In tables 4.2 to 4.5, we focus on the following:

- We first note the presence or absence of a rotationally supported disk. We specify if it is flattened or inflated due to magnetic pressure. In parenthesis we write the aspect ratio (length divided by maximum height).
- We then report the disk mass, using the criteria described in Joos et al. (2012).
- We estimate the radius of the disk, using the same criteria.
- We finally compute the magnetic to rotational support ratio at 20 a.u. and in the middle[6] of the disk.

The next four rows treat the outflow in the 100 a.u. scale.

- We first note the amount of time needed after first core formation for an outflow to develop.
- We then compute the amount of specific angular momentum in the outflow at 100 a.u..
- Last, we report the maximum value of the mass-to-flux ratio at 100 a.u..

Last, we focus on first core properties. All following quantities are taken at the first core formation. The first core formation is associated with an accretion shock and a steep jump in density. As a consequence, the time-step in the simulation falls down as the grid is refined when the first core forms. This allows to consider the first output with a density above the threshold $\rho = 10^{-12}$ g.cm^{-3} as an accurate time for the first core creation and properties.

- We first report the time of first core creation, using a density threshold at $\rho = 10^{-12}$ g.cm^{-3}.
- We extract two radii using the same density threshold at $\rho = 10^{-12}$ g.cm^{-3} to account for oblate cores.
- We calculate the mass of the first core as the amount of matter with a density above $\rho = 10^{-12}$ g.cm^{-3}, when the density threshold is crossed.
- Second to last, we report the maximum of the mass-to-flux ratio and the corresponding radius for which it is obtained.
- We finally calculate the magnetic pressure at the center of the core.

[6] At roughly half the maximum radius of the disk, in the midplane.

Table 4.1: Time after the first core formation (in $\times 10^3$ years) when the flux is released from the densest part of the core.

	$\mu_{\rm BE}=2$	$\mu_{\rm BE}=5$
aligned, Mach= 0	0.6	1
aligned, Mach< 1	0.1	2.5
aligned, Mach> 1	0.1	2
misaligned, Mach= 0	1.4	2.5

Table 4.2: Summary of the main properties for $\mu_{\rm BE}=5$ cases with solid body rotation

setup	Aligned case		Misaligned case	
MHD case	Ideal	AD	Ideal	AD
disk ?	inflated (2)	flat (8)	inflated (3)	flat ($r<60$ a.u.)
$M_{\rm disk}$ ($M_\odot$)	0.12	0.22	0.17	0.27
$R_{\rm disk}$ (a.u.)	80	80	250	200
$P_{\rm magnetic}/\rho\frac{v_\theta^2}{2}$	0.01 & 2	10^{-4} & 10^{-1}	0.1 & 10	10^{-3} & 1
outflow delay (10^3 years)	0.1	0.3	0.7	3.5
$\mathbf{J}^{\mathbf{r=100}\ \rm a.u.}_{\rm specific}$ (10^{20} cm^2.s^{-1})	1.0	1.5	1.0	2.0
$\mu(r=100$ a.u.)	8	15	9	15
first core formation (10^3 years)	19.0	19.0	19.0	18.9
$R_{\rm first\ core}$ (a.u.)	7.4 & 10.5	7.5 & 10.6	9.1 & 10.1	8.5& 10.5
$M_{\rm first\ core}$ ($\times 10^{-2}$ $M_\odot$)	3.1	2.7	2.6	1.9
$\mu(r=10$ a.u.)	7 (10)	25 (9)	7(10)	18(8)
$P_{\rm magnetic}$ (dyn.cm^{-2})	2.3×10^{-2}	6×10^{-4}	1×10^{-2}	1.1×10^{-3}

Table 4.3: Summary of the main properties for $\mu_{\rm BE}=5$ turbulent cases

setup	Mach< 1		Mach> 1	
MHD case	Ideal	AD	Ideal	AD
disk ?	flat (9)	flat (10)	flat (8)	flat (13)
$M_{\rm disk}$ ($M_\odot$)	0.10	0.10	0.08	0.093
$R_{\rm disk}$ (a.u.)	200	200	240	300
$P_{\rm magnetic}/\rho\frac{v_\theta^2}{2}$	10^{-2} & 1	10^{-3} & 1	10^{-2} & 5	10^{-4} & 0.5
outflow delay (10^3 years)	15	8	no	10
$\mathbf{J}^{\mathbf{r=100}\ \rm a.u.}_{\rm specific}$ (10^{20} cm^2.s^{-1})	1.0	1.0	1.0	1.0
$\mu(r=100$ a.u.)	15	20	20	20
first core formation (10^3 years)	19.4	19.0	20.0	20.0
$R_{\rm first\ core}$ (a.u.)	8.5 & 11.1	9 & 13	8.9 & 9	8.9 & 8.9
$M_{\rm first\ core}$ ($\times 10^{-2}$ $M_\odot$)	4.8	2.9	3.3	2.6
$\mu(r=10$ a.u.)	20 (5)	20 (8)	11 (7)	30 (6)
$P_{\rm magnetic}$ (dyn.cm^{-2})	1.6×10^{-2}	1.1×10^{-3}	2.0×10^{-2}	1.1×10^{-3}

Table 4.4: Summary of the main properties for $\mu_{\rm BE} = 2$ cases with solid body rotation

setup	Aligned case		Misaligned case	
MHD case	Ideal	AD	Ideal	AD
disk ?	inflated (1)	flat (10)	inflated (3)	flat (9)
$M_{\rm disk}$ ($M_\odot$)	0.15	0.19	0.15	0.2
$R_{\rm disk}$ (a.u.)	70	60	100	180
$P_{\rm magnetic}/\rho\frac{v_\theta^2}{2}$	5×10^{-2} & 10	5×10^{-3} & 1	$\times10^{-2}$ & 1	5×10^{-4} & 1
outflow delay (10^3 years)	0.2	0.6	0.6	5.5
$\mathbf{J}^{\mathbf{r=100}\ \text{a.u.}}_{\rm specific}$ (10^{20} cm^2.s^{-1})	1.0	0.8	0.9	1.0
$\mu(r = 100$ a.u.)	10	10	20	20
first core formation (10^3 years)	26.4	26.2	26.6	26.5
$R_{\rm first\ core}$ (a.u.)	7.5 & 11.2	7.1 & 10.1	8.8 & 10.2	8.4 & 10.3
$M_{\rm first\ core}$ ($\times10^{-2}$ $M_\odot$)	3.4	1.3	2.5	2.3
$\mu(r = 10$ a.u.)	6 (10)	20(7)	5 (10)	35 (7)
$P_{\rm magnetic}$ (dyn.cm^{-2})	4.3×10^{-2}	4.0×10^{-4}	1.8×10^{-2}	5.2×10^{-4}

Table 4.5: Summary of the main properties for $\mu_{\rm BE} = 2$ turbulent cases

setup	Mach<1		Mach>1	
MHD case	Ideal	AD	Ideal	AD
disk ?	inflated (2)	flat (5)	$\sim$flat (4)	flat (10)
$M_{\rm disk}$ ($M_\odot$)	0.06	0.07	0.08	0.08
$R_{\rm disk}$ (a.u.)	110	90	120	180
$P_{\rm magnetic}/\rho\frac{v_\theta^2}{2}$	6×10^{-2} & 10	3×10^{-4} & 0.5	2×10^{-2} & 0.8	5×10^{-4} & 0.7
outflow delay (10^3 years)	0.5	6	2	no
$\mathbf{J}^{\mathbf{r=100}\ \text{a.u.}}_{\rm specific}$ (10^{20} cm^2.s^{-1})	0.9	1.2	1.1	1.0
$\mu(r = 100$ a.u.)	9	20	20	30
first core formation (10^3 years)	26.5	26.2	27.9	27.6
$R_{\rm first\ core}$ (a.u.)	8.2 & 9.5	8.0 & 8.8	8.1 & 9.3	7.6 & 8.9
$M_{\rm first\ core}$ ($\times10^{-2}$ $M_\odot$)	4.0	2.5	3.7	2.4
$\mu(r = 10$ a.u.)	6 (10)	45 (8)	6(9)	40 (8)
$P_{\rm magnetic}$ (dyn.cm^{-2})	8.3×10^{-2}	4.8×10^{-3}	8.2×10^{-2}	4.7×10^{-3}

4.2.6 Conclusions

We recall here the main results of our numerical simulations of first core collapse.

- Ambipolar diffusion has a strong impact on the stability and evolution of collapsing cores. It helps to reduce counter-rotation and core displacements that are observed mostly in the aligned, and misaligned cases.

- In AD cases the structure of the disk resembles a flat rotationally supported disk. It is however not the case in ideal MHD runs without turbulence, because strong magnetic pressure due to pileup of the magnetic field in the midplane adds additional support against gravity and results in an inflated disk. The disk is still rotationally supported (meaning that $v_\theta > f_{\rm thres} v_r$ with $f_{\rm thres} = 2$) but magnetic pressure dominates over thermal pressure and rotational support in most areas of the disk.

- When using ambipolar diffusion, there are less differences between strongly and weakly magnetized setups. At low densities ($n_{\rm H} \lesssim 10^{11}$ cm^{-3}) the dynamical time is small compared to the magnetic flux loss time, and ambipolar diffusion does not have a major role on the shaping and evolution of the core. At larger densities, corresponding to the first core formation and above, ambipolar diffusion effectively dissipates the magnetic flux and is a hindrance to the magnetic pileup, yielding similar results for high and more moderate initial magnetic fields.

- When using turbulent initial velocity fields, the effects of ambipolar diffusion on the collapsing core are less obvious compared to turbulent diffusion effects, resulting in AD and ideal MHD cases being more alike. In weakly magnetized turbulent cases, there are almost no noticeable differences in the shape and mass of the disk between ideal and AD cases. Differences are still present in the magnetic field repartition inside the disk, and we hypothesize that the steady-state encountered in all the ideal MHD runs is not of physical nature and will not be attained in diffusive simulations.

- The most massive disk in both the ideal MHD case and the AD case is obtained in the misaligned case. However, comparing the disk mass between turbulent and non turbulent cases is not trivial, as the amount of angular momentum and support through either angular momentum or turbulent pressure is not easily comparable. Note that in Joos et al. (2013) both rotational support and turbulence are present in the initial condition, explaining the difference in disk mass between their and our results.

- Supersonic and subsonic turbulence give almost the same disk mass and structure. We even observe flat disks with an aspect ratio greater than 5 using ideal MHD (compared to 2 when the magnetic support dominates) before 1.5 $t_{\rm free\text{-}fall}$.

- The displacement of the core and all associated phenomena happen at about 1.5 free-fall time ($t_{\rm ff}$) in ideal MHD. Second core simulations are necessary to assess the validity of the physics described for $t > 1.5$ $t_{\rm ff}$.

As a conclusion, we can say that ambipolar diffusion has important consequences both qualitatively and quantitatively on the scale of the first core and the formation of rotationally supported disks. We again emphasize that ambipolar diffusion runs did not reach the steady-state observed in the ideal MHD runs, but that we do not expect them to reach it. Moreover, we integrated for about 1.5 free-fall times, which is long enough for the second Larson core to form and change the properties of the cloud at small scales ($\sim$ first core scale and below). This is important in particular for ideal MHD runs in which the densest parts of the cloud were the origin of displacements of the core and

of the release of magnetic energy that led to a steady-state. It is also of major importance because at the first core scale and inside the disk, magnetic field repartition is extremely different between the ideal MHD cases and AD cases, yielding possibly important discrepancies for the second Larson core properties.

4.3 Second core simulations with multigroup radiation non-ideal magnetohydrodynamics

First core simulations consistute the first step in understanding how stars form. As highlighted in the previous section, there are many uncertainties concerning the subsequent evolution of the first core after the second core has formed. In order to study consistently the second Larson core and the second collapse, we must account for dihydrogen dissociation: we use either Saumon et al. (1995) equation of state along with a radiation hydrodynamics solver (see § 2.3), or a barotropic parametrisation of the gas evolution. In both cases, the aim is to study the effects of the non-ideal MHD terms (see § 2.2). We warn the reader that this section is presenting state-of-the-art material, in particular concerning the radiation hydrodynamics simulation. More results will be published later in a refereed paper to discuss in details those results.

4.3.1 The setup

The turbulent setup is similar to the one describe section 4.2 with a turbulent Mach number chosen according to a refined Larson law (see Hennebelle and Chabrier (2013)) and no solid-body rotation. We used a flat density profile for all simulations and controlled the magnetic field using the theoretical mass-to-flux ratio in the case calculated by Mouschovias and Spitzer (1976). The magnetic field permeating the surroundings of the core is calculated with the value of the field permeating the cloud and assuming a constant mass to flux ratio $\mu = 5$. Because we use a density contrast of 100 the field is much weaker outside the core, but as seen in § 4.1 it is unimportant regarding the details of the cores. Last, we use the resistivity coefficients given from the chemical evolution code described § 3.1 truncated at high density to account for high temperature chemistry.

The second core has been studied using a barotropic equation of state and Ohmic dissipation (see Machida et al. (2006)) and only very recently using radiative transfer (see Tomida et al. (2013)). Ohmic dissipation is at play at higher densities that ambipolar diffusion, therefore better suited to act on the second core. Nevertheless, the ambipolar diffusion modifies the topology and structure of the first core and its surroundings which will finally cascade on the second core. We used both effects in resistive dense core simulations, with the implementation described in chapter 2.2.

Second core simulations are very challenging. Even with a barotropic equation of state, non-ideal MHD reduces the Courant condition to a fraction of its already low value in the ideal MHD case. We have spent a lot of time developing the radiative solver with the Saumon et al. (1995) equation of state, and we cannot present fully radiation non-ideal magnetohydrodynamics simulations of core collapse at this moment. Simulations are running, and we prefer to wait for more results than try to extract information from unfinished work. However, we want to use the early results from second collapse ideal-MHD simulations in the aligned case to support our conclusions regarding first core simulations.

4.3.2 Early results from second collapse simulations

In this paragraph, we restrict our study to the fiducial aligned case, therefore without turbulence, using ideal MHD. Rotational to gravitational energy ratio is 2% and thermal to gravitational energy ratio is 25%. In this case, $\mu = 4$. These slightly different values compared to chapter 4.2 yield

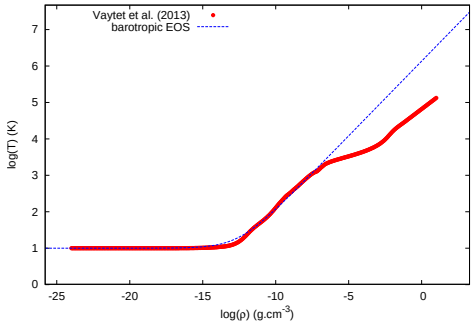

Figure 4.58: Barotropic equation of state, from Vaytet et al. (2013a) 1D radiation hydrodynamics simulations.

first core formation at $t = 23.340$ kyears and a more oblate core (less thermal and more rotational support).

For the non-radiative run, we used a barotropic equation of state (see Fig. 4.58) which is the result of one dimensional radiation hydrodynamics simulations from Vaytet et al. (2013a). The equation of state used in Vaytet et al. (2013a) is the same as the one we use in radiation transfer simulations, and the comparison will therefore be easier and more consistent. The run using a barotropic equation of state will be referred to as SC (standing for second core) and the radiation transfer run as RD (standing for radiation).

We also carried out a simulation where we use an extension of the barotropic equation of states without H_2 dissociation to compare the growth of the outflow and evolution of the disk without second core collapse (as in chapter 4.2 but with the same initial conditions as the radiation transfer simulations). This run will be referred to as FC (standing for first core).

First core formation We first focus on the first core formation, at $t = 23.340$, and we represent Fig. 4.59 the density/velocity field and the temperature. Both FC and SC show similar profiles with higher temperature where the density is higher, as expected. The RD case presents heating on the surroundings of the pseudo-disk (due to magnetic pileup) and the core, while the midplane region stays cool at $T \gtrsim 10$ K. The density/velocity field is however almost identical when the first core forms.

Evolution and timescales after first core formation According to tables 4.2 to 4.5 the typical time for an outflow to be launched after the first core creation (using the same $\rho > 10^{-12}$ g.cm^{-3} criterion) is one hundred to several thousand years. The time at which unphysical motions of the core happen is orders of magnitude higher: about half the free-fall time, ~ 10 kyears. We now focus on a time corresponding to the launching of the outflow, $t \sim 23.5$ kyears. We represent density/velocity maps Fig. 4.60 and Alfvén speed/magnetic field maps Fig. 4.61 for the three cases.

Surprisingly, the FC and SC cases exhibit significant differences even at this early time. The FC case shows a slightly more inflated pseudo disk, which can be explained because of an increased pileup of magnetic field in these regions. At smaller scales (tens of a.u.) strong differences appear. The second collapse has already begun in the SC case, and densities at the center of the core are much higher, as expected. The shape of the first core (isocontour of $\rho = 10^{-12}$ g.cm^{-3} for example) is very different. In the SC case, it looks like a flat round plate, thiner at its center than at its edge. In the FC case, it is more like an oblate core as in the previous chapter. The RD case is also different, and isodensity contours are in-between the two other cases: flatter than the FC case but thicker than the SC case.

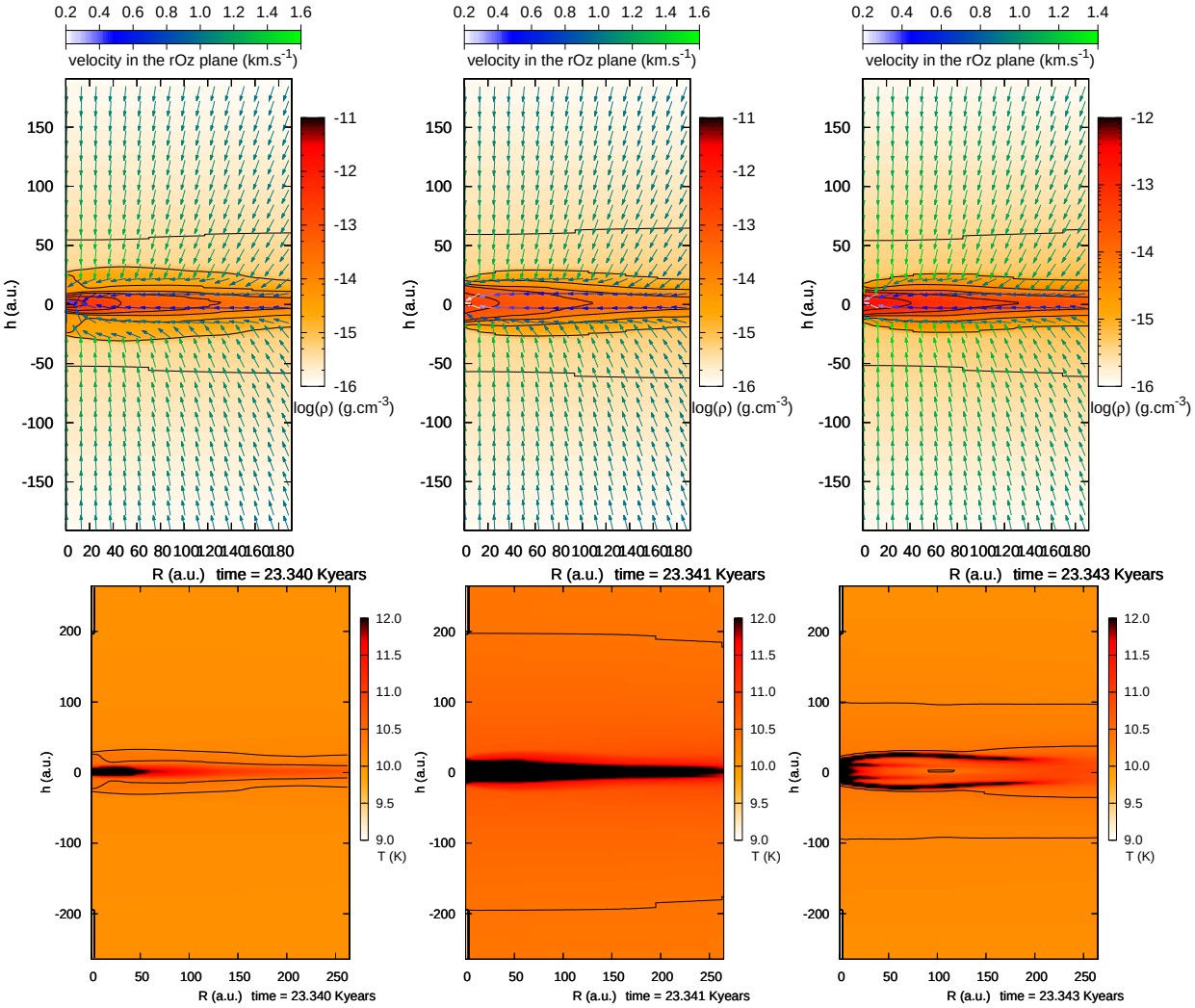

Figure 4.59: Top: density/velocity maps. Bottom: gas temperature maps. From left to right: SC case, FC case and RD case. All plots correspond to $t = 23.340$, time of the first core formation.

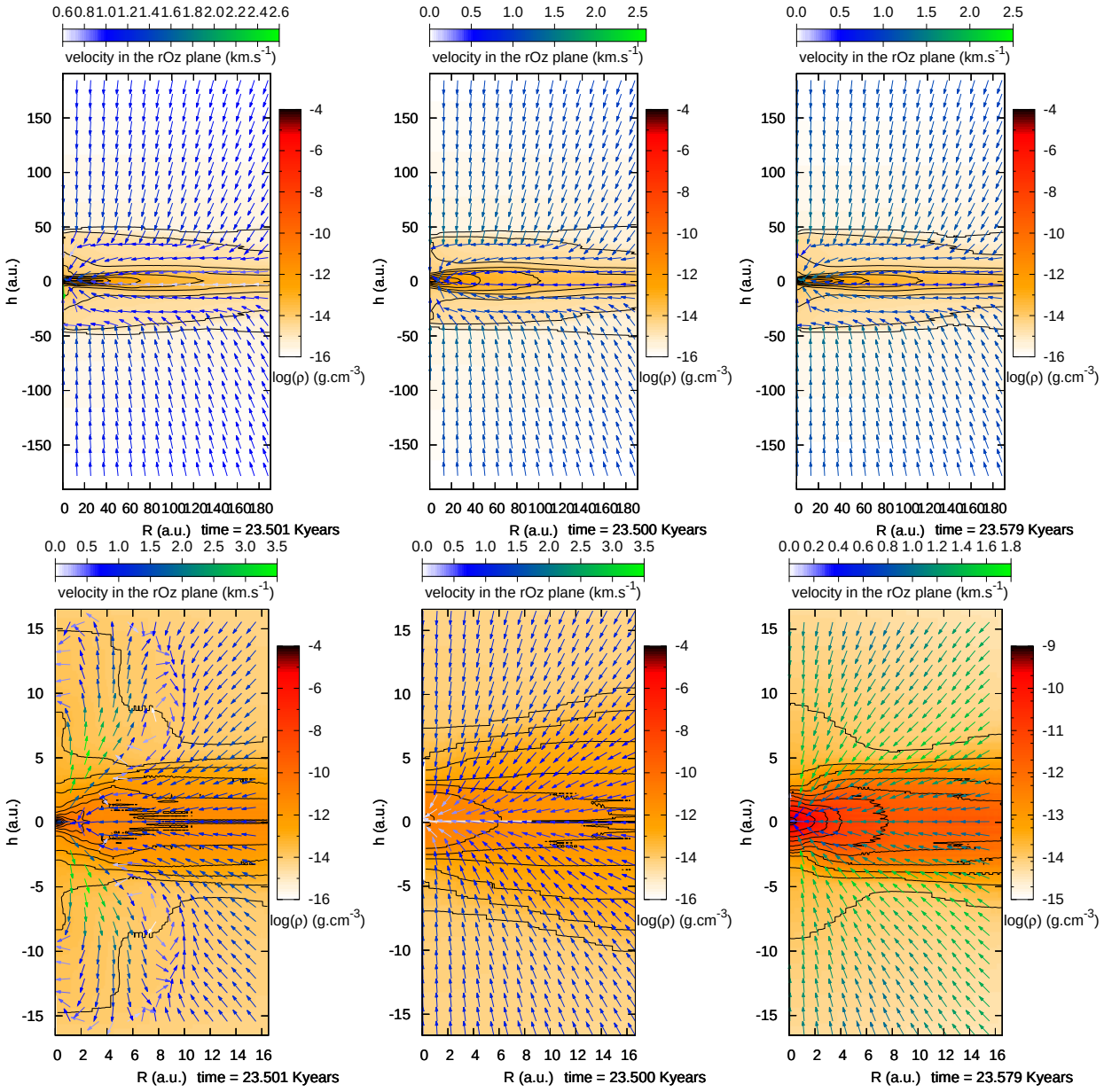

Figure 4.60: Top: density/velocity maps at 100 a.u. scale. Bottom: density/velocity maps at the first core scale. From left to right: SC case, FC case and RD case. Plot correspond to the time of launching of the outflow in the SC case.

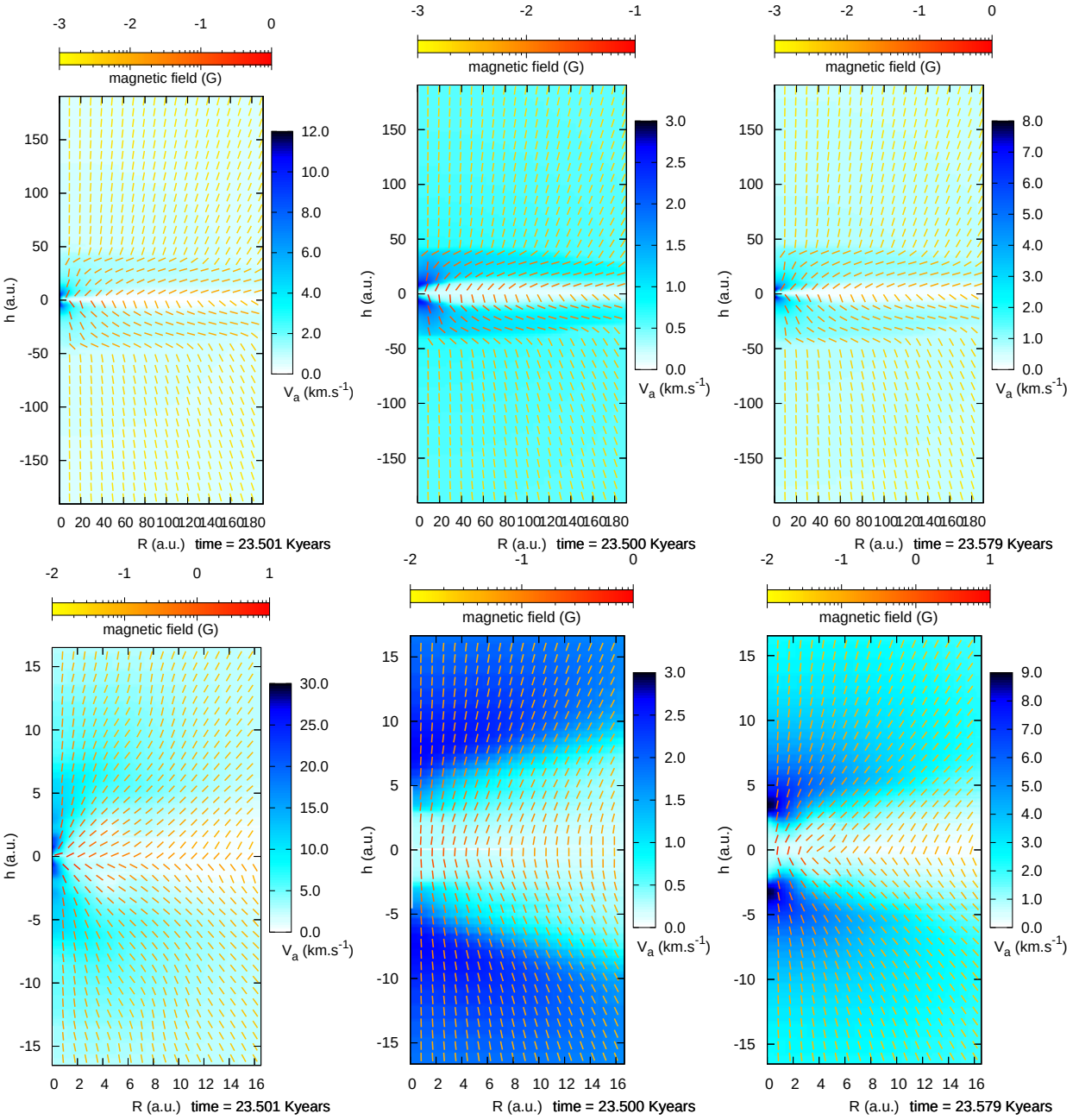

Figure 4.61: Top: Alfvén speed/magnetic field maps at 100 a.u. scale. Bottom: Alfvén speed/magnetic field maps at the first core scale. From left to right: SC case, FC case and RD case. Plot correspond to the time of launching of the outflow in the SC case.

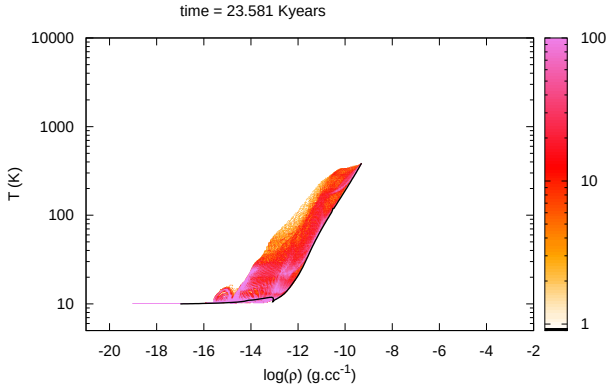

Figure 4.62: Scatter plot of temperature as a function of density, for a given time, in the case of radiative transfer with non-ideal MHD. The solid black line represents the evolution of the central density and temperature from the beginning of the simulation.

In the SC case, an outflow is developing up to about 15 to 20 a.u., but it is not present in the FC case. The RD case also shows the beginning of a structure resembling a magnetic bubble, but in this case it is related to the radiation that slows down infalling matter (see Bate (2011); Schönke and Tscharnuter (2011) for details on the launching mechanism). When looking at Fig. 4.61, we notice that the outflow in the SC case is not of the same nature as previously (see chapter 4.2): there is no clear bending of the magnetic field lines drawing a cavity. Moreover, we do not see strong infall in the vertical direction, contrarily to outflows observed in the first core study. Velocity of the outflow matches the ones observed in chapter 4.2, but we suspect than the launching mechanism can differ slightly. The absence of outflow in the FC case supports this assumption: the outflow in this case is launched a few hundred years after and shares the properties with the ones described in chapter 4.2.

Additional information is extracted from the magnetic field repartition. While we concluded that it is of crucial importance in the study of the long term evolution of the disk and the first core, we see Fig. 4.63 that it is still of preponderant importance in second core studies. In first core simulations, the pileup increases as matter collapses and lead to displacement of the core and release of a large part of the magnetic energy. In second core studies, the fast second collapses prevents these unphysical behaviors as the magnetic energy is brought to high densities, releasing the pressure at lower densities. The fact that the second collapses occurs very quickly (less than $\frac{t_{\rm ff}}{10}$ in this case) is a critical matter: it enables to release the magnetic energy by cascading to small scales, and it happens when we have good confidence in the outcome of ideal MHD simulations.

Last, we can note that the simulation using radiative transfer, even though not at as high densities as the SC case, has already evolved longer. Radiative transfer is an additional hindrance for collapse to occur as the gas is not perfectly following a single path, but is heated by the release of gravitational energy as the collapse proceeds. Hotter gas compared to the barotropic case yields additional support against collapse and the time-scale is in consequence sligthly modified. This is very clear in Fig. 4.62, where the black line is the central evolution of the temperature and the scatter plot represents the temperature as a function of density for a given output.

Second Larson core We finish this chapter with a series of figures corresponding to the second collapse and the formation of the second Larson core, in the ideal MHD framework and using the barotropic equation of state. This is represented Fig. 4.64. We note the expected launching of a fast jet (see Tomida et al. (2013)), without matter falling back along the axis of the jet. Magnetic field along the midplane is strongly pinched but we do not witness unexpected displacements or strange behaviors in this case. The strong jet has an important feedback on the surroundings of the

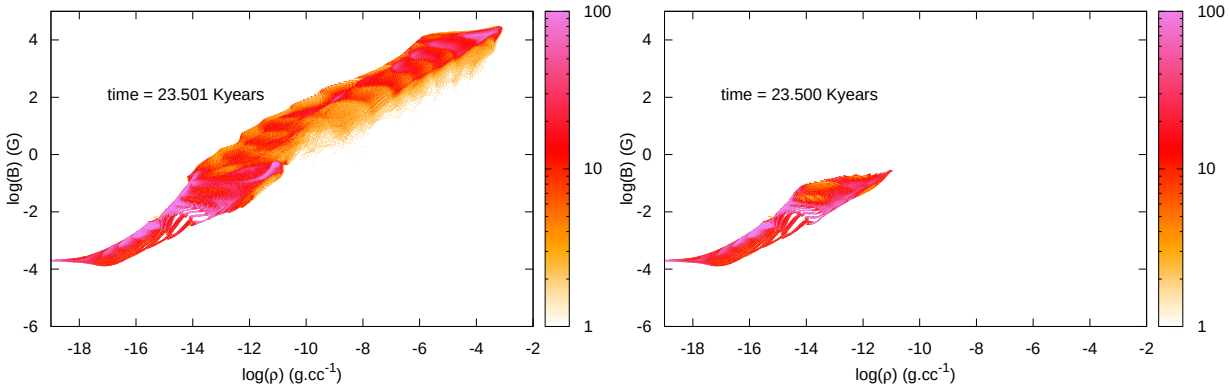

Figure 4.63: Left: SC case. Right: FC case. Magnetic field repartition as a function of density.

second core and supposedly on the first core when the jet will break through it. This has not been studied by Tomida et al. (2013) and we are not yet sure if we will be able to integrate long enough in radiation magnetohydrodynamics simulations to witness it.

4.3.3 Conclusion

We now have a state-of-the-art tool to study core collapse from the dense core to the formation of the second Larson core. Three dimensional effects, multigroup radiative transfer, non-ideal magnetohydrodynamics accounting for a detailed and versatile chemical network allow us to probe the parameter space of low (but not only) mass star formation. In this early outlook of second Larson core formation, we pinpointed the following:

- Even in the barotropic case, the second collapse has consequences on the first core as magnetic pileup is fought by increasing the density and resolution at the center of the core.
- The outflow mechanism is not clearly identical to the classical magnetic tower found in first core simulations. Additionally, radiative transfer is also accountable for the launching of outflows.
- The second collapse occurs within tenths or less of the free-fall time after the formation of the first core. This supports the discussion throughout chapter 4.2 concerning the questionable physical relevance of features seen in ideal MHD calculations.
- We witnessed a jet launched at the scale of the first scale, with velocities of more than 10 km.s^{-1}.

These results are very encouraging, and although we were not able to integrate to second core densities in non-ideal MHD with radiative transfer, we are confident that it is now a matter of computational time before we can present more detailed and thorough results. We have at our disposal a tool with state-of-the-art physics (non-ideal magnetohydrodynamics along with a versatile chemical evolution network, multigroup radiative transfer, an accurate equation of state) that we will use to probe the parameter space and try and increase our knowledge of star formation, or other fields of research.

4.4 ABC dynamo

We have studied the roles of ambipolar and Ohmic diffusion on the shape and evolution of the core in core collapse simulations. We now focus on a study of the fundamental problem of the kinetic

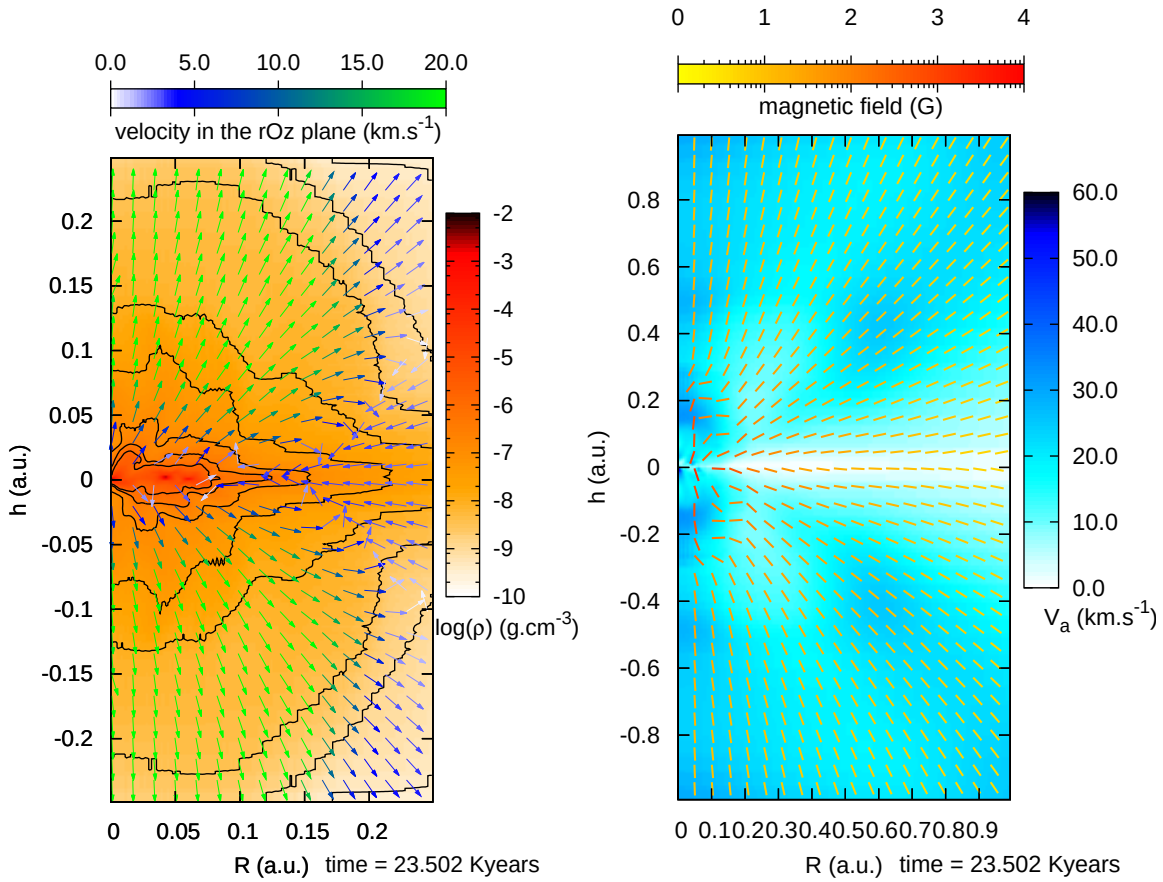

Figure 4.64: Left: SC case. Right: FC case. Magnetic field repartition as a function of density.

ABC dynamo. It is to our knowledge the first study that makes use of the full expression for the ambipolar diffusion and we directly compare the results to simulations using a Laplace operator (e.g. Ohmic diffusion). It is both a new approach to the ABC dynamo and a full use of the non-ideal developments that have been made during this thesis. Results highlight the qualitative and quantitative differences that arise when using ambipolar diffusion instead of Ohmic diffusion to drive the dynamo resulting in exponential growth of the magnetic energy. The kinematic ABC dynamo is a problem that is well defined and whose eigenvalues and eigenvectors in the Ohmic diffusion case are well known: it is a perfect opportunity to characterize precisely the effect of the exact expression of the ambipolar diffusion term in the induction equation. Finally, we confront the results with the experimental measure of the galactic magnetic field and conclude that other effects must be considered (the most immediate of which is the feedback of the Lorentz force on the flow).

4.4.1 Introduction

The ABC-flow dynamo is widely studied (see Dombre et al. (1986) or very recent studies by Bouya and Dormy (2013)). As pointed out by Bouya and Dormy (2013), recent studies in this field (ABC-flows dynamos) mostly focus on non-linear studies (Courvoisier et al. (2005), Archontis et al. (2007)), or on the consequence of the forcing scale for various ABC-flows types (Alexakis (2011)). This motivated the high-resolution study conducted by Bouya and Dormy (2013), which highlighted interesting behaviors of the dominant eigenvalues depending on the magnetic Reynolds number (Rm). Nevertheless, these anaylitical or numerical studies treat the Ohmic diffusion case, while ambipolar diffusion is the diffusion at stake in many cases and in particular in galaxies (see for example Zweibel and Heitsch (2008)). Using the AMR-MHD code `RAMSES` we intend to probe the effect of ambipolar resistivity instead of a pure Ohmic diffusivity on the classical ABC dynamo.

The paper is organized as follows. In subsection 4.4.2 we present rapidly the theory of ambipolar diffusion, and the limits of considering it as a pure diffusion. In subsection 4.4.3 we present the numerical setup used to carry out this study. In subsection 4.4.4 we summarize the results of the *linear* ambipolar diffusion, while in subsection 4.4.5 we present the results using the *non-linear* ambipolar diffusion.

4.4.2 Is ambipolar diffusion a diffusion ?

We recall here some previous results, mentioned in appendix 1.B.

One-fluid approximation Using the one-fluid approximation (Shu et al. (1987)) we end up with the following equation for the induction equation, taking into account only the ambipolar diffusion term:

$$\frac{\partial \mathbf{B}}{\partial t} + \boldsymbol{\nabla} \times (\mathbf{B} \times \mathbf{v_n}) = \boldsymbol{\nabla} \times \Big(\frac{1}{\gamma \rho_i \rho} [(\boldsymbol{\nabla} \times \mathbf{B}) \times \mathbf{B}] \times \mathbf{B} \Big) \tag{4.13}$$

$$= \boldsymbol{\nabla} \times \Big(\frac{1}{\gamma \rho_i \rho} [\mathbf{B} \cdot (\boldsymbol{\nabla} \times \mathbf{B})] \mathbf{B} - (\mathbf{B} \cdot \mathbf{B}) \boldsymbol{\nabla} \times \mathbf{B} \Big) \tag{4.14}$$

$$= -\boldsymbol{\nabla} \times \Big(\frac{\mathbf{B} \cdot \mathbf{B}}{\gamma \rho_i \rho} (\boldsymbol{\nabla} \times \mathbf{B}) \Big) \tag{4.15}$$

with $\mathbf{F}_{\text{drag}} = \gamma \rho_n \rho_i (\mathbf{u_i} - \mathbf{u_n})$.

Equation (4.15) is not easily simplified into a Laplace operator with a diffusion coefficient, since:

$$\boldsymbol{\nabla}\times\Big(\frac{\mathbf{B}\cdot\mathbf{B}}{\gamma\rho_i\rho}(\boldsymbol{\nabla}\times\mathbf{B})\Big)=-\frac{B^2}{\gamma\rho_i\rho}\Delta\mathbf{B}+\boldsymbol{\nabla}(\frac{\mathbf{B}\cdot\mathbf{B}}{\gamma\rho_i\rho})\times(\boldsymbol{\nabla}\times\mathbf{B}) \tag{4.16}$$

$$=-\frac{B^2}{\gamma\rho_i\rho}\Delta\mathbf{B}+2\big[(\frac{\mathbf{B}}{\sqrt{\gamma\rho_i\rho}}\cdot\boldsymbol{\nabla})\frac{\mathbf{B}}{\sqrt{\gamma\rho_i\rho}}+\frac{\mathbf{B}}{\sqrt{\gamma\rho_i\rho}}\times(\boldsymbol{\nabla}\times\frac{\mathbf{B}}{\sqrt{\gamma\rho_i\rho}})\big]\times(\boldsymbol{\nabla}\times\mathbf{B}) \tag{4.17}$$

The difficulty lies in the diffusion coefficient that is an explicit function of the magnetic field, therefore there is no easy way to neglect (and justify it) the second term on the right hand-side. This is very different from the case of the Ohmic diffusion where the diffusion coefficient can be considered constant under reasonable hypothesis and then written as a real diffusion with a Laplace operator.

We chose to keep the first form of the induction equation (4.13) to study the ABC dynamo.

Linearity Equation (4.15), assuming a constant neutrals and ions density and a constant coefficient γ, is non-linear. We rewrite it in the well-known form:

$$\frac{\partial\mathbf{B}}{\partial t}+\boldsymbol{\nabla}\times(\mathbf{B}\times\mathbf{v_n})=\boldsymbol{\nabla}\times\Big(\mathbf{v}\times\mathbf{B}-\eta(\boldsymbol{\nabla}\times\mathbf{B})\Big) \tag{4.18}$$

When typical studies are carried out, η is the Ohmic resistivity as $\eta=\mathrm{Rm}^{-1}$. In order to study the full implications of using the correct ambipolar diffusion term, we separate two different cases, hereafter referred to as the *non-linear* case with $\eta=\eta_{\mathrm{AD}}=\frac{\mathbf{B}\cdot\mathbf{B}}{\gamma\rho_i\rho}$, and the *linear* case with $\eta=\frac{\eta_{\mathrm{AD}}}{B^2}$.

4.4.3 Numerical setup

We use the AMR-MHD code `RAMSES` (Fromang et al. (2006)) which, as should be noted, has already been used in a different way to study ABC dynamos by Teyssier et al. (2006). We use the extension described in Masson et al. (2012) to study non-ideal MHD using this code.

This problem being very dependant on the resolution since there will always be a numerical dissipation limiting the highest Reynolds number attainable, the refinement strategy is not straightforward. After several tests, we chose to take advantage of the more powerful computers at our disposal to perform non-AMR calculations, therefore getting rid of the annoying issue of wrong results because of coarse cells yielding a locally high numerical resistivity. AMR calculations can nevertheless be performed using a refinement strategy based on the ratio of the magnetic energy in the cell to the total magnetic energy for a decent speed-up of the simulation and for qualitative results (see 4.B for more details).

Initial condition We use periodic boundary conditions in a 1:1:1 size box and the commonly used ABC-flow velocity field:

$$\mathbf{u}=\big(A\sin(2\pi z)+C\cos(2\pi y)\big)\mathbf{e_x}+\big(B\sin(2\pi x)+A\cos(2\pi z)\big)\mathbf{e_y}+\big(C\sin(2\pi y)+B\cos(2\pi x)\big)\mathbf{e_z} \tag{4.19}$$

The velocity field is not updated at each time-step, meaning that we restrict ourselves to the kinematic dynamo problem (the flow is unchanged by the magnetic field variations). As in Bouya and Dormy (2013), we only study the case $A:B:C=1:1:1$, which belongs to the largest symmetry class of ABC flows. However, as pointed out by Alexakis (2011), it may not be the best choice for dynamo action as very small chaotic regions can develop.

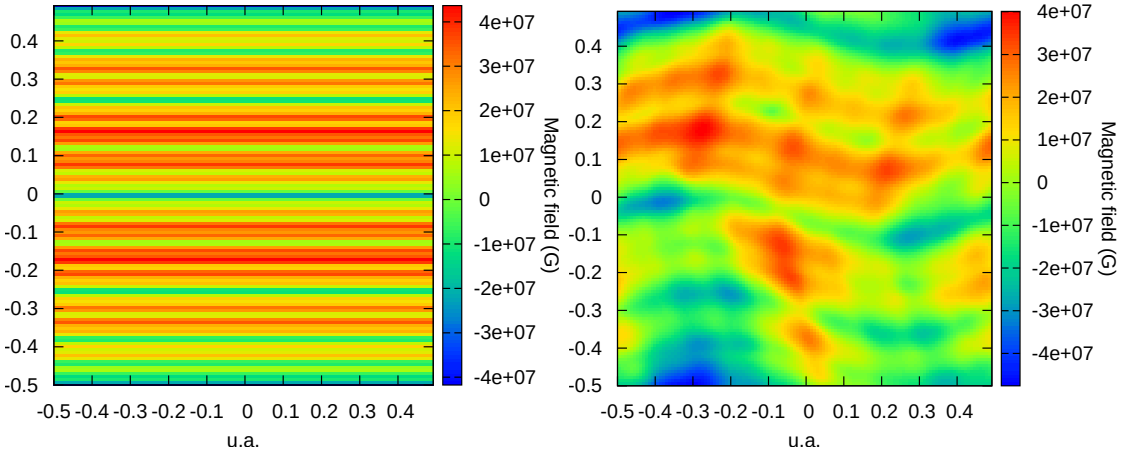

Figure 4.65: Slice in the middle of the box showing the initial magnetic field energy (B^2) (left) and the first time-step (right).

The initial condition for the magnetic field is unimportant in theory, but decisive in practical matters. Since we are using a Godunov-based explicit code, the time-step is a limiting factor as we increase the resolution. Therefore, we need an initial condition in which the most unstable mode will reasonably rapidly be dominant. Using a random yet divergence-free magnetic field is possible, but there are stability issues using this type of field as an initial condition. We ended up using a sum of many different sines, as represented Fig. 4.65.

Numerical resistivity As we probe larger and larger magnetic Reynolds numbers (up to a few hundred), the effective resistivity is shrinked as $\eta_{\text{Ohmic}} \propto \frac{1}{Rm}$ and can be of the same order of magnitude of numerical resistivity (being dependant on the resolution). We first conducted a resolution study in order to assess which correct numerical resolution must be used to guarantee that we have the correct question to the answer to get. In Fig. 4.66 we represent the real and imaginary parts of the eigenvalue of the fastest growing mode for the spectral study by Bouya and Dormy (2013) (solid line, taken as a reference and called "BD" hereafter) and for our simulations using various resolutions (up to 128^3. The main conclusion is that for the range of Rm we are interested in (from Rm = 20 to Rm $\simeq$ 300 we (very, up to a relative error of 0.1%) accurately calculate the real and imaginary parts of the eigenvalue for grids of or finer that 128^3 cells, which is achievable without too much computational power. On the other hand, coarser grids fail to describe the eigenvalue coaslescence happening at Rm $\simeq$ 220, and the imaginary part does not become null. This suggest that at this stage there is a non-physical eigenvalue coming from the numerical resistivity instead of the fast dynamo, and therefore such low resolutions should be avoided.

The method to find the eigenvalue is to fit the square root of the magnetic energy by a straight line (see Fig. 4.67 on the left) and then fit the data which have been cleared from the linear trend by a cosine focusing on the frequency (see Fig. 4.67 on the right). This method grants an accuracy of the order of 10^{-3} when carried out for $20 < t < 200$ as displayed in Fig.4.67.

4.4.4 Linear study

In order to conduct the linear study, we use the resistivity described in § 4.4.2: $\eta = \frac{\eta_{\text{AD}}}{B^2} = \frac{1}{\text{Rm}_{\text{AD}}}$ as well as a reference Reynolds number. We therefore can define an effective resistivity $\tilde{\eta}$ and Reynolds

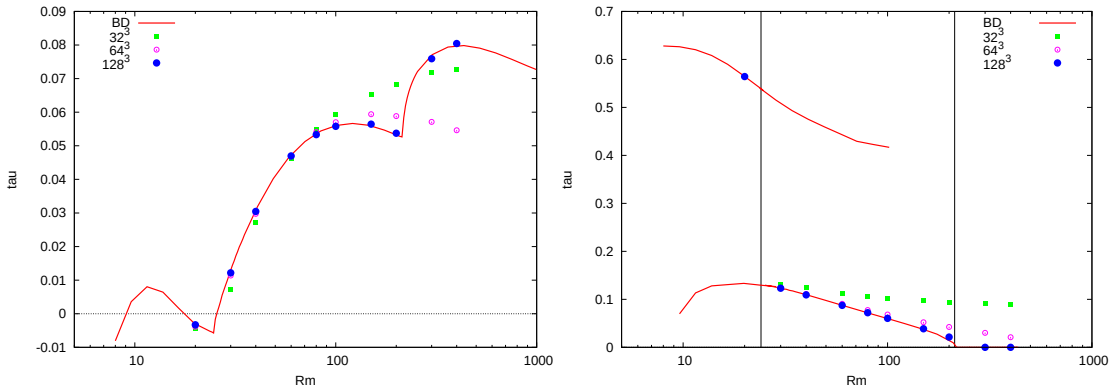

Figure 4.66: Real (left) and imaginary (right) part of the eigenvalues of the fastest growing mode.

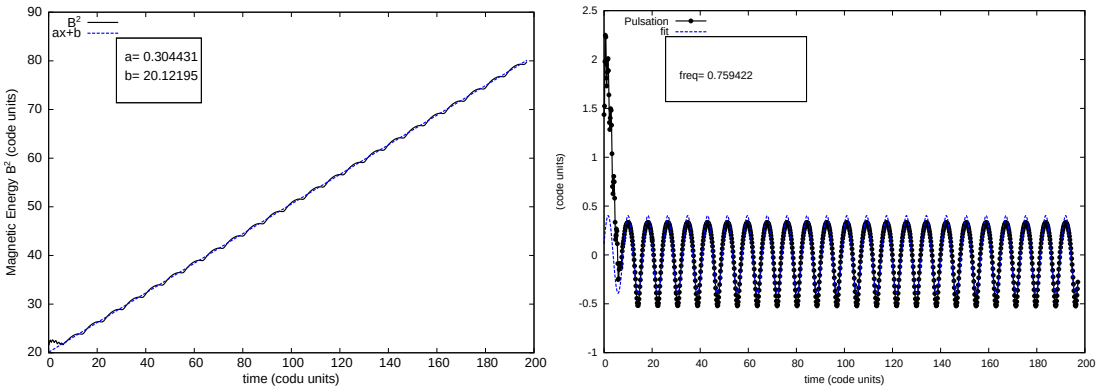

Figure 4.67: Method to extract the real and imaginary part from the magnetic energy against the time. Real part of the eigenvalue (left): linear fit. Imaginary part (right): fit by a cosine.

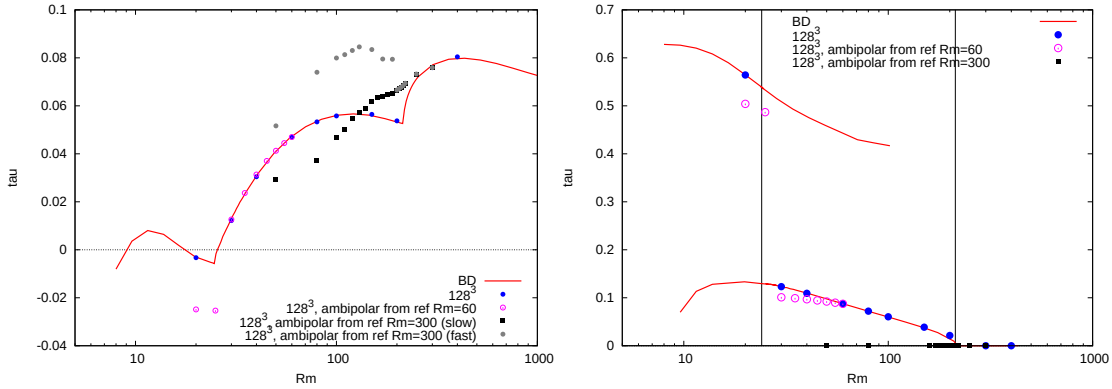

Figure 4.68: Linear study of ambipolar diffusion effect, starting with a reference point Rm = 60. Real (left) and imaginary (right) part of the eigenvalues of the fastest growing mode.

number $\tilde{\mathrm{Rm}}$ of the form:

$$\frac{1}{\tilde{\mathrm{Rm}}} = \tilde{\eta} \tag{4.20}$$

$$= \frac{1}{\mathrm{Rm}} + \frac{1}{\mathrm{Rm_{AD}}} \tag{4.21}$$

We chose to keep the Ohmic diffusion term for the following reasons:

- it serves as a reference point
- it ensures that we are not dominated by numerical resistivity, since we performed resolution tests prior to this
- using only the ambipolar diffusion term would qualitatively give the same result, but with a numerical Reynolds number as reference point instead of the well-defined magnetic Reynolds number in the case of Ohmic diffusion. Moreover, this so-called numerical Reynolds number is large (larger than a few hundred at least) and unknown.

Results are plotted in Fig 4.68. We carried out two sets of simulation, starting from Rm=300 and Rm=60 and gradually increasing the ambipolar diffusion weight.

Starting from Rm=60 Concerning the growth rate, we accurately describe the diminishing magnetic Reynolds number as if using an increasing Ohmic diffusion, up until the eigenvalue crossing at Rm$\simeq$ 24. After that, we do not find back the other eigenvalue and instead keep getting a negative growth rate. On the imaginary part, the results with the linear ambipolar term match qualitatively the global trend with the jump due to the eigen value crossing, but with quantitative differences.

Starting with Rm=300 At higher Rm, the difference is more visible between the ambipolar term and a usual diffusion. There is still a kink in the growth rate, which occurs at lower Rm. However, this kink does not fit with an eigenvalue coalescence since the imaginary part stays equal to 0.

Eigenvectors Last, we can look at the eigenvectors. The highest the Rm, the more localized are the magnetic structures. Results are shown Fig. 4.69. The global Rm seems to be dominating as for Rm= 300 and $\tilde{\mathrm{Rm}}$ = 50 the structures look very similar to the full diffusive case Rm= 50. However on the details (more accurately visible on the top panels, with the logscale for the norm of the

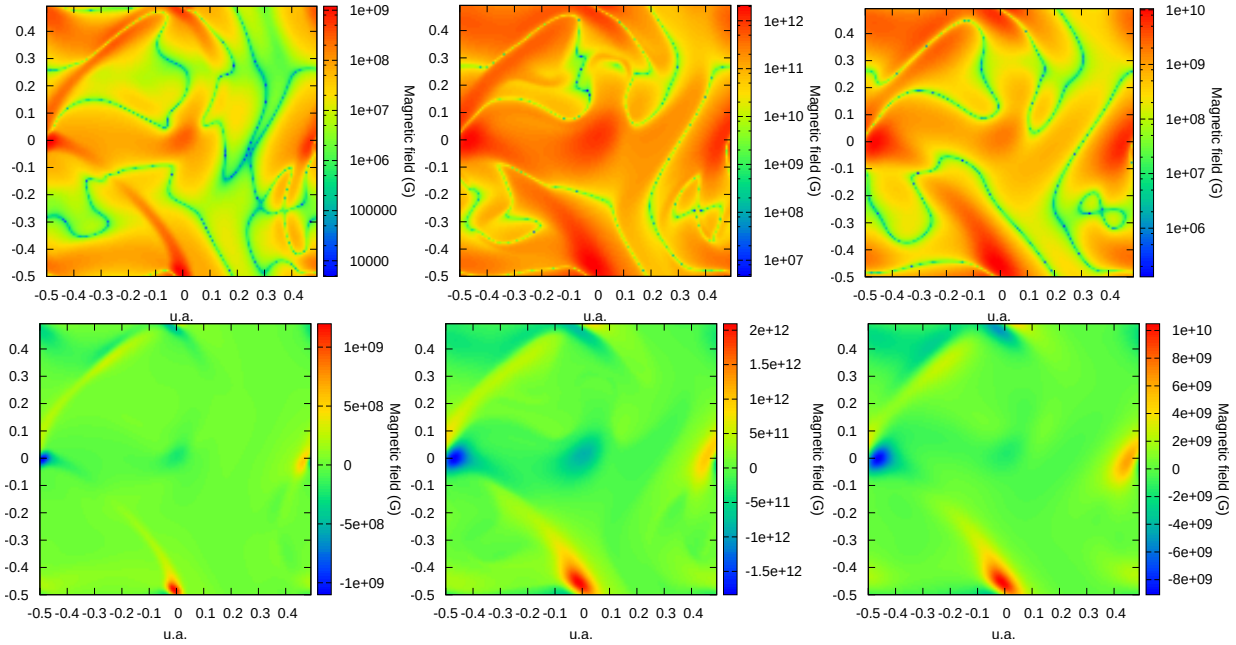

Figure 4.69: Visualization of the eigenvectors for three different cases. Top panels: logscale view of the amplitude of the magnetic field. Bottom panels: classical view of the norm of one component of the magnetic field, keeping the sign in account. From left to right: Rm= 300 and $\tilde{\text{Rm}} = 300$; Rm= 300 and $\tilde{\text{Rm}} = 50$; Rm= 50 and $\tilde{\text{Rm}} = 50$.

magnetic field) the structures are not alike and we retrieve more similarities between the Rm= 300 and $\tilde{\text{Rm}} = 50$ and the fully diffusive Rm= 300 case (less red on the middle of the box). This might be explained by the inability of the ambipolar term to produce magnetic reconnection, which would thus occur only at Rm= 300 and differ from the Rm= 50 case.

Conclusions The ambipolar term, in the linearized case, is able to retrieve some of the results found with a truly diffusive case. Nevertheless, there are some strong discrepancies, in particular at both Rm$\simeq$ 24 and Rm$\simeq$ 220 when the modes crossing and eigenvalue coalescence occur. There are differences in the eigenvectors too, with similarities with both the initial Rm and the global $\tilde{\text{Rm}}$.

4.4.5 Non-linear study

The non-linear study uses the true resistivity $\eta_{\text{AD}} = \frac{\mathbf{B}\cdot\mathbf{B}}{\gamma\rho_i\rho}$, yielding a non-linear differential equation. This non-linearity results in a saturation of the magnetic energy, as can be seen Fig. 4.70. On the left side is the total magnetic energy. There is a linear growth corresponding to the Rm= 40 (or any initial Rm), as can be seen Fig. 4.71 on the left. The pulsation on this linear part matches the one found with the Ohmic diffusion study, which supports the idea that while the ambipolar coefficient scales as B^2 at the beginning only the Ohmic resistivity ($\eta_\Omega = \frac{1}{\text{Rm}}$) is effective. As the field strengthen up, the ambipolar resistivity slowly become dominant and yields the saturation. At this stage, there is still an imaginary part to the dominant eigenvalue is there was one at the beginning. The pulsation during the saturation is slightly larger than the one during the linear part, as can be seen Fig. 4.71 on the right.

Saturation value The saturation value is handled by the ambipolar diffusion coefficient (in our case, $\eta_{\text{AD}} = \frac{B^2}{\gamma\rho_i\rho} = \frac{B^2}{\gamma}$, using $\rho = \rho_i = 1$. A simple analysis gives the following result for the

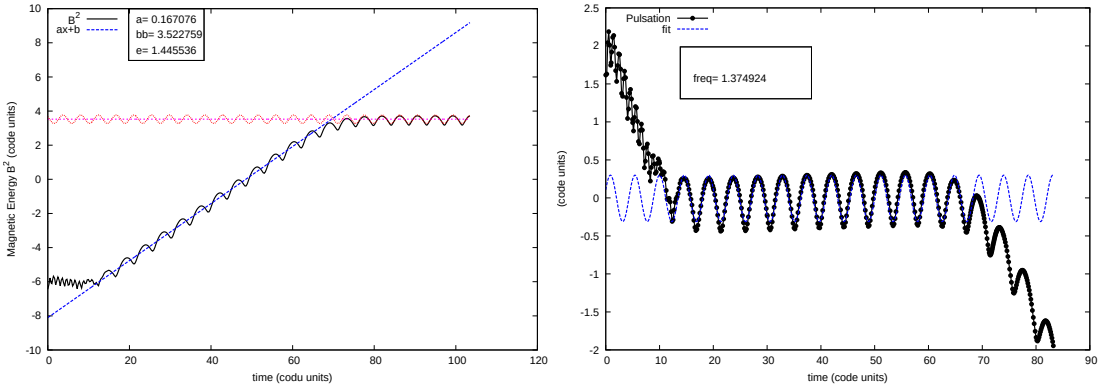

Figure 4.70: Non-linear saturation for Rm= 40 and $\gamma_{\mathrm{AD}} = 1$. Left: total magnetic energy in the box. Right: same figure with the linear growth removed to find more accurately the pulsation.

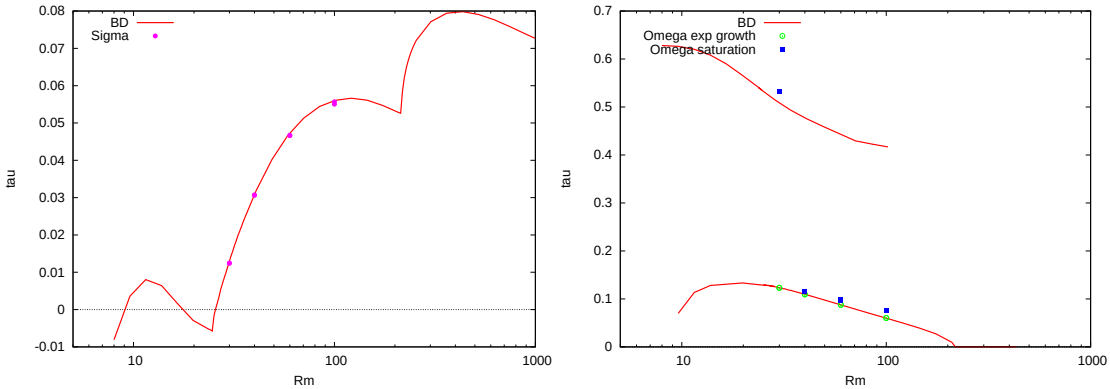

Figure 4.71: Non linear growth rate (left figure) for the linear part of the run, with the initial Rm as abscissa. The pulsation for the linear part and the saturation is represented on the right figure.

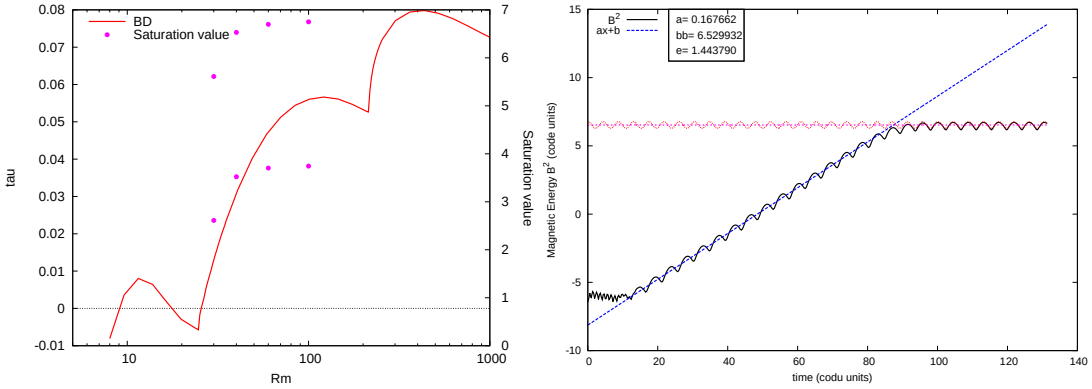

Figure 4.72: Left: saturation value for non-linear runs, with respectively $\gamma = 1$ and $\gamma = 1000$ for the upper and lower points. Right: total magnetic energy contained in the box for Rm= 40 and $\gamma = 1000$.

expected saturation value:

$$\dot{B} = \tau B - \frac{1}{\gamma} B^3 \quad \text{with } \dot{B} = 0: \tag{4.22}$$

$$\tau\gamma = B^2 \tag{4.23}$$

with τ the growth rate of the previous linear study. We verify that we correctly address the problem by multiplying γ by 1000 and expecting the exact same answer with a saturation three orders of magnitude higher, as can be seen in equation (4.23). Results concerning the saturation are displayed Fig. 4.72 along with the magnetic energy for the Rm= 40 and $\tilde{\gamma} = 1000\gamma$ (to be compared to Fig. 4.70, left figure).

Bifurcation Since the saturation only takes place when the field is strong enough (for the ambipolar resistivity to be large compared to the Ohmic resistivity) it is interesting to know whether the saturation will go down to zero when approaching the critical value Rm$\simeq$ 24.

We therefore restart the simulations with Rm= 60 and decrease gradually Rm up to Rm= 20 to try and answer this question. Results are presented Fig. 4.73. We first changed from Rm= 60 to Rm= 40. The saturation value decreases immediately and stabilizes at the saturation value found for a non-linear run starting with Rm= 40 (green solid line). When decreasing again to Rm= 20 the saturation value decreases again and stabilizes with a very different imaginary part for the eigenvalue. This last experiment is interesting as for Rm= 20 the classical growth rate is negative, leading to no saturation since the ambipolar term would never grow to become more important than the Ohmic one. Additionally, the saturation value now does not follow anymore equation (4.23). This is evidence for another higher order non-linearity arising in the development of the ambipolar term $[(\boldsymbol{\nabla} \times \mathbf{B}) \times \mathbf{B}] \times \mathbf{B}$. The same study for Reynolds numbers Rm= 60 decreased to Rm= 30 is represented in the bottom plots, Fig. 4.73.

To more accurately describe the non-linear bifurcation we plot the evolution of the saturation value, Fig. 4.74. We find that the non-linear saturation (full dots) indeed goes down to zero when approaching the critical Rm= 25.5 corresponding to a null growth rate. On the other hand, the hysteresis saturation value, decreasing from a higher Rm after reaching non-linear saturation, does not tend to zero.

Varying the effective Rm Last, we present some experiments starting at a higher Rm, with the imaginary part of the eigenvalue is equal to zero. This setup allows for a precise and instantaneous

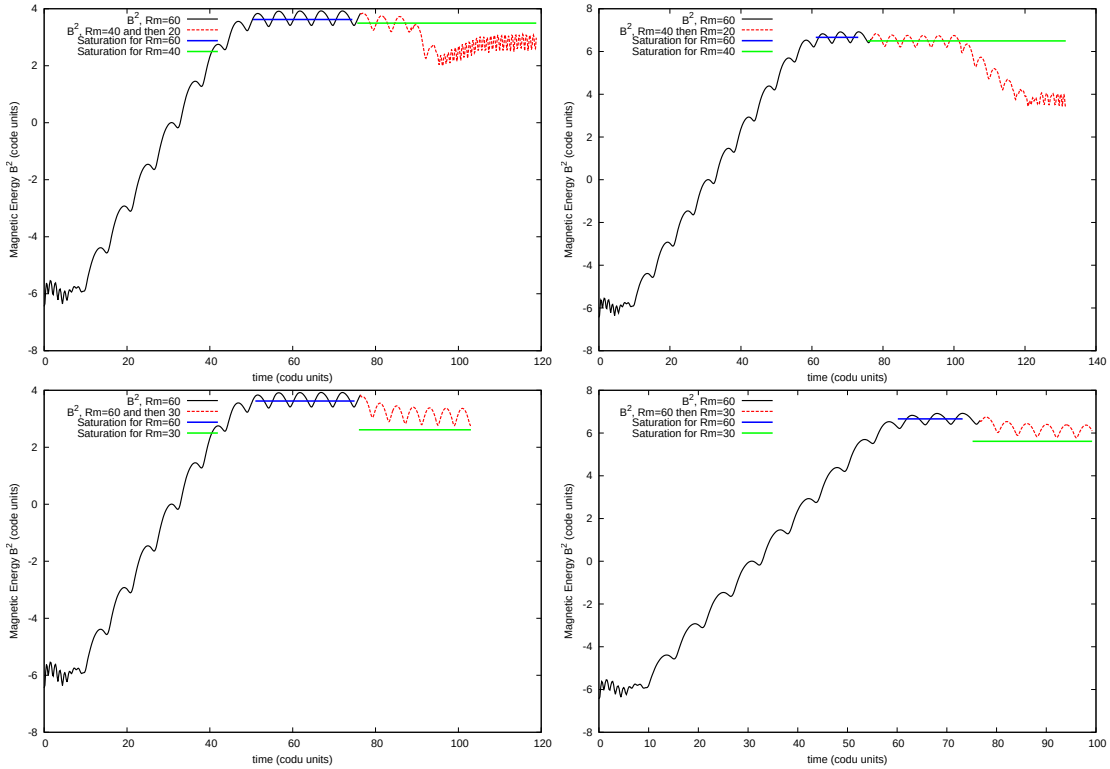

Figure 4.73: Non-linear simulations with a gradually decreasing magnetic Reynolds number. Left: $\gamma = 1$. Right: $\gamma = 1000$. The two top panels correspond to Rm= 60, then 40 and finally 20. The two bottom panels correspond to Rm= 60 and then 30.

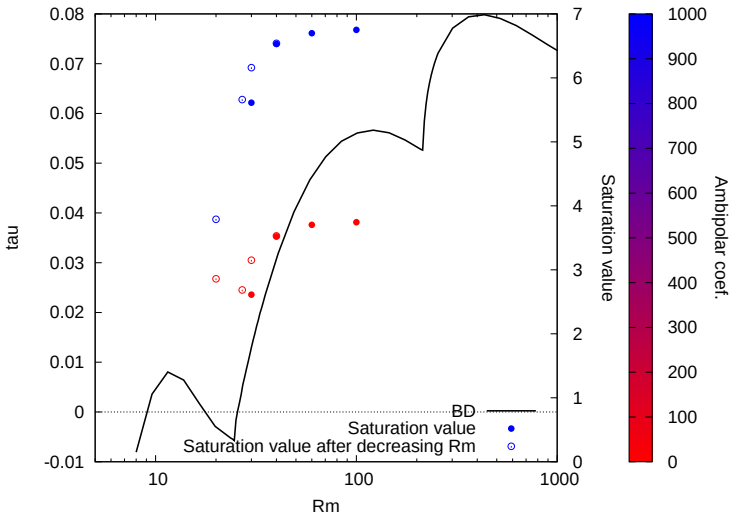

Figure 4.74: Blue points: $\gamma = 1000$. Red points: $\gamma = 1$. Empty dots: hysteresis saturation value, decreasing from a higher Rm after reaching non-linear saturation. Full dot: non-linear saturation value.

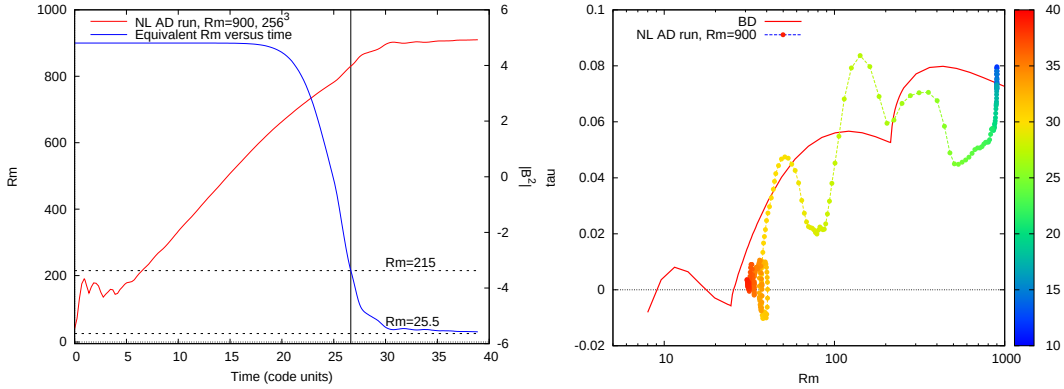

Figure 4.75: Non-linear run with Rm= 900 and a grid of 256^3. Left: growth rate (right axis) and effective Rm as a function of time (left axis) The black dashed lines represent Rm= 25.5 and Rm= 215, two critical values for Rm. The black vertical solid line is the crossing between Rm as a function of time and the dashed solid line Rm= 215. Right: the instantaneous growth rate (calculated with a third order discrete derivative) versus the effective $\tilde{\text{Rm}}$ with the time (code units) coded in the colorbar.

measure of the growth rate not possible with the oscillatory behavior of eigenvalues at lower Rm. As the field grows, the ambipolar resistivity grows and we can still define an effective Reynolds number $\frac{1}{\tilde{\text{Rm}}} = \frac{1}{\text{Rm}} + \frac{1}{\text{Rm}_{\text{AD}}}$. We therefore can plot the evolution of the growth rate (the imaginary part staying equal to zero at all times) with the effective Reynolds number $\tilde{\text{Rm}}$. This is represented Fig. 4.75 on the right. On the left plot is the magnetic energy as a function of time (right tics) and the effective magnetic Reynolds number in terms of time. We added two horizontal lines corresponding to the eigenvalue coalescence at Rm= 215 and to a null growth rate at Rm= 25.5 The vertical line represent the time of crossing the critical Rm= 215, in order to better picture the interesting parts of the magnetic energy curve. If the effective Rm is indeed behaving as an Ohmic Reynolds number, we would expect an increase in the growth rate up until an effective Rm$\simeq$ 500, followed by a decrease until the eigenvalue coalescence, etc. The actual trend is difficult to interpret. Left plot: the time of crossing the critical Rm= 215 accurately matches a strong behavior change in the magnetic energy. The growth rate changes a lot right after, with a small decrease and then a strong increase. At larger times, when the saturation occur, the effective Rm tends to the second critical value Rm= 25.5, which is the point of null growth in the linear case. Right plot: there are several domains with an increase in the growth rate not matching the trend for the Ohmic Reynolds number. Moreover, the value matches at the beginning the Ohmic growth rate, but then it decorrelates from the solid red curve (Ohmic Rm). There seems to be a kink at an effective Rm corresponding to the eigenvalue coalescence which remains present in lower resolution (see Fig. 4.76 for the same experiment with a lower resolution (128^3). We also carried out experiments with Rm= 300, presented Fig. 4.77. According to our previous tests, there should not be resolution issues at Rm= 300. The conclusions remain qualitatively the same: something is happening right after the effective Rm crosses Rm= 215 and then tends to Rm= 25.5. There is an unexplained behavior at the beginning of the saturation: the growth rate oscillates once before stabilizing.

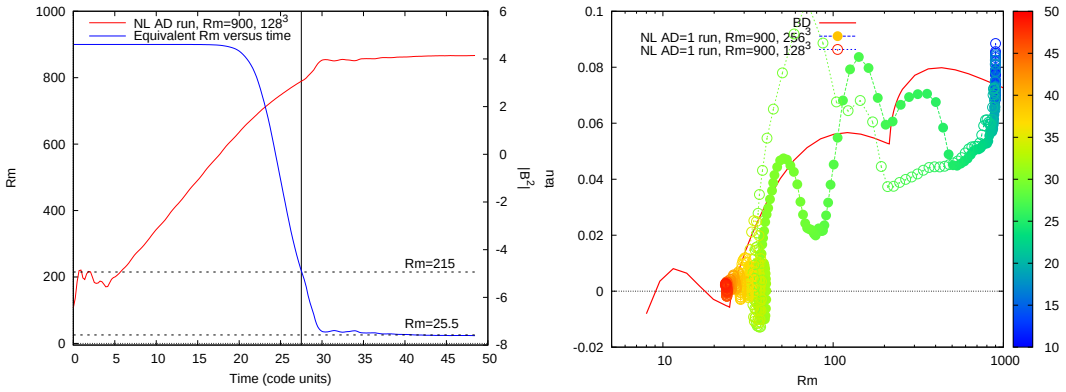

Figure 4.76: Non-linear run with Rm= 900 and a grid of 128^3. Left: growth rate (right axis) and effective Rm as a function of time (left axis) The black dashed lines represent Rm= 25.5 and Rm= 215, two critical values for Rm. The black vertical solid line is the crossing between Rm as a function of time and the dashed solid line Rm= 215. Right: the instantaneous growth rate (calculated with a third order discrete derivative) versus the effective $\tilde{\text{Rm}}$ with the time (code units) coded in the colorbar, for both the low resolution (128^3) and high resolution runs (256^3).

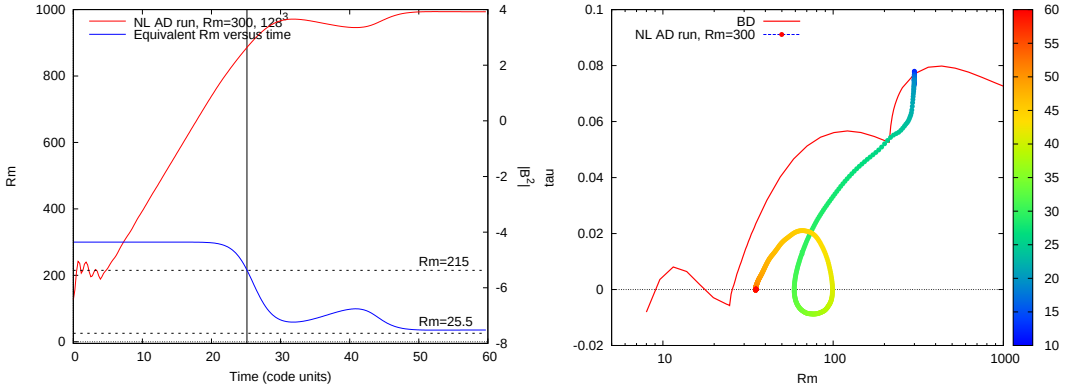

Figure 4.77: Non-linear run with Rm= 300 and a grid of 128^3. Left: growth rate (right axis) and effective Rm as a function of time (left axis) The black dashed lines represent Rm= 25.5 and Rm= 215, two critical values for Rm. The black vertical solid line is the crossing between Rm as a function of time and the dashed solid line Rm= 215. Right: instantaneous growth rate (calculated with a third order discrete derivative) versus the effective $\tilde{\text{Rm}}$ with the time (code units) coded in the colorbar.

Galactic magnetic field We wish to apply the results concerning the non-linear saturation to galactic the large-scale field. As before, we get the order of magnitude for the saturation value:

$$\boldsymbol{\nabla} \times (\mathbf{B} \times \mathbf{v_n} + \frac{1}{\mathrm{Rm}}) = \boldsymbol{\nabla} \times \left(\frac{1}{\gamma \rho \rho_i} \left[((\mathbf{J} \times \mathbf{B}) \times \mathbf{B}) \times \mathbf{B} \right] \right) \tag{4.24}$$

$$B = \sqrt{\tau L^2 \gamma \rho_i \rho} \tag{4.25}$$

with L the typical length-scale for variations of the magnetic field, τ the growth rate in the diffusive case, γ the already defined coefficient for ambipolar diffusion, along with ρ and ρ_i the neutrals and ions density.

For $L \simeq 0.1$ corresponding to Rm$=$ 100, we find $B_{\mathrm{saturation}} \simeq 0.055$. In terms of total magnetic energy in the box, it finally gives $\log(\bar{B^2} \times 2^{level=7}) = 3.8$ to compare to the experimental value $\log(\bar{B^2} \times 2^{level=7}) = 3.74$. As noted previously, the linear dependency of the total magnetic energy with γ is also retrieved. The raw estimate for L is the tricky part, and cannot be estimate much more accurately.

For the galactic mean field, we use the estimates given in Zweibel (2002).

$$n_{\mathrm{neutrals}} = 50\,\mathrm{cm}^{-3} \tag{4.26}$$

$$n_{\mathrm{ions}} = 5 \times 10^{-3}\,\mathrm{cm}^{-3} \tag{4.27}$$

$$B = 3\,\mu\mathrm{G} \tag{4.28}$$

$$L = 1\,\mathrm{pc} = 3.09 \times 10^{18}\,\mathrm{cm} \tag{4.29}$$

$$\tau_{\mathrm{ni}} = \frac{1}{\gamma \rho_i} = \frac{6.7 \times 10^8}{n_{\mathrm{ions}}}\,\mathrm{s} \tag{4.30}$$

$$A_n = 1.4 \tag{4.31}$$

with A_n the atomic weight for the neutrals for gas of cosmic composition and τ_{ni} the neutral-ion collision time.

With these estimates we have:

$$B^2 = \frac{\tau L^2 4\pi n_{\mathrm{neutrals}} n_{\mathrm{ions}} m_p A_n}{6.7 \times 10^8} \tag{4.32}$$

with $m_p = 1.7 \times 10^{-24}$ g the mass of the proton. We finally get with the column density $n_{\mathrm{neutrals}} L \simeq 0.1\,\mathrm{to}\,10 \times 10^{20}$ cm,

$$B \simeq 6\,\mathrm{to}\,600\,\mathrm{G} \tag{4.33}$$

This is orders of magnitude above the observed magnetic fields in the regions with the above-mentioned parameters, where $B \simeq 3\mu$G. A potential explanation is that we overestimated the growth rate due to Ohmic dissipation $\tau = 0.1$ but it would require to be decreased by twelve orders of magnitude to match the observed value of B. In other words, the time-scale for ambipolar diffusion, estimated as $t_{\mathrm{AD}} = \frac{L^2 4\pi n_{\mathrm{neutrals}} n_{\mathrm{ions}} m_p A_n}{B^2 6.7 \times 10^8} \simeq 10^8$ years should match the inverse of the growth rate τ^{-1}, yielding an expected Ohmic growth rate $\tau \simeq 10^{-15}\,\mathrm{s}^{-1}$. This is unrealistic, even taking into account flattened geometries or strong gradients yielding a smaller characteristic length L. Another process must therefore be at stake to explain the galactic mean field saturation.

4.4.6 Conclusions

We recall the main results of this study of the kinetic ABC dynamo:

- First, we retrieved the results found by Bouya and Dormy (2013) using Ohmic resistivity and carried out a resolution study to effectively conduct the next numerical simulations using ambipolar diffusion.
- Using a non-approximate expression for the ambipolar diffusion term yields qualitative and quantitative differences compared to a Laplace operator.
- In the linear case ambipolar diffusion gives qualitatively the same results as Ohmic diffusion for the growth rate (real part of the eigenvalue). We observe a kink approximately at the same effective magnetic Reynolds number, but it is not anymore associated with an eigenvalue coalescence (null imaginary part). The eigenvectors also differ both in shape and size compared to the case in which we used a Laplace operator to describe Ohmic dissipation.
- In the non-linear study, we explore the true expression of ambipolar diffusion as a third order term in $\mathbf{B}$. We observe an exponential growth of the magnetic energy linked to the Ohmic part of the diffusion, followed by a saturation that we were able to explain to the order of magnitude. When probing the stability limit at Rm$=25.5$ we notice a sub-critical bifurcation associated with a non-zero saturation value when diminishing the magnetic Reynolds number down to below the stability value.
- Larger magnetic Reynolds numbers allow to trace the effective Rm evolution with time. We once again observed kinks at Rm$=215$ (the eigenvalue coalescence in the Ohmic diffusion case) and a relaxation to a magnetic Reynolds number close to the stability limit.

Even though the ABC dynamo saturation due to ambipolar diffusion seems unable to explain the galactic mean field, we restricted ourselves to a very peculiar case of a very symmetrical kinetic dynamo. In molecular clouds or larger structures, turbulence is omnipresent and is a viable way to drive the dynamo, as explained in Federrath et al. (2011). They explored the growth of the magnetic field using magnetohydrodynamics and turbulence driven with solenoidal (divergence-free) or compressive (curl-free, e.g. the forcing due to supernova blast) forcing. They found that both types of forcing successfully drive the dynamo. Using both approaches alongside can be the idea for the next step: exploring the role of ambipolar diffusion as a way to drive the dynamo in global turbulent simulations of large clouds.

4.A Disk criteria

We use the disk criteria defined in Joos et al. (2012), using a threshold value $f = 2$:

- rotational support: $v_\theta > f v_r$
- close to hydrostatic equilibrium: $v_\theta > f v_z$
- rotational support larger than thermal support: $\frac{\rho v_\theta^2}{2} > fP$
- density criterion: $\rho > 10^9$ cm^{-3}

He also used a connectivity criterion that we didn't use. Instead, we checked for each case that the disk is a whole and doesn't include spurious spiral arms or parts of the outflow. Note that the connectivity criterion would not prevent to account for separate parts of the disk, as in for example in Fig. 4.29 on top.

These criteria assure a straightforward comparison between different cases. However, they fail to distinguish rotationally supported disks from rotationally dominated structure with a lot of magnetic support. These structures pass all the criteria but are more diffuse and with a aspect ratio closer to 1 than rotationally supported disks. We also tried to add a criterion based on magnetic pressure, but failed to make it useful. The issue is that depending on the case, magnetic pressure can become dominant even inside the disk. Using a stringent criterion therefore ends up defining the disk entirely with the magnetic pressure, loosing all physical notion of rotationally supported structure.

We show some tests Fig. 4.78. It is a simple case of misaligned axis of rotation (3%) and magnetic field lines ($\mu = 5$). We first plot the density/velocity field in two cuts (none of which perpendicular to the magnetic field lines): top two plots. Using all Joos et al. (2012) criteria lead to the second raw of plots, where the disk structure appears. There are on the right plot two areas where connectivity would be broken (bottom left and top right of the disk-like structure) but we keep them for two reasons. First, the account for a negligible amount of the disk-mass. Second, they are close to the disk and not some random parts of the outflow. On the last raw, we show the resulting selected cells using only the density criterion, as in Seifried et al. (2013). We emphasize that a density criterion is indeed a valid choice. It won't accurately describe a rotationally supported disk (Joos et al. (2012) criterion are obviously better at this) but can be used as a stringent criterion to compare masses between simulations. As we showed, even improved criterion can sometimes fail to describe rotationally supporter disks. Using a stringent criterion to compare between different simulations, simple or evolved, is always a valid choice as long as you don't try to extract too much informations from it.

4.B An AMR code for the ABC dynamo

As stated previously in § 4.4, the result is dependant on the numerical resistivity thus making it difficult to use adaptive mesh refinement strategies. The most straightforward way to do it is to use a refinement criteria based on the ratio of the cell's magnetic energy versus the total magnetic energy. We chose to refine when the ratio of the local energy with 32^3 cells (respectively 64^3, 128^3, etc.) is greater than 4 (respectively 16, 64, etc.) as done in Teyssier et al. (2006).

Since the resolution study concluded that 128^3 is enough when working at Rm < 200, we chose to focus on larger Reynolds number for the AMR study. Moreover, the magnetic structures that arise from the dynamo are more localized at large Rm (see Fig. 4.79), making the refinement easier to implement. Nonetheless, even though the refinement strategy seem to be working qualitatively the quantitative results are inaccurate. Fig. 4.80 is a comparison between a fully refined run (left) and two different subcycling strategies (unique time-step on the center and adaptative time-step

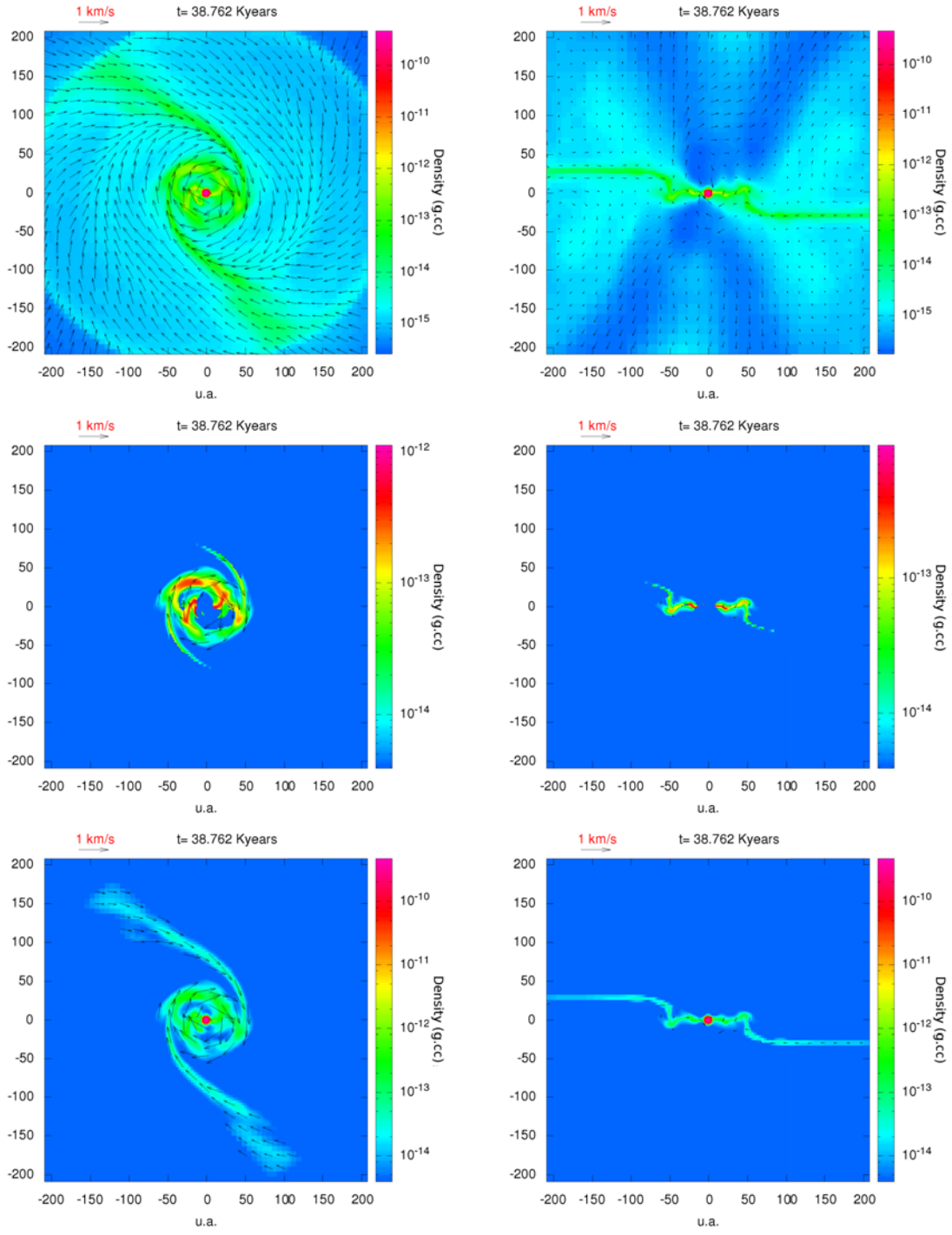

Figure 4.78: Left raw: cut along the xOy plan (perpendicular to the initial axis of solid body rotation). Right raw: cut along the xOz plan. Top: density/velocity map with no selection criteria. Middle: density/velocity map with all Joos et al. (2012) criteria (except connectivity). Bottom: density/velocity map with a density criterion used only.

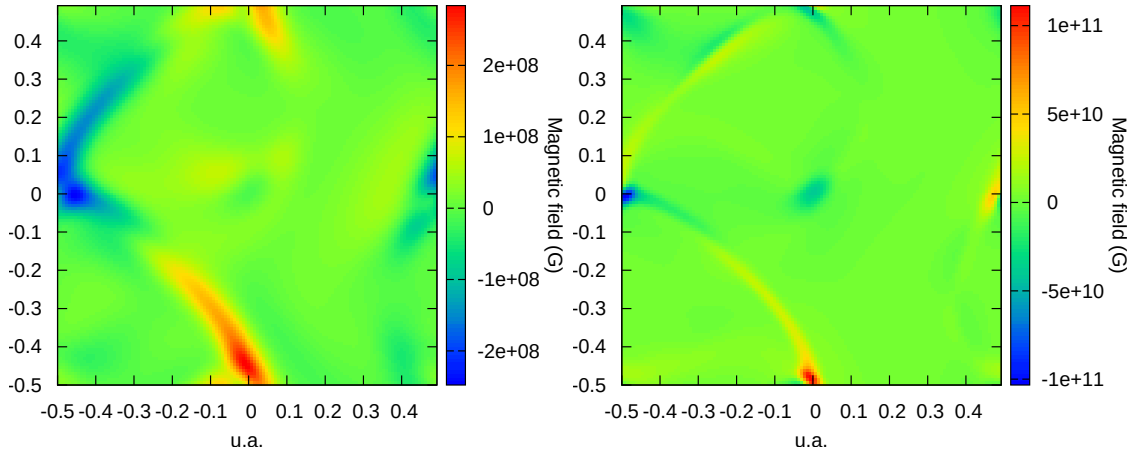

Figure 4.79: The two plots represent one component of the magnetic field in a slice in the middle of the box. Left: slice for Rm = 60. Right: slice for Rm = 400.

on the right), at different times (in arbitrary units). The growing trend of the magnetic energy is maintained, yet the growing rate differs in every case. On a more dangerous path, the imaginary part is kept to zero in the case of the unique time-step but not in the adaptive time-step, meaning that we are polluted by unwanted numerical diffusivity in that case.

4.C Resolution study

We conducted resolution tests in the most turbulent case to confirm the results, which can be seen Fig. 4.81. In this plot, we summarized the disk mass evolution for all the weakly magnetized runs. Resolution tests are represented with green crosses; we used in these tests 20 cells per Jeans length and a coarse grid with 128^3 cells. In this plot, we also retrieve the apparent steady-state in the ideal MHD case that does not significantly differs from one case to another.

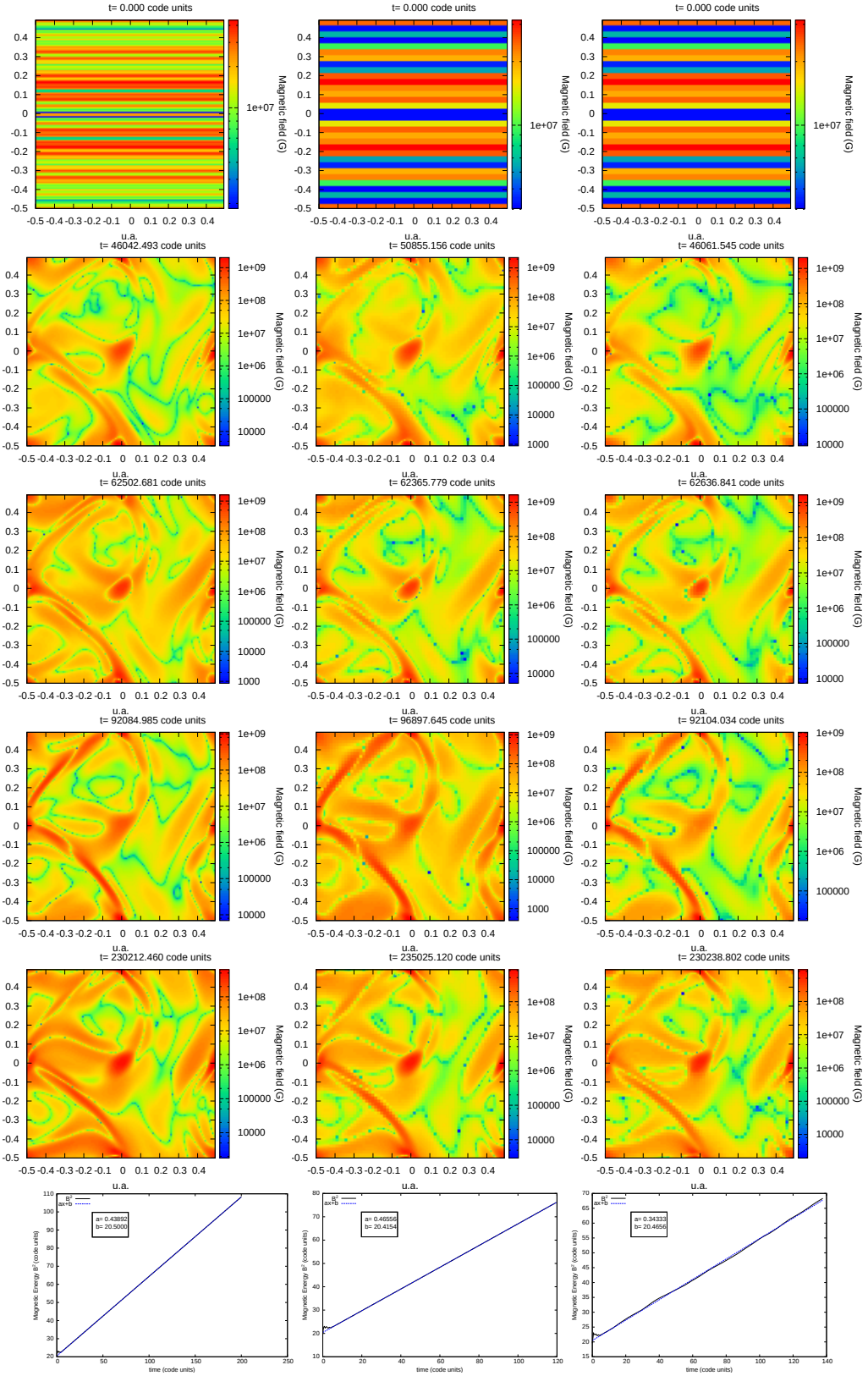

Figure 4.80: Comparison between the fully refined grid (on the left) and AMR grids with two different subcycling strategies (namely a unique time-step on the center, and an adaptive time-step on the right). The bottom plots represent the evolution of the absolute value of a given magnetic component, in log-scale, for each case.

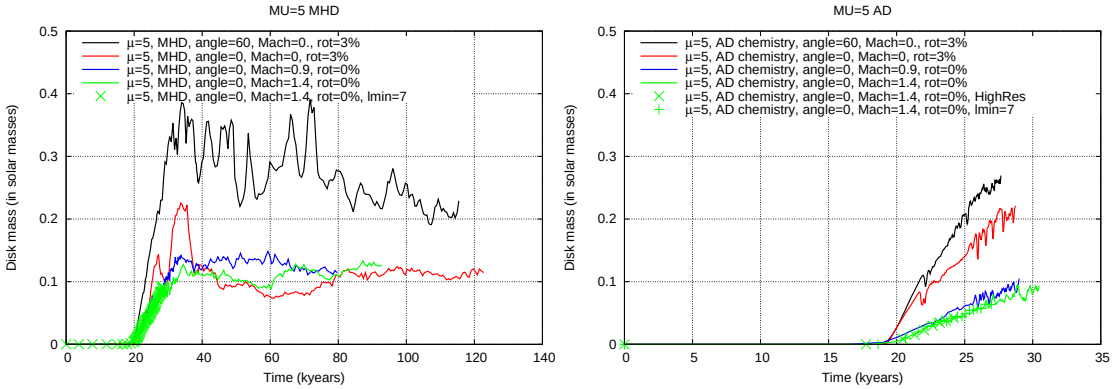

Figure 4.81: $\mu = 5$. Left: ideal MHD case. Right: AD case. Evolution of the mass of matter abiding by the criteria of Joos et al. (2012) as a function of time for all the weakly magnetized runs. The mass is in solar masses. Labels are in the plots.

Conclusion

Summary – We have first drawn a contemporary picture of low-mass stars formation studies. We showed that most of the issues are strongly connected to either angular momentum conservation or magnetic flux conservation.

In order to improve our understanding of low-mass star formation regarding these issues, we implemented in an adaptive mesh refinement code named `RAMSES` non-ideal magnetohydrodynamics. We tested the implementation thoroughly. We also refined the radiation hydrodynamics solver to allow for second core simulations.

We then added new microphysics refinements to better describe the scales at stake. A versatile non-equilibrium chemistry evolution code was developed to derive non-ideal MHD parameters. We also made use of a realistic equation of state to account for dihydrogen molecules dissociation.

We used this code with state-of-the-art physics to carry out simulations of the first Larson core formation in both an ideal and non-ideal MHD framework, including ambipolar diffusion. We find that ambipolar diffusion and turbulence are two important factors in the process of disk formation around low-mass stars. We also noticed important differences concerning the repartition of the magnetic flux, with probable consequences in the properties of the second Larson core. We also showed the improvement concerning counter-rotation when using ambipolar diffusion or turbulence.

We also performed second Larson core simulations using the same code. Because they are very time-consuming, we could not probe the space parameters nor conduct extensive comparisons between idealized and more realistic cases. We validated the method and are now ready to run long-term simulations to describe self-consistently in a very complete way low-mass star formation.

Last, we presented a side-work on kinematic ABC dynamos related to the use of ambipolar diffusion in its full form instead of approximated by a Laplacian. We showed that ambipolar diffusion does not mimic a fully diffusive behavior. We showed changes in eigenvalues and eigenvectors, and a sub-critical bifurcation at low magnetic Reynolds number, absent from the pure diffusive case.

Outlook – We now possess a highly efficient, complete and versatile numerical code to study in details all the steps of low-(and high-)mass star formation. Nevertheless, there are still many improvements that can be made to understand better and better how stars form.

First, we need to probe the space parameter to extract common features and informations. Determining the impact of both radiation and non-ideal MHD in a turbulent medium remains one of the greatest challenges of contemporary star formation studies. For example, it has been pointed out by Panoglou et al. (2009) that ambipolar diffusion may play a major role in the thermal properties of young stellar objects winds.

Second, new numerical developments can be added. First, the Hall effect term in non-ideal MHD calculations is expected to play a dominant role in particular in disks. This effect is implemented in `RAMSES` but has yet to be more extensively tested before it can be used in core-collapse calculations.

Penultimate, improving the microphysics is of great importance. The imperfect knowledge of the details of the chemical processes, of the ionization rate and of the size and growth of grains in dense core environments lead to a great and unknown uncertainty concerning for example the diffusivity coefficients. A better knowledge of the micro-models would, if not allow for a better understanding,

at least considerably constraint the space parameter to probe. Coupling the chemical evolution and ionization rate with `RAMSES` seems the only possible way to do it and is probably one of the major development to be made in the next few years.

Last, we need to interact more and more with observers. Constraining our models for a more effective parameter probing and pinpointing interesting features to observe are two mutual advantages gained by sharing different and complementary knowledge.

Version française

Résumé – Nous avons dressé le portrait contemporain de la formation des étoiles de faible masse. Nous avons montré que la plupart des problèmes sont fortement reliés aux problématiques de conservation du moment angulaire et du flux magnétique.

Pour améliorer notre compréhension de la formation des étoiles en regard de ces problématiques, nous avons implémenté dans un code à grille à maillage adaptatif (`RAMSES`) les équations de la magnétohydrodynamique non idéale. Nous avons également fait les développements nécessaires pour simuler l'effondrement du second cœur de Larson avec ce code.

Nous avons ensuite ajouté des raffinements de microphysique pour décrire de la meilleur manière possible toutes les échelles mises en jeu, grâce au développement d'un code versatile d'équilibre chimique adapté à nos études. Nous avons également utilisé une équation d'état réaliste pour décrire l'évolution thermodynamique du gaz et en particulier la dissociation du dihydrogène.

Nous avons utilisé ce code incluant une physique parmi les plus avancée au monde pour simuler l'effondrement des cœurs denses jusqu'au premier cœur de Larson, en magnétohydrodynamique idéale et non idéale. Nous avons trouvé que la diffusion ambipolaire et la turbulence sont deux facteurs importants dans la formation de disques autour des étoiles de faible masse. Nous avons également noté d'importantes différences concernant la répartition du flux magnétique au niveau du premier cœur avec de probables conséquences sur les propriétés du second cœur de Larson. Nous avons enfin montré une amélioration en ce qui concerne la contre-rotation et l'accumulation de flux lors de l'utilisation de la diffusion ambipolaire ou de la turbulence.

Nous avons également simulé des effondrements jusqu'au second cœur de Larson en utilisant le même code numérique. Ces simulations sont très gourmandes en temps de calcul, et nous n'avons pas pu explorer l'espace de paramètres de manière extensive ni comparer les résultats en magnétohydrodynamique idéale et non idéale. Cependant, nous avons validé la méthode et nous sommes maintenant prêts à simuler des effondrements jusqu'à la formation de la protoétoile de manière complète et cohérente.

Enfin, nous avons présenté un travail parallèle sur la dynamo cinématique ABC qui utilise la forme complète vectorielle de la diffusion ambipolaire plutôt qu'une approximation avec un Laplacien. Nous avons ainsi montré que la diffusion ambipolaire ne peut pas être assimilée à un processus parfaitement diffusif. Nous avons mis en évidence des différences dans les valeurs propres et vecteurs propres, ainsi qu'une bifurcation à faible nombre de Reynolds magnétique qui était absente dans le cas purement diffusif.

Perspectives – Nous possédons maintenant un code numérique hautement versatile et efficace pour simuler en détails toutes les étapes de la formation des étoiles. Cependant, il reste encore de nombreuses améliorations possibles pour mieux comprendre comment les étoiles se forment.

Tout d'abord, il faut explorer l'espace des paramètres pour extraire d'avantage d'informations. Un des grands défis de la formation des étoiles à l'heure actuelle est de comprendre précisément l'impact du transfert radiatif couplé à la magnétohydrodynamique non idéale dans un cœur dense turbulent. Par exemple, il a été mis en évidence par Panoglou et al. (2009) que la diffusion ambipolaire a une grande importance sur les propriétés thermodynamiques dans les vents et jets des protoétoiles.

Deuxièmement, de nouveaux développements numériques sont également possibles. Tout d'abord, l'effet Hall qui est un des termes de la magnétohydrodynamique non idéale, est supposé jouer un rôle dominant en particulier pour la formation et l'évolution des disques. Cet effet est implémenté dans `RAMSES` mais n'a pas encore été utilisé ni testé de manière complète dans des simulations d'effondrement de cœur dense.

Ensuite, améliorer le traitement de la microphysique est d'une grande importance. La connaissance imparfaite des processus chimiques mis en jeu, du taux d'ionisation et de la taille ou de la

forme des grains de poussière dans les environnements des cœurs denses mène à de grandes incertitudes par exemple pour ce qui est des cœfficients de diffusion de la MHD non idéale. Une meilleure connaissance de ces modèles sous-maille, si elle n'apporte pas directement de nouveaux éléments de compréhension, permettrait de mieux délimiter la zone de l'espace des paramètres à explorer. Le développement de cette branche pourrait être de coupler au code `RAMSES` le réseau d'évolution chimique et du taux d'ionisation pour une description encore plus cohérente de la formation des cœurs denses.

Enfin, il nous faut interagir de plus en plus avec les observateurs. Contraindre nos modèles théoriques, se focaliser sur les propriétés intéressantes et visibles dans les observations ainsi que créer des observations synthétiques sont des exemples d'avantages mutuels obtenus en partageant des points de vue et des connaissances différents mais complémentaires.

Appendix A

Simulations of protostellar collapse using multigroup radiation hydrodynamics

We present in this appendix work done with N. Vaytet and others where we study the influence of multigroup radiation transfer on core collapsing clouds with a 1D code named `Heracles`. This study has been carried out on two steps corresponding to the two cores.

A.1 The first collapse

This work have been accepted for publication in A&A. It focuses on the first protostellar core.

A.2 The second collapse

This work have been submitted in A&A. It focuses on the second protostellar core.

Appendix B

Riemann solver from scratch

B.1 Exact Riemann problem: hydrodynamics equations through a shock

B.1.1 Conservative formulation

The one dimensional (assumed to be Ox) hydrodynamics equations in their conservative form are:

$$\frac{\partial \rho}{\partial t} + \frac{\partial \rho v}{\partial t} = 0 \tag{B.1}$$

$$\frac{\partial \rho v}{\partial t} + \frac{\partial \rho v^2 - p}{\partial x} = 0 \tag{B.2}$$

$$\frac{\partial E}{\partial t} + \frac{\partial v(E+p)}{\partial x} = 0 \tag{B.3}$$

Yielding in vector form:

$$U_t + (F(U))_x = 0 \quad \text{with} \quad U_t = \begin{cases} \rho \\ \rho v \\ E \end{cases} \quad \text{and} \quad F = \begin{cases} \rho v \\ \rho v^2 + p \\ v(E+p) \end{cases} \tag{B.4}$$

With the internal energy and soundspeed being expressed with γ the specific heat ratio:

$$e = \frac{p}{(\gamma - 1)\rho} \quad \text{and} \quad C_s = \sqrt{\frac{\gamma p}{\rho}}$$

Using the Jacobian expression of F, it is rewritten as:

$$U_t + \frac{\partial F}{\partial U} \cdot U_x = 0 \quad \text{avec} \quad \frac{\partial F}{\partial U} = \text{Jac}(F) = \left(\frac{\partial f_i}{\partial u_j} \right)_{ij} \tag{B.5}$$

This equation B.5 along with initial conditions such as

$$U(x,0) = U_0(x) = \begin{pmatrix} W_L & \text{si} & x < 0 \\ W_R & \text{si} & x > 0 \end{pmatrix}$$

is called the one dimensional Riemann problem: it consists in solving the set of equations through a shock with particular initial conditions.

We need only to find the complete expression of Jac(F) and to diagonalize it. Using the conservative formulation presented above, we can express F using U:

$$\left\{ \begin{array}{l} f_1 = u_2 \\ f_2 = (\gamma-1)u_3 - \frac{u_2^2}{u_1} \cdot \frac{\gamma-3}{2} \\ f_3 = \frac{\gamma u_3 u_2}{u_1} - \frac{\gamma-1}{2} \cdot \frac{u_2^3}{u_1^2} \end{array} \right. \tag{B.6}$$

and then, a being the thermal soundspeed, we find Jac(F):

$$\left(\begin{array}{ccc} 0 & 1 & 0 \\ \frac{v^2(\gamma-3)}{2} & (3-\gamma)v & \gamma-1 \\ \frac{(\gamma-2)u^3}{2} - \frac{a^2 u}{\gamma-1} & \frac{3-2\gamma}{2}u^2 + \frac{a^2}{\gamma-1} & \gamma v \end{array} \right) \tag{B.7}$$

Eigen values ($\lambda_{[1,2,3]}$) and eigen vectors ($\mathbf{K_{[1,2,3]}}$) are then obtained directly (or can be computed numerically in complicated cases):

$$\left(\begin{array}{l} \lambda_1 = u-a \\ \lambda_2 = u \\ \lambda_3 = u+a \end{array} \right) \quad \text{et} \quad \mathbf{K_1} = \left(\begin{array}{c} 1 \\ u-a \\ H-ua \end{array} \right) \mathbf{K_2} = \left(\begin{array}{c} 1 \\ u \\ \frac{1}{2}u^2 \end{array} \right) \mathbf{K_3} = \left(\begin{array}{c} 1 \\ u+a \\ H+ua \end{array} \right)$$

with $H = \frac{1}{2}v^2 + e + \frac{P}{\rho}$ the enthalpy.

B.1.2 Resolution of the Riemann problem

Each eigen value is linked to a wave propagating from the discontinuity (the shock). One common way to represent this is in a (t, x) diagram, where straight lines emerge from the discontinuity and represent one wave, at a given speed, in a given direction. This allows the definition of several zones separated by the lines (three in this case).

Depending on the problem studied, one can infer some properties for the waves. In our simple case, the central wave will always be a contact wave with constant pressure and speed in the two adjacent zones (labelled $\star$).

In the left and right zones, we can find either rarefaction waves or shock waves. Physical properties differ from one case to another, and detailed studies have to be conducted for every new setup. In the case studied here, we chose arbitrarily to put a rarefaction wave on the left and a shock wave on the right (see Fig. B.1).

$$p_\star = \text{cste} \quad \text{and} \quad v_\star = \text{cste}$$

To solve this problem, we need to determine the pressure $p_\star$ in the central zone and to deduce from it every other physical quantity. In order to do so, we have to solve an equation such as $f(p, , W_L, W_R) = 0$ where $f = f_L(p, W_L) + f_R(p, W_R) + u_R - u_L$, subscripts R and L standing for *Left* and *Right*. The detailed expression for f_L and f_R is problem dependant. Again, in our case,

$$f_K = \left\{ \begin{array}{ll} (p - p_K)\left[\frac{A_K}{p+B_K}\right]^{\frac{1}{2}} & \text{if} \, p > p_K \, \text{(shock wave)} \\ \frac{2a_K}{\gamma-1}\left[\left(\frac{p}{p_K}\right)^{\frac{\gamma-1}{2\gamma}} - 1\right] & \text{if} \, p \leq p_K \, \text{(rarefaction wave)} \end{array} \right. \tag{B.8}$$

with the thermal soundspeed a_K and

$$\left\{ \begin{array}{l} A_K = \frac{2}{(\gamma+1)\rho_K} \\ B_K = \frac{\gamma-1}{\gamma+1} P_K \end{array} \right.$$

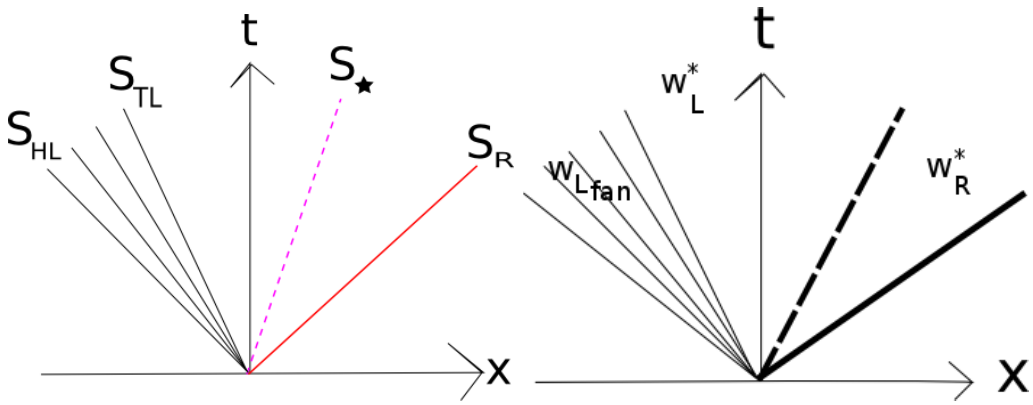

Figure B.1: left: the three propagating waves, represented in (t, x) diagram. Right: the various zones defined by the waves.

As in this case we have an analytical expression for f, we choose to solve for $f(p) = 0$ using Newton's method. A tricky step is to find a raw but precise enough estimate for $p_\star$. There are several strategies, and we chose to follow the method explained in Toro (2009):

$$P_{TR} = \frac{a_L + a_R - \frac{1}{2}(\gamma - 1)(u_R - U_L)}{a_L \left(p_L^{\frac{1-\gamma}{2\gamma}}\right) + a_R \left(p_R^{\frac{1-\gamma}{2\gamma}}\right)} \tag{B.9}$$

Then, we iterate until wanted precision is achieved as

$$p_k = p_{k-1} - \frac{f(p_{k-1})}{f'(p_{k-1})} \tag{B.10}$$

using the following criteria to stop the calculation:

$$|p_k - p_{k-1}| < 10^{-6} \frac{p_k + p_{k-1}}{2} \tag{B.11}$$

One must also keep in mind that we are doing physics, which means that for instance we must have $p > 0$. This leads to the necessary condition $f(p = 0) < 0$ because f is monotonically increasing. Finally we get:

$$(\Delta u)_{critique} = \frac{2a_L}{\gamma - 1} + \frac{2a_R}{\gamma - 1} > u_R - u_L$$

If $p < 0$, there is void creation and the resolution method will differ from the one presented (the problem setup will be entirely different !).

B.1.3 End of the resolution

One $p_\star$ has been calculated, we can deduce all other quantitys from it: $u_\star = \frac{1}{2}(u_L + u_R) + \frac{1}{2}(f_R - f_L)$.

With the following initial conditions

$$\begin{array}{ll} \rho_L = 1.0 & \rho_R = 0.125 \\ p_L = 1.0 & p_R = 0.1 \\ u_L = 0.0 & u_R = 0.0 \end{array}$$

we find $p_\star = 0.303$ which corresponds indeed to a rarefaction wave on the left and a shock wave on the right ($p_\star > p_R$ and $p_\star \leq p_L$). Using the properties of the waves, we finally deduce all other quantities in all the regions: $W_{L_{fan}}$, $W_L^\star$ et $W_R^\star$.

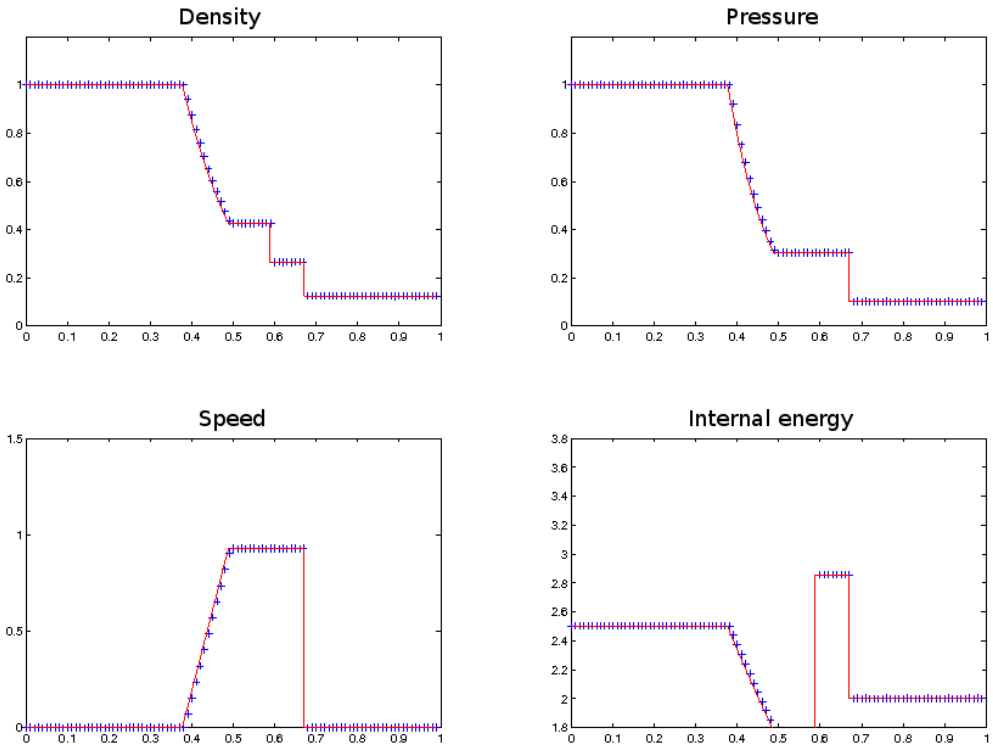

Figure B.2: Resolution exact of the 1D Riemann problem (blue crosses). The analytical solution is given by the red full line. Initial discontinuity is centered at 0.5, the units being code units.

$$W_{L_{fan}} = \begin{cases} \rho = \rho_L \left[\frac{2}{\gamma+1} + \frac{\gamma-1}{(\gamma+1)a_L}(u_L - \frac{x}{t})\right]^{\frac{2\gamma}{\gamma-1}} \\ u = \frac{2}{\gamma+1}\left[a_L + \frac{\gamma-1}{2}u_L + \frac{x}{t}\right] \\ P = P_L \left[\frac{2}{\gamma+1} + \frac{\gamma-1}{(\gamma+1)a_L}(u_L - \frac{x}{t})\right]^{\frac{2\gamma}{\gamma-1}} \end{cases}$$

$$W_L^\star = \begin{cases} \rho = \rho_L \left(\frac{P_\star}{P_L}\right)^{\frac{1}{\gamma}} \\ u = u_\star \\ P = P_\star \end{cases}$$

$$W_R^\star = \begin{cases} \rho = \rho_R \left[\frac{\frac{P_\star}{P_R} + \frac{\gamma-1}{\gamma+1}}{\frac{(\gamma-1)P_\star}{(\gamma+1)P_R} + 1}\right] \\ u = u_\star \\ P = P_\star \end{cases}$$

The last step consists in evaluating the speed of the waves, in order to derive the time-dependant solution for all the physical variables. We have here (again, it is problem dependant): $S_{HL} = u_L - a_L$, $S_{TL} = u_\star - a_\star$, $S_\star = u_\star$ and $S_R = u_R + a_R\left[\frac{(\gamma+1)P_\star}{2\gamma P_R} + \frac{\gamma-1}{2\gamma}\right]$, with the waves as in Fig. B.1 on the left.

Results of this derivation are presented Fig. B.2. The resolution is working !

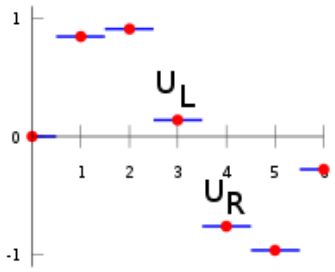

Figure B.3: Variables for each cells are given throught averaging quantities in the cell, and the value is located in the center of the cell. Between two adjacent cells, there is a local Riemann problem.

B.2 Usefulness of the method, and refinements

B.2.1 Godunov's method

Godunov's method is a finite difference method. We seek to solve an equation of the form $u_t + f(x)_x = 0$. In terms of finite differences, it reads

$$u_i^{n+1} = u_i^n + \frac{\Delta t}{\Delta x}(f_{i-\frac{1}{2}} - f_{i+\frac{1}{2}}) \tag{B.12}$$

where the superscripts stand for time and subscript for space discretization. f_i is the flux of the various variables between two adjacent cells.

In this method, the inter-cells fluxes are computed solving local Riemann problems. One key assumption here is that every variable is piecewise constant (constant in a given cell: see Fig. B.3). We then have to solve for each Riemann problem, with various initial conditions consisting simply in the value of the variables in the two adjacent cells. Fluxes are computed using the right zone (the zone which will advect the quantities through the interface), as represented more clearly Fig. B.4, instead of using a combination of every wave as in the exact method presented § B.1.

When differentiating the equation, one have to abide by some rules: the Courant condition in this case. It can be interpreted either as a mathematical condition on the exponential growth of the variables or as a physical phenomena: in an explicit resolution causality must hold, thus the fastest wave at the interface can't be allowed to reach the other side in a single time-step. The first approach can be generalized to more complicated problems and sets of equation, but the second approach yield more physical sense. We end up with:

$$\Delta t < \frac{\Delta x}{S_{max}^n} \tag{B.13}$$

where S_{max}^n is the speed of the fastest wave for the local Riemann problem.

One of the main advantage of this method is what is called constraint transport. It is particularly important in the framework of MHD, where the divergence free constraint ($\boldsymbol{\nabla} \cdot \mathbf{B} = 0$) is to be preserved. In a nutshell it means that everything that enters cell comes from surrounding cells (which can be understood mathematically with equation B.12). Solving the Riemann problem exactly as presented § B.1 or using approximate fluxes may change the final results, but the constraint transport property holds in both cases.

B.2.2 Approximate resolution of a Riemann problem

We saw how to solve the one dimensional Riemann problem exactly for Euler's equation, but it is usually much more complicated. For instance, if magnetohydronynamics equations are added, there

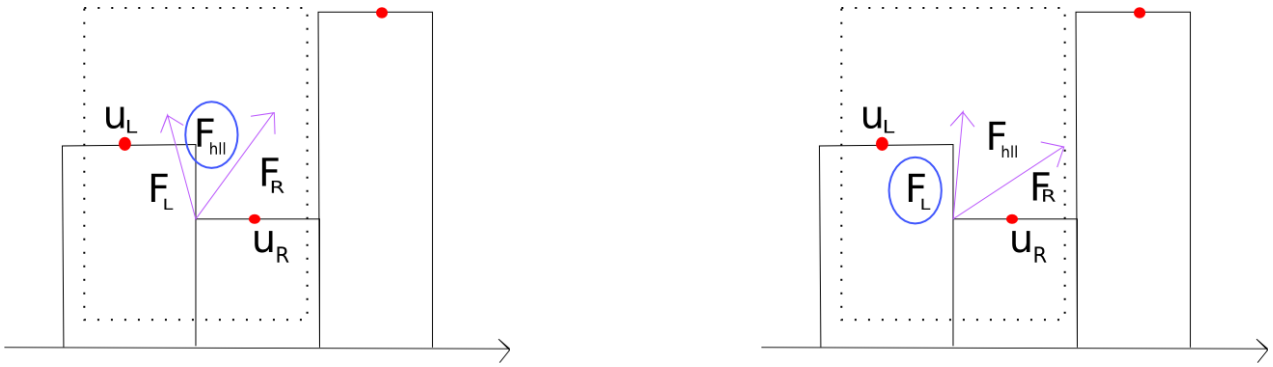

Figure B.4: Left: the advection flux is F_{hll}. Right: we have to use F_L.

are new waves to add and a bigger matrix to diagonalize, and last but not least finding the correct initial values or solving for the speed of the waves is not trivial. In order to keep the computational cost reasonable, approximate method have been developed. They are based on fewer, well-chosen waves which will mimic the real advection. It is already clear that depending on the physical setup, different approximations will be necessary. We will describe quickly some of these methods, and encourage the reader to read Toro (2009) for many more details.

HLL : Harten, Lax and van Leer Riemann Solver

This is one of the simplest method, which is based on only two waves which have a given speed. Using an integral form for the conservation laws gives an approximate expression for the fluxes at the interface. Using only two waves with given speed allows for very efficient calculations, but comes with hindrances such as bad resolution of the interfaces (between two different fluids for example). In order to improve a little the accuracy, a third wave (still with a given speed) can be added. The general idea remains exactly the same for these approximate solvers or for the exact one: find the zone which will participate to the advection, and determine the correct (or approximate) speed at which quantities are advected. The more waves, and the more precise their speed, the more accurate the solver.

Results obtained for the same setup as in Fig. B.2 are presented Fig. B.5. In this case we solved the Riemann problem exactly (red), with the HLL solver (green) and with another solver called HLLC which uses three waves instead of two (blue).

B.2.3 In RAMSES: HLLD

For MHD calculations, Alfvén waves along with slow and fast magnetosonic waves should be taken into account for an exact Riemann solver. Going on with the idea of using approximate waves with given speeds, a solver called HLLD, which uses two Alfvén waves and a contact wave in between.

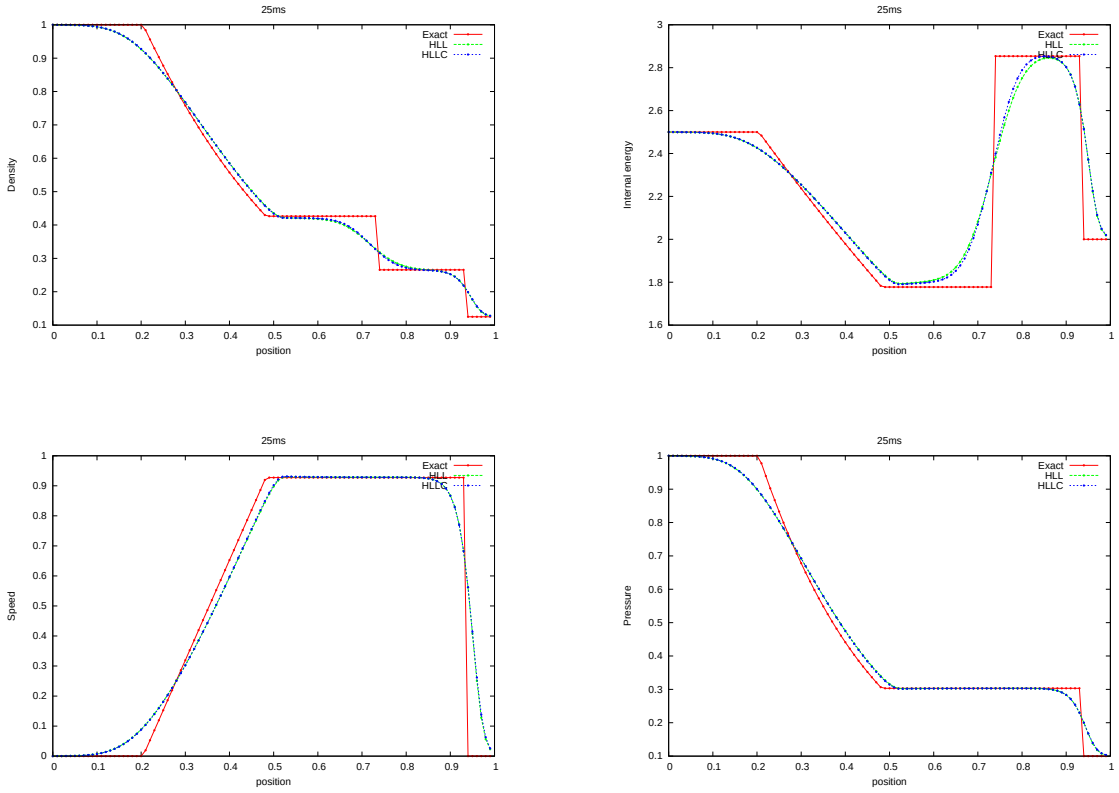

Figure B.5: Riemann problem (Sod test) solved exactly (red), with HLL (green) and with HLLC (blue).

Appendix C

A semi-analytical study of the Kelvin-Helmoltz instability in disks

C.1 Introduction

C.1.1 General context

This project takes place in the general framework of planets formation, and more precisely focus in the growth of grains at the dust-rich midplane in protoplanetary disks. There are many scales, and many physical processus at stake in the context of growing grains : from the tiny scales (sub-mm) where chemical bonds and sticking play a major role, to the biggest scales (km to planet-size) which is the domain of gravity. In the intermediate scale (from cm to m or km) sticking is not efficient anymore, and even though the gravity of individual grains is negligible, it is reasonable to try to focus on collective gravitational processes to form bigger grains.

There are two threshold to cross in order for the gravitational instability to occur in a protoplanetary disk. First, an incompressible fluid at a distance r from a star of mass $M_\star$ can resist the tidal disruption from a star if its density is greater than the Roche value : $\rho \geq \rho_{Roche} = 3.5\frac{M_\star}{r^3}$. This density is 2 to 3 orders of magnitude greater than typical densities in protoplanetary disks, but there is an even more stringent condition for the gravitational instability to occur: the Toomre criteria. The Toomre parameter is a good indication on whether the gravitational instability can occur. It reads:

$$Q = \frac{c\Omega}{\pi G\Sigma} \tag{C.1}$$

If $Q < 1$, the collapse can occur ! Translated in density values, it gives:

$$\rho_Q \geq 10^{-7}(\frac{r}{a.u.})^{-3}\, g.cm^{-3} \tag{C.2}$$

$$\rho_{disk} \simeq 2.7 \times 10^{-9}(\frac{r}{a.u.})^{-\frac{39}{14}}\, g.cm^{-3} \tag{C.3}$$

Is there any means to reach such high densities ? Figure C.1 summarizes four mechanisms helping to get denser and denser densities. The tidal gravity perpendicular to the disk enable the settling of dust particles on the equatorial plane (a). The radiation from the star can increase the relative density of the dusty layer compared to the gas (b). It can then be even more concentrated trhough radial pileup due to the radial Keplerian shear (c), and streaming or drag instabilities (d). Safronov and Zvjagina (1969) and **?** studied these phenomena and concluded that densities *approaching* the density threshold could be attained thanks to these processes (*approaching* meaning still a factor 10 to 20 to go).

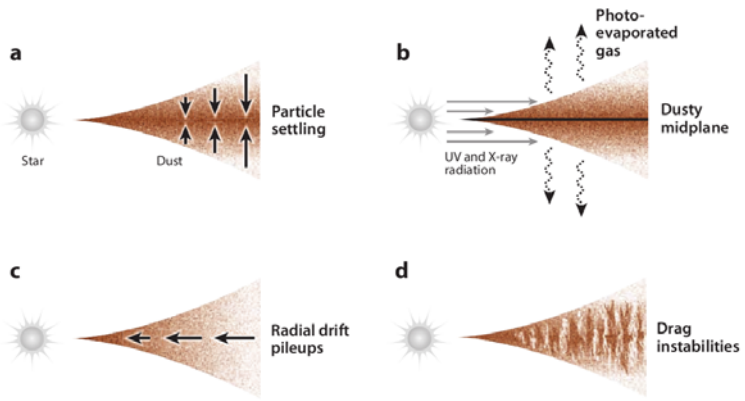

Figure C.1: Four mechanisms for metal enrichment, none of which involving self-gravity (from Chiang and Youdin (2010)).

Nevertheless, and as pointed out after by Weidenschilling (1980), as the dust settles in a thiner and thiner (and denser and denser) layer, at some point the turbulence and/or the Kelvin-Helmholtz instability will destroy this layer, and as a consequence make it impossible to reach the density threshold presented in equation (C.2). An insight of what is the Kelvin-Helmholtz instability can be found in the .1.

One can ask if this physical and qualitative insight has any physical meaning. In other words, at which point the layer becomes unstable, and if it's before it's thin enough to reach the previously highlighted density thresholds. In order to tackle this point, let's rewrite these two conditions in terms of height of the layers. Be H_g the total (half-)height of the gas, and z_d the (half-)thickness of the dust. The two conditions reads:

$$(\frac{z_d}{H_g})_{Q<1} \leq 10^{-4}(\frac{r}{a.u.})^{\frac{3}{14}} \tag{C.4}$$

$$(\frac{z_d}{H_g})_{\text{KHI stable}} \geq 10^{-2}(\frac{r}{a.u.})^{\frac{2}{7}} \tag{C.5}$$

Thus, the layer should become KH instable two orders of magnitude before it can collapse under the action of the collective gravity.

C.1.2 Dust and gas

The differential rotation in the vertical direction arises because the dusty layer rotates at a different speed than the dust-free layer.

The dust-free layer (gas layer) revolves slightly slower than the Kepler velocity, because the pressure gradient in the radial direction supports the gas.

On the other hand, the dust particles don't feel this pressure support, and are assumed to rotate at the full Kepler velocity. Then, provided their stopping time[1] is small enough, they are well coupled to the fluid and *drag* the layer (dust + gas), which then revolves as a whole. The velocity is given by:

$$\Omega = \Omega_K(1 - \frac{\rho_g}{\rho_0}\eta) \tag{C.6}$$

[1]The stopping time τ_s is one key parameter in the study of the growth of grains. It varies according to the size of the grains, and the radius, because different physical processes can dominate (Epstein regime, Stokes regime, etc.). A detailed study can be found in Youdin (2008).

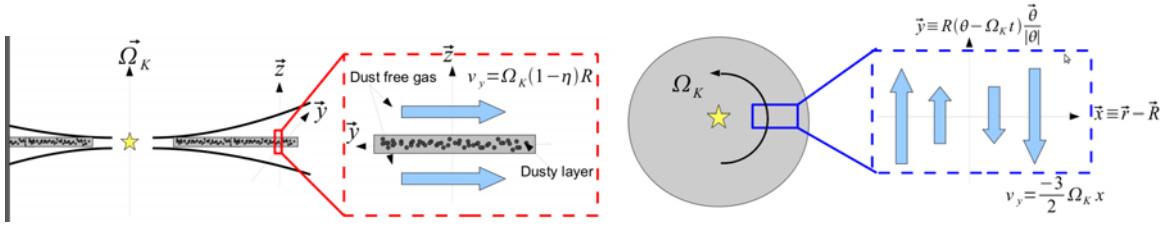

Figure C.2: The local Cartesian coordinates system.

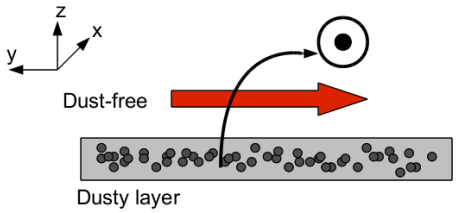

Figure C.3: The action of the Coriolis force in the KHI context.

The non dimensional parameter η is a measure of centrifugal support by pressure:

$$\eta = \frac{-1}{2\rho_g \Omega_K^2 r} \frac{\partial P}{\partial r} \tag{C.7}$$

C.1.3 The KHI in rotating disks

The picture drawn in the previous section is very general, but one has to take into account some refinements on order to try and answer to the problem. The main point is that the problem is not two dimensional, and the Coriolis force as well as the radial Keplerian shear play a critical role.

The local Cartesian coordinate system of interest is illustrated figure C.2. It is a frame whose origin is at a radius R, and comoving at the local Keplerian speed around the star (eg. coupled with the dusty layer):

$$\mathbf{x} = \mathbf{r} - \mathbf{R} \tag{C.8}$$

$$\mathbf{y} = R[\Phi - \Omega t]\frac{\mathbf{\Phi}}{\Phi} \tag{C.9}$$

$$\mathbf{z} = \mathbf{z} \tag{C.10}$$

with $\mathbf{r}$, $\mathbf{\Phi}$ and $\mathbf{z}$ the usual cylindrical coordinates.

In this context of the KHI in a rotating frame, the Coriolis force become one central physical process. Indeed, and as pictured figure C.3, it converts azimuthal motions excited by the KHI (the solid arrow in figure C.3) to radial motions (the inward vector in the same figure). Then, the radial shear dissipates the non-axisymetric motions excited by the KHI by stretching them azimuthally (this is the qualitative picture, as the Keplerian shear rate is at least of the order of the Brunt-Väisälä frequency $|\frac{\partial \Omega_K}{\partial \ln r}| \gtrsim \omega_b$).

As a consequence, the conclusion to draw from this is that the Richardson number, though relevant in two dimensional common KHI, doesn't take into account all the physics at stake in the

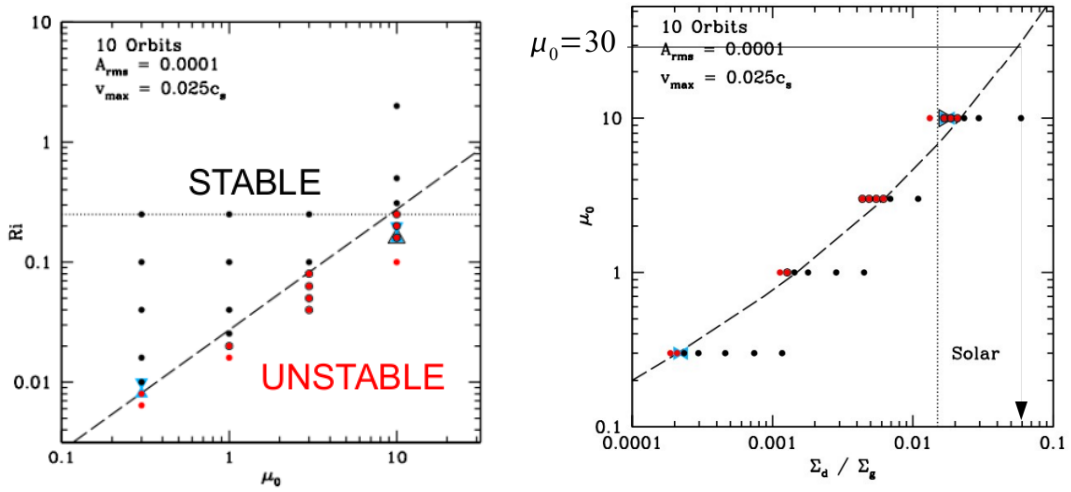

Figure C.4: Several simulations (represented by black or red dots) of a 3D shearing box with Coriolis forces and tidal shear. Black dots correspond to stable runs, whereas red dots correspond to unstable runs. Left: Richardson number as a function of the metallicity, the dotted line correspond to a fit of the marginally stable runs. Dotted line corresponds to $Ri = \frac{1}{4}$. Right: Same data, in a different parameter space, say metallicity in function of the bulk (height-integrated) dust-to-gas ratio. The dotted line corresponds to the solar bulk metallicity. These figures have been taken from Lee et al. (2010), see their paper for a more precise explanation of the making off.

problem of growing grains through the Gravitational instability in dusty layers in protoplanetary disks. Thus, we shouldn't use the value of $Ri = \frac{1}{4}$ blindly.

This has been seen in simulations from Lee et al. (2010) that the correct criteria for marginal stability is not a constant Richardson number, but depends linearly on μ_0, the midplane dust to gas ratio.

$$\mu_0 = \frac{\rho_{dust}(0)}{\rho_{gas}} \tag{C.11}$$

This is represented figure C.4, and is the very motivation for this project: can we explain this behavior through a semi-analytical model based on basic hydrodynamics.

C.1.4 Further motivation

The dependence of the stability on such parameters as the Richardson number and the metallicity (or equivalentlye, the dependence of the Richardson number on the metallicity for marginal stability), is very important in the context of planetesimal growth.

Indeed, according to equations (C.2) and (C.3), we need to achieve a density about 35 times greater than the mean disk density to trigger gravitational collapse.

$$\frac{\rho}{\rho_g} \gtrsim 35 \left(\frac{r}{a.u.}\right)^{\frac{-3}{14}} \tag{C.12}$$

In the relevant parameter space, it means $\mu_0 \gtrsim 35$, and this is drawn on figure C.4 on the right extrapolating the linear relation between the Richardson number and μ_0 to higher metallicities. This leads to the bulk metallicity:

$$\frac{\Sigma_d}{\Sigma_g} \simeq 4 \times \left(\frac{\Sigma_d}{\Sigma_g}\right)_{\text{solar}} \tag{C.13}$$

C.2 Method

C.2.1 Physically driven approximations

This semi-analytical study is based on the work done by Ishitsu and Sekiya (2003), who have performed a three-dimensional linear perturbation analysis in the context of protoplanetary disks.

We use the previously described local Cartesian coordinate system at a radius R (see figure C.2), rotating around the central star with the Kepler angular frequency Ω_K:

$$\mathbf{x} = \mathbf{r} - \mathbf{R} \tag{C.14}$$

$$\mathbf{y} = R[\Phi - \Omega t]\frac{\mathbf{\Phi}}{\Phi} \tag{C.15}$$

$$\mathbf{z} = \mathbf{z} \tag{C.16}$$

We neglect self-gravity, but not the gravity of the central star, which leads to a radial force (competition between gravity of the star and the centrifugal force) and a vertical force (due to the vertical tidal gravity : $\Omega_K^2 z$.

We treat the dusty layer and the dust-free layer as a single (incompressible) fluid with different densities, respectively $\rho_d(z)$ and ρ_g.

This enables us to write the equations of hydrodynamics:

$$\nabla \cdot \mathbf{v} = 0 \tag{C.17}$$

$$\frac{\partial \rho}{\partial t} + \mathbf{v} \cdot \nabla \rho = 0 \tag{C.18}$$

$$\frac{\partial \mathbf{v}}{\partial t} + (\mathbf{v} \cdot \nabla)\mathbf{v} = -\frac{1}{\rho}\nabla P - 2\Omega_K \times \mathbf{v} - \Omega_K^2 \mathbf{z} + 3\Omega_K^2 \mathbf{x} \tag{C.19}$$

In order to eliminate the Keplerian part of the velocity ($v_K = -\frac{3}{2}\Omega_K x$), we introduce the drift velocity relative to the Keplerian velocity:

$$\bar{v} = v - v_K \tag{C.20}$$

C.2.2 Steady state

As we want to do a linear perturbation analysis, we have to define the steady state.

We thus assume an unperturbed state steady and uniform in x and y directions:

$$\frac{\partial}{\partial t} = \frac{\partial}{\partial x} = \frac{\partial}{\partial y} = 0 \tag{C.21}$$

We assume an unperturbed velocity in the azimuthal direction (y direction in the local coordinate system):

$$u_0 = w_0 = 0 \tag{C.22}$$

We then have from equations (C.17), (C.18) and (C.19):

$$\frac{1}{\rho_0}\frac{\partial P_0}{\partial x} = 2\Omega_K \bar{v_0} \tag{C.23}$$

$$\frac{1}{\rho_0}\frac{\partial P_0}{\partial z} = -\Omega_k^2 z \tag{C.24}$$

Given an initial density background $\rho_0(z) = \rho_d + \rho_g$, and η, we calculate the azimuthal velocity:

$$\bar{v_0} = -\frac{\rho_g}{\rho_0}\eta r \Omega_k \tag{C.25}$$

C.2.3 Linearization

We now linearize the equations (C.17), (C.18) and (C.19). In order to perform the Fourier transform in y and x we introduce the shearing coordinate $y' = y + \frac{3}{2}\Omega_K x t$ (same idea as previously with $\bar{v}$). We assume that perturbed quantities (velocities, density and pressure) are written:

$$\tilde{f}_1(x, y, z, t) = f_1(z, t) e^{i(k_y y' + k_x x)} \tag{C.26}$$

where $f_1(z, t)$ is a complex function of z and t.

The equations now read, with $k'_x = k_x + \frac{3}{2} k_y \Omega_K t$:

$$ik'_x u_1 + ik_y v_1 + \frac{\partial w_1}{\partial z} = 0 \tag{C.27}$$

$$\frac{\partial \rho_1}{\partial t} + ik_y \bar{v_0} \rho_1 = 0 \tag{C.28}$$

$$\frac{\partial u_1}{\partial t} + ik_y \bar{v_0} u_1 = -ik'_x \frac{P_1}{\rho_0} + 2\Omega_K \frac{\bar{v_0}}{\rho_0} \rho_1 + 2\Omega_K v_1 \tag{C.29}$$

$$\frac{\partial v_1}{\partial t} + ik_y \bar{v_0} v_1 = -ik_y \frac{P_1}{\rho_0} - \frac{d\bar{v_0}}{dz} w_1 + \frac{1}{2}\Omega_K u_1 \tag{C.30}$$

$$\frac{\partial w_1}{\partial t} + ik_y \bar{v_0} w_1 = \frac{-1}{\rho_0} \frac{\partial P_1}{\partial z} - \frac{\Omega_k^2 z}{\rho_0} \rho_1 \tag{C.31}$$

C.2.4 Boundary conditions

We consider solid-wall boundary condition at $z = 0$ (equatorial plane) and $z = z_0$ (the end of the box). We choose z_0 large enough so that the modes decay sufficiently when reaching this boundary (in practice, twice the height of the dusty layer seems to be enough). Thus, we have:

$$w_1 = 0 \quad \text{at } z = 0 \text{ and } z = z_0 \tag{C.32}$$

$$\frac{\partial P_1}{\partial z} + \Omega_K^2 z \rho_1 = 0 \quad \text{at } z = 0 \text{ and } z = z_0 \tag{C.33}$$

$$\frac{\partial \rho_1}{\partial t} + ik_y \bar{v_0} \rho_1 = 0 \quad \text{at } z = 0 \text{ and } z = z_0 \tag{C.34}$$

Adding another condition such as $\rho_1 = 0$ at $z = 0$ and $z = z_0$ for simplicity gives the final set:

$$\rho_1 = 0 \tag{C.35}$$

$$\frac{\partial P_1}{\partial z} = 0 \quad \text{at } z = 0 \text{ and } z = z_0 \tag{C.36}$$

C.2.5 Initial density background

The density profile we use is the same Lee et al. (2010) used for their simulations. It has been derived by Sekiya (1998), based on the basic assumption of a constant Richardson number in the dust layer. Other profiles can be used (such as the one used in Ishitsu and Sekiya (2003)), for example to compare and test our solutions.

The conditions $Ri = \text{constant}$, $\frac{\partial \rho_g}{\partial z} << \frac{\partial \rho_d}{\partial z}$ and $g = -\Omega_K^2 z$ yield:

$$\rho_0 = \left[\frac{1}{\left(\frac{1}{1+\mu_0}\right)^2 + \left(\frac{z}{z_d}\right)^2} \right]^{\frac{1}{2}} \tag{C.37}$$

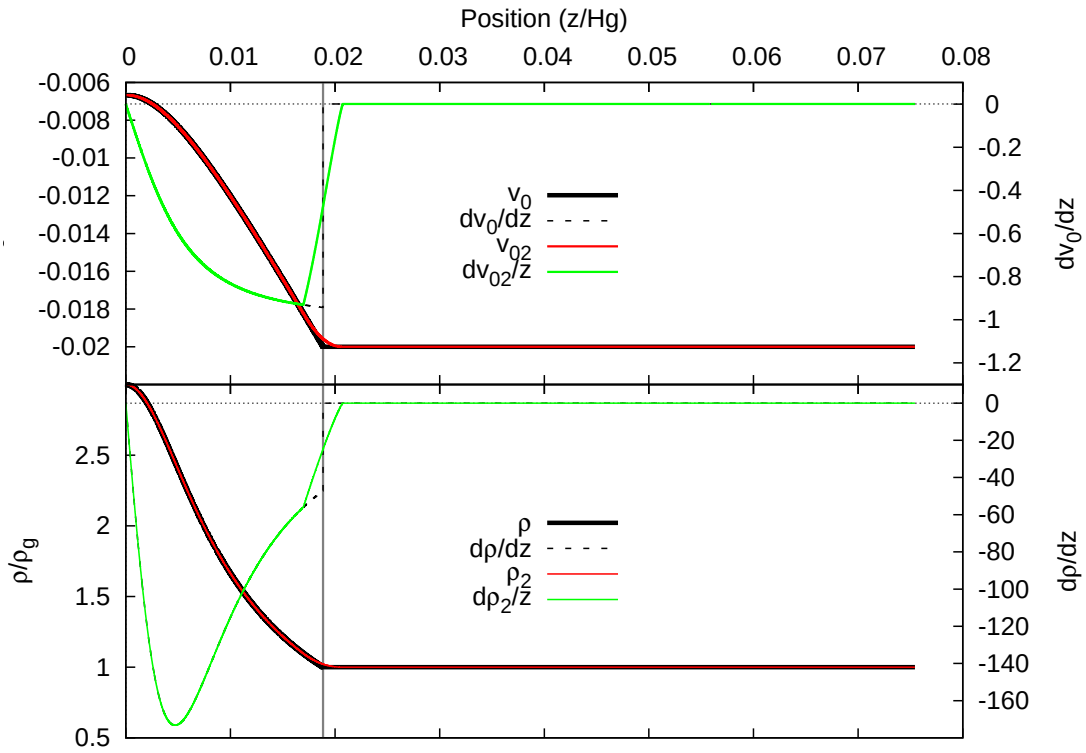

Figure C.5: Top: velocity background $\bar{v_0}$. Bottom: density background $\rho_0 = \rho_g + \rho_d(z)$. The black and red solid lines represent respectively the raw (Sekiya's) background profiles and the smoothed (C^1 class) profile. The black dashed and green lines are the derivatives of respectively the raw (Sekiya's) profile, and the smoothed profile.

where $\mu_0 = \frac{\rho_d}{\rho_g}$, is the initial dust-to-gas ration at the midplane, and

$$z_d = (Ri)^{\frac{1}{2}} \eta R \tag{C.38}$$

is a characteristic dust height. The dust density decrease from the midplane until it reaches zero at z_{max}:

$$|z_{max}| = \frac{\sqrt{\mu_0(2+\mu_0)}}{1+\mu_0} z_d \tag{C.39}$$

Figure C.5 represents the density background (bottom) and the derived velocity background (top). The subscript 2 stands for the smooth background we used in our simulations, to get rid of the discontinuity of the first derivative of the density at the end of the dust layer (details can be found in .2).

C.2.6 Numerical method

We follow the MAC method (Marker And Cell, Harlow and Welch (1965)), where the pressure is determined by demanding that the continuity equation is satisfied at the next step. Any other quantity is then updated using this value.

We have:

$$\nabla \cdot \mathbf{v} = ik'_x u_1 + ik_y v_1 + \frac{\partial w_1}{\partial z} \tag{C.40}$$

Using: (C.29)$\times ik'_x$, (C.30)$\times ik_y$ and taking the partial derivative of (C.31) with respect to z, we obtain:

$$\begin{aligned}\frac{\partial(\nabla\cdot\mathbf{v})}{\partial t} =& - ik_y\bar{v_0}(\nabla\cdot\mathbf{v}) - 2ik_y\frac{d\bar{v_0}}{dz}w_1 - \frac{1}{\rho_0}\left(-k_x'^2 - k_y^2 + \frac{\partial^2}{\partial z^2}\right)P_1 + \frac{1}{\rho_0^2}\frac{d\rho_0}{dz}\frac{\partial P_1}{\partial z} \\ &+ 2i\Omega_K k'_x\frac{\bar{v_0}}{\rho_0}\rho_1 + 2i\Omega_K k'_x v_1 + i\Omega_K k_y u_1 + \Omega_K^2\frac{d}{dz}\left(-\frac{z}{\rho_0}\rho_1\right)\end{aligned} \tag{C.41}$$

Using first order approximation ($\frac{\partial(\nabla\cdot\mathbf{v})}{\partial t} \simeq \frac{(\nabla\cdot\mathbf{v})^{n+1}-(\nabla\cdot\mathbf{v})^n}{\Delta t} = \frac{-(\nabla\cdot\mathbf{v})^n}{\Delta t}$), we finally get:

$$\begin{aligned}\left(-k_x'^2 - k_y^2 + \frac{\partial^2}{\partial z^2}\right)P_1^n = \rho_0\Big\{&\left((\Delta t)^{-1} - 2ik_y\bar{v_0}\right)(\nabla\cdot\mathbf{v})^n - 2ik_y\frac{d\bar{v_0}}{dz}w_1^n + 2i\Omega_K k_x'^n v_1^n \\ &+ i\Omega_K k_y u_1^n + 2i\Omega_K k_x'^n\frac{\bar{v_0}}{\rho_0}\rho_1^n + \Omega_K^2\frac{d}{dz}\left(-\frac{z}{\rho_0}\rho_1^n\right)\Big\}\end{aligned} \tag{C.42}$$

From this equation, we compute P_1^n, which we use to update every other quantity:

$$\rho_1^{n+1} = \rho_1^n + \Delta t\left\{-ik_y\bar{v_0}\rho_1^n - \frac{d\rho_0}{dz}w_1^n\right\} \tag{C.43}$$

$$u_1^{n+1} = u_1^n + \Delta t\left\{-ik_y\bar{v_0}u_1^n - ik_x'^n\frac{P_1^n}{\rho_0} + 2\Omega_K\frac{\bar{v_0}}{\rho_0}\rho_1^n + 2\Omega_K v_1^n\right\} \tag{C.44}$$

$$v_1^{n+1} = v_1^n + \Delta t\left\{-ik_y\bar{v_0}v_1^n - \frac{d\bar{v_0}}{dz}w_1^n - ik_y\frac{P_1^n}{\rho_0} + \frac{1}{2}\Omega_K v_1^n\right\} \tag{C.45}$$

$$w_1^{n+1} = w_1^n + \Delta t\left\{-ik_y\bar{v_0}w_1^n - \frac{1}{\rho_0}\frac{\partial P_1^n}{\partial z} - \frac{\Omega_K^2 z}{\rho_0}\rho_1\right\} \tag{C.46}$$

C.2.7 Second order accuracy

C.2.7.1 In time

In order to reach second order accuracy in time, we need to use a corrector-predictor like method. To do this, we first replace *n-th* quantities on the right-hand side of equation (C.42) by:

$$f_1^{n+\frac{1}{2}} = \frac{f_1^{n+1} + f_1^n}{2} \tag{C.47}$$

We then solve for $P_1^{n+\frac{1}{2}}$.

Using now the quantities $f_1^{n+\frac{1}{2}}$, we compute the new and more accurate (up to the second-order) perturbed velocities and density (equations (C.43) to (C.46)):

$$f_1^{n+1} = f_1^n + \Delta t\{F_1^{n+\frac{1}{2}}\} \tag{C.48}$$

where $F_1^{n+\frac{1}{2}}$ stands for any variable expressed at time $n + \frac{1}{2}$.

C.2.7.2 In space

We use a discretized grid in z of N cells. Each quantity is defined at the grid points.

We have to solve at each time step equation (C.42), written as:

$$A_n X = B_n \tag{C.49}$$

where A_n is an $N \times N$ tridiagonal (or band) matrix, X the vector ($X_i = P_1(i)$) to solve for, and B_n is the right-hand side of the equation.

We use an LU decomposition, which means that we don't explicitly solve for the inverse of A, but the solution X is a given function of L_{ij} and U_{ij}. Writing everything (derivative) up to second order gives the following expression:

$$A_{i,i} = -[2 + (k_x^{'2} + k_y^2)(\Delta x)^2] \tag{C.50}$$

$$A_{i,i+1} = 1 - \frac{1}{2\rho_0(i)}\frac{d\rho_0(i)}{dz} \tag{C.51}$$

$$A_{i+1,i} = 1 + \frac{1}{2\rho_0(i)}\frac{d\rho_0(i)}{dz} \tag{C.52}$$

and the boundary conditions, given by using a ghost cell ($i = 0$ or $i = N + 1$) and enforcing $\frac{\partial P_1}{\partial z} = 0$ at the two borders[2]:

$$A_{1,2} = 2 \tag{C.53}$$

$$A_{N,N-1} = 2 \tag{C.54}$$

C.2.8 Dimensionless quantities

In order to work with dimensionless, order of unity equations, we use dimensionless variables by setting:

$$H_g = 1 \tag{C.55}$$

$$\Omega_K = 1 \tag{C.56}$$

$$\rho_g = 1 \tag{C.57}$$

$$c_s = 1 \tag{C.58}$$

[2]It then gives: $2P_1(1) - (2 + (k_x^{'2} + k_y^2)(\Delta x)^2)P_1(0) = (\Delta x)^2 \times \mathrm{RHS}(i)$ at $z = 0$, and a similar expression at $z = z_{max}$.

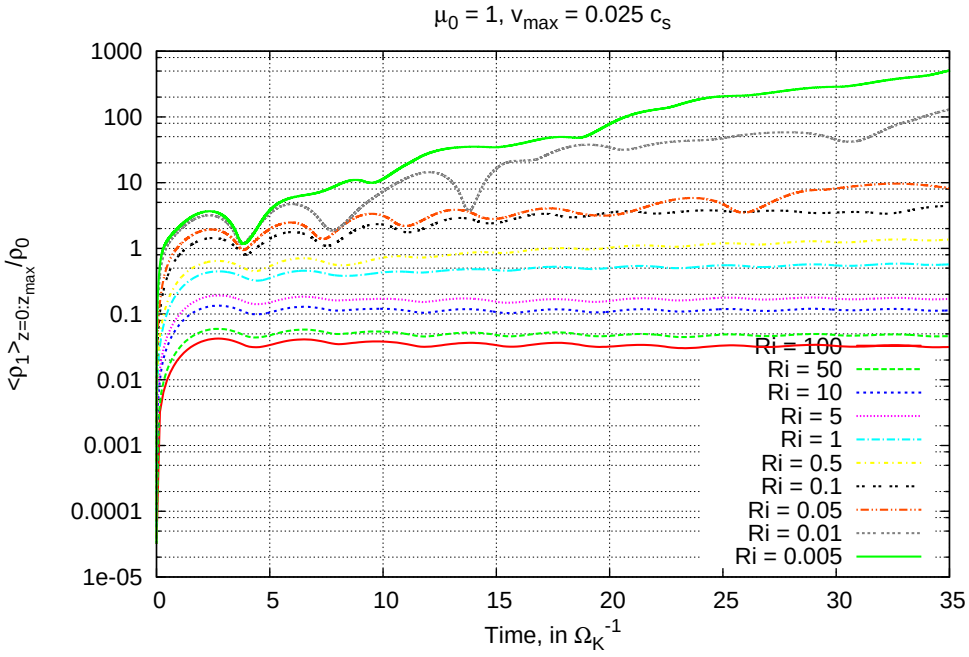

Figure C.6: Example of the given run, at fixed $\mu_0 = 1$ and $v_{max} = 0.025$, for a bunch of Richardson numbers. The value of the first peak (at about $T = 3$) is used in further studies. The normalized value of ρ_1 is plotted in function of the number of Kepler times.

We also define:

$$v_{max} = \eta R \Omega_K = \eta \frac{R}{H_g} c_s \tag{C.59}$$

Each simulation is then characterized by the choice of the density background, three free parameters $\left(Ri,\ \mu_0,\ \frac{v_{max}}{c_s}\right)$ and an initial perturbation $(u_1,\ v_1,\ w_1,\ \rho_1,\ P_1)$.

C.3 Results

The goal is to sample the space parameter in Ri versus μ_0. To do this, we have chosen to use the value of the first peak after an exponential growth for a given perturbed quantity: ρ_1. An example of what it gives is shown figure C.6, in the case $\mu_0 = 1$, and $v_{max} = 0.025$, for a bunch of different Richardson numbers.

The choice of the value of the first peak is motivated by its simplicity, and stability, contrarily to an expected criteria for stability at very long time. In later studies, we seek for a better and more physically justified parameter to measure in the simulations.

Because we carry out linear perturbation analysis, it's difficult to give a precise value for stability (or marginally stable runs). As a consequence, we don't give any typical value for stability, but we prefer to try and find *iso-stable* parameters. In detail, we use the raw value of the first peak in ρ_1, we normalize it to the initial total density $(\rho_g + \rho_d)$ at the midplane to have a scale-free value, and we then multiply it by the same total density to take into account the fact that we perturb the middle always with the same strength regardless of the density[3]. This is justified figure C.7, where we plot two different runs with two different initial *kicks*.

[3] A very dense midplane will be relatively less disturbed by the perturbation than a dust-free midplane.

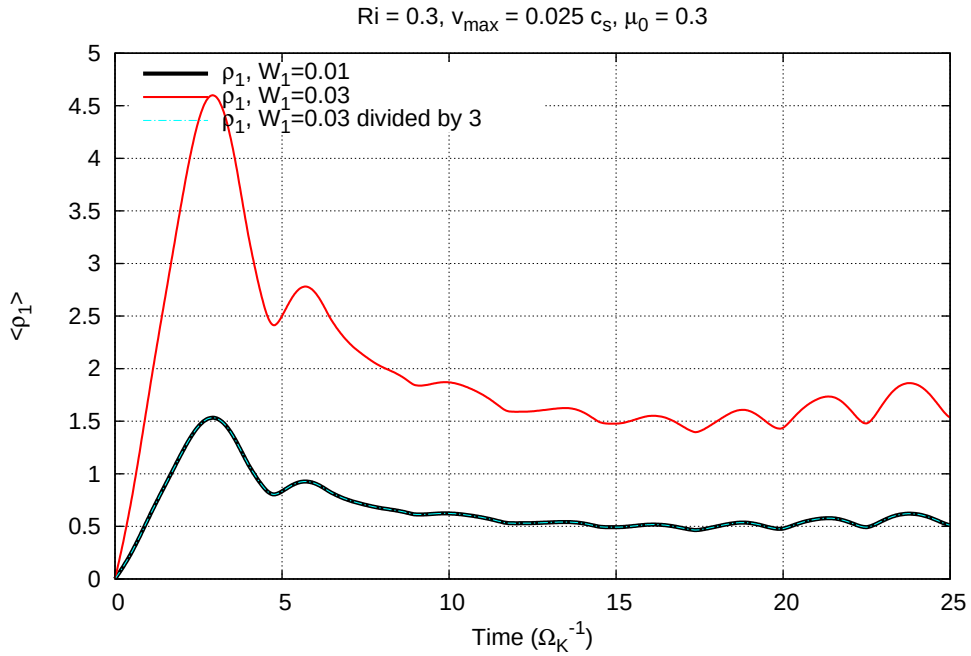

Figure C.7: Two different runs (solid lines) with two different initial conditions (amplitude of the perturbation in w_1 different by a factor 3). The rescaled run (dashed, blue line) give exactly the same result as the original run (solid black line).

C.3.1 Initial conditions

To carry out a simulation, we need to specify the background, as highlighted previously, but also to give the initial perturbation. We first chose to study only odd modes in w_1, and then to choose any other quantity the most simple way. Thus, we choose $\rho_1 = u_1 = 0$, and v_1 is given by equation (C.27):

$$w_1 = C_{w1}(\sin(k_z z) + i\sin(k_z z)) \tag{C.60}$$

$$v_1 = C_{w1}\frac{k_z}{k_y}(-\cos(k_z z) + i\cos(k_z z)) \tag{C.61}$$

These initial conditions are then updated through the process we described in the previous section. Figure C.8 shows two snapshots at $t = 0$ and a later ($t = 3\Omega_K^{-1}$) time.

C.3.2 The answer

We now are ready to answer the initial question, by sampling the space Ri/μ_0.

Figure C.9 is the semi-analytical answer to figure C.4 of Lee et al. (2010). What is important to notice is the dependence of Ri with μ_0 at low $\mu_0 < 10$, which confirms what has been seen in three-dimensional simulations by Lee et al. (2010). The behavior at larger metallicity ($\mu_0 > 10$) is qualitatively different: a constant Richardson number seems to be the right criteria to assess the stability of the layer. This doesn't contradict entirely previous simulations: the high-μ_0 runs in Lee et al. (2010) might not have reached convergence yet (blue triangles figure C.4 are values for marginal stability with twice the resolution, and have lower critical Richardson number.

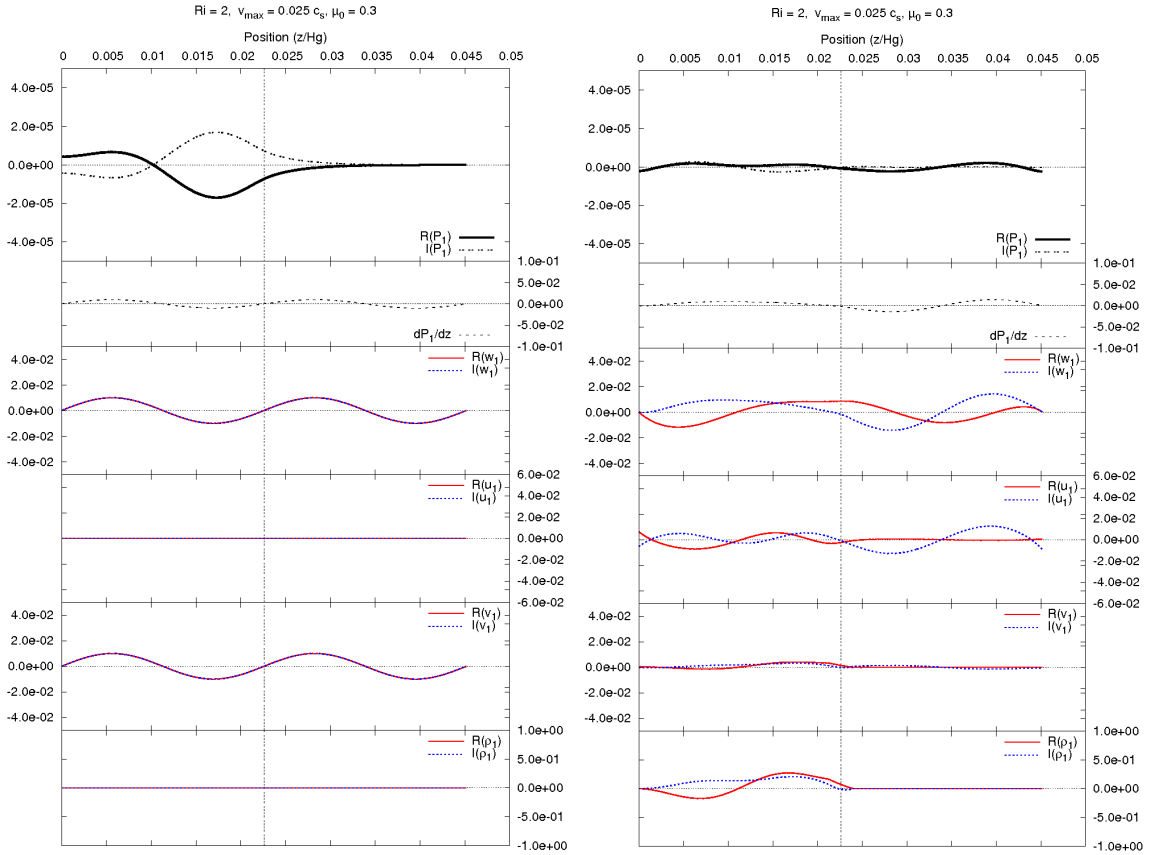

Figure C.8: Solid lines represent the real part of each quantity, and dashed lines the imaginary part. Left: initial perturbation ($t = 0\Omega_K^{-1}$). Right: later time ($t = 3\Omega_K^{-1}$).

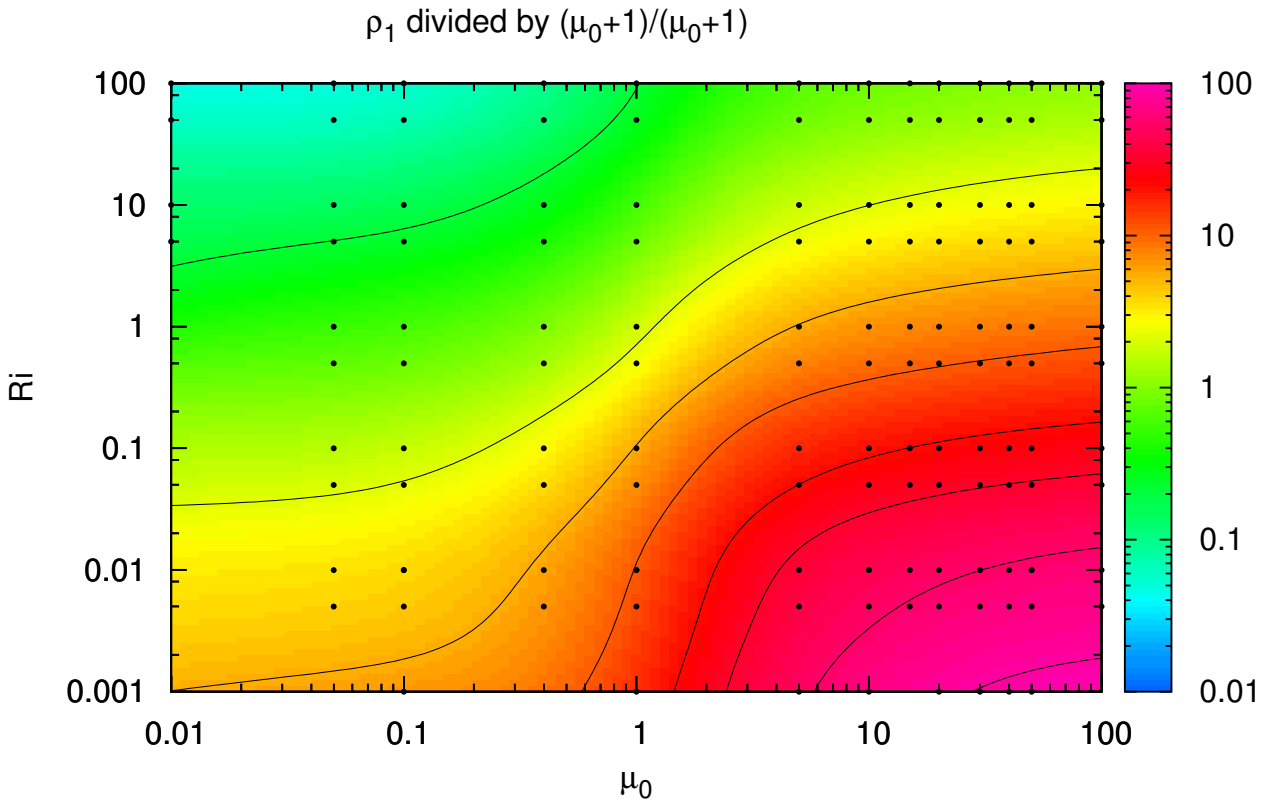

Figure C.9: This plot is an extrapolation to the whole Ri/μ_0 plane of several runs. Each dot represents a given simulation: Ri, v_{max} and μ_0, and then a value for ρ_1. The color-scale is the value of ρ_1 at the first peak, normalized and corrected according to the initial totel density at the midplane. The isolines are drawn in solid black lines.

C.3.3 Another criteria ?

This study supports the fact that the Richardson number is not the (only) relevant criteria to assess of the stability of the dust-rich midplane, as it had been foreseen by Lee et al. (2010) and Chiang (2008). Following Lee et al. (2010), we can try to derive a better fitted parameter, say the Shearing number, defined by analogy with the Richardson number as the square of the stabilizing effect (Kepler shearing frequency) over the vertical shearing rate:

$$Sh = \frac{|\frac{\partial \Omega_K}{\partial \ln r}|^2}{(\frac{\partial v_\phi}{\partial z})^2} \propto (\frac{\Delta z}{\Delta v_\phi})^2 \propto Ri \frac{1+\mu_0}{\mu_0} \tag{C.62}$$

If we assume that a marginally stable layer has a constant shearing number (we assume this number is the right criteria tu use), then we get:

$$Ri_{crit} \propto \mu_0 \quad \text{for } \mu_0 << 1 \tag{C.63}$$

$$Ri_{crit} \sim \text{constant} \quad \text{for } \mu_0 \gtrsim 1 \tag{C.64}$$

and this is what is seen figure C.9 !

C.4 Conclusions and work in progress

We have studied the stability of the equatorial, dust-rich midplane in protoplanetary disks, and found two trends. At low μ_0, the critical Richardson number goes linearly with μ_0, while at high μ_0, the critical Richardson number is constant.

The underlying consequence of this result for the formation of planetesimals is that a constant Richardson number for high μ_0 would lead to a requirement even lower than four times the solar nebula's bulk metallicity in order to trigger the gravitational instability in the dust-rich midplane (four times is what gives the linear fit on figures C.4).

Achieving supersolar bulk metallicities can be done locally, for example through radial pileup (Youdin and Shu (2004)). There are also other promising ways to achieve greater density (maybe up to the Toomre threshold !) with the streaming instability or turbulent concentration of particles, but they have not been studied here.

In the near future, we are going to continue this study, and try to represent in real coordinates the behavior of a particle (drawing the field lines).

Acknowledgement

I want to thank Takayuki Muto and Eugene Chiang, my two advisors for the duration of the project, for all the work they have done and all the help they gave me. Also, Pascale Garaud and all the local team, for making this program possible.

.1 Kelvin-Helmholtz instability

The Kelvin-Helmholtz instability (hereafter KHI) occurs in parallel shear flows, and is not to be mistaken as turbulence. This instability is not only of interest in astrophysics, but in almost any hydrodynamical process : clouds in earth, flows in pipes, or the giant vortex in Saturn. Basically, it is a competition between a destabilization: the shear between the two fluids which tends to mix

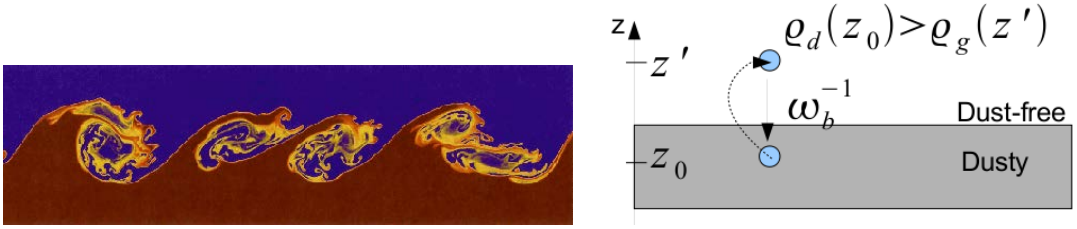

Figure 10: Left: illustration of the Kelvin-Helmholtz instability in a numerical simulation. Right: illustration of the buoyancy, the stabilisation of two layers of different density against the shear.

them in a single fluid; and a stabilisation: either the buoyancy (see figure 10 on the right) in the classical KHI, or another stabilizing effect such as the Keplerian shear in others contexts.

A good indicator for the stability of the layers against the KHI is the squared ratio of the Brunt-*Väisälä* frequency ($\omega_b = (\frac{g_z}{\rho}\frac{\partial \rho}{\partial z})^{\frac{1}{2}}$) over the shearing rate ($\omega_{shear} = \frac{dv_\phi}{dz}$): the Richardson number.

$$Ri = (\frac{\omega_b}{\omega_{shear}})^2 = \frac{\frac{g_z}{\rho}\frac{\partial \rho}{\partial z}}{(\frac{dv_\phi}{dz})^2} \tag{65}$$

For parallel two dimensional shear flows, the Richardson number is a good criteria to assess of the stability of the flows: the necessary condition for instability is $Ri < \frac{1}{4}$. Nevertheless for non parallel, three dimensional flows in a rotating frame, it is not obvious that the same criteria should apply !

.2 Smooth density background

Sekiya's (Sekiya (1998)) profile is discontinuous in the first derivative at the end of the dust layer. In order to make it continuous, with a Richardson number strictly increasing, various smoothing functions can be used. Two solutions based on powerlaws functions are implemented in the code.

The idea is to replace Sekiya's profile by a given function from a fixed height z_l to z_{up}. We use the following function:

$$\tilde{\rho_0} = 1 + a(z_{up} - z)^b \tag{66}$$

keeping one over the three parameters (a, z_{up}, b) fixed. This function guaranties a strict decrease in ρ_0, and the needed boundary conditions at $z = z_{up}$:

$$\rho_0(z_{up}) = 1 \tag{67}$$
$$\partial_z \rho_0(z_{up}) = 0 \tag{68}$$

We can solve for the two free parameters, using the fact that $\frac{\rho_0 - 1}{\partial_z \rho_0} = \frac{z_{up} - z}{-b}$ and the given boundary conditions:

$$\rho_0(z_l) = \tilde{\rho_0}(z_l) \tag{69}$$
$$\partial_z \rho_0(z_l) = \partial_z \tilde{\rho_0}(z_l) \tag{70}$$

Case 1: $z_{up} = z_l$ is fixed We have in that case:

$$b = \frac{(z_{up} - z_l)\rho_0^3}{(\rho_0 - 1)z_d^2} z_l \tag{71}$$

$$a = (\rho_0 - 1)(z_{up} - z_l)^{-b} \tag{72}$$

with $\rho_0 = \rho_0(z_l)$.

Case 2: $b = 3$ is fixed In this case, the upper limit of the smoothing is not fixed. We now have:

$$z_{up} = \frac{3(\rho_0 - 1)z_d^2}{z_l \rho_0^3} + z_l \tag{73}$$

$$a = \frac{1 - \rho_0}{(z_l - z_{up})^3} \tag{74}$$

Bibliography

Alexakis, A. (2011). Searching for the fastest dynamo: Laminar ABC flows. *Phys. Rev. E*, 84(2):026321.

Alexiades, V., Amiez, G., and Gremaud, P. A. (1996). Super Time Stepping acceleration of explicit schemes for parabolic problems. *Communications in Numerical methods in engineering*, 12:31–42.

Alfven, H. (1976). On frozen-in field lines and field-line reconnection. *J. Geo. Reas.*, 81:4019–4021.

André, P. (2002). The Initial Conditions for Protostellar Collapse: Observational Constraints. In Bouvier, J. and Zahn, J.-P., editors, *EAS Publications Series*, volume 3 of *EAS Publications Series*, pages 1–38.

Andre, P., Ward-Thompson, D., and Barsony, M. (2000). From Prestellar Cores to Protostars: the Initial Conditions of Star Formation. *Protostars and Planets IV*, page 59.

Archontis, V., Dorch, S., and Nordlund, Å. (2007). Nonlinear mhd dynamo operating at equipartition. *Astronomy and Astrophysics*, 472(3):715–726.

Balbus, S. A. and Hawley, J. F. (1991). A powerful local shear instability in weakly magnetized disks. I - Linear analysis. II - Nonlinear evolution. *Astrophys. J.*, 376:214–233.

Balbus, S. A. and Terquem, C. (2001). Linear Analysis of the Hall Effect in Protostellar Disks. *Astrophys. J.*, 552:235–247.

Balsara, D. S. (1996). Wave Propagation in Molecular Clouds. *Astrophys. J.*, 465:775–+.

Balsara, D. S. (2001). Divergence-Free Adaptive Mesh Refinement for Magnetohydrodynamics. *Journal of Computational Physics*, 174:614–648.

Basu, S. and Ciolek, G. E. (2004). Formation and Collapse of Nonaxisymmetric Protostellar Cores in Planar Magnetic Molecular Clouds. *Astrophys. J. Lett.*, 607:L39–L42.

Basu, S., Ciolek, G. E., Dapp, W. B., and Wurster, J. (2009). Magnetically-regulated fragmentation induced by nonlinear flows and ambipolar diffusion. , 14:483–495.

Basu, S. and Dapp, W. B. (2010). Long-lived Magnetic-tension-driven Modes in a Molecular Cloud. *Astrophys. J.*, 716:427–432.

Bate, M. R. (2011). Collapse of a molecular cloud core to stellar densities: the formation and evolution of pre-stellar discs. *MNRAS*, 417:2036–2056.

Bate, M. R. and Bonnell, I. A. (2005). The origin of the initial mass function and its dependence on the mean Jeans mass in molecular clouds. *MNRAS*, 356:1201–1221.

Belloche, A., André, P., Despois, D., and Blinder, S. (2002). Molecular line study of the very young protostar IRAM 04191 in Taurus: infall, rotation, and outflow. *A&A*, 393:927–947.

Berger, M. J. and Oliger, J. (1984). Adaptive Mesh Refinement for Hyperbolic Partial Differential Equations. *Journal of Computational Physics*, 53:484.

Black, D. C. and Scott, E. H. (1982). A numerical study of the effects of ambipolar diffusion on the collapse of magnetic gas clouds. *Astrophys. J.*, 263:696–715.

Bok, B. J. and Reilly, E. F. (1947). Small Dark Nebulae. *Astrophys. J.*, 105:255.

Bonnell, I. A., Clarke, C. J., and Bate, M. R. (2006). The Jeans mass and the origin of the knee in the IMF. *MNRAS*, 368:1296–1300.

Bonnor, W. B. (1956). Boyle's Law and gravitational instability. *MNRAS*, 116:351.

Bouya, I. and Dormy, E. (2013). Revisiting the ABC flow dynamo. *Physics of Fluids*, 25(3):037103.

Burkert, A. and Alves, J. (2009). The Inevitable Future of the Starless Core Barnard 68. *Astrophys. J.*, 695:1308–1314.

Chandrasekhar, S. and Fermi, E. (1953). Magnetic Fields in Spiral Arms. *Astrophys. J.*, 118:113.

Chiang, E. (2008). Vertical Shearing Instabilities in Radially Shearing Disks: The Dustiest Layers of the Protoplanetary Nebula. *Astrophys. J.*, 675:1549–1558.

Chiang, E. and Youdin, A. N. (2010). Forming Planetesimals in Solar and Extrasolar Nebulae. *Annual Review of Earth and Planetary Sciences*, 38:493–522.

Choi, E., Kim, J., and Wiita, P. J. (2009). An Explicit Scheme for Incorporating Ambipolar Diffusion in a Magnetohydrodynamics Code. *Astrophys. J., Suppl. Ser.* , 181:413–420.

Commerçon, B. (2009). *Formation d'étoiles : étude de l'effondrement des coeurs prestellaires*. PhD thesis, PhD Thesis, 2009.

Commerçon, B., Hennebelle, P., Audit, E., Chabrier, G., and Teyssier, R. (2010). Protostellar collapse: radiative and magnetic feedbacks on small-scale fragmentation. *A&A*, 510:L3.

Commerçon, B., Teyssier, R., Audit, E., Hennebelle, P., and Chabrier, G. (2011). Radiation hydrodynamics with adaptive mesh refinement and application to prestellar core collapse. I. Methods. *A&A*, 529:A35.

Courvoisier, A., Gilbert, A., and Ponty, Y. (2005). Dynamo action in flows with cat's eyes. *Geophysical and Astrophysical Fluid Dynamics*, 99(5):413–429.

Crutcher, R. M. (2009). OH and CN Zeeman Observations of Magnetic Fields in Molecular Clouds. In *Revista Mexicana de Astronomia y Astrofisica Conference Series*, volume 36 of *Revista Mexicana de Astronomia y Astrofisica Conference Series*, pages 107–112.

Crutcher, R. M., Hakobian, N., and Troland, T. H. (2009). Testing Magnetic Star Formation Theory. *Astrophys. J.*, 692:844–855.

Crutcher, R. M., Roberts, D. A., Troland, T. H., and Goss, W. M. (1999). The Magnetic Field of the NGC 2024 Molecular Cloud. *Astrophys. J.*, 515:275–285.

Dapp, W. B. and Basu, S. (2010). Averting the magnetic braking catastrophe on small scales: disk formation due to Ohmic dissipation. *A&A*, 521:L56+.

Dombre, T., Frisch, U., Henon, M., Greene, J. M., and Soward, A. M. (1986). Chaotic streamlines in the ABC flows. *Journal of Fluid Mechanics*, 167:353–391.

Duffin, D. F. and Pudritz, R. E. (2008). Simulating hydromagnetic processes in star formation: introducing ambipolar diffusion into an adaptive mesh refinement code. *MNRAS*, 391:1659–1673.

Ebert, R. (1955). Über die Verdichtung von H I-Gebieten. Mit 5 Textabbildungen. *Zeitschrift für Astrophysik*, 37:217.

Elmegreen, B. G. (1979). Magnetic diffusion and ionization fractions in dense molecular clouds - The role of charged grains. *Astrophys. J.*, 232:729–739.

Falle, S. A. E. G. (2003). A numerical scheme for multifluid magnetohydrodynamics. *MNRAS*, 344:1210–1218.

Falle, S. A. E. G. and Hartquist, T. W. (2002). Generation of density inhomogeneities by magnetohydrodynamic waves. *MNRAS*, 329:195–203.

Federrath, C., Chabrier, G., Schober, J., Banerjee, R., Klessen, R. S., and Schleicher, D. R. G. (2011). Mach Number Dependence of Turbulent Magnetic Field Amplification: Solenoidal versus Compressive Flows. *Physical Review Letters*, 107(11):114504.

Field, G. B. (1970). Theory of Star Formation, Introductory Report. *Memoires of the Societe Royale des Sciences de Liege*, 19:29.

Fromang, S., Hennebelle, P., and Teyssier, R. (2006). A high order Godunov scheme with constrained transport and adaptive mesh refinement for astrophysical magnetohydrodynamics. *A&A*, 457:371–384.

Galli, D., Lizano, S., Shu, F. H., and Allen, A. (2012). ERRATUM: "Gravitational Collapse of Magnetized Clouds. I. Ideal Magnetohydrodynamic Accretion Flow" <A href="/abs/2006ApJ...647..374G">(2006, ApJ, 647, 374)</A>. *Astrophys. J.*, 754:78.

Galli, D. and Shu, F. H. (1993). Collapse of Magnetized Molecular Cloud Cores. II. Numerical Results. *Astrophys. J.*, 417:243–+.

Gillis, J., Mestel, L., and Paris, R. B. (1974). Magnetic Braking During Star Formation, I. *Astrophys. and Space Science*, 27:167–194.

Gillis, J., Mestel, L., and Paris, R. B. (1979). Magnetic braking during star formation. II. *MNRAS*, 187:311–335.

Godunov, S. K. (1959). A Difference Scheme for Numerical Solution of Discontinuous Solution of Hydrodynamic Equations. *Math. Sbornik*.

González, M., Audit, E., and Huynh, P. (2007). HERACLES: a three-dimensional radiation hydrodynamics code. *A&A*, 464:429–435.

Goodman, A. A., Barranco, J. A., Wilner, D. J., and Heyer, M. H. (1998). Coherence in Dense Cores. II. The Transition to Coherence. *Astrophys. J.*, 504:223.

Goodman, A. A., Benson, P. J., Fuller, G. A., and Myers, P. C. (1993). Dense cores in dark clouds. VIII - Velocity gradients. *Astrophys. J.*, 406:528–547.

Grundy, R. E. and McLaughlin, R. (1982). Eigenvalues of the Barenblatt-Pattle Similarity Solution in Nonlinear Diffusion. *Proc. R. Soc. Lond.*, 383:89–100.

Harlow, F. H. and Welch, J. E. (1965). Numerical Calculation of Time-Dependent Viscous Incompressible Flow of Fluid with Free Surface. *Physics of Fluids*, 8:2182–2189.

Harten, A. (1983). High Resolution Schemes for Hyperbolic Conservation Laws. *Journal of Computational Physics*, 49:357.

Hayes, J. C., Norman, M. L., Fiedler, R. A., Bordner, J. O., Li, P. S., Clark, S. E., ud-Doula, A., and Mac Low, M.-M. (2006). Simulating Radiating and Magnetized Flows in Multiple Dimensions with ZEUS-MP. *Astrophys. J., Suppl. Ser.* , 165:188–228.

Heiles, C. and Crutcher, R. (2005). Magnetic Fields in Diffuse HI and Molecular Clouds. In Wielebinski, R. and Beck, R., editors, *Cosmic Magnetic Fields*, volume 664 of *Lecture Notes in Physics, Berlin Springer Verlag*, page 137.

Hennebelle, P. and Chabrier, G. (2011a). Analytical Star Formation Rate from Gravoturbulent Fragmentation. *Astrophys. J. Lett.*, 743:L29.

Hennebelle, P. and Chabrier, G. (2011b). Theories of the initial mass function. In J. Alves, B. G. Elmegreen, J. M. Girart, & V. Trimble, editor, *IAU Symposium*, volume 270 of *IAU Symposium*, pages 159–168.

Hennebelle, P. and Chabrier, G. (2013). Analytical Theory for the Initial Mass Function. III. Time Dependence and Star Formation Rate. *Astrophys. J.*, 770:150.

Hennebelle, P. and Ciardi, A. (2009). Disk formation during collapse of magnetized protostellar cores. *A&A*, 506:L29–L32.

Hennebelle, P., Commerçon, B., Joos, M., Klessen, R. S., Krumholz, M., Tan, J. C., and Teyssier, R. (2011). Collapse, outflows and fragmentation of massive, turbulent and magnetized prestellar barotropic cores. *A&A*, 528:A72+.

Hennebelle, P. and Fromang, S. (2008). Magnetic processes in a collapsing dense core. I. Accretion and ejection. *A&A*, 477:9–24.

Hennebelle, P. and Teyssier, R. (2008). Magnetic processes in a collapsing dense core. II. Fragmentation. Is there a fragmentation crisis? *A&A*, 477:25–34.

Hily-Blant, P., Falgarone, E., and Pety, J. (2008). Dissipative structures of diffuse molecular gas. III. Small-scale intermittency of intense velocity-shears. *A&A*, 481:367–380.

Hincelin, U. (2012). *Chemical and physical characterization of the first stages of protoplanetary disk formation.* PhD thesis, Université de Bordeaux, Observatoire Aquitain des Sciences de l'Univers, 2 rue de l'Observatoire, BP 89, 33271, Floirac Cedex, France ; CNRS, UMR 5804, Laboratoire d'Astrophysique de Bordeaux, 2 rue de l'Observatoire, BP 89, 33271, Floirac Cedex, France <EMAIL>ugo.hincelin@gmail.com</EMAIL>.

Holman, K., Walch, S. K., Goodwin, S. P., and Whitworth, A. P. (2013). Mapping the core mass function on to the stellar initial mass function: multiplicity matters. *MNRAS*, 432:3534–3543.

Hoyle, F. (1953). On the Fragmentation of Gas Clouds Into Galaxies and Stars. *Astrophys. J.*, 118:513.

Hunter, C. (1977). The collapse of unstable isothermal spheres. *Astrophys. J.*, 218:834–845.

Ishitsu, N. and Sekiya, M. (2003). The effects of the tidal force on shear instabilities in the dust layer of the solar nebula. *icarus*, 165:181–194.

Joos, M., Hennebelle, P., and Ciardi, A. (2012). Protostellar disk formation and transport of angular momentum during magnetized core collapse. *A&A*, 543:A128.

Joos, M., Hennebelle, P., Ciardi, A., and Fromang, S. (2013). The influence of turbulence during magnetized core collapse and its consequences on low-mass star formation. *A&A*, 554:A17.

Khokhlov, A. (1998). Fully Threaded Tree Algorithms for Adaptive Refinement Fluid Dynamics Simulations. *Journal of Computational Physics*, 143:519–543.

Kolmogorov, A. N. (1941). Dissipation of Energy in Locally Isotropic Turbulence. *Akademiia Nauk SSSR Doklady*, 32:16.

Krasnopolsky, R., Li, Z., and Shang, H. (2010). Disk Formation Enabled by Enhanced Resistivity. *Astrophys. J.*, 716:1541–1550.

Krasnopolsky, R., Li, Z.-Y., Shang, H., and Zhao, B. (2012). Protostellar Accretion Flows Destabilized by Magnetic Flux Redistribution. *Astrophys. J.*, 757:77.

Kroupa, P., Weidner, C., Pflamm-Altenburg, J., Thies, I., Dabringhausen, J., Marks, M., and Maschberger, T. (2013). *The Stellar and Sub-Stellar Initial Mass Function of Simple and Composite Populations*, page 115.

Krumholz, M. R., Crutcher, R. M., and Hull, C. L. H. (2013). Protostellar Disk Formation Enabled by Weak, Misaligned Magnetic Fields. *Astrophys. J. Lett.*, 767:L11.

Krumholz, M. R., Klein, R. I., and McKee, C. F. (2012). Radiation-hydrodynamic Simulations of the Formation of Orion-like Star Clusters. II. The Initial Mass Function from Winds, Turbulence, and Radiation. *Astrophys. J.*, 754:71.

Kunz, M. W. and Mouschovias, T. C. (2009). The Nonisothermal Stage of Magnetic Star Formation. I. Formulation of the Problem and Method of Solution. *Astrophys. J.*, 693:1895–1911.

Kunz, M. W. and Mouschovias, T. C. (2010). The non-isothermal stage of magnetic star formation - II. Results. *MNRAS*, 408:322–341.

Larson, R. B. (1969). Numerical calculations of the dynamics of collapsing proto-star. *MNRAS*, 145:271–+.

Larson, R. B. (1981). Turbulence and star formation in molecular clouds. *MNRAS*, 194:809–826.

Lazarian, A. (2013). Reconnection Diffusion, Star Formation and Numerical Simulations. *ArXiv e-prints*.

Leão, M. R. M., de Gouveia Dal Pino, E. M., Santos-Lima, R., and Lazarian, A. (2012). Cloud core collapse and the role of turbulent magnetic reconnection diffusion. *ArXiv e-prints*.

Lee, A. T., Chiang, E., Asay-Davis, X., and Barranco, J. (2010). Forming Planetesimals by Gravitational Instability. I. The Role of the Richardson Number in Triggering the Kelvin-Helmholtz Instability. *Astrophys. J.*, 718:1367–1377.

Lee, C. W., Myers, P. C., and Plume, R. (2004). A Survey for Infall Motions toward Starless Cores. III. CS (3-2) and DCO^+ (2-1) Observations. *Astrophys. J., Suppl. Ser.* , 153:523–543.

Lesaffre, P. and Balbus, S. A. (2007). Exact shearing box solutions of magnetohydrodynamic flows with resistivity, viscosity and cooling. *MNRAS*, 381:319–333.

Levrier, F. (2004). Velocity centroids and the structure of interstellar turbulence. I. Analytical study. *A&A*, 421:387–398.

Li, Z.-Y., Krasnopolsky, R., and Shang, H. (2011). Nonideal MHD Effects and Magnetic Braking Catastrophe in Protostellar Disk Formation. *ArXiv e-prints*.

Li, Z.-Y., Krasnopolsky, R., and Shang, H. (2013). Does Magnetic Field-Rotation Misalignment Solve the Magnetic Braking Catastrophe in Protostellar Disk Formation? *ArXiv e-prints*.

Li, Z.-Y. and Shu, F. H. (1996). Magnetized Singular Isothermal Toroids. *Astrophys. J.*, 472:211–+.

Lizano, S. and Shu, F. H. (1987). Heating of molecular cloud cores. *RMxAA*, 14:587–594.

Mac Low, M., Norman, M. L., Konigl, A., and Wardle, M. (1995). Incorporation of ambipolar diffusion into the ZEUS magetohydrodynamics code. *Astrophys. J.*, 442:726–735.

Machida, M. N., Inutsuka, S., and Matsumoto, T. (2006). Second Core Formation and High-Speed Jets: Resistive Magnetohydrodynamic Nested Grid Simulations. *Astrophys. J. Lett.*, 647:L151–L154.

Machida, M. N., Inutsuka, S., and Matsumoto, T. (2007a). Magnetic Fields and Rotations of Protostars. *Astrophys. J.*, 670:1198–1213.

Machida, M. N., Inutsuka, S., and Matsumoto, T. (2008). High- and Low-Velocity Magnetized Outflows in the Star Formation Process in a Gravitationally Collapsing Cloud. *Astrophys. J.*, 676:1088–1108.

Machida, M. N., Inutsuka, S., and Matsumoto, T. (2009). The Circumbinary Outflow: A Protostellar Outflow Driven by a Circumbinary Disk. *Astrophys. J. Lett.*, 704:L10–L14.

Machida, M. N., Inutsuka, S.-i., and Matsumoto, T. (2007b). Driving Mechanism of Jets and Outflows in Star Formation Process. *ArXiv e-prints*.

Machida, M. N., Inutsuka, S.-i., and Matsumoto, T. (2010). Effect of Magnetic Braking on the Circumstellar Disk Formation in a Strongly Magnetized Cloud. *ArXiv e-prints*.

Machida, M. N. and Matsumoto, T. (2011). The origin and formation of the circumstellar disc. *MNRAS*, pages 284–+.

Machida, M. N., Matsumoto, T., Tomisaka, K., and Hanawa, T. (2005). Collapse and fragmentation of rotating magnetized clouds - I. Magnetic flux-spin relation. *MNRAS*, 362:369–381.

Masson, J., Teyssier, R., Mulet-Marquis, C., Hennebelle, P., and Chabrier, G. (2012). Incorporating Ambipolar and Ohmic Diffusion in the AMR MHD Code RAMSES. *Astrophys. J., Suppl. Ser.* , 201:24.

Mathis, J. S., Rumpl, W., and Nordsieck, K. H. (1977). The size distribution of interstellar grains. *Astrophys. J.*, 217:425–433.

Matrà, L., Merín, B., Alves de Oliveira, C., Huélamo, N., Kóspál, A., Cox, N. L. J., Ribas, Á., Puga, E., Vavrek, R., Royer, P., Prusti, T., Pilbratt, G. L., and André, P. (2012). A new Herschel view of the young star T54: not a transitional disk? *A&A*, 548:A111.

Matsumoto, T. and Tomisaka, K. (2004). Directions of Outflows, Disks, Magnetic Fields, and Rotation of Young Stellar Objects in Collapsing Molecular Cloud Cores. *Astrophys. J.*, 616:266–282.

Maury, A. J., André, P., Hennebelle, P., Motte, F., Stamatellos, D., Bate, M., Belloche, A., Duchêne, G., and Whitworth, A. (2010). Toward understanding the formation of multiple systems. A pilot IRAM-PdBI survey of Class 0 objects. *A&A*, 512:A40.

Mellon, R. R. and Li, Z. (2009). Magnetic Braking and Protostellar Disk Formation: Ambipolar Diffusion. *Astrophys. J.*, 698:922–927.

Mestel, L. and Paris, R. B. (1979). Magnetic braking during star formation. III. *MNRAS*, 187:337–356.

Mestel, L. and Spitzer, Jr., L. (1956). Star formation in magnetic dust clouds. *MNRAS*, 116:503–+.

Mihalas, D. and Mihalas, B. W. (1984a). *Foundations of radiation hydrodynamics*.

Mihalas, D. and Mihalas, B. W. (1984b). On the Propagation of Acoustic Waves in a Radiative Fluid. *Astrophys. J.*, 283:469.

Mouschovias, T. C. (1978). Magnetic braking and ambipolar diffusion in dense interstellar clouds: star formation. In *Stars and Star Systems*, page 34.

Mouschovias, T. C. (1979). Magnetic braking of self-gravitating, oblate interstellar clouds. *Astrophys. J.*, 228:159–162.

Mouschovias, T. C. and Paleologou, E. V. (1978). The Angular Momentum Problem and Magnetic Braking: An Exact, Time-Dependent Solution. In *Bulletin of the American Astronomical Society*, volume 10 of *Bulletin of the American Astronomical Society*, page 680.

Mouschovias, T. C. and Paleologou, E. V. (1979). The angular momentum problem and magnetic braking - an exact time-dependent solution. *Astrophys. J.*, 230:204–222.

Mouschovias, T. C. and Paleologou, E. V. (1980a). Magnetic braking of an aligned rotator during star formation - an exact, time-dependent solution. *Astrophys. J.*, 237:877–899.

Mouschovias, T. C. and Paleologou, E. V. (1980b). The angular momentum problem and magnetic braking during star formation - Exact solutions for an aligned and a perpendicular rotator. *Moon and Planets*, 22:31–45.

Mouschovias, T. C. and Spitzer, Jr., L. (1976). Note on the collapse of magnetic interstellar clouds. *Astrophys. J.*, 210:326–+.

Myers, P. C., Linke, R. A., and Benson, P. J. (1983). Dense cores in dark clouds. I - CO observations and column densities of high-extinction regions. *Astrophys. J.*, 264:517–537.

Nakamura, F. and Li, Z. (2008). Magnetically Regulated Star Formation in Three Dimensions: The Case of the Taurus Molecular Cloud Complex. *Astrophys. J.*, 687:354–375.

Nakano, T., Nishi, R., and Umebayashi, T. (2002). Mechanism of Magnetic Flux Loss in Molecular Clouds. *Astrophys. J.*, 573:199–214.

Neufeld, D. A., Lepp, S., and Melnick, G. J. (1995). Thermal Balance in Dense Molecular Clouds: Radiative Cooling Rates and Emission-Line Luminosities. *Astrophys. J., Suppl. Ser.* , 100:132.

Nishi, R., Nakano, T., and Umebayashi, T. (1991). Magnetic flux loss from interstellar clouds with various grain-size distributions. *Astrophys. J.*, 368:181–194.

O'Sullivan, S. and Downes, T. P. (2006). Numerical Modeling of Weakly Ionized Plasmas. In G. P. Zank & N. V. Pogorelov, editor, *Numerical Modeling of Space Plasma Flows*, volume 359 of *Astronomical Society of the Pacific Conference Series*, page 178.

Padovani, M. and Galli, D. (2013). Cosmic-Ray Propagation in Molecular Clouds. In Torres, D. F. and Reimer, O., editors, *Cosmic Rays in Star-Forming Environments*, volume 34 of *Advances in Solid State Physics*, page 61.

Pandey, B. P. and Wardle, M. (2008). Hall magnetohydrodynamics of partially ionized plasmas. *MNRAS*, 385:2269–2278.

Panoglou, D., Cabrit, S., Pineau Des Forêts, G., Garcia, P. J. V., Ferreira, J., and Casse, F. (2012). Molecule survival in magnetized protostellar disk winds. I. Chemical model and first results. *A&A*, 538:A2.

Panoglou, D., Garcia, P. J. V., Cabrit, S., and Forêts, G. P. D. (2009). *Survival of H_2 and CO in MHD Disk Winds of Class 0, Class I and Class II Stars*, pages 595–596.

Penston, M. V. (1969). Dynamics of self-gravitating gaseous spheres-III. Analytical results in the free-fall of isothermal cases. *MNRAS*, 144:425.

Pineda, J. E., Goodman, A. A., Arce, H. G., Caselli, P., Foster, J. B., Myers, P. C., and Rosolowsky, E. W. (2010). Direct Observation of a Sharp Transition to Coherence in Dense Cores. *Astrophys. J. Lett.*, 712:L116–L121.

Pinto, C. and Galli, D. (2008). Three-fluid plasmas in star formation. II. Momentum transfer rate coefficients. *A&A*, 484:17–28.

Pinto, C. and Galli, D. (2009). *Three-Fluid Magnetohydrodynamics in Star Formation*, pages 597–599.

Pinto, C., Galli, D., and Bacciotti, F. (2008). Three-fluid plasmas in star formation. I. Magnetohydrodynamic equations. *A&A*, 484:1–15.

Press, W. H., Teukolsky, S. A., Vetterling, W. T., and Flannery, B. P. (2007). *Numerical Recipes 3rd Edition: The Art of Scientific Computing*. Cambridge University Press, New York, NY, USA, 3 edition.

Safronov, V. S. and Zvjagina, E. V. (1969). Relative Sizes of the Largest Bodies during the Accumulation of Planets. *icarus*, 10:109–+.

Saumon, D., Chabrier, G., and van Horn, H. M. (1995). An Equation of State for Low-Mass Stars and Giant Planets. *Astrophys. J., Suppl. Ser.* , 99:713.

Sauty, C., Cayatte, V., Lima, J. J. G., Matsakos, T., and Tsinganos, K. (2012). Counterrotation in Magnetocentrifugally Driven Jets and Other Winds. *Astrophys. J. Lett.*, 759:L1.

Schmalzl, M., Kainulainen, J., Quanz, S. P., Alves, J., Goodman, A. A., Henning, T., Launhardt, R., Pineda, J. E., and Román-Zúñiga, C. G. (2010). Star Formation in the Taurus Filament L 1495: From Dense Cores to Stars. *Astrophys. J.*, 725:1327–1336.

Schönke, J. and Tscharnuter, W. M. (2011). Protostellar collapse of rotating cloud cores. Covering the complete first accretion period of the stellar core. *A&A*, 526:A139.

Seifried, D., Banerjee, R., Pudritz, R. E., and Klessen, R. S. (2013). Turbulence-induced disc formation in strongly magnetized cloud cores. *MNRAS*.

Sekiya, M. (1998). Quasi-Equilibrium Density Distributions of Small Dust Aggregations in the Solar Nebula. *icarus*, 133:298–309.

Shu, F. H. (1977). Self-similar collapse of isothermal spheres and star formation. *Astrophys. J.*, 214:488–497.

Shu, F. H. (1992). Books-Received - the Physics of Astrophysics - V.2 - Gas Dynamics. *Journal of the British Astronomical Association*, 102:230–+.

Shu, F. H., Lizano, S., and Adams, F. C. (1987). Star formation in molecular cloud cores. In M. Peimbert & J. Jugaku, editor, *Star Forming Regions*, volume 115 of *IAU Symposium*, pages 417–433.

Sicilia-Aguilar, A., Henning, T., Linz, H., André, P., Stutz, A., Eiroa, C., and White, G. J. (2013). Protostars, multiplicity, and disk evolution in the Corona Australis region: a Herschel Gould Belt Study. *A&A*, 551:A34.

Spezzi, L., Cox, N. L. J., Prusti, T., Merin, B., Ribas, A., Alves de Oliveira, C., Winston, E., Kospal, A., Royer, P., Vavrek, R., Andre, P., Pilbratt, G. L., Testi, L., Bressert, E., Ricci, L., Menshchikov, A., and Konyves, V. (2013). The Herschel Gould Belt Survey in Chamaeleon II - Properties of cold dust in disks around young stellar objects. *ArXiv e-prints*.

Spitzer, Jr., L. (1949). The Formation of Stars. *Leaflet of the Astronomical Society of the Pacific*, 5:336.

Stone, J. M. and Norman, M. L. (1992). ZEUS-2D: A radiation magnetohydrodynamics code for astrophysical flows in two space dimensions. I - The hydrodynamic algorithms and tests. *Astrophys. J., Suppl. Ser.* , 80:753–790.

Teyssier, R. (2002). Cosmological hydrodynamics with adaptive mesh refinement. A new high resolution code called RAMSES. *A&A*, 385:337–364.

Teyssier, R., Fromang, S., and Dormy, E. (2006). Kinematic dynamos using constrained transport with high order Godunov schemes and adaptive mesh refinement. *Journal of Computational Physics*, 218:44–67.

Tilley, D. A. and Balsara, D. S. (2008). A two-fluid method for ambipolar diffusion. *MNRAS*, 389:1058–1073.

Tilley, D. A. and Balsara, D. S. (2011). Two-fluid ambipolar diffusion for molecular clouds with realistic heating and cooling. *MNRAS*, 415:3681–3692.

Tomida, K., Tomisaka, K., Matsumoto, T., Hori, Y., Okuzumi, S., Machida, M. N., and Saigo, K. (2013). Radiation Magnetohydrodynamic Simulations of Protostellar Collapse: Protostellar Core Formation. *Astrophys. J.*, 763:6.

Toro, E. F. (2009). *Riemann Solvers and Numerical Methods for Fluid Dynamics*. third edition edition.

Toth, G. (1994). Numerical study of two-fluid C-type shock waves. *Astrophys. J.*, 425:171–194.

Toth, G. and Roe, P. (2002). Divergence- and curl-preserving prolongation and restriction formulas. *Journal of Computational Physics*, 180:736–750.

Tsap, Y. T., Stepanov, A. V., and Kopylova, Y. G. (2012). Ambipolar diffusion and magnetic reconnection. *Astronomy Reports*, 56:138–145.

Umebayashi, T. and Nakano, T. (1990). Magnetic flux loss from interstellar clouds. *MNRAS*, 243:103–113.

van Leer, B. (1979). Towards the ultimate conservative difference scheme. V - A second-order sequel to Godunov's method. *Journal of Computational Physics*, 32:101–136.

van Loo, S., Falle, S. A. E. G., Hartquist, T. W., and Barker, A. J. (2008). The effect of ambipolar resistivity on the formation of dense cores. *A&A*, 484:275–280.

Vaytet, N., Audit, E., Chabrier, G., Commerçon, B., and Masson, J. (2012). Simulations of protostellar collapse using multigroup radiation hydrodynamics. I. The first collapse. *A&A*, 543:A60.

Vaytet, N., Chabrier, G., Audit, E., Commerçon, B., Masson, J., Ferguson, J., and Delahaye, F. (2013a). Simulations of protostellar collapse using multigroup radiation hydrodynamics. II. The second collapse. *A&A*, 557:A90.

Vaytet, N., González, M., Audit, E., and Chabrier, G. (2013b). The influence of frequency-dependent radiative transfer on the structures of radiative shocks. *Journal of Quantitative Spectroscopy and Radiative Transfer*, 125:105–122.

Vaytet, N. M. H., Audit, E., Dubroca, B., and Delahaye, F. (2011). A numerical model for multigroup radiation hydrodynamics. *Journal of Quantitative Spectroscopy and Radiative Transfer*, 112:1323–1335.

von Hoerner, S. (1951). Eine Methode zur Untersuchung der Turbulenz der interstellaren Materie. Mit 10 Textabbildungen. *Zeitschrift für Astrophysik*, 30:17.

von Hoerner, S., Burbidge, G. R., Kahn, F. D., Ebert, R., and Temesvary, S. (1959). *Die Entstehung von Sternen durch Kondensation diffuser Materie*.

Wardle, M. (1991). Instability in oblique C-type shocks. *MNRAS*, 251:119–127.

Watson, A. M., Stapelfeldt, K. R., Wood, K., and Ménard, F. (2007a). Multiwavelength Imaging of Young Stellar Object Disks: Toward an Understanding of Disk Structure and Dust Evolution. *Protostars and Planets V*, pages 523–538.

Watson, D. M., Bohac, C. J., Hull, C., Forrest, W. J., Furlan, E., Najita, J., Calvet, N., D'Alessio, P., Hartmann, L., Sargent, B., Green, J. D., Kim, K. H., and Houck, J. R. (2007b). The development of a protoplanetary disk from its natal envelope. *Nature*, 448:1026–1028.

Weidenschilling, S. J. (1980). Dust to planetesimals - Settling and coagulation in the solar nebula. *icarus*, 44:172–189.

Youdin, A. (2008). From Grains to Planetesimals: Les Houches Lecture. *ArXiv e-prints*.

Youdin, A. N. and Shu, F. H. (2004). Planetesimal Formation by Gravitational Instability - The Goldreich-Ward Hypothesis Revisited. In A. Penny, editor, *Planetary Systems in the Universe*, volume 202 of *IAU Symposium*, pages 250–+.

Zhou, S., Evans, II, N. J., Koempe, C., and Walmsley, C. M. (1993). Evidence for protostellar collapse in B335. *Astrophys. J.*, 404:232–246.

Zweibel, E. G. (2002). Ambipolar Drift in a Turbulent Medium. *Astrophys. J.*, 567:962–970.

Zweibel, E. G. and Heitsch, F. (2008). Fast Dynamos in Weakly Ionized Gases. *Astrophys. J.*, 684:373–379.